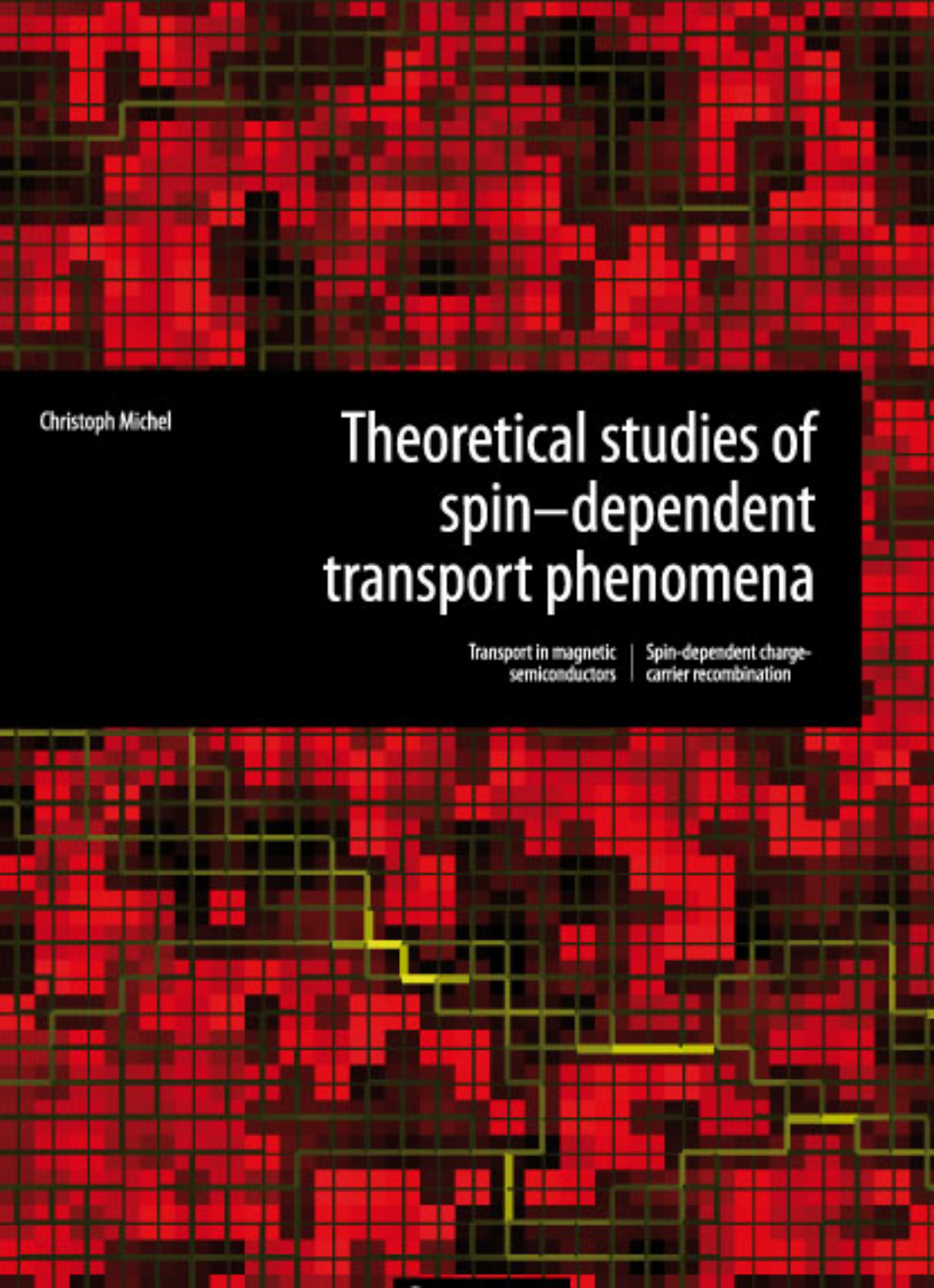
Christoph Michel
Theoretical studies of spin–dependent transport phenomena
Transport in magnetic semiconductors
Spin-dependent charge-carrier recombination

Theoretical studies of spin-dependent transport phenomena

Dissertation

zur
Erlangung des Doktorgrades
der Naturwissenschaften
(Dr. rer. nat.)

dem
Fachbereich Physik
der Philipps-Universität Marburg
vorgelegt von

Christoph Michel

aus
Frankenberg/Eder

Marburg/Lahn, 2007

Vom Fachbereich Physik der Philipps-Universität Marburg
als Dissertation angenommen am 26.11.2007.

Erstgutachter: Prof. Dr. Peter Thomas
Zweitgutachter: Prof. Dr. Peter J. Klar, Justus-Liebig Universität Gießen

Tag der mündlichen Prüfung: 04.12.2007

Bibliografische Informationen der Deutschen Nationalbibliothek
Die Deutsche Nationalbibliothek verzeichnet diese Publikation in der Deutschen Nationalbibliografie; detaillierte bibliografische Daten sind im Internet über http://dnb.ddb.de abrufbar.

1. Aufl. - Göttingen: Cuvillier, 2007
Zugl.: Marburg, Univ., Diss., 2007
ISBN 978-3-86727-485-2

Nonnenstieg 8, 37075 Göttingen
Telefon: 0551-54724-0
Telefax: 0551-54724-21
www.cuvillier.de

In memory of Erika and Werner Marburger

Preface

Compared with nothing, little is much.

Marburg, Germany,
April 2004

C.M.

Abstract

The work presented here deals with spin-dependent transport properties in semiconductors.
The phenomenologic model developed in the first part describes activated semiconductor band-transport in a disordered system using a network approach. It is shown that in (Ga,Mn)As considered as the archetype of a dilute magnetic semiconductor, the measured non-Arrhenius dependence of the resistivity can be explained in the framework of band transport. This finding is not limited to the special choice of the material and is in contrast to the common belief reported in the literature, that such a characteristic feature of the resistivity is indicative for hopping transport. In addition the influence on the transport properties of an external magnetic field is analyzed which interacts with the localized magnetic moments of the Mn ions. This interaction, called giant Zeeman splitting, leads to spin-dependent splittings of the heavy and light hole valence-band proportional to the local Mn concentration and thus reflects the spatially disordered incorporation of Mn ions. The resulting disordered potential landscape is converted into a network of resistors. By use of the model one can describe even quantitatively the experimentally obtained transport properties of a series of differently annealed $Ga_{1-x}Mn_xAs$ samples from the ferromagnetic metallic regime via a paramagnetic semiconducting regime up to a two-phase hybrid where the segregation of MnAs has set in. An extension to MnAs/GaAs:Mn hybrid structures shows that experimental results can be explained at least qualitatively assuming spin conservation, the formation of a Schottky barrier and taking into account the interaction between the ferromagnetic clusters and the paramagnetic matrix. Based on this description tailored hybrid structures are proposed which show strongly enhanced magnetoresistance effects.

The second part deals with the microscopic simulation of spin-dependent charge-carrier recombination as it can be observed e.g. in hydrogenated microcrystalline silicon (μc-Si:H) by pulsed electrically detected electron-spin resonance (pEDMR). The recombination process via a two particle system, the so-called *intermediate pair*, is mapped on the dynamics of a four level system. Besides the regimes of different light-field coupling-strength different strengths of the exchange coupling are studied and criteria are shown that allow us to assign the measured data to one of the regimes. It is shown that present deviations between experimental results and the theoretical description can be eliminated by introducing a particular, well defined disorder in the model calculations.

Kurzfassung

Die vorliegende Arbeit behandelt die theoretische Beschreibung von spinabhängigem Transport in Halbleitern.
Das im ersten Teil entwickelte phänomenologische Modell beschreibt aktivierten Halbleiter-Bandtransport in einem ungeordneten System mittels einer Netzwerkbeschreibung. Das in (Ga,Mn)As, dem Archetyp eines magnetischen Halbleiters, gemessene nicht-Arrheniussche Widerstandsverhalten kann in diesem Transportregime unter der Annahme von Unordnung erklärt werden. Diese Aussage ist nicht auf das spezielle Material beschränkt und steht im Widerspruch zur häufig in der Literatur vertretenen Meinung, eine solche Widerstandscharakteristik sei nur im Rahmen von Hopping-Transport erklärbar. Untersucht wird auch der Transporteinfluss eines äußeren Magnetfeldes, welches mit den lokalisierten magnetischen Momenten der Mn-Ionen wechselwirkt. Die resultierende *giant Zeeman splitting* genannte spinabhängige lokale Aufspaltung der Valenzbänder ist proportional zur (lokalen) Mn-Konzentration und reflektiert den räumlich ungeordneten Einbau der Mn-Ionen. Die sich ergebende ungeordnete Potentiallandschaft wird in ein Netzwerk lokaler Widerstände umgerechnet. Das Model ist in der Lage, die experimentellen Transportergebnisse einer Serie von getemperten $Ga_{1-x}Mn_xAs$ Proben vom ferromagntischen metallischen Regime über einen paramagnetischen Halbleiter bis zur Segregation einer zweiten Phase aus MnAs sogar quantitativ zu beschreiben. Die Ausdehnung auf MnAs/GaAs:Mn Metal-Halbleiter Hybride zeigt, dass experimentelle Ergebnisse durch Annahme von Spinerhaltung, einer Schottky-Barriere sowie der Wechselwirkung des ferromagnetischen Clusters mit der Matrix zumindest qualitativ zu erklären sind. Darauf basierend werden maßgeschneiderte Hybridsysteme vorgeschlagen, welche stark erhöhte Magnetowiderstandseffekte zeigen.

Der zweite Teil beschäftigt sich mit der mikroskopischen Simulation von spinabhängiger Rekombination, welche z.B. in wasserstoffgesättigtem mikrokristallinem Silizium (μc-Si:H) mittels gepulster elektrisch detektierter Elektronenspinresonanz (pEDMR) gemessen werden kann. Diese Rekombination über *intermediate pair* genannte Zweiteilchen-Zustände wird auf die Dynamik eines vier-Niveau Systems abgebildet. Neben den Regimes verschiedener Lichtfeldkopplung werden unterschiedliche Austauschkopplungen simuliert und Charakteristika aufgezeigt, die es erlauben, die gemessenen Daten den verschiedenen Regimes zuzuordnen. Die Abweichungen zwischen bisherigen theoretischen Beschreibungen und den gemessenen Daten können durch Einbeziehung einer speziellen, wohldefinierten Unordnung in den Modellrechnungen beseitigt werden.

Contents

List of Figures

Part I

Transport in magnetic semiconductors

1

Introduction

1.1 Introduction

Both ferromagnetic and paramagnetic dilute magnetic semiconductors (DMS) are currently of interest in the context of spintronics and spin optoelectronics. These technologies combine the merits of semiconductor-electronic and magneto-electronic devices [1, 2].

Magnetoresistance measurements on DMS are well established techniques to analyze the interplay of electronic and magnetic properties in dilute magnetic semiconductors. So far spin-dependent scattering was applied successfully for the interpretation of transport measurements in ferromagnetic metallic GaMnAs random alloys, where the ferromagnetic coupling can be explained by a Ruderman-Kittel-Kasuya-Yosida (RKKY) mechanism [3, 4, 5]. However, these theories are no longer applicable for semiconducting samples in the paramagnetic phase (e.g. obtained by annealing at elevated temperatures) or DMS materials which even show segregation of clusters. The RKKY-based theories are limited to metallic random GaMnAs alloys where disorder effects can be neglected to a first approximation. Recently hybrid systems formed out of ferromagnetic clusters embedded in a paramagnetic host matrix raised particular attention [6, 7, 8, 9]. They are considered as possible candidates for the creation of spintronic devices working at room temperature. Along with this interest, there is the need to find a proper theoretical model for the description of the material and transport properties of this highly complex material class, e.g. beyond the the scope of (microscopic) RKKY theories. It is the aim of this work to show that the transport properties of the matrix material and of the hybrid structures can be described taking into account disorder aspects as a major issue. The (macroscopic) description we use is rather empirical, but it may serve as a first step towards a microscopic theory.

We start by introducing a network model for the description of the magnetotransport in p-type dilute magnetic semiconductors in the paramagnetic phase. The model is based on a simplified description of the valence-band structure and the acceptor state of the DMS. Band filling effects, magnetic-field splitting of the band states due to the p-d exchange interaction as well as effects of magnetic-field independent disorder are accounted for. We do not include carrier-carrier interactions other than those responsible for the local magnetism of the Mn ions. Despite the exclusion of many-body effects[1] in the bands, positive as well as negative MR effects are predicted by the model [10] which show a qualitative agreement with experiments on paramagnetic p-type DMS [11, 12]. The model is adopted to the quantitative description of Mn doped GaAs which serves as the archetypal dilute magnetic semiconductor. As a physical by-catch on the way towards a fundamental description of this material (from the limit of a very dilute Mn incorporation over annealed samples which show segregation trends to the other limit of paramagnetic/ferromagnetic hybrid samples), an alternative explanation of a non-Arrhenius temperature dependence of the resistivity is given. It is clearly shown that in contrast to common oppinion a non-Arrhenius temperature dependence is not inevitably indicative of hopping transport. This rather fundamental conclusion is not limited to the special choice of dilute magnetic semiconductors.
In chapter 3 the model is extended to provide a quantitative description of a series of annealed $Ga_{0.98}Mn_{0.02}As$ samples. It also serves for the first systematic theoretical study of the magnetotransport properties of $Ga_{1-x}Mn_xAs/MnAs$ hybrid structures in chapter 5. The first part of this work ends with a prediction for the design of hybrid structures tailored to show strongly enhanced magnetoresistance effects for possible future spintronic applications.

1.2 Dilute magnetic semiconductors – an overview

A dilute magnetic semiconductor is a semiconductor with a small (dilute) fraction of magnetic ions incorporated on lattice sites. Due to the exchange interaction between the localized spins of the magnetic ions and the spins of the free carriers they exhibit unusual magnetic properties. Two major classes of DMS are wide-gap (II,Mn)VI and (III,Mn)V alloys [13, 14, 15]. The magnetism of such DMS will strongly depend on the Mn content, the electronic configuration of the Mn ion and on the degree of doping. While in

[1] As a matter of fact, whenever in the following 'many-body effects' are claimed to be excluded, all many-body effects are neglected except the p-d exchange interaction which is expressly included.

(II,Mn)VI compounds the Mn is built in isoelectronically on group II cation sites, in (III,Mn)V alloys the Mn ions are incorporated on cation sites acting as acceptors. In particular the intrinsic correlation of transport and magnetic properties in the III-Mn-V semiconductors aroused the interest of researchers [16, 17, 18, 19]. The most prominent and best studied representative of the (III,Mn)V alloys is $Ga_{1-x}Mn_xAs$. In ideal $Ga_{1-x}Mn_xAs$ the Mn ions are spatially randomly incorporated on Ga sites Mn_{Ga} acting as acceptors [20], whilst the half filled Mn 3d-shell provides $S = \frac{5}{2}$ localized magnetic moments [21]. Since (II,Mn)VI compounds exhibit paramagnetic behavior up to very high Mn contents, the combination of free holes and large localized magnetic moments yields ferromagnetism in $Ga_{1-x}Mn_xAs$ alloys. An Ruderman-Kittel-Kasuya-Yosida (RKKY) mechanism is considered to be responsible for the origin of ferromagnetism in this material. This is where the ferromagnetic coupling between the localized Mn spins is mediated by the free holes in the valence band [3, 22, 23, 24, 25]. Even though GaAs:Mn shows a paramagnetic phase down to very low temperatures in the dilute regime, possible Curie temperatures above room temperature are predicted theoretically for higher Mn contents [26, 27]. However, the highest Curie temperature realized experimentally so far in this alloy system is $T_C = 173\,K$ [28].

For temperatures above T_C the magnetization of dilute magnetic semiconductor alloys is usually described by a modified Brillouin function accounting for residual magnetic coupling between the magnetic ions. In paramagnetic (II,Mn)VI alloys (where the magnetic properties are determined solely by superexchange between Mn ions) the residual coupling is reflected by the temperature dependence of the susceptibility, the inverse susceptibility follows a linear Curie-Weiss temperature dependence at higher temperatures, but shows a clear down bend when the temperature decreases [29, 30, 31, 32, 33]. This behavior shows the temperature-induced change of the magnetic coupling. The origin of this unusual behavior is the formation of antiferromagnetically coupled nearest-neighbor Mn spins at low temperatures which break up with increasing temperature [31]. It is worth noting that somewhat similar effects may be anticipated for the magnetization of (III,Mn)V alloys above T_C, leading to a Curie-Weiss parameter Θ which will depend on the sample properties as well as on temperature. A detailed study of the influence of Θ on the magnetotransport properties of a $Ga_{1-x}Mn_xAs$ alloy and a first attempt to clarify its dependence on the beforehand mentioned sample properties as well as on temperature by comparison with experimental data is given in chapter 3.

Possible DMS-based designs consist either of ferromagnetic DMS [13], paramagnetic DMS [34, 35, 36, 37] or paramagnetic-ferromagnetic hybrid structures [38]. (Ga,Mn)As/MnAs is a typical example of such a hybrid structure. In this hybrid, ferromagnetic MnAs clusters are embedded in a paramag-

netic $Ga_{1-x}Mn_xAs$ host matrix. Several current studies show that DMS-based hybrid systems exhibit large positive and negative magneto-resistance (MR) effects. Examples are the MR behavior of $Ga_{1-x}Mn_xAs$/MnAs [39, 40, 41], of GaAs/ErAs [42], of GaAs:Mn/MnSb [43, 44] and of $Ge_{1-y}Mn_y$:$Mn_{11}Ge_8$ [45]. However, so far the microscopic mechanisms are not at all understood because the galvano-magnetic properties of such granular ferromagnetic hybrid systems depend strongly on the electronic transport properties of the paramagnetic matrix material, the magnetic properties of the clusters and on the interaction of the electronic states of the host matrix with the ferromagnetic clusters. Of course, one essential prerequisite for understanding the galvano-magnetic properties of the hybrids are detailed experimental and theoretical studies of the transport in the paramagnetic DMS materials which act as host matrix for the clusters.

Multiple magneto-transport experiments were reported on wide-gap DMS alloys covering n-type $Cd_{1-x}Mn_xTe$ [46] and $Cd_{1-x}Mn_xSe$ [47] and more recently p-type DMS such as $Zn_{1-x}Mn_xTe$:N [11] and paramagnetic $Ga_{1-x}Mn_xAs$ [12]. It is worth noting that already the paramagnetic DMS alloy alone (i.e. without clusters) exhibits positive as well as negative MR effects [11, 12, 46, 47, 48]. However, these are different from those in the corresponding hybrids [41]. The unusual MR effects of the paramagnetic DMS are commonly explained by the interplay of band filling, magnetic-field induced tuning of the band structure, carrier-carrier interactions and quantum corrections [48, 49, 50, 51, 52, 53]. As an example, the influence of the magnetic-field induced tuning of the alloy disorder on the galvano-magnetic properties of DMS was included so far only in the magnetic polaron picture [54]. It arises due to fluctuations in the Mn concentration which, in an applied magnetic field, lead to local fluctuations of the Mn-induced band splitting. Magnetic-field tuning of alloy disorder is a well known feature of DMS [55, 56, 57, 58]. On the other hand, it is well established that disorder in crystalline semiconductor alloys and even more in amorphous semiconductors has a considerable impact on the transport properties [59].

1.3 The transport model

According to the transport theory of Drude in a system which is considered to be isotropic the resistivity ρ and the conductivity $\nu = \frac{1}{\rho}$ can be represented in terms of carrier density n and carrier mobility μ as

$$\rho = \frac{1}{n \cdot q \cdot \mu} \tag{1.1}$$

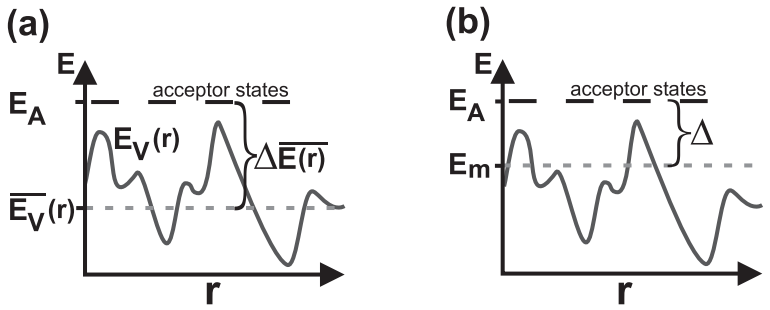

Fig. 1.1. For a doped semiconductor with a spatially disordered valence-band edge it holds $\Delta < (E_A - \overline{E_V}(r))$ (a) shows the energy spacing $\overline{\Delta E}(r)$ between the average valence-band edge $\overline{E_V}(r)$ (dashed grey line) and the acceptor level E_A. (b) illustrates the activation energy $\Delta = (E_A - E_m)$ given by the energy spacing between the acceptor energy E_A and the mobility edge E_m (dashed grey line).

where q denotes the carrier's charge. In the framework of a semiclassical transport description the mobility μ can be decomposed as $\mu = \frac{q \cdot \tau}{m^\star}$ where τ represents the average time between two scattering events and $m^\star$ is the effective mass. The density of carriers in a semiconductor[2] is given by

$$n = \int_{-\infty}^{E_V} N(E) F^h(E) dE \tag{1.2}$$

where E_V is the band-edge energy-level of the unperturbed valence band, $N(E)$ is the density of states in the valence band and $F^h(E)$ is the Fermi distribution of holes. Usually this direct current resistivity ρ in doped semiconductors can be simplified and represented by an Arrhenius temperature dependence

$$\rho = \tilde{\rho} \cdot exp(\Delta / k_\mathrm{B} T) \tag{1.3}$$

where $\tilde{\rho}$ is a pre-exponential factor, Δ is the activation energy and k_B is the Boltzmann constant. A detailed analysis of the validity of such a simplification depending on specific material parameters is given in chapter 2.

Disorder in the transport dominating band of a semiconductor can be taken into account e.g. by a modification (a disorder-dependent reduction) of the mobility. It is obvious that the mean free path (herewith τ) gets reduced with increasing spatial fluctuations of the potential. Also the carrier density gets affected by disorder. Besides a change of the position of the Fermi level,

[2] Since $Ga_{1-x}Mn_xAs$ that is in the focus of this work is a p-type semiconductor, we leave here the general description and concentrate on a semiconductor with hole transport in the valence band.

due to the fluctuations of the local valence-band edge $E_V(r)$, holes on acceptor states do not have to be activated to the spatial average of the valence-band edge $\overline{E_V}(r)$ but merely to an energy level E_m, the so-called mobility edge. As illustrated in Fig. 1.1 the required activation energy Δ is given by $\Delta = (E_A - E_m)$. It holds $\Delta < (E_A - \overline{E_V}(r))$. Descriptions of the transport properties in (doped) disordered semiconductors following this approach can be found e.g. in [59, 60, 61] as well as in [10] where a comparison with the alternative description given in the following is presented. Another attempt to handle a transport description in the presence of disorder is to separate a given disordered system into a number of subsystems which are so small, that inside each single subsystem the influence of disorder can be neglected. The transport properties of each of these ordered subsystems can be calculated according to Eqn. 1.1 and 1.2. The members of this ensemble of subsystems have to be connected somehow to represent the physical realities and the macroscopic transport variables of the global system have to be derived.

1.3.1 General limitation of the approach

There is, however, one problem with the used description which should not be concealed: Apart from the issue of finding the correct subsystem size which represents the disorder in the system (discussed in detail in section 1.4.1), one should keep in mind, that there exists a lower boundary of this subsystem size. For subsystem sizes below this boundary the transport properties have to be described quantum mechanically [62, 63]. Finding the exact value of this lower boundary and its connection to parameters of the system is a field of current research [64]. Therefore we follow a very pragmatic route and hope that all subsystem sizes of use are large enough - an assumption that indeed does not make the treatment of the given problem simple but at least drastically simplifies it compared to the universal approach[3].

1.3.2 The magnetoresistance

The material system we analyze is the magnetic semiconductor $Ga_{1-x}Mn_xAs$ which in this work is in the main described in its paramagnetic phase. The obtained results form a basis of the study of so-called paramagnetic-ferromagnetic hybrid structures built out of a $Ga_{1-x}Mn_xAs$ host matrix with embedded ferromagnetic MnAs clusters as shown in chapter 5. Discussed in

[3] "It would mean that the only possibility that remains is to describe the whole universe at once by using one huge Hilbert space. It goes without saying that such an approach will lead to many other problems" [63].

more detail in section 1.3.3 the interaction of the localized magnetic moments of the Mn-ions with an external magnetic field and their exchange interaction with the valence-band states lead to a strong spin-selective splitting of the valence band. According to this local variations of the carrier densities n as well as a modified mobility μ arise due to the magnetic field induced disorder effects. These modifications of quantities appearing in Eqn. 1.1 cause a noticeable change of the resistivity. To access the magnetic fields influence on the resistivity the macroscopic observable magnetoresistance (MR) is introduced

$$\mathrm{MR} = \frac{\rho_m - \rho_0}{\rho_0}, \tag{1.4}$$

ρ_m is the resistivity in the presence of an external magnetic field while ρ_0 is the resistivity at zero field. Negative values of MR represent a resistivity that decreases in the presence of an external magnetic field (in other words the conductivity increases). The lower boundary of the magnetoresistance for $\rho_m \leq \rho_0$ is given by MR$= -1$. For positive values of the MR the opposite situation holds with $\rho_m < \rho_0$ and no general upper boundary exists.

1.3.3 Interaction with an external magnetic field

In this section the interaction of a DMS with an external magnetic field $\mathbf{H}$ is described briefly. For all further considerations the magnetic field is taken as a weak perturbation and eigenvalues of the system Hamilton operator for $\mathbf{H} = 0$ are assumed to be known i.e. the band structure in the absence of an external magnetic field is given. For simplicity the energy gets normalized by the value of the unperturbed valence-band edge using $E_V = 0$ at $\mathbf{H} = 0$. Starting point is the magnetic part $\mathcal{H}_\mathrm{m}$ of the single-particle system Hamilton operator $\mathcal{H}$ describing the interaction between a free carrier with spinoperator $\mathbf{s}$, an external magnetic field $\mathbf{H} = (0, 0, H)$ oriented in z-direction and the system of magnetic ions with spinoperators $\mathbf{S}_i$

$$\begin{aligned}&\mathcal{H}_\mathrm{m}(\mathbf{s}, \mathbf{S_i}) = \\ &\underbrace{\mathcal{H}_\mathrm{L} + g\mu_\mathrm{B}\mu_0 \mathbf{s}\cdot\mathbf{H}}_{I} \underbrace{- 2\sum_i J_i \mathbf{S_i}\cdot\mathbf{s}}_{II} + \underbrace{g'\mu_\mathrm{B}\mu_0\mathbf{H}\sum_i \mathbf{S_i} - \sum_{i\neq j} J'_{i,j}\mathbf{S_i}\cdot\mathbf{S_j}}_{III}.\end{aligned} \tag{1.5}$$

Part I describes the diamagnetic Landau quantization by $\mathcal{H}_\mathrm{L}$ and the contribution of the paramagnetic Zeeman splitting as for a pure diamagnetic material. In part II the exchange interaction between the carrier and the localized magnetic ions is taken into account while part III covers the interaction between the magnetic ions and the external field as well as the interaction among the

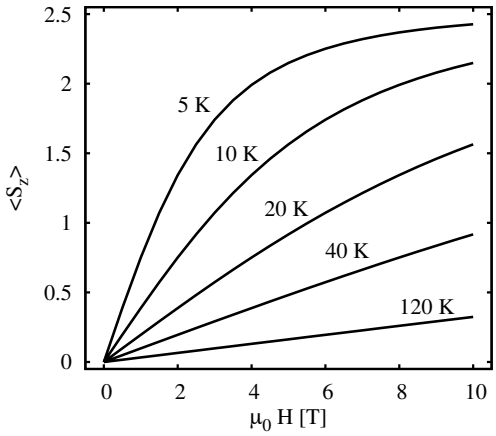

Fig. 1.2. The graphs show the average orientation of the Mn $\frac{5}{2}$-spins depending on an external magnetic field for different temperatures as indicated in the figure. The value of $\langle S_z \rangle$ is basically given by use of the Brillouin function in Eqn. 1.9.

magnetic ions. $J'_{i,j}$ and J_i are constants given in Heisenberg notation describing the strength of the microscopic coupling between the magnetic ions and the interaction between the magnetic ions and the free carrier spin, respectively. We neglect the influence of the free carriers on the magnetic ions. Thus a ferromagnetic coupling of the localized magnetic moments mediated by the band states as well as a carrier induced polarization of the magnetic ions is disregarded. Such a restriction seems arguable since the description of the paramagnetic phase is in the focus of this work. This approach allows the decoupling of the magnetic ion- and carrier spin-operators yielding a separation of $\mathcal{H}(\mathbf{s}, \mathbf{S_i})$ given by

$$\mathcal{H}_{\mathrm{m}}(\mathbf{s}, \mathbf{S}_i) \;=\; \mathcal{H}_{\mathrm{m}}(\mathbf{S}_i) + \mathcal{H}_{\mathrm{m}}(\mathbf{s}) \tag{1.6}$$

with

$$\mathcal{H}_{\mathrm{m}}(\mathbf{S}_i) = g' \mu_{\mathrm{B}} \mu_0 \mathbf{H} \sum_i \mathbf{S}_i - \sum_{i \neq j} J'_{i,j} \mathbf{S}_i \cdot \mathbf{S}_j \tag{1.7}$$

$$\mathcal{H}_{\mathrm{m}}(\mathbf{s}) = \mathcal{H}_{\mathrm{L}} + g \mu_{\mathrm{B}} \mu_0 \mathbf{s} \cdot \mathbf{H} - 2 \sum_i J_i \mathbf{S}_i \mathbf{s} \tag{1.8}$$

$\mathcal{H}_{\mathrm{m}}(\mathbf{S_i})$ describes the system of localized magnetic moments while $\mathcal{H}_{\mathrm{m}}(\mathbf{s})$ represents the magnetic field induced change of the band structure. Firstly we set $J'_{i,j} = 0$ neglecting the coupling between the d-shells of different Mn ions.[4] Using the molecular-field approximation one can substitute the summation

[4] In general we consider the dilute limit, where the spatial separation between the Mn ions is sufficiently large to neglect direct coupling.

over the lattice sites occupied by Mn ions in Eqn. 1.8 with the thermal average of the Mn-ion spin $< S_z >$ in respect of the direction of the external field. $< S_z >$ is basically given by

$$< S_z >= a \cdot S \cdot B_f(\zeta') \tag{1.9}$$

where $B_f(\zeta') = \frac{6}{5} coth\left(\frac{6\zeta'}{5}\right) - \frac{1}{5} coth\left(\frac{\zeta'}{5}\right)$ is the Brillouin function for a particle with spin $S = \frac{5}{2}$ with $\zeta' = \frac{2\mu_B \mu_0 H}{k_B(T-\Theta)}$. B_f does basically depend on the fraction $\frac{H}{T}$. With increasing magnetic-field strength $< S_z >$ increases almost linearly and finally saturates at $< S_z >= \frac{5}{2}$ (for $a = 1$). With increasing temperature the increase of $< S_z >$ gets weaker and the saturation orientation is reached at higher magnetic fields. The characteristic development of the $< S_z >$ values depending on the magnetic field for various temperatures is shown in Fig. 1.2; for a derivation of B_f see appendix C.

The (antiferromagnetic) coupling between the Mn ions which was neglected when setting $J'_{i,j} = 0$ can be taken into account phenomenologically by use of the parameter a in Eqn. 1.9. In all calculations $a = 1$ is used if not stated explicitly. The parameter Θ in the denominator of the Brillouin function's argument plays the role of the Curie-Weiss temperature. It accounts for an antiferromagnetic coupling when $\Theta < 0$ while a ferromagnetic coupling of the Mn ions spins is represented by $\Theta > 0$. The Curie Weiss parameter plays an important role for the quantitative modelling of annealed $Ga_{1-x}Mn_xAs$ samples as it is shown in chapter 3. As a summary of the discussed interactions with an external magnetic field, that are considered in the model, the interaction diagram given in Fig. 1.3 can be used.

In the next step $\mathcal{H}_m(\mathbf{s})$ accounting for the spin-dependent modifications of the band structure can be simplified. We start with the third part of Eqn. 1.5 which describes the exchange interaction between the localized spins of the Mn ions and the spins of the carriers: Considering that the carrier wave function is extended over several Mn ions their spin becomes independent of the lattice site and can be substituted by the average value $< S_z >$ given by Eqn. 1.9, which can be treated as a pre-summation factor. Now the virtual crystal approximation comes into play. Instead of a summing over all lattice sites occupied by Mn ions and the local evaluation of the microscopic coupling constant $J_i(\mathbf{r} - \mathbf{R_i})$ an infinite crystal is assumed, leading to a coupling constant which becomes a constant value independent of the spatial coordinate i and weighted with the average Mn concentration x: $\sum_i J(\mathbf{r}-\mathbf{R_i}) \approx x \sum_R J(\mathbf{r}-\mathbf{R}) = x \cdot N_0 \beta$. The used parameter is the p-d (s-d) exchange integral $N_0\beta(\alpha)$ where N_0 denotes the number of cations per cm^3 while $\beta(\alpha)$ gives the strength of the interaction of the Mn spin with a valence-band (conduction-band) state. This weighting with the average value of the spatial Mn concentration is justified

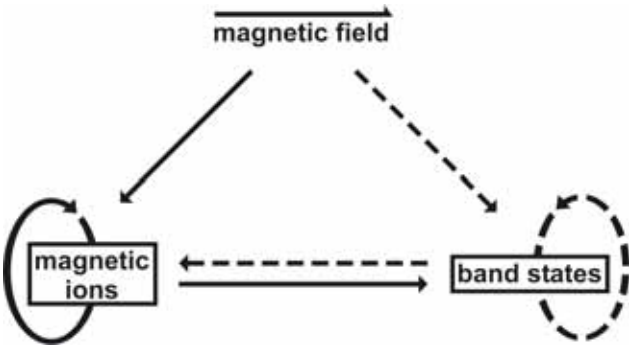

Fig. 1.3. The interaction diagram shows the interactions with the external magnetic field. Dashed lines denote interactions which are neglected while solid lines denote interactions that are taken into account such as the orientation of the Mn spins and the p-d exchange interaction between the local Mn spins and the band states.

only in the case of a homogeneous distribution of the Mn ions. As soon as the distribution of Mn ions shows sufficiently large local fluctuations the Hamilton operator of the system varies spatially. In this case the averaging over the local Mn concentration that neglects this spatial dependence is no longer a good approximation. Thus when taking into account significant spatial fluctuations of the magnetic ion concentration this approximation has to be improved. A possible treatment is given in Sect. 1.3.4.

The resulting expression for the exchange part $\mathcal{H}_{\rm ex}$ of $\mathcal{H}_{\rm m}(\mathbf{s})$ is

$$\mathcal{H}_{\rm ex} \approx -\frac{1}{3}\mathbf{s} < S_z > xN_0\beta \tag{1.10}$$

where the sum over the microscopic coupling constant J is replaced and gets represented in terms of the p-d exchange integral $N_0\beta$. This yields a macroscopic description of the exchange interaction. For the description of exchange effects in the conduction band, the corresponding exchange integral $N_0\alpha$ has to be used.

For the materials which are in the focus of our description the effects of the Landau diamagnetism as well as the Pauli paramagnetism which leads to the usual Zeeman splitting are much less than the so-called *giant Zeeman splitting* (GZS) described by $\mathcal{H}_{\rm ex}$. Thus both remaining parts of $H_{\rm m}(\mathbf{s})$ are neglected.

By using the Hamilton operator in Eqn. 1.10 the pseudospin-dependent energy shifts $\Delta E_V(j_z, H, T)$ of the heavy- and light-hole valence-band states are given by

$$\Delta E_V(j_z, H, T) = -\frac{1}{3}xN_0\beta < S_z > j_z \tag{1.11}$$

where $j_z = \pm\frac{3}{2}(\pm\frac{1}{2})$ are the pseudospins of the heavy holes (light holes). The influence of the magnetic field is solely included by the average orientation of the Mn $\frac{5}{2}$-spin given by the Brillouin function in Eqn. 1.9.

In conclusion, Eqn. 1.11 describes the giant Zeeman splitting of the valence-band subbands with the pseudospins $\pm\frac{3}{2}$ and $\pm\frac{1}{2}$ if an external magnetic field in z-direction is applied on an ideal $Ga_{1-x}Mn_xAs$ crystal[5] in the pure paramagnetic phase. This forms the basis of all further calculations.

1.3.4 The mesoscopic virtual-crystal approximation

As shown in the previous section the interaction of $Ga_{1-x}Mn_xAs$ with an external magnetic field H can be reduced in a first step to the effects of the giant Zeeman splitting only. The exchange interaction between the valence-band states of heavy- and light holes, respectively, and the Mn d-electrons leads to a pseudospin-dependent splitting of the valence bands given by Eqn. 1.11. It can be interpreted as the development of four so-called valence-band subbands $V(j_z)$ with half the density of states (DOS) $N_V^{j_z}$ compared with the degenerate heavy- and light-hole DOS at $H = 0$, and with the corresponding valence-subband edges $E_V(j_z, H, T) = -\frac{1}{3}xN_0\beta < S_z > j_z$. To bare the influence of H on the transport properties this splitting given by Eqn. 1.11 is included when the hole density is derived according to Eqn. 1.2 as

$$n = \sum_{j_z=\pm\frac{3}{2},\pm\frac{1}{2}} \int_{-\infty}^{E_V(j_z,H,T)} N_V^{j_z}(E)F^h(E)dE. \tag{1.12}$$

It should be mentioned that besides the obvious influence of the magnetic field on the integration limits the implicit influence on the position of the Fermi energy E_F has also to be taken into account. To calculate the position of the Fermi level the neutrality equation

$$n = n_A + n_C \tag{1.13}$$

has to be solved with respect to E_F to ensure charge neutrality in the system[6]. n_A is the density of negatively charged acceptor states while n_C denotes the density of electrons in the conduction band.[7] Doing so with use of Eqn. 1.1

[5] We consider an isotropic crystal.

[6] Since the voltages applied on the sample during the measurement are sufficiently small to ensure that one is in the linear response regime, the Fermi energy is a global constant.

[7] Since the unperturbed valence-band edge is the fixed reference energy in all calculations, the temperature dependence of the gap energy is given as the temperature

and the material parameters given in Tab. 1.1, the magnetic-field dependent resistivity ρ_m can be derived.

As discussed briefly in section 1.3.3 a homogeneously distributed incorporation of the Mn ions was assumed when deriving the Hamilton operator that describes the magnetic interaction in Eqn. 1.10. By use of the virtual crystal approximation the carrier is considered to average over all Mn ions in the sample. This procedure had the advantage that the microscopic local coupling strength J_i of the exchange interaction could be replaced by the macroscopic p-d exchange integral $N_0\beta$. The disadvantage of such an approach which makes it unfeasible for the quantitative description of real samples is the negligence of disorder. Both a spatial inhomogeneity of the magnetic-ion density (which will cause a magnetic-field dependent disorder) as well as possible alloy disorder (which does not depend on the magnetic properties of the Mn ions but still is related with the non uniform distribution of foreign atoms in the GaAs lattice) are not taken into account. The crucial points are how to include effects related with a disordered Mn ion incorporation and how to keep the model simple enough to be solvable with reasonable numerical effort. Both can be done by a slight modification of the virtual-crystal approximation: Instead of using a Mn content equally smeared out and represented by the average concentration x in Eqn. 1.10 the Mn concentration is considered to show an 'increased spatial dependence'. An averaging of the carrier not over the sample as a whole but only over some smaller volume V is taken into account. Following this idea, $N_0\beta$ the macroscopic expression of the coupling constant J, still can be used but the density of Mn ions interacting with the carrier becomes a local however still averaged quantity. This assumption contains a certain self-consistency: Due to the incorporation of a local Mn concentration the accompanying disordered valence-band landscape may cause a localization of the carrier. This localization was implicitly plugged in initially when assuming an averaging over the volume V instead over the total system. This procedure is referred to as a mesoscopic virtual-crystal approximation and leads to a modification of Eqn. 1.11 expressing the giant Zeeman splitting of the valence-band subbands as

$$\Delta E_V(j_z, H, T) = -\frac{1}{3} x_{loc} N_0 \beta < S_z > j_z \tag{1.15}$$

---

dependence of the conduction band. This is accounted for by the Varshi formula [65] as

$$E_C(T) = E_C(T=0) - (1000 * ((5.5 * 0.0001 * T^2)/(225.0 + T))). \tag{1.14}$$

with x_{loc} denoting the local Mn concentration. The basic question how to define the volume V over which the Mn concentration is averaged is discussed in detail in Sect. 1.4.1. Within V the holes are assumed to behave as free carriers with band mobility μ_h of heavy and μ_l of light holes, respectively.

Table 1.1. Material parameters used for the calculations [66]

l_U $[nm]$ [8]	m_h [9]	m_l	$\mu_h[\frac{cm^2}{Vs}]$	$\mu_l[\frac{cm^2}{Vs}]$	E_G $[meV]$
0.57	0.50	0.082	130	1060	1500

1.4 The network model

In principle the macroscopic transport properties of (Ga,Mn)As can be calculated now, using the refinement of the magnetic-field influence given in the previous section as well as the basic transport description given by Eqn. 1.1. For the calculations, an advancement of a network model introduced for describing electronic transport in disordered semiconductors [59, 67, 68, 69] was developed. It is used to describe transport at $H = 0$ as well as magnetotransport in DMS, i.e. effects due to magnetic-field induced band splitting and tuning of the disorder potential are included. For readers who are interested in a detailed description of the network model and the accompanying set of equations the study of appendix A is reprehended. For all others, who are more interested in the general problem of the description of transport phenomena in disordered systems and less in the technical details of the modelling, only a brief summary of the model and its features is given below.

The basic idea of the network model is to divide the crystal into cubic cells of equal size (characterized by an edge length l) and to assign a local resistance to each cell. The resistances are connected to a network. We use a two-dimensional $K \times K$ square array of cubic cells with index $m \in K^2$ to model the transport in an epitaxial layer. By solving Kirchhoff's equations for the network the macroscopic resistance is derived. Such a network approach instead of the direct calculation of a uniform system attends to be required as it allows one to take into account spatial disorder e.g. due to the non-uniform incorporation of the Mn ions. In the model the Mn ions are distributed randomly between the cells such that the average of the local Mn

[8] l_U denotes the lattice constant of the cubic unit cell of the zinc-blende lattice.

[9] The heavy- and light-hole mass (m_h, m_l) is given in units of the free electron mass.

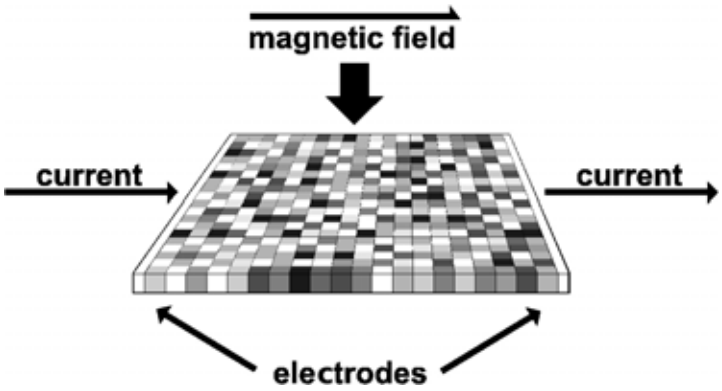

Fig. 1.4. Image of the calculated system of network cubes. Different grey tones of the cubes represent different concentration of Mn ions.

concentrations[10] x_{loc} remains x. Fig. 1.4 shows such a system of cubes with different Mn concentrations serving as the basis of the applied model. The variation of x_{loc} causes locally different band shifts $E_V^m(j_z, H, T)$ according to Eqn. 1.15 for $k = 0$ by use of $V = l^3$. Besides the influence of an external magnetic field one is also able to add a field-independent contribution given by

$$\Delta E_D^m = m_D(x_{loc} - x) \tag{1.16}$$

to account for alloy disorder in the valence band. m_D represents the derivative of the average valence-band edge E_V with respect to x_{loc} at x. Thus locally different transport properties, e.g. carrier concentrations arise.

In the calculation of the Fermi level of the entire system the changes of the density of states due to the local band splittings covered by Eqn. 1.11 need to be accounted for. This is done by solving the equation for charge neutrality

$$\sum_{j_z} \sum_{m \in K^2} p_V^{m,j_z}(T) = \sum_{m \in K^2} [n_A^m(T) + n_C^m(T)] \tag{1.17}$$

numerically; $n_A^m(T) = x_m F^e(E_A, T)$ denotes the local density of ionized acceptors in each cell with index m. For simplicity, we assume as a first approximation a δ-like acceptor density. Further is assumed that every Mn ion acts as an acceptor. $n_C^m(T)$ is the density of intrinsic electrons excited via the band gap.

[10] x_{loc} will be used in the following, whenever the general role of a local Mn ion distribution is of interest. If the properties of a specific cell related to its local Mn ion content are of interest, the variable x_m is used, which denotes the specific local Mn concentration of a cell with label m.

This density is given by

$$n_C^m(T) = \sum_{j_z=\pm\frac{1}{2}} \left(\int_{E_C^{m,j_z}}^{\infty} N_C^{mj_z} F^e(E,T) dE \right), \tag{1.18}$$

E_C^{m,j_z} is the band edge of the conduction-band subband with pseudospin j_z at cell m and $N_C^{mj_z}$ denotes the density of states of the conduction-band subband with pseudospin j_z of the cell with index m. $F^e(E,T) = \frac{1}{1+e^{E-E_F/k_B t}}$ is the Fermi distribution of electrons. As an extension a more realistic description taking into account both a broad energetic distribution of acceptor states as well as a separation of acceptor density and the density of magnetic ions is given in chapter 3. The possibility of such a separation is a valuable feature of the model as it makes it applicable even for materials with an immanent decoupling of magnetic ion- and dopant density, such as $Zn_{1-x}Mn_xTe$:N for example.

For wide gap DMS with band-gap energies of $E_G \geq 1\,\mathrm{eV}$ as in the discussed case with $E_G \approx 1.5\,\mathrm{eV}$ and at low temperatures $T \leq 100\,\mathrm{K}$, no thermal activation of carriers via the band gap into the conduction band takes place and to a first approximation $n_C^m(T) = 0$. Eqn. 1.17 has to be solved for all sets of (T,H) to gain the Fermi energy which depends on the local densities $p_V^{m,j_z}(T)$ of heavy and light holes for all subband pseudospins j_z which are given by

$$p_V^{m,j_z}(T) = \int_{-\infty}^{E_V^m(j_z,H,T)+\Delta E_D^m} N_V^{m,j_z}(E)(1 - F^e(E,T))\, dE, \tag{1.19}$$

$N_V^{m,j_z}(E)$ is the local density of states of the valence-band subband with angular momentum j_z given by

$$N_V^{m,j_z}(E) = \frac{2\pi(2m_{j_z})^{\frac{3}{2}}}{h^3} \sqrt{-(E + E_V^m(j_z,H,T) + \Delta E_D^m)}. \tag{1.20}$$

The resistivity of an individual cell ρ^m is given as the parallel connection[11] of

[11] As soon as a resistivity of an individual cell is formulated in the way given by Eqn. 1.21, the information about carrier angular-momentum (pseudospin) is lost, when connecting the cells to the network. In the case of a single-phase material the majority band is of the same pseudospin in all cells. The conservation of the carrier pseudospin is fulfilled automatically. For the description of hybrid samples, where the spin of the majority band may differ from cell to cell the situation changes and additional assumptions have to be made when a conservation of the carrier pseudospin is required.

the four resistivities of subbands with different j_z by

$$\rho^m = \frac{\rho^m_{-\frac{1}{2}}\rho^m_{\frac{3}{2}}\rho^m_{-\frac{3}{2}} + \rho^m_{\frac{1}{2}}\rho^m_{\frac{3}{2}}\rho^m_{-\frac{3}{2}} + \rho^m_{\frac{1}{2}}\rho^m_{-\frac{1}{2}}\rho^m_{-\frac{3}{2}} + \rho^m_{\frac{1}{2}}\rho^m_{-\frac{1}{2}}\rho^m_{\frac{3}{2}}}{\rho^m_{\frac{1}{2}}\rho^m_{-\frac{1}{2}}\rho^m_{\frac{3}{2}}\rho^m_{-\frac{3}{2}}}. \tag{1.21}$$

The resistivity $\rho^m_{j_z}$ of the hole bands of band mobility μ_{j_z} (different mobilities μ_h and μ_l are used for heavy and light holes) are given by

$$\left(\rho^m_{j_z}\right)^{-1} = q \cdot \mu_{j_z} \cdot p_V^{m,j_z}(T) \tag{1.22}$$

with $p_V^{m,j_z}(T)$ defined in Eqn. 1.19.

The cell resistances R_m are calculated for each cell by multiplication of ρ^m with $\frac{1}{l}$.
To define the network, the following assumptions were made:

- For each cubic cell of the square array the transport can only take place through its four surfaces perpendicular to the plane of the array; i.e. a central cube has four conducting connections with nearest-neighbor cubes.
- The knots of the network are centered in the cells. Thus the resistance $R_{n,m}$ of a conducting connection between two adjacent knots K_m and K_n is $R_{n,m} = \frac{1}{2}(R_n + R_m)$. For every knot K_m of the network it holds

$$\sum_{i=1}^{4} I^i_m = 0 \tag{1.23}$$

  where I^i_m are incoming and outgoing currents at K_m. Ohm's law relates voltage $U_{n,m}$, current $I_{n,m}$ and resistance $R_{n,m}$ between knots K_n and K_m as

$$U_{n,m} = R_{n,m} \cdot I_{n,m}. \tag{1.24}$$

- The electrodes are modelled by two additional knots on opposite edges of the array. Both electrodes are connected to all K knots of the corresponding edge. One of the electrodes is grounded i.e. its electric potential is set to zero. To calculate the potential values at the remaining $K^2 + 1$ knots (and thus the total resistance R of the array) a systems of $K^2 + 1$ linear equations needs to be solved employing standard network-analysis algorithms.

In Fig. 1.5 the model of a one dimensional chain of network cubes as a connection of the accompanying resistors is shown. Most calculations were performed for arrays with $K = 40$ cells. Since it was assured for all parameter sets for the simulated materials, that K was chosen large enough i.e. the results do not depend on the specific value of K. For most studies it was assumed that

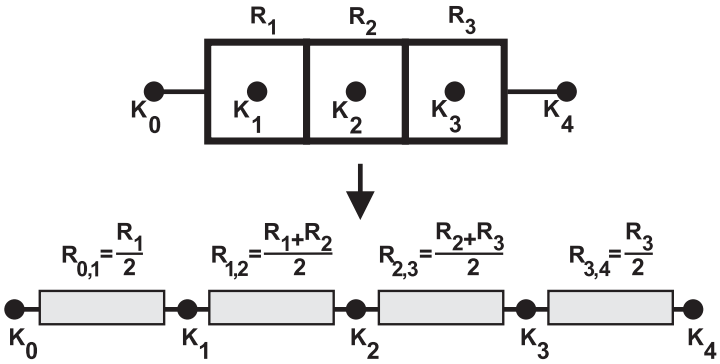

Fig. 1.5. Model of a 1-dimensional resistor network. The chain of three cubes on top is described by the connection of the resistors given below. The two additional knots K_0 and K_4 represent the electrodes.

$\mu_l \approx 10 \cdot \mu_h \approx 1000 \frac{\mathrm{cm}^2}{\mathrm{Vs}^2}$ (remaining parameters see Tab. 1.1). It should be noted that despite the network model is applied on the modelling of transport and magnetotransport phenomena in DMS the magnetic properties of the material as well as interactions with an external magnetic field are only considered as the origin of spatial disorder in the transport carrying bands. After the local valence-band edges are calculated neither further influence of the external field nor of the magnetic ions are taken into account. In more simple words: On the basis of the network model the transport properties of a semiconductor with a spatially fluctuating activation energy are described. The requirement for such a treatment is that beside the validity of the general transport mechanism (activated band transport) the transport properties are represented basically by the local fluctuations of the carrier density. If this is not the case and the transport properties are determined predominantly by many-body effects such as the formation of e.g. magnetic polarons, the used model is not applicable any more.

At first view the use of a constant mobility (for heavy and light holes each) may be astonishing since the carrier mobility is expected to be reduced due to an increase of disorder. One has to keep in mind that only the *local* mobility stays constant in the model. Using the calculated resistivity ρ and the carrier density[12] n one can use Eqn. 1.1 to define an *effective* mobility for all sets of parameters (H, T). This effective mobility is not constant any more and its disorder induced change is implicitly taken into account by the model. This

[12] The definition of the carrier density is likewise artificial in disordered systems since predominantly the density of carriers on the perculation path is of interest. Nevertheless in this framework we use the carrier density as if it was well defined.

artificial parameter (the effective mobility) plays the role of a mathematical by-catch as it is in principle obtainable by the calculations but of no further use and even of doubtful physical meaning.

1.4.1 The length-scale

Whenever a description of disordered media has to be developed, one key problem is the treatment of the present disorder on a length-scale well adapted to reflect the physical properties of the system. Depending on the chosen approach this length-scale may be somehow "hidden" as e.g. it is implicitly given as the standard deviation of the assumed spatial potential fluctuation, or (as in the case discussed here), it is obviously present as the length l of the network cubes.

As a standard model for the description of electronic transport in disordered media one may regard the Anderson model [60, 61]. This description is unfortunately featured by the high degree of difficulty to remain applicable in case of hybrid structures. Therefore it is not considered to be functional in our situation.

Nonetheless taking a look at these models is worthwhile, as other descriptions based on this theory exist that also claim to provide a satisfactory description of transport phenomena in DMS, see e.g. [5]. As a starting point the question arises, whether the electronic wave functions are extended over the considered system or localized around some spatial position i[13]. A given spatially fluctuating potential gets filled up with electronic states which are treated as being localized and do not contribute to transport.[14] As long as the energy of the carriers is below the critical value E_m (called the mobility edge), they are localized. The carriers on states above E_m are extended over the whole system and may be described as free carriers. Carriers in such extended states interact by definition with the entire system, thus their mobility gets affected by scattering processes, e.g., with potential fluctuations or impurity states [60]. Such an approach is useful as soon as it can be assumed

[13] We will not address in detail the formulation of localization which indeed is a mathematically bold venture. Localization is used in the sense of Anderson [70], in very brief words: One considers an electron wave function $\Phi_i(t)$ which is prepared at time $t = 0$ at a lattice site i and which is not eigenfunction of the system Hamiltonian. If $\lim_{t\to\infty} \mid \Phi_i(t) \mid = 0$ the electron is not localized, it corresponds with an extension of the particle over the infinite system.

[14] It should be mentioned here, that this kind of localized states may contribute to transport in terms of hopping- or rather variable range hopping (VRH) conductivity, which is not subject of the present work. Descriptions of the VRH regime in DMS can be found in e.g. [42, 71, 72].

that the disordered potential exists independently from the presence of electronic states (carriers) within it. It has to be assumed that whether a carrier is in a localized or extended state the potential landscape is not altered. As a comprehensible analogy one may look at water flowing through valleys of mountains: For the moment of observation the change of the mountains due to the river can be neglected, the valley exists even in the absence of any water. This still is the case for the disordered potential related with alloy disorder as described by Eqn. 1.16, but not in the case of the potential fluctuations related with the giant Zeeman splitting given (see Eqn. 1.11). This exchange interaction inherently requires the existence of electronic states (in our case valence-band hole states) interacting with the magnetic ions. In this regard two distinct influences of the carriers on the potential can be considered:

1.) a direct (active) polarizing influence of a carrier aligning the spins of the magnetic ions in its vicinity in a energetically favored way. This influence is assumed when introducing magnetic polarons (MP) as quasi-particles who carry the transport. As the antipodal analogy to the situation discussed above one may think in this context of the potential felt by a metal ball rolling on a soft matter as a mattress for example, in the absence of the ball, the potential is plain and a minimum as felt by the ball in its vicinity simply does not exist. The influence of polaronic effects, i.e. self trapped MP [73] as well as bound MP [42, 71, 72, 74, 75, 76, 77], is neglected in the theoretical description given here.

2.) the pure passive influence of the valence-band hole due to its exchange interaction with the Mn ions according to Eqn. 1.11. The spins of the magnetic ions are treated to be unpolarized by the hole state.

In the latter case the influence of the hole comes into play when the concentration of magnetic ions is of interest. Based on extended states within the virtual-crystal approximation (VCA) the hole averages over all K^2 lattice sites and the average Mn concentration x enters Eqn. 1.11. All spatial fluctuations of the Mn concentration are averaged out herewith. This procedure predicts too large negative MR effects, due to the neglect of GZS-induced disorder, it is not taken into account. On the other hand strong localization due to the GZS that requires the description of carriers as point-like and therefore classical particles is devoid of any foundation since an exchange interaction does not exist is this framework.

As possible alternative a length-scale l is introduced. This parameter is used as an effective value representing the quantum-mechanical properties in a classical picture as if they were completely known. The VCA is substituted by the mesoscopic virtual-crystal approximation to make clear that the averaging over the Mn ions takes place over a finite space of volume l^3. The crucial point of this approach is obvious: The solution of the full problem should be known

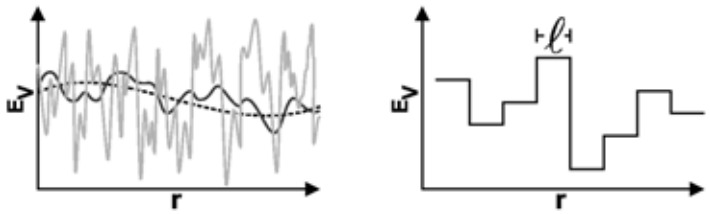

Fig. 1.6. In the left figure three of the infinite number of possible potentials fluctuating on different length-scales are depicted. The right side illustrates the translation of this variety of all possible scales into a fluctuation with a fixed length-scale l.

when fixing the numerical value of l which then is used to find an advanced solution. The value of l influences the potential landscape as it is proportional to the average amount of the fluctuations of the valence-band subbands given by to the GZS: $\Delta E_V \propto \frac{1}{l^{\frac{2}{3}}}$. (For details see appendix B). The model representation of the potential landscape which fluctuates in principle on all possible scales by a single fluctuation with length-scale l is illustrated in Fig. 1.6. In this context the inelastic scattering length l_i is a lower boundary of l. For $l < l_i$ the classic description of transport as used in this work fails. But even if the assumption $l > l_i$ is fulfilled[15], the choice of a small value of l leads to large fluctuations of the local valence-band splits $E_V^{j_z,m}$. This corresponds to large fluctuations of the local carrier densities as well as enhanced fluctuations of the local resistivity. Thus an underestimation of l will cause an overestimation of the influence of disorder. If the potential fluctuates on short length-scales with the corresponding large fluctuation amplitudes, the classic percolation theory predicting a continuously decreasing conductivity that finally reaches zero with increasing disorder is no longer applicable. Below a certain minimum value of the conductivity (corresponding to this, below a minimum value of l) the conductivity does not decrease further since quantum-mechanical tunnelling between the states 'localized' by the disordered potential becomes the essential transport mechanism [78]. This transport mechanism is not taken into account in the network model used in this work. In the opposite case when l is chosen too large, almost all fluctuations get averaged out and no influence of disorder remains in the model. Fig. 1.7 shows the dependence of the resistivity on l for three different temperatures. The influence of an increase of disorder with decreasing value of l is obvious as the resistivity strongly increases. For increasing l when the amplitude of the potential fluctuations in the system vanishes the resistivity converges against an l-independent limit.

[15] We assume $l > l_i$ for all calculations presented in this work.

In this context it should be noted that against intuition the choice of a small value of l and herewith incorporation of disorder does not for all sets of parameters cause an increase of the resistivity: Whether a decrease of l (that modifies the mobility edge, reduces the activation energy, increases the amplitude of disorder and leads to an elongation of the percolation path) will reduce or increase the resistivity depends finally on the system parameters. For all calculations the value of l was chosen large enough for not to overestimate the influence of disorder. This ensures that the physical properties of the system do not become covered up by model artifacts, while l is set small enough not to neglect disorder and end up with a simple VCA[16]. Even against the background of this free model parameter it is nevertheless possible to gain some new insights into the transport properties by a comparison between experimental data and calculation. If one is able to reproduce even quantitatively the measured data for different samples using material parameters in a reasonable range and with a physically motivated tendency of parameter changes, one can conclude that the influence of the considered effect (the local band splittings due to an external magnetic field) cannot be neglected within a future microscopic theory. Possible many-body effects that are neglected in the present approach have to be included on top of the given mechanism. On the other hand if one cannot reproduce the experimental data by use of proper sets of material parameters (which are known in certain limits) the approach has to be rejected. Beside the possibilities of the present model it has of course its limits: Since a variation of l requires at least a slight modification of the values of most material parameters to gain still a quantitative description of the experiment, this model cannot be used to determine these material parameters.

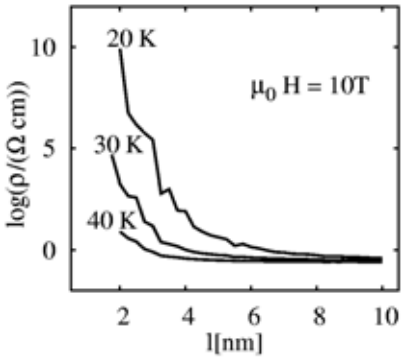

Fig. 1.7. Calculated resistivity at an external magnetic field of 10 T versus the length-scale of the resistor network for three different temperatures as indicated in the figure. For parameters see third sample in Tab. 3.1 except for: $m_D = 0$ and $\sigma = 60\,\mathrm{meV}$.

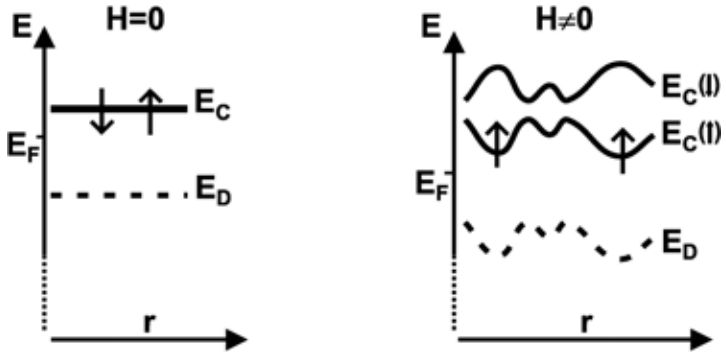

Fig. 1.8. The left side depicts the energy landscape of a n-type DMS at $\mu_0 H = 0$. The right side shows the situation at $\mu_0 H \neq 0$. The donor energy level fluctuates spatially, since it is assumed to be connected with the local conduction-band edge.

1.4.2 A remark on the acceptor level

In all calculations the acceptor energy level E_A is treated as a fixed global value. It is particularly independent from the spatial fluctuations of the valence-band edge. This assumption is required so assure the existence of negative MR effects due to the giant Zeeman splitting. If a coupling of the energetic level of the impurity atoms on the local valence-band edge is assumed, the external magnetic field leads to an increase of disorder while the (averaged) activation energy stays nearly constant. Such a regime leads to predominantly positive MR effects and can be excluded by comparison with the experimental data. In contrast to the p-type III-Mn-V DMS with a comparatively deep acceptor energy level the situation may change for the description of n-type DMS with a donor level close to the conduction band such as ZnMnSe:Cl. For this material the choice of a fluctuating donor level, connected somehow to the local conduction-band energy as shown in Fig. 1.8 seems appropriate since the corresponding disorder causes a strong positive MR as observed in experiments.

[16] Based on a simple VCA the experimental results cannot be described.

2

Transport in single-phase materials

2.1 Introduction

Indispensable for a proper description of the magnetotransport properties is not only the knowledge of the influence of magnetic fields but headmost the knowledge of the transport regime in general and the accurate description of the transport properties in absence of a magnetic field. Only if the theoretical model is able to provide a quantitative description of the experimentally obtained zero field temperature dependence of the resistivity, it makes sense to extend it and to take into account the interaction with the external magnetic field.

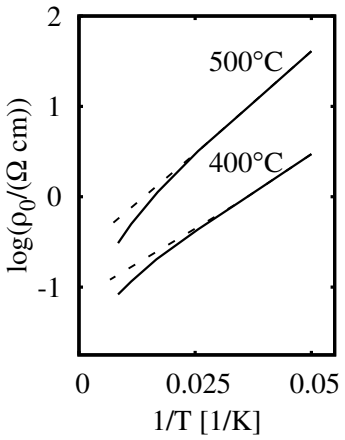

Fig. 2.1. Measured temperature dependence of ρ_0 of two $Ga_{0.98}Mn_{0.02}As$ samples annealed at 400 and 500°C in Arrhenius depiction. The curves deviate from the expected linear behavior, which is indicated by the dashed lines.

The initial point of the considerations in this section is the measured temperature dependence of two GaAs:Mn samples as shown in Fig. 2.1. The experimental data shows a clear nonlinear behavior of the logarithmic resistivity plotted versus the inverse temperature. When such a strong, though non-Arrhenius temperature dependence of electrical resistivity is observed, one usually concludes that the underlying mechanism is variable-range hopping.

Unexpectedly, such observations are also made for many semiconductor systems at elevated temperatures, as in the present case, where a variable-range hopping mechanism seems unlikely. A satisfactory explanation for this observation was lacking so far. In the following it is demonstrated that a non-Arrhenius resistivity behavior may also arise in a band-transport picture by thermal activation of charge carriers from a reservoir into the transport-carrying band states, provided the energy distribution of reservoir states is sufficiently broadened or the density of band states exhibits tails. This description including a broad acceptor-energy distribution (alternatively band tail-states) represents the basis of all further calculations. Even though the motivation to analyze possible origins of a non-Arrhenius temperature dependent resistivity in this work is related with the description of the magneto-transport properties of DMS samples, the results are not limited to the choice of this special class of semiconductors.

2.2 Basic transport equations

In studies of transport properties of solid-state materials researchers usually devote particular attention to the temperature dependence of electrical resistivity, since this dependence is indicative for the underlying transport mechanism. Usually the direct current resistivity in doped semiconductors can be described by an Arrhenius temperature dependence

$$\rho = \tilde{\rho} \cdot \exp(\Delta / k_{\mathrm{B}} T) \tag{2.1}$$

where $\tilde{\rho}$ is a pre-exponential factor, Δ is the activation energy, and k_{B} is the Boltzmann constant. At high temperatures the so-called intrinsic resistivity is provided by thermal activation of charge carriers over the band gap and the activation energy Δ is related to the band gap energy E_{G}: $\Delta \approx E_{\mathrm{G}}/2$. With decreasing temperature the so-called impurity resistivity mechanism takes over according to which charge carriers in the band are supplied by thermal activation from impurity atoms (donors or acceptors). The activation energy Δ in this transport mode is related to the depth of electronic levels on impurities with respect to the band edge (conduction band for donors and valence band for acceptors) [79]. At even smaller temperatures the so-called hopping transport mechanism comes into play, in which carrier transport does no longer take place via band states, but instead is provided by tunnelling (hopping) of charge carriers between the impurity atoms. In the latter case, the activation energy Δ is usually determined by the width of the energy distribution of charge carriers on impurity atoms. Detailed description of hopping conduction along with quantitative calculations of the activation energy Δ for this regime

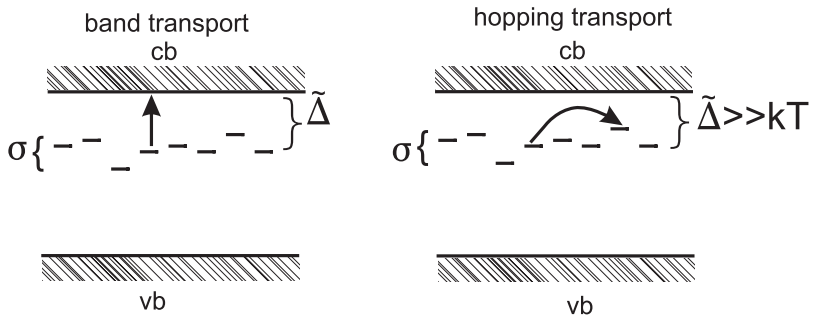

Fig. 2.2. Left: band transport regime, right: hopping regime where Δ is the activation energy, $\tilde{\Delta}$ is the energy spacing between the localized states and the extended band states, and kT is the thermal energy.

can be found in [60]. At extremely low temperatures electrical conduction is provided by the so-called variable-range hopping (VRH). In this transport regime the Arrhenius law for $\rho(T)$ is not valid anymore. The temperature dependence of the resistivity in the VRH has the form $\rho = \tilde{\rho}\exp[(\Delta/k_{\mathrm{B}}T)^{\beta}]$, where β is determined by the shape of energy-dependent distribution of impurity atoms (DOI). For an energy-independent DOI is $\beta = 1/4$, while for the parabolic Coulomb gap in the DOI it is $\beta = 1/2$ [60].

2.3 A non-Arrhenius transport behavior - indicative for hopping transport?

Surprisingly, there are many experimental results of typical semiconductor systems in the literature which exhibit a strong non-Arrhenius temperature dependence of ρ at elevated temperatures. Very often, it is claimed in these cases that the underlying transport mechanism is the VRH transport mode [80, 81, 82, 83]. However, one should keep in mind that the VRH regime in semiconductors is usually valid only for extremely low temperatures when the thermal energy $k_{\mathrm{B}}T$ is much smaller than the width σ of the energy distribution of impurity levels (illustrated in Fig. 2.2) which is not the case in most semiconductor systems at elevated temperatures. Therefore one must consider other transport mechanisms for explaining the corresponding experimental data. The most natural approach is to seek for an explanation in the regime of charge carrier transport via extended band states, where the carriers are supplied by thermal activation from impurity states, as this transport regime is usually valid in doped semiconductors in the relevant temperature range. The possible occurrence of a strong non-Arrhenius temperature dependence of

ρ in the case of traditional band charge-transport is the main message of this section and forms the basis for the quantitative modelling of the transport and magnetotransport properties of a series of (Ga,Mn)As samples annealed at different temperatures given in chapter 3.

To refer to Eqn. 1.1, in the isotropic case the electrical resistivity in the band-transport regime can be represented by

$$\rho = (nq\mu)^{-1} \tag{2.2}$$

where q is the charge of the carrier, n is the concentration of charge carriers in transport states, and μ is their mobility. For p-type (n-type) semiconductors, the transport states are the extended band states for holes (electrons) in the valence (conduction) band. In such states charge carriers move as free particles with an effective mass. In semiconductors, the mobility of the carriers via extended states depends comparatively weakly on temperature (i.e. weak power-law form) due to the temperature dependence of scattering cross sections, e.g. in scattering by impurities ($\mu \propto T^{3/2}$) below about 40 K and in scattering by phonons ($\mu \propto T^{-\gamma}$ with $\gamma > 0$) above about 80 K in GaAs [84]. The carrier mobility cannot therefore be in any sense responsible for the observed, strong non-Arrhenius behavior of ρ. Hence the only factor in Eqn. (2.2), which can be responsible for the observed temperature dependence is the concentration of charge carriers n in the transport-carrying band. The crucial question then is why the temperature dependence of this concentration can be non-Arrhenius if charge carriers are supplied into the extended bands by thermal activation from acceptor (donor) states. Two possible disorder-related explanations in the framework of the band transport regime shall be discussed in the following.

2.4 Influence of disorder on the temperature dependence of the resistivity

Two different scenarios both based on effects of disorder are introduced and analyzed with regard to their influence on the temperature dependence of the resistivity in the activated transport regime:

- Scenario 1: The energy levels of holes (electrons) on acceptors (donors) have a broad energy distribution.
- Scenario 2: The density of states (DOS) of the extended band states in the vicinity of the band edge possesses a low-energy exponential tail.

Both, a distribution of dopants as well as an exponential tail of the DOS lead to a non-linear shift of the Fermi-level as a function of temperature

and thus result in a non-Arrhenius temperature dependence of the resistivity. In what follows the case of holes in the valence band of a semiconductor with zincblende or diamond structure is addressed. Calculations for electrons can be carried out in the same manner and yield similar results. The carrier concentration is calculated according to

$$n = \int_{-\infty}^{E_V} \tilde{N}(E) F^h(E)\, dE \tag{2.3}$$

where $F^h(E)$ is the Fermi distribution of holes and $\tilde{N}(E)$ is the DOS of the valence band. Defining $N(E)$ as the ideal square-root like DOS in the approximation of parabolic valence bands taking into account both heavy holes and light holes, disorder of the band states can be included by adding an exponential tail yielding

$$\tilde{N}(E) = \begin{cases} N(E) & : \quad N(E) \geq \alpha \\ \alpha \cdot \exp\left(-\frac{(E - N(E)^{-1}(\alpha))\, \ln 2}{\delta}\right) & : \quad N(E) < \alpha \end{cases} \tag{2.4}$$

where α is the onset of the tail, $N(E)^{-1}$ is the inverse function of the ideal DOS, and δ is a damping in form of a half-width energy, which is treated as a free parameter. In the calculation corresponding to the first scenario an ideal square-root like DOS was used, i.e. $\alpha = 0$. In the second scenario, α was non-zero and δ was varied.

The concentration of charge carriers n is decisively determined by the position of the Fermi level. The latter is calculated using the neutrality condition. In the second case of a delta-like DOI of the acceptor, the Fermi level is given by the neutrality condition in the form

$$\int_{-\infty}^{E_V} \tilde{N}(E) F^h(E)\, dE = N_A F^e(E_A) \tag{2.5}$$

where N_A and E_A are the concentration and the energy depth of acceptors, respectively, and $F^{h(e)}(E)$ is the Fermi-distribution of holes (electrons). With the assumption of a broad DOI of the acceptor states (first scenario), the right-hand side of Eqn. (2.5) has to be replaced by

$$n = \int N_A(E) F^e(E)\, dE \tag{2.6}$$

where $N_A(E)$ is the DOI of acceptor states.

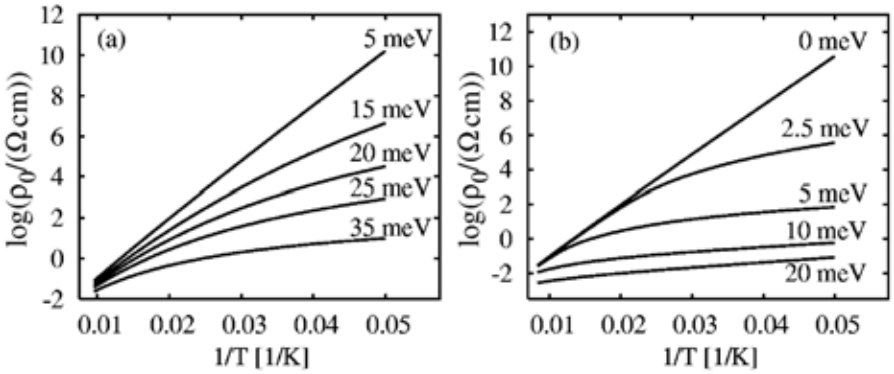

Fig. 2.3. Logarithmic plots of the calculated resistivity versus 1/T for a $Ga_{0.998}Mn_{0.002}As$ sample. In (a) the calculation was performed with different values of σ as indicated in the figure. The valence band DOS has the ideal square-root shape. In (b) the calculation was performed with different values of δ as indicated in the figure. The energy distribution of the acceptor states is a delta function.

This Gaussian distribution

$$N_A(E) = \frac{1}{\sqrt{2\pi\sigma^2}} \exp\left(-\frac{(E-E_A)^2}{2\sigma^2}\right) \tag{2.7}$$

is assumed to be centered at $E_A = 110\,\text{meV}$ above the unperturbed valence-band edge. The width σ of this distribution is treated as a free parameter.

Results of calculations for the first scenario using Eqs. (2.2)-(2.7) are shown in Fig. 2.3 for different values of σ. For the narrowest band the temperature dependence of the resistivity can be approximated by the Arrhenius-law. With increasing broadening of the acceptor DOI the results of calculations for the temperature dependence of the resistivity deviate more and more from the Arrhenius-behavior. The broadening of the acceptor distribution leads to a non-linear temperature dependence of the Fermi-level. Such a nonlinearity of the temperature dependent Fermi energy can be found in Fig. 2.4, where the calculated Fermi energy is plotted against temperature for different width of the acceptor-energy distribution. For a very narrow acceptor distribution with $\sigma = 5$ meV, E_F shows an almost linear behavior. With increasing acceptor-band width σ both a reduction of the accompanying E_F, what can be interpreted in terms of a reduction of the activation energy, as well as a non-linear down bend at higher T appear. If such a non-linear behavior of E_F is considered in Eqn. 1.3 its crucial influence on the appearance of a non-linear

Arrhenius depiction of ρ becomes visible. With

$$\rho = \tilde{\rho} \cdot exp\left(\frac{\Delta}{k_{\mathrm{B}}T}\right) \tag{2.8}$$

where $\Delta = E_{\mathrm{F}}(T) - E_V$ where E_V denotes the valence-band edge, one gets

$$\rho = \tilde{\rho} \cdot exp\left(\frac{E_{\mathrm{F}}(0) + \iota T + \mathcal{O}(T^2) - E_V}{k_{\mathrm{B}}T}\right) \tag{2.9}$$

$$\Leftrightarrow$$

$$\log(\rho) \approx \iota + \frac{E_{\mathrm{F}}(0) - E_V}{k_{\mathrm{B}}} \cdot \frac{1}{T} + \mathcal{O}(T). \tag{2.10}$$

The broader the energy distribution of holes on acceptors, the weaker is the temperature dependence of the concentration of thermally activated holes in transport states at the valence-band edge. Therefore, the introduction of disorder into the reservoir of charge carriers, i.e. on the right-hand side of Eqn. (2.5) (energetically distributed acceptor levels), can cause the non-Arrhenius temperature dependence of the resistivity although no disorder is present in the transport-carrying band. The theoretical curves for the resistivity are very sensitive to the choice of the parameter σ as can be seen from Fig. 2.3(a). Changing σ to 20 meV or to 30 meV leads to an order of magnitude change of the resistivity and a different curvature of the plot. Therefore, for a known impurity depth E_A, the comparison of theory and experiment might allow one to determine the energy width σ of the DOI.

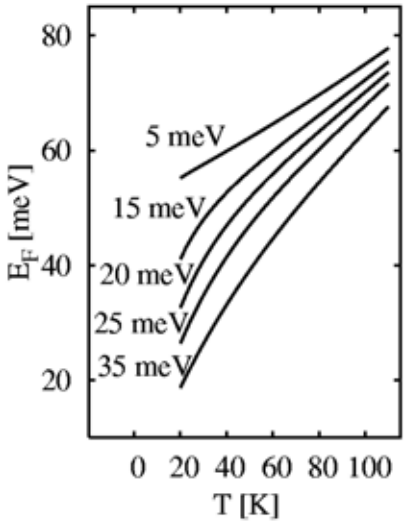

Fig. 2.4. Calculated temperature dependence of the Fermi energy for different widths σ of the acceptor-energy distribution as indicated in the figure. The valence band DOS has the ideal square-root shape.

Results of the second scenario obtained using different values of δ in the calculation (see Eqn. (2.4)) are shown in Fig. 2.3(b). It can be seen that in the absence of an exponential tail the resistivity shows the usual Arrhenius-dependence. With increasing δ the low temperature resistivity drastically

drops leading to a non-Arrhenius temperature dependence. The reason for this is similar to that in the first scenario discussed above: The disorder accounted for by the variable extension of the exponential tail enters the neutrality equation Eqn. (2.5) as a modification of the DOS leading to a non-linear dependence of the Fermi energy with increasing temperature. Again the calculation shows a strong dependence of the shape of the resistivity curves on the free parameter δ which allows one (if a broad impurity distribution can be excluded), to determine the extension of such a tail by comparison with experimental data.

2.5 Conclusion

In this chapter it has been shown that a strong non-Arrhenius temperature dependence of the electrical resistivity can occur in the framework of a traditional semiconductor band-transport mechanism. Therefore, a non-Arrhenius dependence of the resistivity of a semiconductor system alone, is no proof of variable-range hopping being the dominant transport mechanism. It is worth noting that this statement is basically independent of the semiconductor material.

3

Influence of annealing

3.1 Introduction

In this chapter the model developed previously for the description of magnetotransport in dilute magnetic semiconductors, is applied to a series of (Ga,Mn)As samples annealed at different temperatures. It is the aim to show that by use of the model the magnetotransport in the series of samples can be described in the regime of activated transport neglecting many-body effects. The changes of resistivity and MR observed in a series of $Ga_{0.98}Mn_{0.02}As$ of parent material divided into pieces of the same specimen and annealed at different temperatures are analyzed in terms of the annealing-induced structural changes. The magnetic properties of the (Ga,Mn)As alloys, in particular, the magnetic-field induced changes of the density of states, potential fluctuations due to the giant Zeeman splitting in the paramagnetic phase and spontaneous magnetization effects in the ferromagnetic phase are accounted for in the mean-field fashion as introduced in chapter 1. The energy distribution of the acceptor states is realistically specified as given in chapter 2.
The magnetotransport is described in the different magnetic phases occurring in the annealing process. This is unlike the overwhelming majority of publications in the field of (III,Mn)V semiconductors (e.g. [5, 85, 86, 87, 88, 89, 90, 91, 92, 93, 94, 95]) which are concentrating on ideal metallic (Ga,Mn)As alloys in the ferromagnetic phase.
Annealing in the temperature range considered leads to significant changes of the electronic, structural and magnetic properties of the specimen, e.g. the samples change from a metallic ferromagnetic random alloy to an almost insulating paramagnetic-ferromagnetic hybrid structure as given schematically by the diagram shown in Fig. 3.1. Thus depending on the annealing conditions

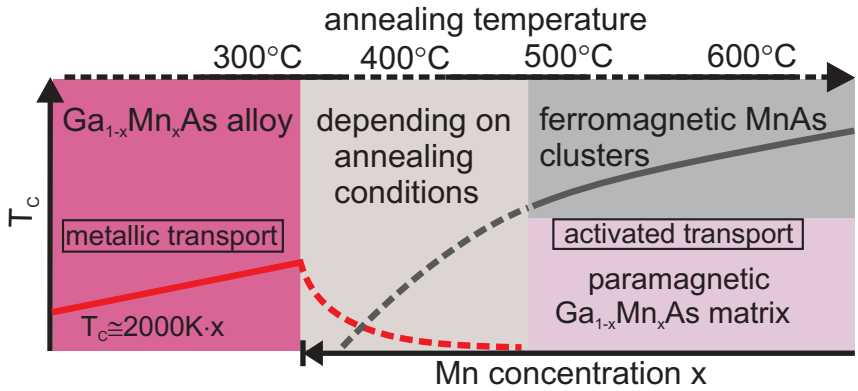

Fig. 3.1. The diagram illustrates the structural change of $Ga_{1-x}Mn_xAs$ depending on the annealing process (for $x < 0.1$). Due to the annealing the sample changes from single-phase ferromagnetic metal via an intermediate state to a two-phase hybrid structure formed by ferromagnetic MnAs inclusions embedded in a paramagnetic GaAs:Mn matrix. The red line denotes the Curie temperature of the single-phase material, the grey line denotes the Curie temperature of the hybrid due to the ferromagnetic MnAs precipitates. Note that the increase of T_C in the regime of moderate annealing temperature is illustrated for a sample with a fixed Mn concentration.

such a treatment of LT MBE[1] grown samples provides a method to study segregation and the formation of MnAs precipitates blow-by-blow. The possibility to study the intersection from a paramagnetic sample with spatially random incorporated Mn ions via spatially non-random Mn incorporation up to the formation of very small MnAs precipitates is solely governed by the chosen approach using well adapted annealing conditions. It cannot be provided e.g. by growth of the hybrids due to MOVPE[2][96].

It is shown that the model yields a reasonable agreement between theory and experiment and allows to extract changes of the material parameters induced by annealing. Thus it can be used to shed some light on the underlying microscopic processes. In this regard it is obvious that the use of a simple molecular-field approach as given in section 3.2.1 does not provide an enclosing description of the ferromagnetism in the system. This approach only serves as the simplest extension of the paramagnetic model to check its validity in the range of limited condition.
Regarding to section 1.2 the RKKY interaction, is considered to be the origin of ferromagnetism in GaMnAs alloys by means of a coupling between the lo-

[1] Low temperature molecular-beam epitaxy
[2] Metalorganic vapor phase epitaxy

calized Mn spins that is mediated by free holes in the valence band. The Curie temperature depends sensitively on the free hole concentration p as well as on the Mn concentration x, i.e. $T_C \propto p^{1/3} \cdot x$. In ideal metallic $Ga_{1-x}Mn_xAs$ samples, where $p = x$, the simple relation yields $T_C \propto x^{4/3}$. In experiments one basically observes a linear change of T_C with x followed by a plateau or even a decrease of T_C at higher x [3, 97, 98, 99]. The plateau or decrease of T_C typically occurs in the range of Mn concentrations between 5% and 8% depending on the growth and annealing conditions of the $Ga_{1-x}Mn_xAs$ alloy. The microscopic causes of this behavior are manifold and originate from the low growth temperatures employed in molecular-beam epitaxy of these alloys. The low growth temperatures are required to yield the non-equilibrium conditions necessary to overcome the low solubility of Mn in GaAs and thus to reach Mn concentrations in the range of a few percent in the alloys. However, as a side effect of the low growth temperatures not all of the Mn atoms are incorporated on Ga sites, i.e. as Mn_{Ga}, and a variety of defects is formed which may affect the magnetic as well as the electric properties of the alloys [100, 101]. Two prominent defects are Mn interstitials Mn_I (Mn atoms not incorporated on a lattice site) and arsenic antisites As_{Ga} (As atoms on the Ga sublattice) which both act as double donors in the alloy, i.e. they compensate the Mn_{Ga} acceptor. In particular, the Mn_I are considered to play a dominant role in the compensation process [102, 103, 104]. It can also be anticipated that the defects will affect the average magnetic properties of the alloys. Several calculations predict that Mn_I tend to form Mn_{Ga}-Mn_I-Mn_{Ga}-complexes under certain growth conditions. These complexes should lead to a ferromagnetic coupling of the adjacent substitutional Mn ions [105].

It is established that annealing in a moderate temperature regime close to the growth temperature leads to an increase of T_C, of the carrier density p and of the saturation magnetization [106, 107, 108, 109, 110]. The major reason for this is a diffusion of Mn_I to the surface and therefore a reduction of the compensation [104, 111, 112]. At low annealing temperatures the arsenic antisites do not contribute to the annealing induced changes since they remain stable up to 450 °C [104, 109, 113]. At temperatures above 400 °C, segregation and formation of MnAs precipitates sets in leading to a structural transition from a random alloy via a non-random alloy to a granular hybrid structure [9, 114, 115]. The sample properties are profoundly sensitive to the annealing duration and temperature. Whether the transport properties of hybrid samples are defined predominantly by the clusters and the interplay between the ferromagnetic clusters and the paramagnetic matrix or solely by the paramagnetic matrix depends strongly on the amount of clusters in the sample and the strength of the cluster-matrix interaction. For low Mn concentrations as in the case of the annealed $Ga_{0.98}Mn_{0.02}As$ sample described

in this chapter the direct influence of the MnAs precipitates can be neglected as the effective cluster concentration[3] is below the percolation threshold. The formation of Schottky barriers at the boundary between the grains and the matrix can be neglected as well but it may play a role at higher cluster concentrations and low carrier density [116]. The influence of Schottky barriers in hybrid samples of valuable cluster concentration is discussed in detail in section 5.2.3. To summarize: In the parameter regime discussed here only the corresponding reduction of the Mn-ion concentration in the matrix due to the annealing induced cluster formation needs to be considered [114].
The mesoscopic magnetic properties are also affected by the annealing procedure. The ferromagnetic domain size is reported to be in the micrometer range, depending on the annealing conditions between 2 and 100 μm [117, 118, 119]. Regions which exhibit ferromagnetism above T_C are reported as well. The microscopic origin of these ferromagnetic islands is still not fully understood. It may be associated with the existence of small precipitates or spatially increased hole and Mn ion densities. An additional magnetic disorder on a smaller length-scale even within a single domain was also observed. Studies of such a local fluctuating T_C and non-random Mn incorporations are shown in chapter 4. In addition to the magnetic disorder it has been shown that low temperature MBE grown $Ga_{1-x}Mn_xAs$ contains a significant alloy disorder which is believed to be reduced during annealing [120]. The influence of this disorder on the Curie temperature is still controversially discussed: On one hand there are predictions that a fully ordered situation can be considered as an upper limit to T_C [121]. On the other hand there are both experiments [120] and theoretical considerations [122] claiming that the presence of disorder leads to an increase of T_C.

3.1.1 Experimental details

Details of the growth and transport measurements are described elsewhere [114]. In brief, a $Ga_{0.98}Mn_{0.02}As$ layer with a thickness of 50 nm was grown on GaAs (311A) substrate by LT MBE. The growth temperature was about 290 °C. After the growth five pieces of this specimen were annealed at 300 °C, 350 °C, 400 °C, 500 °C and 600 °C, respectively, for 10 minutes in an As-rich atmosphere. Magnetotransport measurements were performed in a temperature range from 20 to 100 K. An external magnetic field up to 10 T was applied perpendicular to the sample surface.

[3] Effective cluster concentration means the concentration of cluster cells and matrix cells which are under the influence of the cluster.

3.2 Model properties

We apply the transport description developed in the previous chapters. For the derivation of the temperature and magnetic field dependent resistivity curves of the series of alloys, full network calculations are performed for different sets of temperature/magnetic field pairs (T, H). To describe the material properties we use the ideal square-root density of states in the approximation of parabolic valence bands for each of the four valence-band subbands of pseudo-spin j_z as given by Eqn. 1.20. To account for the residual coupling between the Mn spins the Curie-Weiss parameter Θ as introduced in section 1.3.3 is used. This residual coupling is ferromagnetic for $\Theta > 0$ and is antiferromagnetic for $\Theta < 0$. In the model Θ is treated as a free parameter (see Table 3.1). The exchange integral $N_0\beta$ is an average of the local p-d exchange constants J_i defined between the localized spin of a Mn ion and a hole spin (see Eqn. 1.5). The local p-d exchange strongly depends on the local configuration of the Mn ion, i.e. substitutional Mn acting as an acceptor, compensated substitutional Mn, and interstitial Mn, will have different J_i constants. Therefore the average exchange integral $N_0\beta$ in $Ga_{1-x}Mn_xAs$ alloys is somewhat ill defined [123]. The corresponding values in the literature for $|N_0\beta|$ vary between 1 eV and 4.5 eV [3, 124, 125].

Besides the disorder induced by the giant Zeeman splitting, we also take into account a magnetic field independent disorder given by Eqn. 1.16.

For a quantitative modelling of the resistivity dependence attempted here, not only a realistic description of the local density of states of the valence band of $Ga_{1-x}Mn_xAs$ is essential but also a realistic modelling of the acceptor states. Typical hole densities in ferromagnetic $Ga_{1-x}Mn_xAs$ alloys with x of a few percent are in the range of 10^{18} to $10^{20}\,cm^{-3}$, i.e. they can be considerably lower than the actual Mn content. Since not all Mn ions which are incorporated into the crystal act as acceptors, we treat x and the density of acceptors N_A as two independent model parameters. Moreover, instead of a simple delta-like acceptor density N_A, we model the acceptor density by an acceptor band with a Gaussian distribution of acceptor energies centered at 110 meV (depth of an isolated Mn acceptor in GaAs [126, 127, 128]) and with a halfwidth σ according to Eqn. 2.7. The halfwidth σ discussed in detail in section 2.3 is treated as a free parameter. The existence of such an acceptor band is essential for explaining a non-Arrhenius behavior of the resistivity in the framework of traditional semiconductor band transport [129]. Such a non-Arrhenius behavior of the resistivity can clearly be seen in the experimental data in Fig. 3.4.

In the model an interaction between the magnetic field and the acceptor states is neglected. The acceptor distribution only serves as a reservoir of hole states and no formation of an acceptor band which directly contributes to

the transport process is taken into account. Therefore, the model can only give a crude approximation of the transport situation for a metallic ferromagnetic semiconductor alloy such as the as-grown sample below T_{C}. Nevertheless, we will show that a reasonable description of the temperature-dependent magneto-transport behavior can be obtained. The effects are crudely accounted for in the model by a large half-width σ which shifts the Fermi-energy into the valence-band states leading to a quasi-metallic behavior and the zero-field splitting of the valence-band states due to the Weiss molecular-field.

Accounting for both, the influence of the external magnetic field on the band states as well as the broadened acceptor energy levels, the neutrality equation

$$\int_{-\infty}^{max_{K^2}(E_{\mathrm{V}})} \check{N}(E) F^{\mathrm{h}}(E)\, dE = \int N_A(E) F^{\mathrm{e}}(E)\, dE, \tag{3.1}$$

is solved to determine the position of the Fermi energy E_{F}. The upper bond of the integration $max_{K^2}(E_{\mathrm{V}})$ denotes the maximum of all K^2 local valence-band subband edges. $\check{N}(E)$ is the normalized sum over the (K^2) different local valence-band densities of states

$$\check{N}(E) = \frac{1}{K^2} \sum\nolimits_{m=1}^{K^2} \sum_{j_z} N_{j_z}^{m}(E) \tag{3.2}$$

which includes the external field induced splitting of the valence-band states in each network cell covered by Eqn. 1.15.

3.2.1 Description of the ferromagnetic phase

Furthermore, we extend the model to the ferromagnetic phase below the Curie temperature T_{C}, where the magnetic moments of the Mn ions exhibit a spontaneous magnetization. The simplest approach to do so is to introduce a Weiss molecular-field, where the magnetization M at $T < T_{\mathrm{C}}$ is given by

$$M = M_0 B_f \left(\frac{g \mu_{\mathrm{B}} \mu_0 S}{k_{\mathrm{B}} T} (H + W M) \right) \tag{3.3}$$

where M_0 is the magnetization at saturation, W is the molecular-field constant, S is the spin of the Mn 3-d shell and B_f is the corresponding Brillouin-function. For simplicity, H and M are treated as scalars, i.e. we do not account for magnetic anisotropy. The magnetic anisotropy leads to anomalies, the so-called anisotropic magnetoresistance effect in the magnetoresistance at low fields ($\mu_0 H < 1\,\mathrm{T}$) [130]. However, the effects are rather small compared with the MR effects occurring up to 10 T which are in the focus of this work.

At fields above 1 T the treatment of H and M as scalars is justified as the magnetization is aligned along the external magnetic-field direction.

Without an external field one can rewrite and expand Eqn. 3.3 to

$$\frac{M}{M_0} = B_f\left(\frac{g\mu_B\mu_0 SWM}{k_\mathrm{B}T}\right) \approx \frac{S+1}{3S}\frac{g\mu_B\mu_0 SWM}{k_\mathrm{B}T} \tag{3.4}$$

where

$$W = \frac{3k_\mathrm{B}T_\mathrm{C}}{(S+1)g\mu_0\mu_\mathrm{B}M_0}. \tag{3.5}$$

Eqn. 3.4 is an implicit equation for the magnetization and can be solved numerically using the Curie temperature as an input parameter determined by experiment. For $T < T_\mathrm{C}$ Eqn. 3.4 is solved and the obtained molecular field is added to the external magnetic field when calculating the average Mn spin orientation $\langle S_z\rangle$ which is used to calculate the giant Zeeman splitting of the valence-band subbands given by Eqn. 1.15. The Curie temperature of the samples annealed at 400-600 °C which show paramagnetism in the full temperature range down to 20 K is set to 0 in the model (see Tab. 3.1). Even though the samples will have Curie temperatures slightly above 0 K basing on the simplified treatment of the ferromagnetic phase as given by the molecular-field theory, the molecular field is 0 for all temperatures $T > T_\mathrm{C}$. Therefore the choice of $T_\mathrm{C} = 0$ K is justified and holds exactly the same result as if the real value of the systems T_C was known and used in the model.

3.3 Correlation of transport properties and model parameters

It is demonstrated that, despite the considerable number of model parameters (i.e. acceptor density N_A, halfwidth σ of the acceptor energy distribution, Mn concentration x, alloy disorder parameter m_D, p-d exchange integral $N_0\beta$, and Curie-Weiss parameter Θ) a combined analysis of temperature dependence of the resistivity and a set of MR curves at different temperatures yields a very narrow range of possible values for each model parameter. Therefore, the entire set of parameters determined for a particular sample can be considered as a characterization of its microscopic state. Furthermore, the trends observed for the parameter sets of the series of samples annealed at different temperatures gives valuable insight into the microscopic changes due to thermal treatment.

The resistivity in zero-magnetic field in the paramagnetic phase is independent of the 'magnetic' parameters $N_0\beta$ and Θ. It mainly depends on the energetic arrangement between acceptor states (serving as the carrier reservoir only) and the valence-band states (where the transport takes place). This

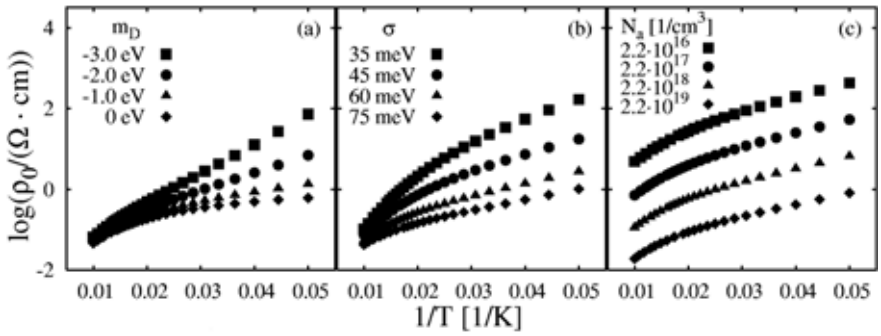

Fig. 3.2. Effect of the model parameters on the temperature dependence of the resistivity ρ_0 based on the model parameters used for the sample annealed at 400 °C. (a) Influence of disorder: $|m_D|$ varied from 0 to 3.0 eV; (b) Influence of halfwidth σ of the Gaussian distribution of acceptor energies varied from 35 to 75 meV; (c) Influence of the acceptor density N_A varied from $2.2{\cdot}10^{16}$ cm^{-3} to $2.2{\cdot}10^{19}$ cm^{-3}.

situation is characterized almost entirely by the three model parameters m_D, σ, and N_A. Graphs (a), (b), and (c) of Fig. 3.2 depict the behavior of the temperature dependence of the resistivity on varying each of these parameters. As expected, the resistivity at low temperatures in graph (a) increases with increasing $|m_D|$. It is worth noting that the calculated resistivity in zero-field is independent of the sign of m_D in contrast to the MR as discussed below. In addition, the disorder influences the temperature dependence of the Fermi energy resulting in a change of the curvature of the Arrhenius plot of the temperature-dependent resistivity [67]. As is depicted in graph (b), mainly the resistivity at low temperatures is significantly affected by the choice of σ. Basically with decreasing σ the effective activation energy is increased and approaches $E_A = 110$ meV (activation energy of an isolated Mn acceptor) for $\sigma \to 0$. A non-zero σ corresponds to a distribution of acceptor energies leading to the curvature of the Arrhenius plots of the temperature-dependent resistivity (see detailed discussion in Ref. [129]). For very large values of σ the Fermi energy lies within the valence band at low temperatures, leading to a quasi-metallic temperature behavior of the resistivity. Graph (c) presents the dependence of the temperature dependent resistivity on the acceptor density N_A. The decrease of the acceptor density simply leads to a downshift of the resistivity-curves basically without changing their curvature.

Using only the zero-field results it is impossible to determine both parameters m_D and σ. Additional information is required, which is given by the MR data. The MR mainly depends on the 'magnetic' parameters $N_0\beta$ and Θ, but also significantly on the sign of the alloy disorder m_D [10]. Exemplarily,

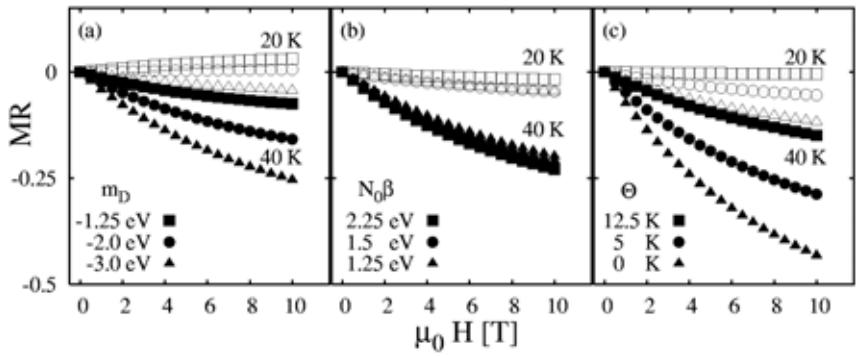

Fig. 3.3. Effect of the model parameters on the calculated magnetoresistance at 20 and 40 K for the as-grown $Ga_{0.98}Mn_{0.02}As$ sample. (a) Influence of disorder: m_D varied from $-1.25\,\mathrm{eV}$ to $-3.0\,\mathrm{eV}$ (fixed parameters: $\Theta = 7.5\,\mathrm{K}$, $N_0\beta = 2.0\,\mathrm{eV}$); (b) Influence of the p-d exchange integral: $|N_0\beta|$ varied from $1.25\,\mathrm{eV}$ to $2.25\,\mathrm{eV}$ (fixed parameters: $\Theta = 7.5\,\mathrm{K}$, $m_D =,-2.75\,\mathrm{eV}$); (c) Influence of the residual coupling between Mn ions: Θ varied from $0\,\mathrm{K}$ to $12.5\,\mathrm{K}$ (fixed parameters:$N_0\beta = 2.0\,\mathrm{eV}$, $m_D = -2.75\,\mathrm{eV}$).

Figs. 3.3 and 3.4 show calculated MR results for the as-grown $Ga_{0.98}Mn_{0.02}As$ layer and the sample annealed at 400 °C, respectively. Both figures consist of three graphs (a) to (c) where the model parameters m_D, $N_0\beta$ and Θ, respectively, were varied whereas all other model parameters remained fixed at the values given in Table 3.1. The MR curves were calculated for 20 and 40 K in each case.

In the graphs (a) of Figs. 3.3 and 3.4 the dependence of the MR on the magnitude of the magnetic field independent disorder m_D is shown. In both cases the MR increases with increasing absolute value of the negative m_D. The situation arising from a negative value of m_D is a disordered valence-band energy landscape where regions (cells in the model) with a local Mn concentration x_loc below the average Mn content x have a reduced activation energy. This reduced activation energy arises as their local valence-band edge is closer to the (global) Fermi level. An external magnetic field splits the valence bands according to Eqn. 1.15 and the valence-band subband density of states belonging to the majority spin orientation is shifted towards the acceptor level. In contrast to the valence-band shift towards the acceptor induced by the alloy disorder, this magnetic-field induced shift is the stronger the higher the local Mn concentration is. Therefore the two shifts may compensate each other in the subbands dominating the transport, if the values of $m_\mathrm{D}(x_\mathrm{loc} - x)$ and $E_V(j_z, T, H)$ are in a comparable range. The disordered potential landscape determined by m_D in zero-field will be smoothed out with

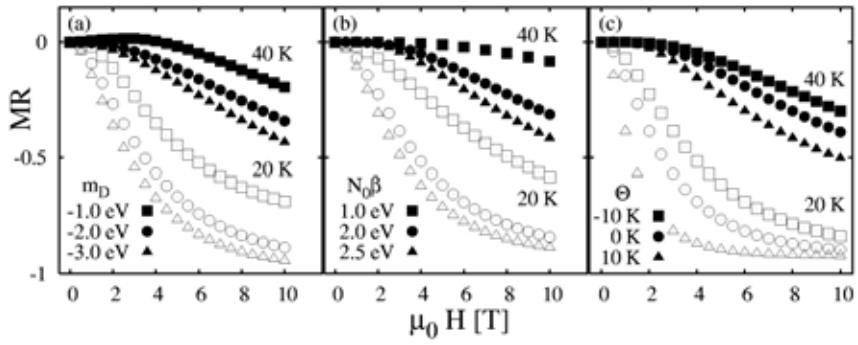

Fig. 3.4. Effect of the model parameters on the calculated magnetoresistance of the sample annealed at 400 ° C. (a) Influence of disorder: m_{D} varied from $-1.0\,\mathrm{eV}$ to $-3.0\,\mathrm{eV}$ (fixed parameters: $\Theta = -12.5\,\mathrm{K}$, $|N_0\beta| = 1.85\,\mathrm{eV}$); (b) Influence of the p-d exchange integral: $|N_0\beta|$ varied from $1.0\,\mathrm{eV}$ to $2.5\,\mathrm{eV}$ (fixed parameters: $\Theta = -12.5\,\mathrm{K}$, $m_{\mathrm{D}} = -1.5\,\mathrm{eV}$); (c) Influence of the residual coupling between Mn ions: Θ varied from $-10\,\mathrm{K}$ to $10\,\mathrm{K}$ (fixed parameters:$|N_0\beta| = 1.85\,\mathrm{eV}$, $m_{\mathrm{D}} = -1.5\,\mathrm{eV}$).

increasing magnetic field leading to a negative MR. Vice versa, if the absolute value of the negative m_{D} is too small or m_{D} is positive, one obtains a positive MR since the disorder increases in the presence of an external magnetic field. Therefore, the combined analysis of ρ_0 and MR data allows one to determine the magnitude as well as the sign of m_{D}.

Furthermore, in graph (a) of Fig. 3.4 the negative MR effects calculated for $T = 20\,\mathrm{K}$ are more pronounced than those at 40 K. The reason is that the giant Zeeman splitting of the sample annealed at 400 °C, which is paramagnetic in the entire temperature range under study, decreases with increasing temperature. Thus the influence of the magnetic effects is reduced with increasing temperature. The situation for the as-grown sample shown in graph (a) of Fig. 3.3 is different because the sample has a Curie temperature of $T_{\mathrm{C}} \approx 44\,\mathrm{K}$. The MR curves calculated for 40 K are more negative than those at 20 K. The reason is that the further the temperature is reduced below the Curie temperature, the closer is the spontaneous magnetization to the saturation magnetization. This spontaneous magnetization yields a giant Zeeman splitting already for zero external magnetic field. Therefore, in the approximation of a Weiss molecular-field the influence of the external magnetic field on the band structure decreases with decreasing temperature in the ferromagnetic phase.

We will now turn to the discussion of the 'magnetic' parameters $N_0\beta$ and Θ. The variations of both parameters exhibit clear and distinguishable trends. The former mainly scales the magnitude of the MR effects whereas

the latter mainly affects the curvature of the MR as it determines the value of the saturation field of the Brillouin function. The dependence of the MR of the ferromagnetic and paramagnetic sample on $N_0\beta$ at 20 and 40 K is demonstrated in Figs. 3.3 and 3.4. The results for the paramagnetic sample are easily understood: Since the value of $N_0\beta$ scales the influence of the external magnetic field, the negative MR increases with increasing $N_0\beta$. In the calculations performed to describe the ferromagnetic sample, the magnitude of the MR as well as the influence of the value of $N_0\beta$ on the MR are much smaller. Again the reason is the existence of the spontaneous magnetization which reduces the influence of the external magnetic field as discussed above. It is remarkable here that the negative MR at the lower temperature of 20 K decreases with increasing value of $N_0\beta$, whereas at 40 K close to T_C it shows almost the opposite behavior and the negative MR increases with increasing $N_0\beta$. At temperatures far below the Curie temperature, the Weiss molecular-field $W \cdot M$ given by Eqn. 3.3 becomes very large. Even though the molecular field is a global value and does not vary spatially throughout the sample, the resulting potential landscape given by this inner magnetic field via Eqn. 1.15 will fluctuate as the Mn ions are incorporated randomly in the system. For large values of $N_0\beta$ these fluctuations are saturated already without an external field and the influence of the additional external magnetic field is almost negligible. At higher temperatures just below the Curie temperature, the molecular field is still present though much weaker and hence the effect of an external magnetic field can yield the dominant contribution to the MR and the negative MR increases with increasing $N_0\beta$.

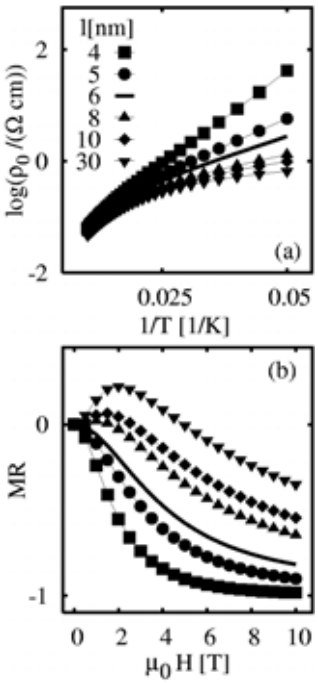

Fig. 3.5. Calculated resistivity (a) and MR (b) for the sample annealed at 400 °C for different values of the cube-edge length l. Solid line indicates $l = 6$ nm as it is used in the calculations.

In graphs (c) of Figs. 3.3 and 3.4 the dependence of the MR on the Curie-Weiss temperature Θ is shown for both samples at both temperatures. In the case of the ferromagnetic sample the effect of the external field decreases with increasing positive value of Θ since the ferromagnetic order, i.e. the spontaneous magnetization, at a given temperature

is increased. In the case of the paramagnetic sample the MR is shown for values of Θ ranging from 10 K to −10 K. Since the sample shows paramagnetism, Θ has no impact on the transport behavior at zero-field as the Weiss molecular-field $W \cdot M = 0$. However, it affects the effects of an external field. For a given temperature, the influence of the external field gets boosted for positive values of Θ, which leads to an earlier saturation of the Brillouin function compared to $\Theta = 0$ K due to the residual ferromagnetic coupling between the Mn ions, while for negative values of Θ the influence of the external field gets damped compared to $\Theta = 0$ K because of the residual antiferromagnetic coupling between Mn ions.

Fig. 3.5 depicts the influence of the choice of the network-cube length l on the calculated results of the resistivity (a) and the magnetoresistance (b). This is done with use of the parameters which were applied to describe the sample annealed at 400°C as given in Tab 3.1. In (a) one can see that the resistivity at low temperatures gets enhanced with decreasing l. This can be understood since with decrease of l the amplitudes of the potential fluctuations leading to a localization of carriers at low temperatures increase. A strong localization due to the alloy disorder resulting in a strong increase of ρ_0 at low T does not agree with the experimental data. Thus a lower boundary for the choice of l is obvious. With increase of l all influences of the magnetic field independent disorder vanish as the concentration of x_{loc} reaches its average value x. In (b) the choice of large values of l corresponding to the virtual-crystal approximation averaging out all spatial fluctuations of the Mn concentration result in a much too small negative MR. The large negative MR values are obtained for small l. Due to the corresponding large amplitude of the potential fluctuations induced by the giant Zeeman splitting, a percolation path of low conductivity can be obtained. In this scenario the reduction of the activation energy along the percolation path overcompensates the effect of localization due to enhancement of disorder. Nevertheless, there exists a (physically not meaningful) value of l below which the amplitude of the spatial fluctuation becomes that large, that localization effects lead to a strong enhancement of the MR. In conclusion, the dependence of the calculated resistivity ρ_0 and

Table 3.1. Model parameters

T_a [°C]	x	N_{A} [cm^{-3}]	$N_0\beta$ [eV]	σ [meV]	m_{D} [eV]	θ [K]	T_{C} [K]
ag	0.02	$5.47 \cdot 10^{19}$	2.0	85	−2.75	7.5	44
350	0.019	$3.64 \cdot 10^{19}$	2.0	75	−2.5	5	42
400	0.018	$5.92 \cdot 10^{18}$	1.85	60	−1.5	−12.5	< 20
500	0.014	$1.37 \cdot 10^{18}$	1.75	47	−1.5	−12.5	< 20
600	0.01	$2.28 \cdot 10^{16}$	1.65	45	−1.5	−12.5	< 10

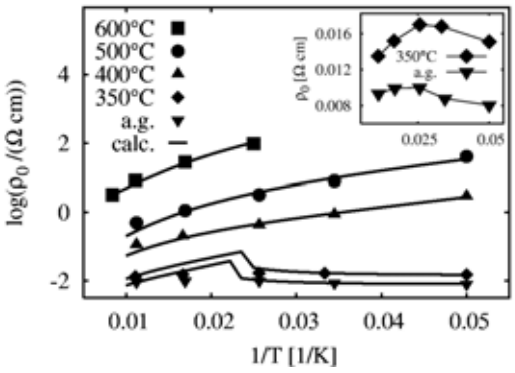

Fig. 3.6. Comparison between experimental data and calculated values of the logarithmic resistivity versus $1/T$ for the as grown $Ga_{0.98}Mn_{0.02}As$ samples and the samples annealed at different temperatures. Symbols denote the experimental values while full lines are calculated curves. Inset: anomaly of the measured resistivity around T_C for the two metallic samples.

magnetoresistance on the model parameter l can be well understood [10]. The value of l only can be chosen in a certain range, where still remains a freedom of choice. A different choice of l requires a modification of the choice of the remaining parameters connected with the influence of disorder such as e.g. m_D and $N_0\beta$. Thus this model cannot be used to determine their exact values as long as the choice of l stays a free parameter. The main statement of this work stays untouched by this uncertainty: The transport properties of the discussed DMS in its paramagnetic phase can be described using the discussed effects of magnetic field independent disorder and giant Zeeman splitting induced shifting of the local valence-band edge while commonly discussed many-body effects such as the formation of magnetic polarons are neglected.

3.4 Comparison between theory and experiment

We demonstrate that the effects of annealing on the resistivity and the MR of series of $Ga_{0.98}Mn_{0.02}As$ samples at temperatures below 100 K can be well described using the model developed in Sect. 3.2. Furthermore, we show that the temperature-independent set of model parameters obtained for the best description of the experimental data of each sample is in agreement with the literature. In the following, we assume that annealing of MBE grown $Ga_{1-x}Mn_xAs$ in the temperature range between 350 and 600 °C mainly causes segregation and leads to the formation of MnAs precipitates. In terms of the transport behavior of the samples this will mainly reduce the amount of Mn x in the matrix as the MnAs cluster densities are too low to affect the main transport path through the sample (i.e. are below the percolation threshold).

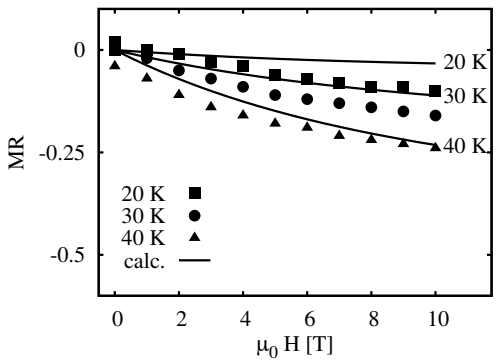

Fig. 3.7. Comparison of experimental and calculated values of the magnetoresistance versus Hfield at various temperatures between 20 and 40 K for the as-grown $Ga_{0.98}Mn_{0.02}As$ sample. Symbols denote the experimental values, full lines are calculated curves. Model parameters used are given in Table 3.1.

Fig. 3.6 depicts a comparison of the Arrhenius plots of the resistivity of the as-grown $Ga_{0.98}Mn_{0.02}As$ sample and the corresponding series of samples annealed at different temperatures. It is worth noting at this point that the transport properties of the sample annealed at 300°C are within the experimental uncertainties almost identical with those of the as-grown sample. This indicates that 10 min annealing at this moderate temperature has almost no impact on the structural properties of the alloy. The plots cover the temperature range below 100 K. The as-grown sample (triangles down) as well as that annealed at 350 °C (diamonds) exhibit a metallic behavior in this range and, as can be clearly seen in the inset, show an anomaly in the resistivity curve indicative for the ferromagnetic to paramagnetic phase transition. This transition occurs in both samples at about 40 K. The samples annealed at 450 (triangles up), 500 (circles), and 600 °C (squares) show activated transport behavior, which becomes more pronounced with increasing annealing temperature. The corresponding Arrhenius plots exhibit the bowing indicative for a distribution of acceptor energies as discussed in section 3.3, i.e. it is not a linear Arrhenius plot which would be indicative for a delta-like acceptor energy distribution.

The calculated curves are presented by the solid lines. First, we will address the two metallic samples. The assumption of a very broad acceptor band in Eqn. 3.1 leads to a Fermi energy which is located within the valence band. This results in a metal-like temperature dependence of the resistivity at low temperatures. With increasing temperature one leaves the range where the model is approximately valid for metallic samples. After all acceptors are ionized, the Fermi energy moves into the band gap, which results in an activated transport behavior. Although this is only a crude approximation of the metallic state, we use such a broadened acceptor to model the temperature

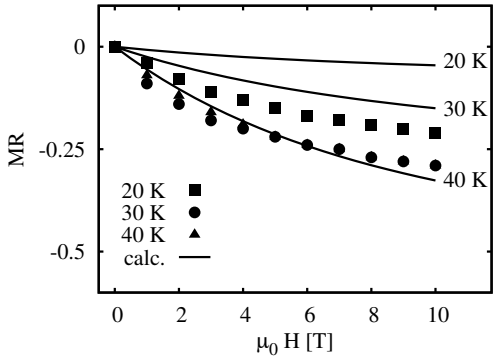

Fig. 3.8. Comparison of experimental and calculated values of the MR versus H-field at temperatures between 20 and 40 K for the sample annealed at 350 °C. Symbols denote the experimental values, full lines are calculated curves. Model parameters used are given in Table 3.1.

dependence of the resistivity of the as-grown sample and the sample annealed at 350 °C in the temperature range below 100 K. The calculated values coincide with the measured data below the Curie temperature T_C. The magnetic phase transition at the Curie temperature is clearly visible in the calculated curves as a strong peak of the resistivity appearing at T_C. The corresponding anomaly in the measured data shows a much weaker maximum at T_C which is considerably broadened, such that it is hardly visible in the logarithmic plot.

This difference between the measured and calculated curves potentially originates from two assumptions made in the model: (a) the phase transition from paramagnetic to ferromagnetic occurs throughout the entire sample at T_C (the Curie temperature is taken as a global parameter) and (b) the sample acts as a single domain. Both assumptions do not hold for the real system. Neither will it have a single domain structure nor does it exhibit a global transition from the paramagnetic to the ferromagnetic state. Instead it will exhibit a domain structure which will become ferromagnetic at slightly different temperatures in dependence on the local Mn concentration and the local concentration of carriers. The calculated curves for the three semiconducting samples (annealed at 400, 500, and 600 °C) are in good agreement with the experimental data. The observed transition from metallic behavior via semiconducting to almost insulating behavior on annealing can be reproduced in the model by mainly adjusting two parameters. The acceptor density N_A and the halfwidth σ of the distribution of acceptor energies. The acceptor density decreases from about $5 \times 10^{19}\,\mathrm{cm}^{-3}$ for the as-grown sample to $2 \times 10^{16}\,\mathrm{cm}^{-3}$ for the sample annealed at 600 °C and σ decreases from 85 meV to 45 meV. A decrease of the halfwidth of the acceptor energy distribution is expected on reducing acceptor density as the mean distance between acceptors increases leading to a more isolated behavior, i.e. a well defined activation energy of 110 meV for acceptors which are infinitely far apart. The reduction of the ac-

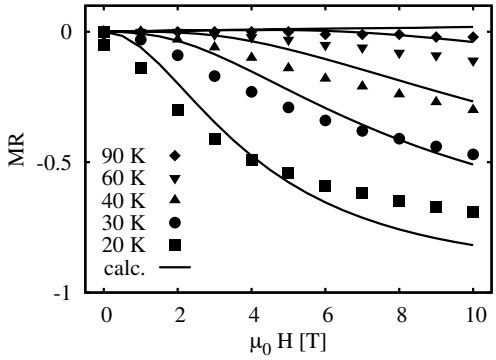

Fig. 3.9. Comparison of experimental and calculated MR versus H-field at various temperatures between 20 and 90 K for the sample annealed at 400 °C. Symbols denote the measured values, full lines are calculated curves. Model parameters used are given in Table 3.1.

ceptor density N_A itself, which becomes significant, can be explained by the structural transition from a random alloy via an alloy with a non-random Mn distribution to a granular hybrid where MnAs inclusions have formed inside a Mn-doped GaAs matrix. The onset of the formation of MnAs clusters will occur typically at an annealing temperature of 400 °C. For the corresponding sample, there is a rapid decrease of the parameter N_A in the calculation. Indeed, ferromagnetic resonance measurements of the sample annealed at 600 °C show clear signatures of MnAs hexagonal clusters with the c-axis parallel to the GaAs [111] directions as observed previously in GaAs:Mn/MnAs hybrids grown by MOVPE [131]. However, in contrast to their MOVPE grown counterparts [41], the density of the MnAs clusters is too small to affect the magneto-transport behavior of the hybrids.

In Figs. 3.7 and 3.8 the comparison between the calculated and measured magnetoresistance is shown for the two metallic samples. It is obvious that the model yields a good description of the MR curve in the vicinity of the paramagnetic phase at 40 K while the deviations between experiment and theory are more significant in the case of the ferromagnetic phase at 20 and 30 K. Here the theoretical values for the negative MR are too small. However, this is somewhat expected as the model can only crudely approximate the ferromagnetic phase as discussed in Section 3.2.

A possible explanation is that the model is based on a global Curie temperature and does not account for spatial fluctuations of T_C. In reality, there are still paramagnetic regions in the sample present at temperatures of 20 or 30 K (i.e. below the global T_C of about 40 K). The percolation path which determines the transport properties of the sample will connect only regions of ferromagnetic order simply because of their higher carrier density. The percolation path is smoothed and shortened with increasing external field and corresponding giant Zeeman splitting of the paramagnetic regions which re-

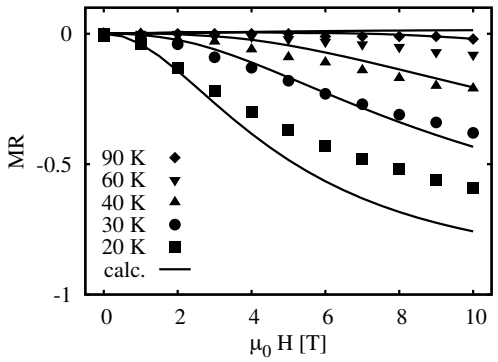

Fig. 3.10. Comparison of experimental and calculated values of the MR versus H-field at various temperatures between 20 and 90 K for the sample annealed at 500 °C. Symbols denote the measured values, full lines are calculated curves. Model parameters used are given in Table 3.1.

duces the disorder in the sample. This will lead to an enhancement of negative MR effects at these temperatures. However, even in its simplicity, the model shows the observed trend of the experiments: The lower the temperature below T_C, the smaller is the negative MR effect.

Figs. 3.9, 3.10, and 3.11 show the good quantitative agreement of the calculated and measured MR for the three semiconducting samples annealed at 400 °C, 500 °C, and 600 °C. Especially for the two samples annealed at 400 °C and 500 °C the calculated values are in a good quantitative agreement with the experimental data for all temperatures except the lowest temperature at 20 K. Here the model predicts a negative MR effect which is too large compared to experiment.

One possible explanation of the differences between theory and experiment is again the assumption of a global T_C in the model. A ferromagnetic percolation path will only persist up to T_C, however, in a real sample at least small regions with ferromagnetic order will be still present at temperatures above T_C. The size and density of these regions will decrease with increasing temperature. The effect of the external magnetic field on the regions with ferromagnetic order is weaker than that on the surrounding paramagnetic environment. Therefore the negative MR effect in the presence of ferromagnetic regions will be smaller than in a pure paramagnetic phase assumed in the model. An other possible explanation is an annealing induced non-random Mn ion incorporation which is studied in detail in chapter 4.

We will now discuss the annealing-induced changes of the temperature-independent parameters derived from the analysis of the transport data (Table 3.1). First of all, it should be stated that the values of all model parameters throughout the series are in realistic parameter ranges and show monotonic trends on annealing. Annealing considerably above the growth temperature leads to the formation of MnAs precipitates and the observed transport be-

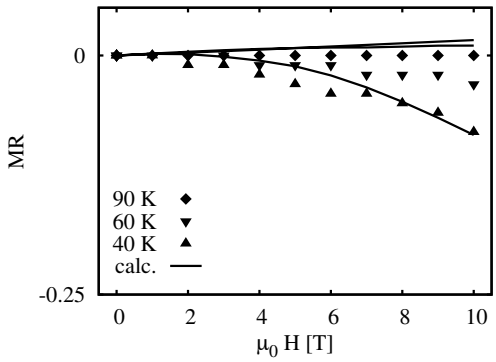

Fig. 3.11. Comparison of experimental and calculated MR versus H-field at various temperatures between 40 and 90 K for the sample annealed at 600 °C. Symbols denote the experimental values, full lines are calculated curves. Model parameters are given in Table 3.1.

havior is determined almost solely by the surrounding alloy-like matrix and not directly by the MnAs precipitates. The observed reduction of x with increasing annealing temperature reflects the extraction of Mn from the matrix for forming MnAs precipitates. In particular, x decreases more rapidly between 400 and 600 °C, where the precipitate formation is known to become significant. Furthermore, the acceptor density N_A and width σ of the acceptor energy distribution also show a decrease with increasing annealing temperature. We do not expect an increase of N_A at these high annealing temperatures as the dominant structural effect is not the reduction of compensating defects but rather precipitation formation.

The remarkable decrease of N_A at the highest annealing temperature (where one observes clear FMR[4] signatures of hexagonal MnAs clusters as discussed above) may be explained by trapping of holes at the matrix-precipitate interfaces (as for the MOVPE counterparts see Refs [41, 132, 133]) which leads to an additional reduction of free holes, i.e. a low effective acceptor concentration N_A. The weak change of σ between 500 and 600 °C annealing temperature supports this view, as the almost constant σ indicates that the real distribution of acceptors is very similar. The alloy-disorder parameter m_D is constant for all paramagnetic samples, as somewhat anticipated. The origin of the slightly different values for the ferromagnetic samples is not obvious. The trends for the two 'magnetic' parameters $N_0\beta$ and Θ are related to the observed reduction of the free hole concentration reflected by the reduction of N_A on annealing. It is well established that $N_0\beta$ depends on the carrier concentration [123], it is even of different sign for p-type and n-type GaAs:Mn. Therefore, a reduction of the absolute value of $N_0\beta$ with decreasing N_A appears reasonable. The change of sign of Θ from positive to negative

[4] Ferromagnetic resonance

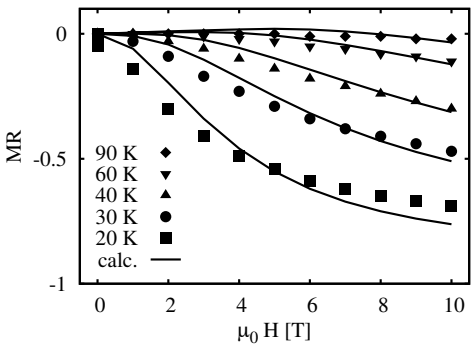

Fig. 3.12. Comparison of experimental and calculated MR versus H-field at temperatures between 20 and 90 K for the sample annealed at 400 °C. Symbols denote experimental values, full lines are calculated curves. In the calculation a temperature dependence of $N_0\beta$ and Θ was assumed: Pairs of Θ and $N_0\beta$ of 2.5 K/1.0 eV; 5.0 K/1.2 eV; 7.5 K/1.35 eV; 15 K/1.7 eV; 25 K/2.75 eV were used for temperatures in ascending order from 20 to 90 K. Additional parameters are given in Table 3.1.

with increasing annealing temperature manifests the change from residual ferromagnetic coupling to residual antiferromagnetic coupling between Mn ions in the paramagnetic phase which is also anticipated with decreasing free hole concentration.

An alternative explanation of the deviation of the calculated MR curves from the experiment (other than spatial fluctuations of T_C) can be given for the paramagnetic samples. It is based on the fact that the free hole concentration increases almost exponentially with increasing temperature. Furthermore, it is well established that the coupling between the Mn ions in $Ga_{1-x}Mn_xAs$ is governed by the RKKY mechanism, i.e. depends strongly on the free hole concentration. This influence is not restricted to the ferromagnetic phase, but should also determine the residual coupling between Mn ions in the paramagnetic phase, i.e. affect the corresponding model parameters $N_0\beta$ and Θ. We have refined the description of the MR data of the sample annealed at 400 °C allowing for a temperature dependence of these two magnetic parameters. The best agreement between theory and experiment obtained for these assumptions is shown in Fig. 3.12. The model parameter $N_0\beta$ is found to increase with increasing temperature from 1.0 eV at 20 K to 2.75 eV at 90 K corresponding to an increased p-d exchange. The Curie-Weiss parameter Θ also increases from 2.5 K at 20 K to 25 K at 90 K corresponding to an increase of the residual ferromagnetic coupling between Mn ions with increasing carrier density as expected.

3.5 Conclusion

The annealing induced changes of the temperature-dependent resistivity and magnetoresistance of series of (Ga,Mn)As samples (an as-grown $Ga_{0.98}Mn_{0.02}As$ sample and annealed samples of the same specimen) were studied. The samples, whose transport properties were simulated here, were annealed at various temperatures between 350 and 600 °C. In this temperature range the main effects of annealing are structural changes from a random alloy with metallic behavior to a granular hybrid with almost insulating behavior. Modelling the transport data with the network model introduced in Sect. 1.3, which accounts for the peculiarities of the $Ga_{1-x}Mn_xAs$ dilute magnetic semiconductor in a realistic way, allows one to extract sets of material parameters. These parameters reflect the microscopic changes induced by the thermal annealing procedure. The model yields an astoundingly satisfactory quantitative description of the transport properties of (Ga,Mn)As samples in the entire range of resistivity, from metallic to insulating. We demonstrate that the complexity of the measured resistivity curves can be condensed into a few microscopically meaningful model parameters with realistic values and that these parameters characterize the microscopic state of the samples due to the strong correlation between magnetic, transport and structural properties. Due to the apparent mismatch between the high degree of complexity of the discussed materials and the simplicity of the applied model the even quantitative agreement of experimental data and theory is rather astonishing. However, it is undoubted that a full description of the transport properties of the discussed materials is missing still and the present work only provides an indication for the principal transport mechanism on top of which the influence of many-body interactions have to be clarified prospectively.

4

Non-random Mn incorporation

4.1 The Curie temperature − from a global towards a local parameter

As discussed in detail in previous chapters, the network model was primarily developed to describe the transport properties of an ideal DMS in its paramagnetic phase. It was extended to stay applicable for the description of the ferromagnetic phase even in a metal like transport regime.

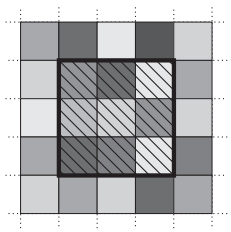

Fig. 4.1. Hatched area shows a cell of the Curie temperature meta-network for a coordination number of 3, over which the local Mn concentration of the ground laying network cells is averaged. The monochrome cells belong to the transport network. Different grey tones indicate different Mn concentrations.

On the basis of the used Weiss molecular-field model (for more details see appendix D), the Curie temperature T_C is the only free parameter which is needed to take into account a ferromagnetic coupling between the Mn ions. So far T_C is a global parameter. It does not depend on the spatial position e.g. the local density of Mn ions. As the ferromagnetism in $Ga_{1-x}Mn_xAs$ alloys is explained in the framework of the RKKY mechanism [3, 23] where the coupling between the spins of the Mn ions is mediated by carriers, the transition temperature will be strongly affected by the carrier concentration. As shown previously spatial fluctuations of the carrier density play an essential role for the transport properties of the studied system. Against the background of the underlying ferromagnetic coupling mechanism it seems reasonable to consider not solely the spatial fluctuations

of the carrier density but resulting spatial fluctuations of the ferromagnetic ordering temperature and their influence on the (macroscopic) transport properties as well. Indeed there are some experimental studies that support the existence of magnetic disorder within a single domain of size between 2 and 100μm. Their influence on the transport properties and the characteristic length-scale of this disorder remains unsettled so far [117, 118, 119].
It is well established that for ideal $Ga_{1-x}Mn_xAs$ samples with $x \leq 0.05$ the Curie temperature depends almost linearly on the concentration of Mn ions [3] and can be described by the relation

$$T_C = \alpha \cdot x \tag{4.1}$$

with $\alpha \approx 2000\,K$. This simple relation providing a connection between Mn concentration and Curie temperature serves as the basis of the following calculations.

4.1.1 Model details and results

When modelling a local Curie temperature the question arises again what the characteristic length-scale of this fluctuation should be. The answer is similar to that given when the length-scale l of the network was studied in Sect. 1.4.1: If magnetic disorder represented by a fluctuation of local Curie temperatures plays a role and if its influence is studied, one has to assume a length-scale that is small enough to keep disorder effects visible in the observed quantities.[1]

In the framework of this assignment the most natural approach is to presume the length-scale l of the network (in this section referred to as the transport network) as the length-scale of the local Curie temperature fluctuations. Doing so a cube with the edge length $l = 6\,nm$ contains the average number of Mn ions given by $N_{Mn} = x \cdot \frac{4}{(0.56nm)^3} \cdot l^3$. Under the assumption of $x = 0.02$ this leads to an average value $N_{Mn} = 394$ of ferromagnetically coupled Mn atoms. As slightly modified version of Eqn. 4.1 is used to calculate the local Curie temperature as

$$T_{C^{loc}} = \alpha \cdot x_{loc}. \tag{4.2}$$

This replaces the Curie temperature introduced in Sect. 3.2 as a free constant parameter by a local value determined by the factor α. It should be noted that

[1] Since ferromagnetism is a collective phenomenon which vanishes if the number of spins to be coupled is below a certain critical level, a physically motivated lower limit for the length-scale of such a fluctuation of the Curie temperature represented by our network approach should exist. As the existence of this lower boundary is clear its value is impossible to derive using the theoretical description at hand.

α is not accessible by theoretical considerations on the basis of our model. α is a free parameter which is used to set the (averaged) Curie temperature upon the experimentally observed value.

To study the intersection between strong local changes of T_C and a fully ordered situation, a linear filter function is used. In Eqn. 4.2 the local Mn concentration x_{loc} fluctuating on the length-scale of the cube-edge length l resulting in the largest possible fluctuation amplitudes[2] was substituted by a filtered value x^f_{loc}. This is calculated for each cell (i, j) of the transport network as given by

$$x^f_{i,j} = \frac{1}{o^2} \sum_{\substack{i-\frac{o}{2}<i'<i+\frac{o}{2} \\ j-\frac{o}{2}<j'<j+\frac{o}{2}}} x_{i',j'} \tag{4.3}$$

where the parameter o defines the filter size. In this attempt the Mn concentration of the o^2 cells centered around the cell with the coordinates (i, j) is averaged.

4.1.2 Influence of the local Curie temperature on the transport properties

In Fig. 4.2 the influence of the spatially varying Curie temperature and different filter sizes o on the temperature dependent resistivity are shown. In each of the three graphs the calculated resistivity ρ_0 is plotted logarithmically against the inverse temperature for three different (average) Curie temperatures of 35, 40 and 45 K. The three different graphs differ with respect to the considered local fluctuations of the Curie temperature: In graph (a) the T_C used in the calculations fluctuates on the length-scale of the transport network. This is the smallest possible scale leading to the largest possible amplitudes of the spatial fluctuation of T_C. In graph (b) $o = 3$ and in graph (c) $o = 5$ is used. As expected the width of the resistivity anomaly around the phase transition, which is the region of a strongly enhanced resistivity between the pure metallic transport regime at $T \ll T_C$ and the activated transport regime at $T \gg T_C$ gets broadened from (c) to (a) with decreasing length-scale of $T_{C^{loc}}$. The more the system deviates from the ordered case with a global magnetic ordering temperature, the more cells exist which show paramagnetism

[2] Since the average deviation δT_C of the local Curie temperature from its mean value is proportional to the average deviation δx of the local Mn content from its mean value as given by Eqn. 4.2 and under the assumption that x is a normal variable one gets $\delta T_C = \alpha \cdot \delta x \propto \frac{1}{l_C^{\frac{3}{2}}}$ where the l_C denotes the cube-edge length used for the derivation of the local Curie temperatures. Since the minimal value of l_C can be l, a Curie temperature fluctuation on the transport network cube-edge length l shows the largest possible amplitudes.

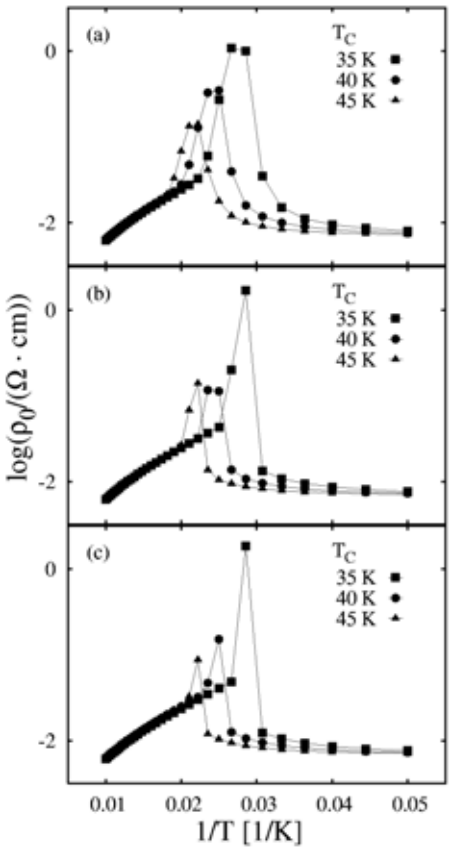

Fig. 4.2. Arrhenius plots of the calculated temperature dependence of ρ_0 on a local Curie temperature which fluctuates on different length-scales. In (a) the Curie temperature varies on the length-scale of the transport network, in (b) T_C gets filtered on the threefold length-scale and in (c) it gets filtered on the fivefold length-scale. For details about the filter procedure see text. The values of T_C indicated in the cut line correspond to the average Mn concentration. The factors of proportionality α defined by Eqn. 4.1 are: 45 K: 2368.4, 40 K: 2105.3, 35 K: 1842.1. The used material parameters belong to the sample annealed at 350 °C as given in Table 3.1.

even at temperatures below T_C. In such a case T_C is the average value of all $T_{C^{loc}}$. In contrast to the ferromagnetic regions which still show metallic conductivity, the paramagnetic cells exhibit an activated transport behavior with a larger resistivity. In the absence of ferromagnetic order (no accompanying Weiss molecular-field) no valence-band subband is shifted towards the Fermi level. Even though the amount of such paramagnetic regions below T_C is small enough not to intercept the percolation path through ferromagnetic (and thus metallic) regions, such paramagnetic islands will however elongate the path and contribute to an increase of the resistivity even below T_C.
The second dominant feature visible in the graphs in Fig. 4.2 is the maximum peak which decreases with increasing T_C. We concentrate in the following on the temperatures $T < T_C$. To interpret the calculated data, one has to keep in mind that only the cells which show paramagnetism are responsible for de-

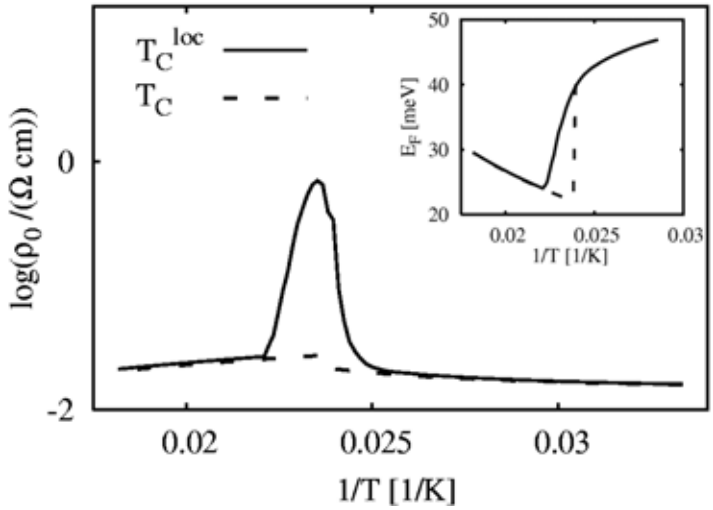

Fig. 4.3. Graph shows the resistivity around the Curie temperature in Arrhenius depiction. Solid lines indicate a calculation with a local Curie temperature (l = 15 nm), dashed lines a global Curie temperature The inset shows the corresponding Fermi energy for easier comparison plotted versus $1/T$. Images of the corresponding carrier densities and current paths of the sample with $T_{C^{loc}}$ can be found in Fig. 4.5. The used sample parameters are as given for the sample annealed at 350°C given in Tab. 3.1.

viation from the metallic conductivity. The resistivity of such semiconducting paramagnetic regions is determined sensitively by the ratio between thermal- and activation energy $\frac{k_B T}{\Delta}$ as given by Eqn. 1.3. With decrease of T_C the thermal energy of the cells which show paramagnetism at low temperatures slightly above T_C decreases as well whilst Δ stays nearly constant. Herewith the decrease of the maximum of the resistivity with increasing T_C as given by the calculations can be understood.

Another feature of the three graphs scilicet the large value of the resistivity peak stays questionable from the background of the following points:

1. The theory does not include effects related with different magnetic domains or grain boundaries such as localization at interfaces. In addition to the discussed influence of the Weiss molecular-field no further influence of the magnetic ordering of the Mn ions is included.
2. The band structure of a cell (i,j) is not affected by the value of the Curie temperature as soon as $T \geq T_{C^{i,j}}$.
3. For cells with $T < T_{C^{i,j}}$ an additional Weiss molecular-field is taken into account. This cells show metallic transport behavior due to the position of

the Fermi level which is energetically located almost inside the most shifted valence-band subband.

But nevertheless the maximum of the resistivity in all three graphs of Fig. 4.2 slightly around T_C is much larger than an extrapolation out of the semiconducting phase down to $T < T_C$ would predict. For a proper illustration Fig. 4.3 shows the calculated ρ_0 around the critical temperature which was performed using a local Curie temperature with $T_C = 42\,\mathrm{K}$ in comparison with the calculated resistivity of a reference system exhibiting a global Curie temperature of the same value. To suppress all additional influences of disorder $m_D = 0$ was used. The origin of this pronounced maximum of the resistivity is the dependence of the activation energy of paramagnetic cells on the amount of ferromagnetic cells in the system: Within a cell (i, j) fulfilling $T < T_{C^{i,j}}$ the Weiss molecular-field leads to a giant Zeeman splitting of the valence-band subbands as discussed more detailed in Sect. 1.3.3. Even slightly below the Curie temperature the strength of the molecular field is large in comparison with the external fields usually applied during the discussed experiments[3]. The calculated temperature dependence of the strength of the Weiss molecular-field for a system with $T_C = 40$ K is given in Fig. 4.4.

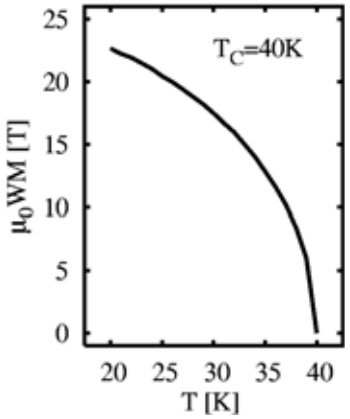

Fig. 4.4. Calculated strength of the Weiss molecular-field for a sample with T_C=40 K.

The combination of the high molecular field and the Mn concentration $x_{(i,j)} > x$ of the mentioned cells[4] leads to exceedingly large subband splits. These large shifts of the majority bands in the ferromagnetic cells also influence the neutrality equation and lead to an increase of the Fermi level. Despite the fact, that the resulting Fermi energy lies inside or at least close to the shifted valence-band subbands of the ferromagnetic cells[5], its energetic spacing from the valence-band edge of the paramagnetic cells is drastically enhanced. The proof that indeed such kind of magnetic disorder bears re-

[3] The MR measurements discussed in this work were performed with external fields up to $\mu_0 H = 10\,\mathrm{T}$.

[4] For cells which show ferromagnetism even at $T > T_C$, $x_{(i,j)} > x$ is fulfilled according to Eqn. 4.2.

[5] We focus here on the transport leading subbands which are shifted towards the acceptor level.

sponsible for the enhancement of the Fermi energy and for this reason responsible for the strong increase of ρ_0 is given in the inset of Fig. 4.3. In this inset the calculated Fermi energy of calculations using a local- and a global Curie temperature is shown. The Fermi energy is plotted versus $\frac{1}{T}$ simplifying the comparison with the Arrhenius plot of the resistivity given in the same figure. Whilst the Fermi energy of the sample calculated by use of a global Curie temperature drops immediately down for temperatures above T_{C}, the result of the calculation with a local Curie temperature shows a significantly slower decrease in the temperature regime slightly above T_{C}. According to this the activation energy of the paramagnetic cells will be enhanced at this temperature range. Their carrier density n gets reduced drastically and as a direct consequence of Eqn. 1.1 the resistivity of these cells increases. This indirect influence is not in contradiction to 2.) where only the direct influence of $T \geq T_{\mathrm{C}^{i,j}}$ on a cell (i, j) was considered. In other words, the scenario of a network system with local Curie temperatures leads to a strong localization of carriers in ferromagnetic cells while the paramagnetic cells act as insulators. The pronounced maximum of the resistivity at temperatures slightly above the average of the local Curie temperatures can easily be understood in terms of percolation theory: In this temperature regime almost 50 percent of all cells are insulators. This coincides exactly with the predicted percolation barrier for the given 2-dimensional geometry[6] of the network. In this context the influence of the disordered spatial incorporation of Mn ions gets strongly amplified around the critical temperature. To complete the illustration of this localization of carriers due to the ferromagnetic cells Fig. 4.5 is used. In this figure snap-shots of the carrier and current density distributions in the system with $T_{\mathrm{C}^{loc}} = 42\,\mathrm{K}$ are shown for five different temperatures. Without magnetic disorder (pure paramagnetic $T \gg T_{\mathrm{C}}$ (55 K) and pure ferromagnetic $T \ll T_{\mathrm{C}}$ (30 K)) almost all cells provide the same carrier density and straight-lined current paths. Fluctuations arise solely due to the fluctuating Mn concentration which is comparatively small for the underlying length-scale $l = 15\mathrm{nm}$. A contrary situation can be found for temperatures around T_{C}: The carrier density shows a large separation into two phases. One phase with very high carrier density (dark areas) and one with low density (red areas). As a simple consequence the current paths connecting dark areas of low resistivity show a strong non-linear behavior with many intersections. As mentioned above the amount of ferromagnetic cells (dark areas in Fig. 4.5) decreases with increasing temperature reaching 50 percent at $T = T_{\mathrm{C}}$. It should be noted that a quantitative comparison between different images based on the colors shown in the figure is not feasible. Due to the large carrier- density changes for the different temperatures the color scales change from image to image.

[6] In the limit of ideal infinitely small cells

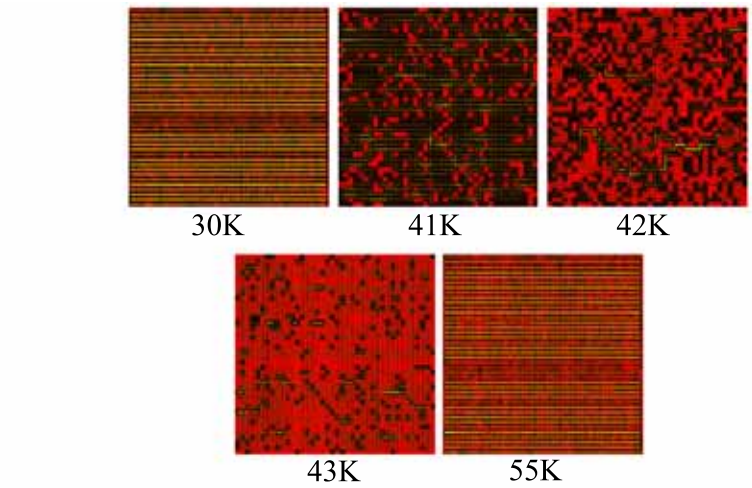

Fig. 4.5. Images show the calculated carrier densities and current paths for a network calculation with use of a local Curie temperature for different temperatures around $T_C = 42\,K$. The corresponding resistivity characteristics can be found in Fig. 4.3. The darker the color the higher the carrier density, yellow lines denote paths of high current density. Note that the colors cannot be compared among different images, since the underlying scales change. $l = 15\,nm$, the parameters are used as for the sample with 350 °C annealing temperature given in Tab. 3.1.

4.2 Non-random Mn incorporation

So far the incorporation of Mn ions in $Ga_{1-x}Mn_xAs$ alloys was assumed to be randomly i.e. without any correlation between the local Mn ion densities. This description ensures that basic physical properties such as disorder are taken into account without hiding some fundamental important effects behind the choice of statistics. Although a random Mn incorporation seems to be a reasonable approach to study an ideal paramagnetic DMS, it may be less adequate to model systems where due to the growth technique or post growth treatment such as e.g. annealing a non-random Mn incorporation is likely. In these systems the observed transport data reflects the interplay of material specific properties and mechanisms (e.g. the giant Zeeman splitting) and local properties (e.g. non-randomness of the Mn ions or a MnAs cluster incorporation). In the following we analyze whether the assumption of a spatially non-random Mn-ion incorporation in $Ga_{1-x}Mn_xAs$ alloys will cause significant changes of the calculated transport properties.

4.2.1 Model details and results

The total number of Mn ions n_{Mn} in the system is given by

$$n_{\mathrm{Mn}} = \chi \cdot x(l/l_U)^3 K^2 \tag{4.4}$$

where χ is the number of atoms per cubic unit-cell, K is the number of cubes in x- and y-direction and l_U is the lattice constant of the cubic unit cell of the zinc-blende lattice. Each of these Mn ions is individually allocated to one of the K^2 cubes in n_{Mn} separate distribution runs. In case of a spatially random Mn incorporation the probability $\rho^0_{\mathrm{Mn}} = 1/K^2$ of a cell to receive the Mn ion is equal for all cubes and during all runs. The tendency of Mn ions to cluster is modelled such that the probability of a cell to receive an additional Mn ion is the larger the more Mn ions are already in the cell. This is expressed by the parameter n_1 as

$$\rho_{\mathrm{Mn}} = \zeta \left(\rho^0_{\mathrm{Mn}} + n_1 \cdot n^*_{\mathrm{Mn}} \rho^0_{\mathrm{Mn}}\right) \tag{4.5}$$

where n^*_{Mn} is the number of Mn ions in the cube of the network at the time of the distribution run, ζ is a normalization factor. The introduced parameter n_1 describes the correlation of the non-random Mn ion incorporation i.e. $n_1 = 0$ corresponds to the non-correlated case, $n_1 > 0$ corresponds to the attractive Mn incorporation and $n_1 < 0$ to the repulsive case. Beside this capability of the cell to influence the probability to obtain a Mn ion on its own during the distribution process, (which is a direct influence weighted with n_1), the non-random incorporation of Mn ions due to the influence of neighbor cells (the indirect influence) can also be considered. To take this indirect influence into account a second parameter n_2 is introduced. The model is based on the assumption that each cell influences the probability ρ_{Mn} of each of the four neighbor cells (for the four-fold coordinated network) to obtain a Mn ion. To describe the probability for a cell to receive a Mn ion at a specific distribution run taking into account the indirect and the direct influence covered by n_1 and n_2 an extended version

$$\rho_{Mn} = \zeta \left(\rho^0_{Mn} + n_1 \cdot n^*_{Mn} \rho^0_{Mn} + \sum_{\substack{\text{neighbor} \\ \text{cells}(i)}} n_2 \cdot n^*_{Mn}(i) \rho^0_{Mn} \right). \tag{4.6}$$

of Eqn. 4.5 has to be used. To eliminate artifacts related to cubes at the border of the network which have less neighbors than inner cubes the distribution procedure is performed with a "shadow" network of $(K+2) \cdot (K+2)$ cubes. After all Mn ions are distributed a smaller inner structure of $K \cdot K$ network cubes is used in the actual calculation.

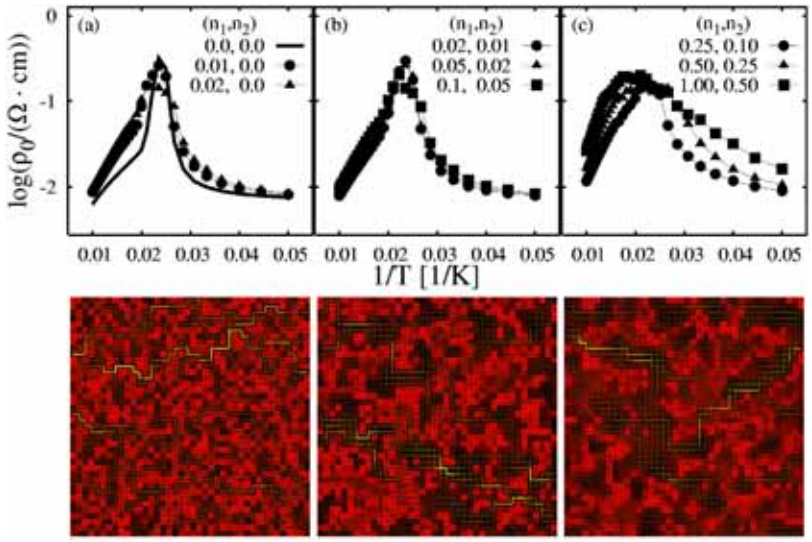

Fig. 4.6. The upper part shows the Arrhenius plots of the resistivity around the critical temperature for a series. The attraction factors n_1 and n_2 which are given in the legends. The used material parameters belong to the sample annealed at 350 °C as given in Table 3.1. The lower part shows the images of the corresponding networks. Each network image belongs to the calculation with the largest values of the attraction factors in the Arrhenius plot above. The lower the resistivity of a cell (the high carrier concentration) the darker is the color. Paths of high current density are indicated by yellow lines, the thicker the lines the higher the carrier density. [8]

Fig. 4.6 depicts the influence of n_1 and n_2 on the temperature-dependent resistivity around the critical temperature for parameters of the sample annealed at 350 °C as given in Table 3.1. The calculations were performed using a local Curie temperature with $\alpha = 2105.3\,\mathrm{K}$ corresponding to an averaged $T_\mathrm{C} = 40\,\mathrm{K}$. With increasing attraction factors the anomaly of the resistivity gets broadened until for the largest simulated values of $(n_1,n_2) = (1.0,0.5)$ the peak of the resistivity is smeared out even down to 20 K. This can be understood on the basis of the given model. In the case of a strong non-random distribution of Mn ions it exists even at 20 K a fraction of network cells which show paramagnetism and thus semiconducting transport properties.

[8] It should be noted that the color scales of each of the three images are different. The images just serve as an illustration and allow no further quantitative consideration.

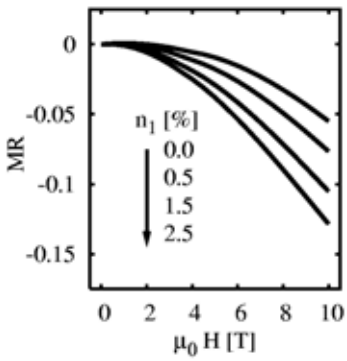

Fig. 4.7. Calculated MR versus external magnetic field at 40 K for different values of n_1 of a $Ga_{0.992}Mn_{0.008}As$ sample. Remaining parameters are given in Tab. 3.1 for the sample annealed at 600 °C.

As their resistivity is larger than that of the metallic (and ferromagnetic) network cells, the semiconducting regions almost define the resistivity if their amount or the distribution of them is such that the percolation path has to pass them. The increase of the resistivity with increasing temperature is the direct consequence of the growing amount of paramagnetic regions. The three color images illustrate the carrier-density distribution and the main current paths in the system for $n_1 = 0.02$ (left), $n_1 = 0.1$, $n_2 = 0.05$ (middle) and $n_1 = 1.0$, $n_2 = 0.5$ (right). A trend from a pure random distribution of the local carrier density reflecting the (almost) random Mn-ion distribution for $n_1 = 0.02$ towards a clustering of carriers in the calculation with the largest values of n_1 and n_2 is clearly visible. The calculations presented in Figs. 4.6 and 4.2 performed using a local Curie temperature and taking into account a non-random Mn-ion incorporation can be understood on the basis of the applied model. Nevertheless they are not able to reproduce the experimental data more accurately than the calculations performed without these two modifications. In particular the anomaly of the resistivity around the critical temperature which is measured to be much weaker than given by previous calculations (see Fig. 3.4) cannot be reproduced more satisfactorily by introducing $T_{C^{loc}}$. This suggests that for a more realistic description of the resistivity around the phase change more sophisticated models beyond the macroscopic description given here have to be applied, which e.g. take into account the scattering of carriers on the fluctuations of the magnetization [134, 135]. As the antipode of the ferromagnetic sample one can consider the sample annealed at 600 °C. Since the experimental data shows that the sample is paramagnetic even at low temperatures (down to at least 10 K) and that possible precipitates have no direct influence on the transport properties, the model should be well adopted for a proper description. It seems reasonable that the high annealing temperature goes along with a spatial non-random rearrangement of Mn ions. The question arises whether due to the assumption of a correlated distribution of magnetic ions a certain weakness of the choice of material parameters (shown in Tab. 3.1) namely the assumption of a comparatively large concentration of magnetically active Mn ions even at high annealing temperatures can be eliminated. Fig. 4.7 serves

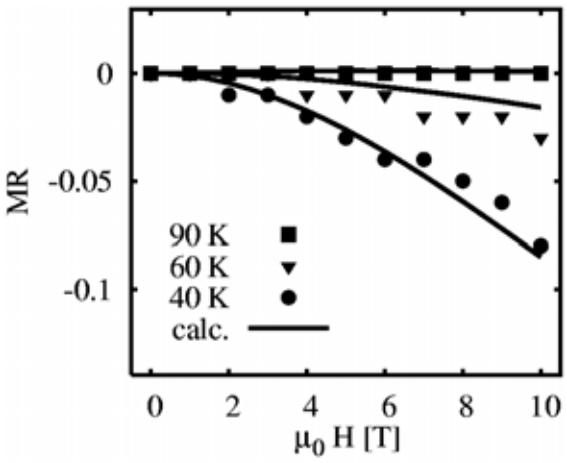

Fig. 4.8. Comparison of calculated and measured MR versus external magnetic field for different temperatures for a $Ga_{0.98}Mn_{0.02}As$ sample annealed at 600 °C. Symbols denote experimental results, solid lined the calculations. For the calculations $n_1 = 0.25$ and $x = 0.004$ were used. The remaining model parameters are given in Table 1.1

as a first hint that this question can be answered positively. In this figure the calculations of the MR at 40 K for different values of n_1 show that the negative MR increases with increasing strength of the attraction factor. The percolation path connects cells an enhanced amount of Mn ions and thus the resistivity shows a stronger dependence on the magnetic field as in the case of a pure random incorporation of Mn ions. In other words the non-random Mn distribution simply enhances the *effective* amount of Mn ions which are relevant for the magnetotransport properties of the sample.

Fig. 4.8 shows the comparison of calculated and measured MR of a $Ga_{0.98}Mn_{0.02}As$ sample annealed at 600°C where the annealing led to the formation of MnAs clusters such that their density is below the percolation threshold and the Mn content in the surrounding paramagnetic matrix is significantly reduced to about $x = 0.004$. The non-random Mn ion incorporation was accounted for by $n_1 = 0.25$. The experimental results can be described quantitatively in the entire temperature range considered which is hardly possible assuming a random Mn incorporation as shown in Fig. 3.11.

4.3 Conclusion

In this chapter the influence of a local Curie temperature and a non-random incorporation of Mn ions in (Ga,Mn)As alloys on the transport properties was analyzed. The deviations between the calculated and the experimentally obtained resistivity around the critical temperature cannot be eliminated by introducing a local Curie temperature. But as a supplement it can be concluded

that the model calculations of the series of annealed $Ga_{1-x}Mn_xAs$ samples do not only substantiate a reduction of the density of Mn ions acting as acceptors and the reduction of the density of magnetically active Mn ions but also suggest a spatially non-random rearrangement of Mn ions with increasing annealing temperature. This is the main result of this chapter. Herewith the gap of how the annealing process influences the transition from a single-phase $Ga_{1-x}Mn_xAs$ random alloy towards a two-phase hybrid structure is bridged plausibly.

5

Transport in hybrid structures

5.1 Introduction

Another subclass of the (Ga,Mn)As system is granular hybrid structures consisting of ferromagnetic MnAs clusters embedded in a paramagnetic $Ga_{1-x}Mn_xAs$ host matrix. Such hybrids allow one to combine semiconducting and magnetic properties [39, 40, 41, 44, 131, 133]. The high attractiveness results from the fact that the MnAs clusters exhibit ferromagnetism with a T_C above room temperature which is necessary for future commercial use in spintronic devices, while the host matrix can easily be integrated into existing III-V non-magnetic semiconducting systems. Unfortunately this very 'entanglement' of magnetic and electronic properties, which makes this material class predestinated for spintronic applications, leads to a markedly high complexity of the material properties. This high degree of complexity is reflected in the fact that even fundamental questions like those about the dominant transport mechanism, about the interaction between cluster and host matrix and about the band structure of the cluster are still under discussion or even entirely open. This may be the reason why from the theoretical point of view the system attracted only little attention, as a comprehensive microscopic description, even if possible, is a distant prospect. On the other hand, experimentalists considered the discussed hybrid structures often more as an undesired side effect when attempting to enhance the solubility limit of Mn in GaAs, rather than as an interesting system to be analyzed systematically. Recently the situation changed and clusters were even considered to be a *new paradigm of condensed matter physics* [137]. A couple of experimental studies appeared e.g. dealing with cluster formation [6, 9, 138] or during post-growth

[2] Transmission electron microscopy

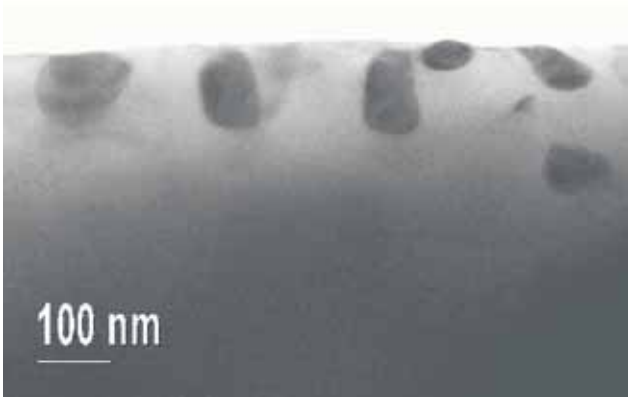

Fig. 5.1. TEM[2]image of a ferromagnetic MnAs cluster embedded in a paramagnetic GaAs:Mn matrix originated from MOVPE growth. [136]

annealing of MBE grown samples and optical [7] as well as transport properties [8] of hybrids. This arising interest may be correlated with the moderate success of researchers to increase the Curie temperature of the single-phase (Ga,Mn)As random alloy up to room temperature − an ambition that, despite promising theoretical studies [26], has turned out to be a highly complex and tedious quest [102, 121, 139, 140].
Based on the results of the studies of the paramagnetic single-phase (Ga,Mn)As, a minimal-model is developed to describe the transport properties of ferromagnetic-paramagnetic MnAs/GaAs:Mn hybrid structures over a broad range of temperatures and external magnetic fields. For the first systematic theoretical study of this material class, we used an adequately small set of assumptions and parameters whose influence on the macroscopic transport properties were analyzed. The specification of the analyzed parameter space and of the studied effects was performed on a purely phenomenological basis. It was attempted to identify qualitatively physical mechanisms that explain the remarkable differences between the transport properties of hybrids and the pure $Ga_{1-x}Mn_xAs$ host matrix [133]. These main differences are:

- A strongly enhanced resistance of hybrid samples at low temperatures
- A strong increase of the gradient of the resistivity in Arrhenius representation at low temperatures
- A large negative MR at low temperatures ($T < 50$ K)
- A pronounced positive MR effect up to several hundred percent in an intermediate temperature regime

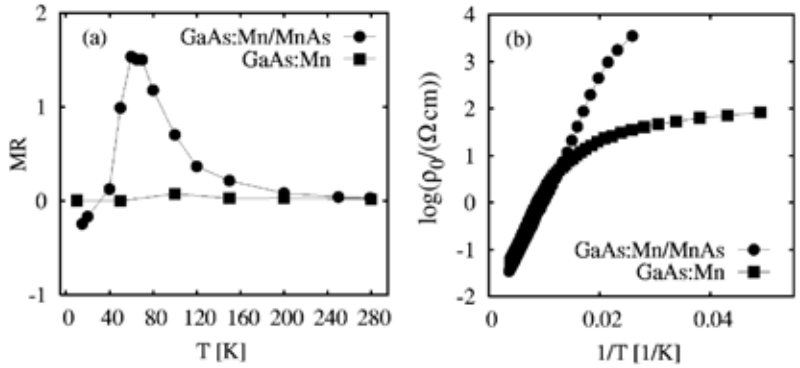

Fig. 5.2. (a) Measured temperature dependence of the MR at μ_0H= 10 T of a GaAs:Mn/MnAs hybrid sample and of a $Ga_{1-x}Mn_xAs$ sample in the paramagnetic phase. The strongly enhanced positive MR observed for the hybrid sample is clearly visible. (b) Arrhenius plot of the measured ρ_0 of a GaAs:Mn/MnAs hybrid sample and for a $Ga_{1-x}Mn_xAs$ sample in the paramagnetic phase. For details see [136] .

For the quantitative analysis of the dependence of the transport properties on the model parameters a multiplicity of numerical calculations was performed. Therefore an extended version of the network model, introduced in a previous chapter, was applied. The influences of effects that in principle can be considered to be able to lead to the measured temperature dependence of the conductivity and magnetotransport behavior are firstly studied individually in order to reduce the parameter space. A strong emphasis was placed on the analysis of the influence of local cluster configurations inside the matrix on the magnitude of the magnetotransport effects. In this context it is shown that by use of controlled positioning of clusters e.g. gate-like or sandwich structures the simulated positive MR effects can be enhanced considerably in comparison with a pure random or a centered incorporation.

5.1.1 Dependence on growth conditions

The formation of ferromagnetic MnAs clusters within the host matrix can occur under certain conditions by ion implantation of Mn into LT GaAs and subsequent annealing [39, 141], or in the MBE growth followed by annealing above the growth temperature [6, 9, 40, 142, 143]. Another possibility for hybrid structures to form is in the metalorganic vapor phase epitaxy (MOVPE) growth [96] where it takes place during the actual growth process. Under such growth conditions the clusters form in a region near the surface leading to a top layer of remarkably high cluster density and cluster size up to a di-

ameter of several hundred nm. Below this top layer the material is almost free of MnAs precipitates. Fig. 5.1 shows an image of such a cluster grown by MOVPE, the image was taken by transmission electron microscopy (TEM) at the Central Technology Laboratory of the Philipps University in Marburg [136].

5.2 General model properties

The basic ingredients of the model developed to describe the magneto transport properties in hybrid structures are:

- The cluster is assumed to be a half-metal [144, 145]. The spin degeneracy of its bands is lifted. The Fermi energy is energetically located inside the subband of one spin orientation. The carriers in this subband show metal-like conductivity. The minority subband has an energy spacing of E_{AC} between the Fermi energy and the subband edge and therefore shows activated transport behavior.
- To be able to describe the strong positive MR effects that are observed solely in hybrid structures and which do not occur in pure matrix samples (see Fig. 5.2) we assume that the pseudospins of the majority subbands of the matrix and the cluster are of opposite orientation. In simple terms: While the spin-down subband of the matrix has the lower resistivity (for $H > 0$) inside the cluster the spin-up subband has the lower resistivity (independent of the external field).
- When connecting the cluster cells with the surrounding matrix cells, a spin conservation is assumed (see Fig. 5.3): In the presence of an external magnetic field the spin degeneracy in the matrix materials valence bands is lifted, the carriers are not allowed to change their spin when entering the cluster. Therefore they have to pass the cluster via the minority band or have to avoid it and stay in the majority band of the matrix increasing the length of the current path.
- Due to different inherent Fermi energies of the cluster and the matrix (in respect to the vacuum level), the formation of a Schottky barrier at the cluster-matrix interface can be considered. Depending on the sign of this barrier it is either attractive or repulsive for the carriers in the matrix. The influence of the barrier on the matrix material is taken into account when solving the neutrality equation for the derivation of the Fermi energy.
- The clusters exhibit ferromagnetism. The influence of their spontaneous magnetization on the matrix is taken into account in the simplest possible way: We assume an additional magnetic field felt by the matrix cells in the vicinity of the cluster. This cluster field leads to a GZS induced splitting

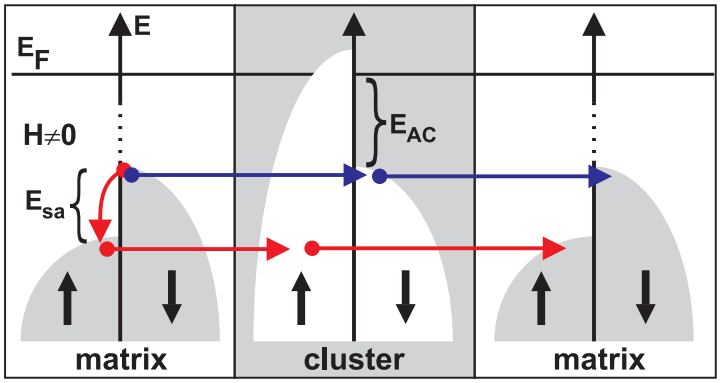

Fig. 5.3. The arrows denote the possible transport paths through a matrix-cluster-matrix sandwich-structure in the presence of an external magnetic field $H \neq 0$. The corresponding resistor network is imaged by Fig. 5.6.

of the valence-band subbands even in the absence of an external magnetic field.

- A direct influence of an external magnetic field on the band states of the cluster is not taken into account.

To explain the strong deviations in transport properties between pure matrix and hybrid samples (e.g. Fig. 5.2) the basic effects taken into account in the model (the formation of a Schottky barrier, the magnetic field of the cluster and its half-metallic character) are studied independently of each other at the beginning. This was necessary even though these effects influence each other. However without such a radical decoupling the dimension of the parameter sphere is simply too high to gain new insights by performing parameter studies. In the following the boundaries of the parameter space are identified, within which a description of the experimental data is possible. By comparison of numerical with experimental data, one is not only able to exclude certain effects, but also to obtain a reduction down to defined sets of parameters and effects. Nonetheless the phenomenological model does not allow one to identify particular points in the parameter sphere and to provide definite weighting of different physical effects, since the system exhibits a remarkably high degree of complexity.

5.2.1 The cluster itself

Seeing as the existing theoretical studies for the band structure of MnAs suggest it to be a half-metal (but differ at least quantitatively [144, 146, 147,

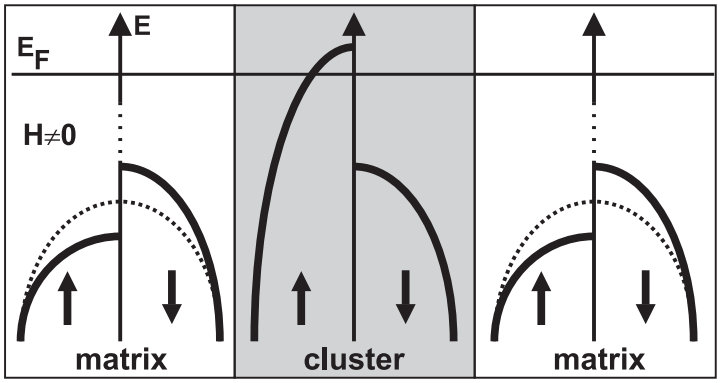

Fig. 5.4. Schematic illustration of the band structure of the cluster as it is used in the calculations in comparison with the majority bands of the matrix material in presence of an external magnetic field. The dashed lines denote the spin degenerate band structure in the matrix at $H = 0$.

148, 149]) the assumption of a convenient half-metallic band structure seems reasonable. Based on the presumed material properties of the cluster, the experimentally observed transport properties should be allegeable. At least no known experimental or theoretical statement suggests that the assumptions made about the cluster are wrong. In the calculations the cluster is considered to be a half-metal as schematically shown in Fig. 5.4. For the resistivity of the majority band a temperature independent value $\rho_{MaC} = 2 \cdot 10^{-4} \Omega\,\mathrm{cm}$ is used. This majority-band resistivity is below the resistivity of the matrix cells in the observed temperature range. The assumed resistivity ρ_{MiC} of the minority band is governed by activated transport given by[3]

$$\rho_{MiC} = \rho_C^0 exp\left(\frac{E_{AC}}{k_\mathrm{B}T}\right) \tag{5.1}$$

where ρ_C^0 plays the role of the pre-exponential factor as introduced in Eqn. 2.1. The energy E_{AC} required by carriers for thermal activation into the minority band of the cluster has to be chosen sufficiently large to assure that ρ_{MiC} is larger than the resistivity of the majority band of the matrix cells. If this condition is not fulfilled a positive MR related with different majority-subband spins as discussed in detail in section 5.2.2 cannot be achieved. Fig. 5.5 shows the influence of the calculated tem-

[3] As the band structure of the cluster is unknown, we use this simplified description instead of a self consistent determination of the Fermi energy and the carrier density as done for the matrix e.g. in Eqs. 1.1 and 1.2.

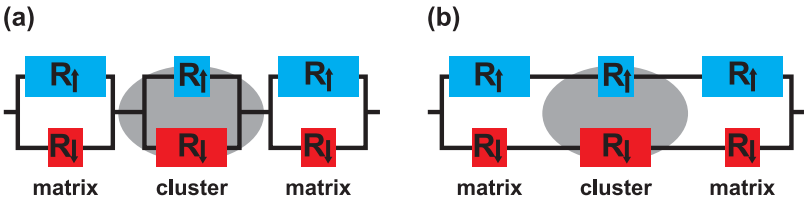

Fig. 5.6. Illustration of the different ways to connect the resistors representing the spin up and spin down subbands. (a) shows the connection where all channels are switched in parallel in each cell, all spin information gets lost. (b) illustrates a two-channel model, one single resistance for each spin direction is calculated and the resulting two channels are switched in parallel at the end. The spin information of a carrier does not get lost when passing from cell to cell, such a connection represents the conservation of the carrier spin.

perature dependence of the MR at $\mu_0 H_{ex} = 10\,\mathrm{T}$ for a hybrid sample. For a simple comparison with the transport properties of the surrounding matrix material the inset depicts the calculated Fermi level of the matrix cells. This represents the average activation-energy of the matrix. With increasing E_{AC} the positive MR effect gets more pronounced and persists up to higher temperatures. This trend is anticipated, since only if E_{AC} is large enough to ensure a resistivity larger than that of the surrounding matrix cells, thus the current avoid the cluster, resulting in a positive MR effect. Nevertheless just by increasing E_{AC} the maximum of the positive MR can be increased and shifted towards higher temperatures. Although this shift is limited due to the fact that at elevated temperatures the spin splitting of the valence-band states in the matrix breaks down. Thus the spin conservation covered by Eqn. 5.2, which will be discussed in detail in the following section plays no crucial role anymore and the current can pass througt the clusters majority band. Under

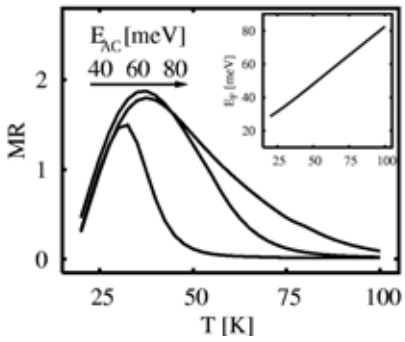

Fig. 5.5. Dependence of the calculated MR at $\mu_0 H = 10$ T versus T of a hybrid sample on values of E_{AC}. Inset shows the calculated temperature dependence of E_F of the matrix material. Calculation uses *spin conservation* as introduced in Sect. 5.2.2. Single centered cluster $x_C = 0.3$, parameters see sample No. 1 Tabs. 5.1,5.2.

this condition the activation energy E_{AC} determining the transport properties of the minority band of the cluster is of negligible influence on the transport properties of the system.

5.2.2 Consequence of opposite alignment of majority spins of cluster and matrix

The resistivity of the hybrid system is modelled by

$$\rho = (1-\eta)\cdot\rho_{sc} + \eta\cdot\rho_p \tag{5.2}$$

with the pre-factor $\eta = e^{-E_{sa}/k_{\mathrm{B}}T}$ representing the probability of thermal activation of a carrier from the top of the majority band with $j_z = -\frac{3}{2}$ into the minority valence-band subband with $j_z = \frac{1}{2}$. The resistivity ρ_p is the result of the (usual) network calculation, while ρ_{sc} is the resistivity assuming spin conservation. This description assures to study the influence of a cluster whose majority band providing metal-like conductivity has an opposite spin projection than the majority band of the surrounding semiconducting matrix (in the case that $H_{ex} \neq 0$). $E_{sa} = \frac{2}{3}xN_0\beta < S_Z >$ is given by the energy difference originating in the giant Zeeman splitting according to Eqn. 1.11[4]

$$\begin{aligned} E_{sa} &= E_v(-\frac{3}{2},H,T) - E_v(\frac{1}{2},H,T) \\ &= -\frac{1}{3}(-\frac{3}{2})xN_0\beta < S_z > -\left((-\frac{1}{3})\frac{1}{2}xN_0\beta < S_z >\right) \\ &= \frac{2}{3}xN_0\beta < S_z > . \end{aligned} \tag{5.3}$$

On the basis of the usual network calculation the resistivity of a cell ρ^m is given by Eqn. 1.21. To obtain ρ^m the resistivity ρ_{j_z} of each of the four subbands is connected in parallel

$$\rho^m = \frac{\rho^m_{-\frac{1}{2}}\rho^m_{\frac{3}{2}}\rho^m_{-\frac{3}{2}} + \rho^m_{\frac{1}{2}}\rho^m_{\frac{3}{2}}\rho^m_{-\frac{3}{2}} + \rho^m_{\frac{1}{2}}\rho^m_{-\frac{1}{2}}\rho^m_{-\frac{3}{2}} + \rho^m_{\frac{1}{2}}\rho^m_{-\frac{1}{2}}\rho^m_{\frac{3}{2}}}{\rho^m_{\frac{1}{2}}\rho^m_{-\frac{1}{2}}\rho^m_{\frac{3}{2}}\rho^m_{-\frac{3}{2}}}. \tag{5.4}$$

The information about the carrier spin is lost when Eqn. 5.4 is solved. The carrier spin only plays a role for the spin selective splitting of the valence-band subbands. As soon as the resistivity of each subband is calculated and the resistivity of each cell is derived no further distinction between carriers

[4] The global Mn concentration is used as an approximation. The additional magnetic field of the cluster is neglected, thus the activation energy E_{sa} is a constant average value for all cells.

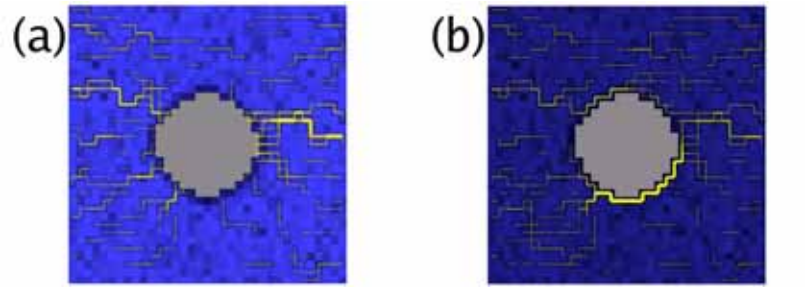

Fig. 5.7. Illustration of the current path through a hybrid sample including a centered cluster (grey area), $\mu_0 H_{ex} = 10\,\mathrm{T}$. Different intensities of bluetones denote different resistivity of the cells, yellow lines denote the current path, thickness of the lines indicates the current density. The calculation was performed (a) for a system in absence of spin conservation, (b) including spin conservation.

of different spin is made. This situation is illustrated by Fig. 5.6 (a) where a hybrid system of 1·3 cubes (matrix - cluster - matrix) is represented by a resistor network. In each cell the resistors of both spin directions representing the two spin channels (up and down) are connected in parallel. The resulting three resistors (one for each cell) are consequently connected in series. This connection allows a carrier to pass the majority bands of both the matrix and the cluster to achieve the lowest resistance independently from the spin orientation in the bands. In Fig. 5.7 the current path through a two dimensional hybrid structure (at $\mu_0 H_{ex} = 10\,\mathrm{T}$) including a centered cluster is shown. Since no spin conservation was assumed the current passes through both the majority band of the matrix cells as well as the highly conductive metal-like subband of the cluster. Under the assumption of (i) the spins of the majority bands of the matrix and the cluster are different and (ii) $\eta \approx 1$ or even smaller, a carrier keeps its spin during the transport process and an approach which does not take this into account is maladjusted. If (i) and (ii) are fulfilled a carrier in the majority band of the host matrix has to pass the cluster via its minority band or has to circumvent it. In the following this effect is referred to as the regime of *spin conservation*. A possibility to represent this in terms of the present model is to introduce an independent resistor network for each spin orientation[5].

[5] For simplification only one network for spin up (spin down) is introduced. In this network the resistors belonging to $j_z = \frac{3}{2}$ and $\frac{1}{2}$ ($j_z = -\frac{3}{2}$ and $-\frac{1}{2}$) are connected in parallel. Such an approximation is justified due to the same reason as the parallel connection of all four resistors in each cell in the absence of spin conservation.

Doing so ρ_{sc} is given as

$$\rho_{sc} = \frac{\rho_\uparrow \rho_\downarrow}{\rho_\uparrow + \rho_\downarrow}; \tag{5.5}$$

$\rho_\uparrow$ ($\rho_\downarrow$) is the result of a network calculation where the resistivity in each cell are given by the parallel connection of the two subbands with spin $\frac{3}{2}$ and $\frac{1}{2}$ ($-\frac{3}{2}$ and $-\frac{1}{2}$). In Fig. 5.6(b) such a connection of resistors is shown that provides spin conservation. The total resistance of the matrix-cluster-matrix chain is given by the parallel connection of a spin-down and a spin-up channel. Since a carrier is not allowed to change its spin when entering a new cell, a spin-down carrier in the majority band of the matrix has to pass through the minority band of the cluster and vice versa.
In the case of a real 2-d network assuming spin conservation, instead of passing the minority band of the cluster the carrier circumvents the cluster in the majority band of the matrix. Fig. 5.7(b) shows the calculated current path developing through a hybrid system avoiding the cluster as a consequence of the spin conservation regime.[6] This basically geometric origin of the positive MR effect leads to another important aspect: The influence of the arrangement of the clusters in the sample on the transport phenomena. The elongation of the current path leads to an enhancement of the MR while the choice of different spatial arrangements of clusters should lead to different current paths which avoid the clusters. These different paths should have a considerable influence on the MR properties. Fig. 5.8 serves as a first illustration of this influence of the cluster positions and cluster size. In this figure the calculated maximum value of the MR at $\mu_0 H_{ex} = 10\,\mathrm{T}$ is shown versus the concentration of cluster cells x_C for two different cluster distributions (a) and (b). While (a) represents a structure of five clusters arranged in a very specific way as shown in the inset[7], (b) corresponds to a single cluster centered inside the matrix material. The observed difference in the maximum value of the MR reflects the influence of the cluster position on the increase of the current-path length. This length scales the size of the positive MR. In the case of the centered cluster given in (b) even for very high concentrations up to 40% always areas of matrix cells remain where the current paths are not affected by the presence of the cluster. This is in contrast to distribution (a) where for high x_C the four clusters located at the fringe of the sample form a gate-like

[6] Whether passing the cluster on a short but highly resistive path or circulating around it with lower resistivity but increased path length provides the smallest resistance depends sensitively on the chosen parameters. Most relevant parameters are: ρ_{MaC}, ρ_{Mic},the valence-band subband-splittings $\Delta E_V(j_z, H, T)$ as well as the geometry, the size and distribution of the clusters.

[7] If not mentioned separately the current direction always is from left to right.

structure which all carriers have to pass. The fifth cluster is located right in the middle of this gate. Therefore almost all carriers in the system are affected by the clusters at some stage of their way through the sample.
In Fig. 5.8 this influence can be found clearly reflected. For high concentrations of cluster cells the maximum MR of the two samples strongly differs and sample (a) shows a much stronger increase with increasing x_C up to more than 600% for $x_C = 0.4$. Not to cover effects of different additional mechanisms which are discussed in the following sections, by the influence of statistics (cluster arrangements), further calculations are performed with a single cluster centered in the sample. An extensive analysis of the influence of the cluster position and the possibility of a tailoring of hybrid structures to provide MR effects on a preferably large scale is given in section 5.3.

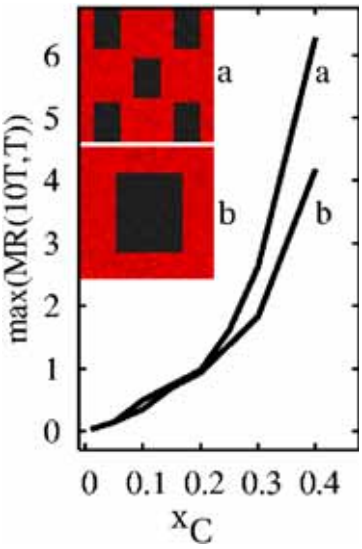

Fig. 5.8. Calculated MR at $\mu_0 H = 10\,\mathrm{T}$ versus x_C for two different cluster geometries as given in the inset. Calculation with spin conservation, without Schottky barrier and H_C. Parameters see sample No. 5,Tabs. 5.1, 5.2.

Besides its large influence on the magnetotransport properties, the discussed spin-conservation mechanism alone is not able to explain the strong enhancement of the resistivity of hybrid samples in comparison with their matrix counterparts at zero field and low temperatures. Fig. 5.9 (b) shows the calculated temperature dependence of the resistivity in absence of an external field. As expected the calculated resistivity depends neither on the size of the cluster nor on spin conservation. Similarly no significant difference between the low temperature resistivity of hybrid structures and the accompanying pure matrix material (depicted by a solid line) can be found. This result of the current model is in appreciable contrast to the experimental data shown in Fig. 5.2 (b).

If no external field is applied and no spin-dependent splitting of the valence bands is present, the resulting resistivity with and without spin conservation is still almost equal.[8] The influence of clusters with almost metal-like conductivity (as in this regime the current can pass through the majority band of the

[8] The splitting of the valence-band subbands induced by the magnetic field of the cluster is neglected so far in terms of its influence on spin conservation.

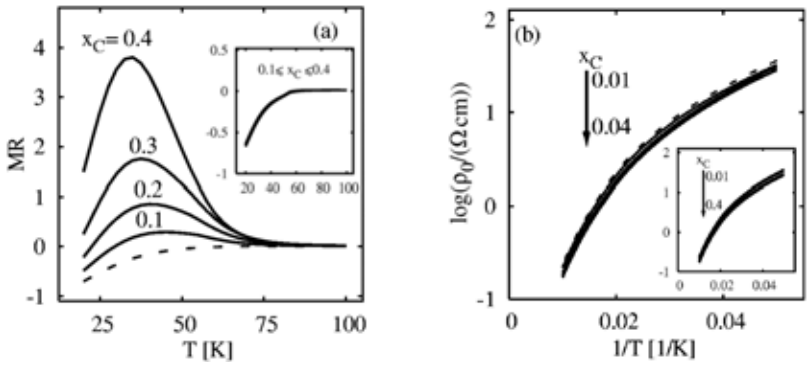

Fig. 5.9. (a) shows the calculated MR versus T at $\mu_0 H_{ex}$ =10 T assuming spin conservation for a series of hybrid samples with a centered cluster of various size as indicated. The dashed line denotes the pure matrix behavior. The inset shows the same calculation without spin conservation. (b) shows the calculated resistivity for the same series of samples with spin conservation, the inset shows the calculation performed without spin conservation. Parameters as sample No. 5, Tabs. 5.1, 5.2.

clusters) has only a weak influence on the conductivity of the whole sample as soon as their concentration is much below the percolation limit [60].

Without the special choice of the majority-band spin-directions of the cluster and the matrix, and in the absence of spin conservation, the experimentally obtained strong positive MR at $\mu_0 H = 10$T cannot be found in the calculations. Thus the cluster band-structures required as well as the two channel model, providing the spin conservation are assumed in further calculations.
To summarize, it was shown that the assumptions of (i) an opposite orientation of majority spins in cluster and matrix and (ii) spin conservation are essential for obtaining positive MR effects[9] as observed in experiments. However, they are not sufficient to explain the differences in the temperature-dependent resistivity observed with and without clusters. Therefore additional effects have to be added. The influence of Schottky-barrier formation and the magnetic field of the cluster are both studied separately in the sections 5.2.3 and 5.2.4. They are assumed in addition to the assumptions about the band structure of the cluster and the spin conservation.

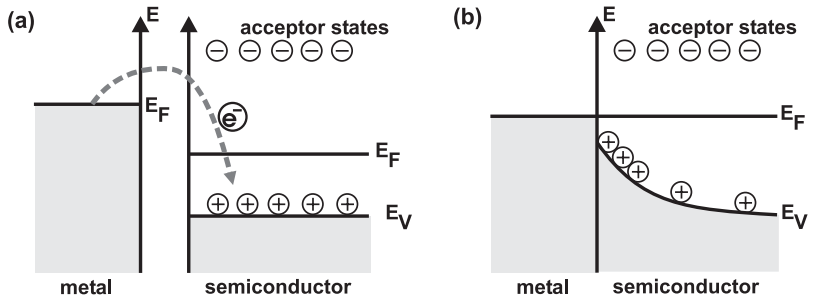

Fig. 5.10. Schematic illustration of the band alignment at the cluster to matrix interface (a) before both were brought into contact and (b) after having realized a perfect contact (e.g. in absence of surface/interface states) [150]. The transfer from electrons out of the metal (dashed line in (a) leads to the formation of a Schottky barrier of ohmic type ($E_{\mathrm{S}} > 0$) that causes a trapping of carriers in the vicinity of the cluster as assumed in most calculations.

5.2.3 The Schottky barrier

The possible formation of a Schottky barrier at the interface between the cluster and the semiconducting matrix can be taken into account in the model as well. This is basically done by adding an additional and magnetic-field independent energy shift E_{S} to the valence-band energy of all matrix cells in the neighborhood of cluster. Since the decrease of the Schottky barrier with increasing distance from the cluster is not known to us an arbitrary decay as $1/(\Delta_C(m))^5$ is assumed[10]. $\Delta_C(m)$ denotes the distance of a cell with index m from the nearest cluster cell measured in units of network cubes (as no decay of the valence-band energy is resolvable at smaller length-scales). Taking this into account the valence-band subband-edge $\check{E}_V^m(j_z, T, H)$ of a matrix cell in a hybrid structure is described by

$$\check{E}_V^m(j_z, T, H) = E_V^m(j_z, T, H) + E_D^m + E_{\mathrm{S}} \cdot \frac{1}{(\Delta_C(m))^5}. \tag{5.6}$$

With $E_{\mathrm{S}} > 0$ the Schottky barrier leads to a trapping of carriers in the vicinity of the cluster as schematically shown in Fig. 5.10 and forms a semiconductor-metal contact of ohmic type. If $E_{\mathrm{S}} < 0$ a rectifying contact is formed which leads to a repulsion of carriers away from the cluster. In this context it should be noted that the formation of a perfect contact between the cluster and

[9] One anticipates that on the basis of the model given in 5.2 no other effect can cause this pronounced positive MR.

[10] The exponent is a rather noncritical value which scales the *effective cluster density*. A decay $\propto 1/(\Delta_C(m))^4$ or $1/(\Delta_C(m))^6$ leads to qualitatively similar results.

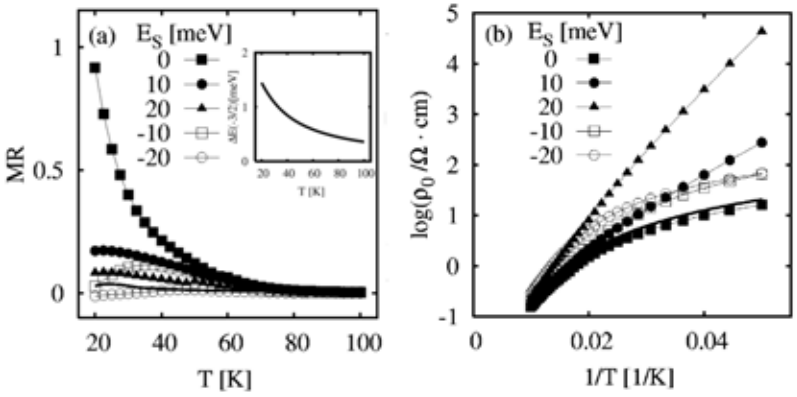

Fig. 5.11. In (a) the calculated MR at $\mu_0 H = 10\,\mathrm{T}$ for a hybrid sample with $x = 0.1\,\%$ depending on T for samples with different Schottky-barrier depths as indicated in the key are shown. The solid line denotes the MR of the pure matrix material. The inset shows the average energy shift of the majority band with $j_z = \frac{3}{2}$ at $\mu_0 H = 10\,\mathrm{T}$ versus T. (b) shows the corresponding resistivity ρ_0 at zero field versus T. The solid line denotes the resistivity of the pure matrix. For parameters see sample No. 3, Tabs. 5.1, 5.2, single centered cluster.

the matrix material is assumed, i.e. interfacial defects are neglected. Fig. 5.11 shows the results of the calculated temperature dependence of the MR at $\mu_0 H = 10\,\mathrm{T}$ and the temperature dependent resistivity at zero field for a hybrid structure assuming a variety of different Schottky-barrier depths of both ohmic and rectifying type. In the absence of a Schottky barrier the result basically reflects the exponential decay of the spin conservation regime as given by Eqn. 5.2[11]. The situation becomes more complex with increasing values of $\mid E_\mathrm{S} \mid$. First we study only the interplay of the spin conservation and the Schottky barrier (i.e. without the interplay between the (ohmic) Schottky barrier induced trapping of carriers and the matrix induced delocalization due to the giant Zeeman splitting). Thus the Mn concentration in the calculations was chosen sufficiently small and the influence of the matrix is negligible for the interpretation of the calculation. This results in an almost vanishing MR of the pure matrix as well as the average split of the most shifted subband (depicted in the inset of Fig. 5.11(a)) which is very small compared with the value of the Schottky-barrier depth.

For increasing positive values of E_S the positive MR at low temperatures breaks down. The ohmic Schottky barrier leads to a trapping of carriers in the vicinity of the cluster. In other words, it leads to a formation of a belt

[11] Since the elongation of the current path breaks down exponentially.

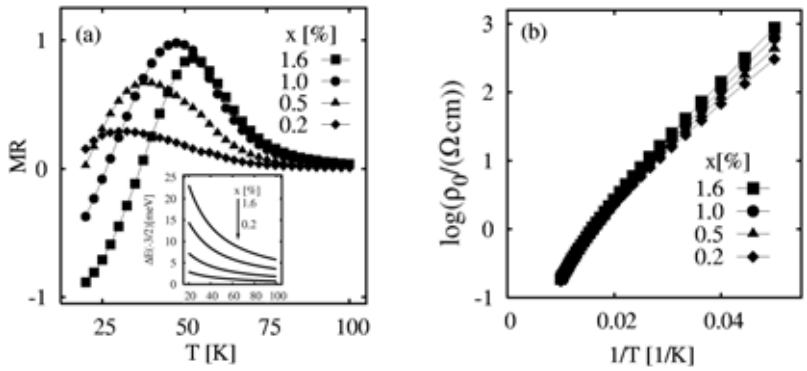

Fig. 5.12. In (a) the calculated MR at $\mu_0 H = 10\,\mathrm{T}$ for a series of hybrid samples with different x and E_S=10meV is shown. The inset depicts the corresponding average split of the matrix majority-band at $\mu_0 H = 10\,\mathrm{T}$. (b) shows the resistivity at zero field versus T for the same series. For parameters see sample No. 4, Tabs. 5.1, 5.2, single centered cluster.

around the cluster consisting of cells with high conductivity. This conductivity increases with increasing positive value of E_S. The influence of the spin conservation on the MR, that forces the current path to avoid the cluster, gets damped with increasing E_S since the conductivity of the cells on the (elongated) current path around the cluster is strongly enhanced. In the opposite case increasing values of a rectifying Schottky barrier reduce the influence of spin conservation. Even in the absence of a magnetic field the current does not pass through the cluster as the almost carrier-free neighboring cells show an enhanced resistivity. From this background it is quite obvious that the spin conservation in conjunction with a rectifying Schottky barrier does not lead to an increase of the MR as the main current paths are only affected weakly. The dependence of the resistivity at zero field shown in Fig. 5.2(b) helps to clarify the sign of a possible Schottky barrier. A strong enhancement of the low-temperature resistivity (as required in order to reproduce the experimental data shown in Fig. 5.2) can be found only in the calculations performed using an ohmic type of contact. As mentioned, the carriers are trapped at low temperatures in the vicinity of the cluster due to the Schottky barrier. Compared with the absence of the barrier or a rectifying contact, the resistivity increases drastically since the carrier concentration in the remaining matrix cells, through which the current has to pass, drops down. With increasing temperature the carriers become delocalized from the cluster surface and contribute to the transport.

After the sign of a possible Schottky-barrier formation has been determined

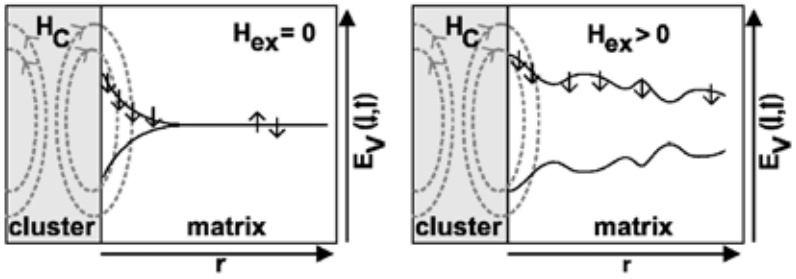

Fig. 5.13. Image of the splitting of the matrix valence-band in the vicinity of the cluster due to its magnetic field H_C.

by a comparison of experimental and model data, the additional interaction with the giant Zeeman splitting of the matrix cells is switched on. This can be done easily in the model by an increase of the Mn ion concentration. Fig. 5.12 shows the calculated MR at $\mu_0 H = 10\,\mathrm{T}$ versus temperature for a hybrid sample with $E_\mathrm{S} = 10\,\mathrm{meV}$ for different Mn concentrations ranging from $x = 0.002$ to 0.016. The visible strong negative MR at low temperatures, which is more pronounced with increasing Mn concentration, results from the large splittings of the matrix valence-band states. Depending on x the size of this giant Zeeman effect-induced splittings is at low temperatures even larger than the value of the Schottky barrier. To illustrate this the inset of Fig. 5.12 (a) shows the energy shift of the valence-band subband shifted most towards the acceptor state. If an external magnetic field is applied the carriers are no longer localized at the belt surrounding the cluster (due to the influence of the Schottky barrier) but are distributed almost over the entire system into cells showing a low activation energy. This negative MR scales with the concentration of magnetically active Mn ions and persists up to higher temperatures. In contrast to the magnetoresistance the resistivity at zero field shown in Fig. 5.12 (b) is affected only weakly by the variation of x. On the basis of the model this is obvious since the strong MR effects were related to the giant Zeeman splitting which vanishes at zero field. The slight increase of the resistivity at low temperatures with increasing x visible in the results is a pure matrix effect due to the magnetic field independent disorder given in Eqn. 1.16, and therefore independent of the hybrid character of the sample.

5.2.4 The cluster field

The ferromagnetism of the cluster is assumed to be a dipolar field. It is treated as an additional magnetic field of strength H_C which acts on the cells near the cluster surface. It decays with increasing distance of the cell from the interface

with $1/\Delta_C(m)^3$ where $\Delta_C(m)$ is defined as in 5.2.3. The magnetic field acting on a matrix cell in a hybrid structure is given by

$$H = H_{ex} + \frac{1}{\Delta_C(m)^3} \cdot H_C \tag{5.7}$$

where H_{ex} denotes the external magnetic field while H represents the total field acting on a matrix cell. Due to the additional contribution of H_C a splitting of the valence-band subbands in the vicinity of the cluster cells can occur even at $H_{ex} = 0$ as the cluster field alone leads to a giant Zeeman splitting. This is illustrated in Fig. 5.13. The splitting of the valence band subbands induced by H_C is given by $\Delta E_V(j_z, H_C, T) = -\frac{1}{3} x_{loc} N_0 \beta < S_z > j_z$ in the vicinity of the cluster, with $< S_z >$ is given by Eqn. 1.9. This splitting and the resulting localization of carriers in the vicinity of the cluster at small H_{ex} and T does not only depend on the value of H_C but also on x.

This significant dependence on both parameters is shown in Fig. 5.14, where the calculated logarithmic resistivity at $H_{ex} = 0\,\mathrm{T}$ for a hybrid sample including a centered cluster of 30 percent of the total sample volume is plotted against the inverse temperature. In (a) $\mu_0 H_C = 6\,\mathrm{T}$ and a series of different Mn concentration in the matrix ranging from 0.2 up to 1.0 percent were assumed. While at higher temperatures ($T > 40\,\mathrm{K}$) the calculated results do not depend on x, (as the giant Zeeman splitting breaks down) for small temperatures a strong dependence on the Mn content is visible. With increasing x the resistivity increases and for the largest value $x = 0.01$ the Arrhenius plot is even bent upwards. This is caused by the aforementioned phenomenon, whereby carriers get localized near the cluster surface which leads to an enhancement of the resistivity in the remaining matrix cells. With increasing temperature the localization of carriers breaks down, leading to an even stronger than exponential increase of the conductivity as illustrated in Fig. 5.14(a). The inset of this figure depicts the dependence of the resistivity of the pure matrix material on the change of x. Since the calculation was performed with $m_\mathrm{D} = 1.5\,\mathrm{eV}$ the potential landscape at zero field also depends on x. With increasing average fluctuation amplitude (Eqn. 1.16) the activation energy of the cells which contribute to the percolation path is reduced and the resistivity is decreased with increasing x. With increasing temperature this weak reduction of the activation energy due to alloy disorder becomes irrelevant and the curves coincide. Fig. 5.14(b) shows almost the same calculation as in Fig. 5.14(a) but the Mn content in the matrix is a fixed value ($x = 0.006$) and the curves indicated by symbols belong to different strength of H_C ranging from 2 T up to 15 T. The solid line denotes the pure matrix behavior. It is remarkable that for weak H_C the field does not lead to any trapping of the carriers. Since no external field H_{ex} is applied and thus no

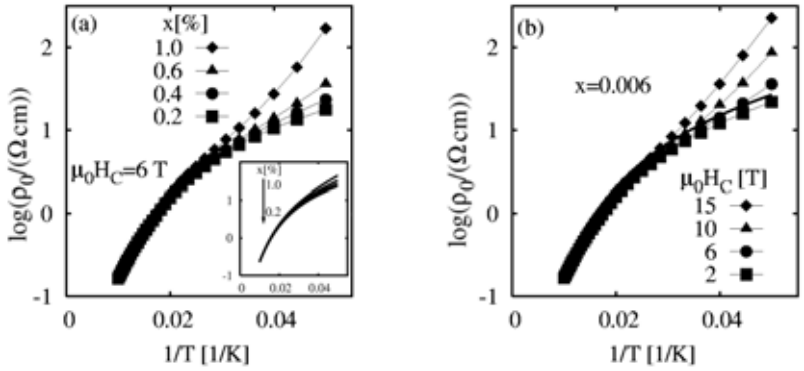

Fig. 5.14. Calculated dependence of the zero field resistivity ρ_0 on the strength of the clusterfield H_C for a sample with a centered cluster with a size of 30% of the total sample. (a) shows ρ_0 for $\mu_0 H_C = 6\,\mathrm{T}$ for matrix materials with different Mn concentrations in Arrhenius depiction. The insert shows the Arrhenius plot of ρ_0 for the pure matrix material for corresponding x. (b) shows the resistivity for different magnetic fields H_C of the cluster for a sample with $x = 0.006$. The solid line denotes the MR of the pure matrix material. For remaining parameters see sample No. 2 in Tabs. 5.1, 5.2.

spin conservation is considered the total resistance of the hybrid sample is even slightly below that of the matrix sample. If H_C increases up to 10 T a small up bend of the Arrhenius plot is visible at temperatures around 20 K. At $H_C = 15\,\mathrm{T}$ this upwards bend is well pronounced. Similarly to the results shown in Fig. 5.14(a) this is caused by the strong localization of carriers at the interface which leads to a carrier depletion in the surrounding matrix.

The concentration of magnetically active Mn ions which was needed to calculate the observed characteristics is found to be large (e.g. between 0.6 and 1.0 %) compared to experiment. But one should keep in mind that such large values of x are particularly required in the vicinity of the cluster. In the calculations the same average concentration was assumed within the whole sample. At least for the hybrid samples obtained by thermal annealing of MBE grown $Ga_{1-x}Mn_xAs$, where precipitates are assumed to form in regions of high Mn concentration, the existence of a slightly enhanced Mn concentration in the vicinity of these precipitates seems not unreasonable. On the contrary, a non-random incorporation of Mn ions is even suggested by the results of chapter 4.

Fig. 5.15 shows the dependence of the magnetoresistance for an external field $\mu_0 H_{ex} = 10\,\mathrm{T}$ versus temperature. In (a) the calculated MR using a fixed clusterfield $\mu_0 H_C = 6\,\mathrm{T}$ are shown for a series with different x. For the lowest

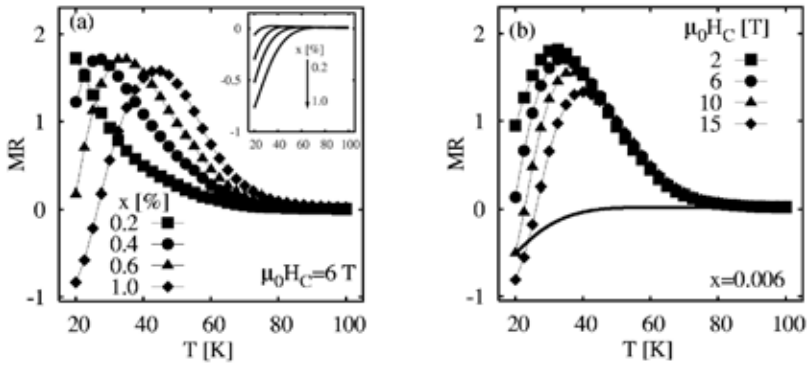

Fig. 5.15. Calculated dependence of the MR on the strength of the clusterfield H_C for a sample with a centered cluster with a size of 30 percent of the total sample. (a) shows the MR at 10 T for $\mu_0 H_C = 6$T for matrix materials with different Mn concentrations. The insert shows the MR for the pure matrix material for corresponding x. (b) shows the MR for different magnetic fields H_C of the cluster for a sample with $x = 0.006$. The solid line denotes the MR of the pure matrix material. For remaining parameters see sample No. 2 in Tabs. 5.1, 5.2.

Mn concentration $x = 0.002$ the sample shows no dependence on the external field, which can be connected with the properties of the matrix material. The calculated positive MR effect that decreases with increasing T is solely determined by the effect of spin conservation. A trapping of carriers at the cluster surface or magnetic field induced splittings of the matrix bands play no role. With increasing x the situation changes. The MR starts at low T at small, even negative values for the largest amount of x, increases up to a maximum and vanishes with further increase of the temperature. For moderate values of x and H_C the MR of the hybrid sample does not significantly deviate from that of the matrix material at small temperatures. With increase of x and H_C the delocalization of carriers becomes visible again as the MR of the hybrid sample reaches larger negative values than that of the matrix as shown in Fig. 5.16. This delocalization can be understood on the basis of the model presented so far: At $\mu_0 H_{ex} = 0$ T the hybrid sample shows a valence-band landscape which is almost flat (We neglect the influence of magnetic field independent disorder as it is not a crucial feature for the discussed mechanism.). Only at the cells close to the cluster a strong giant Zeeman effect induced splitting of the valence bands occurs. We now concentrate only on its effect on the subband which is shifted mostly towards the acceptor level since this subband determines the transport properties. Due to the shift of the valence-band edge the states in this subband get filled with holes and to fulfil the neutrality

condition (Eqn. 1.17) the Fermi energy is shifted towards the acceptor. The resulting effect is an increase of the carrier density in the vicinity of the MnAs cluster and a depletion of carriers in the remaining matrix cells. If an additional external magnetic field H_{ex} is applied, the valence bands in all other matrix cells also split. This split increases more strongly than the splitting of valence-band states in the vicinity of the cluster, since the Brillouin function $B_f(\frac{H_{ex}+H_C}{T})$ almost reached its saturation while $B_f(\frac{H_{ex}}{T})$ increases linearly. This increasing split of band states in cells which are not in the vicinity of the cluster reduces their activation energy and thus results in a higher carrier density. It should be noted that a shift of the valence-band states indeed reduces the activation energy of an average matrix cell as the Fermi level does not shift away by the same amount. Indeed the Fermi level does not shift substantially. The Fermi function is strongly non-linear, when solving Eqn. 1.17 the position of E_F is predominantly determined by cells with the smallest activation energy. In the discussed case these are the cells in the cluster vicinity whose splitting is not essentially affected by an additional external field. Taking this into account the reduction of the resistivity due to an external magnetic field can be understood.

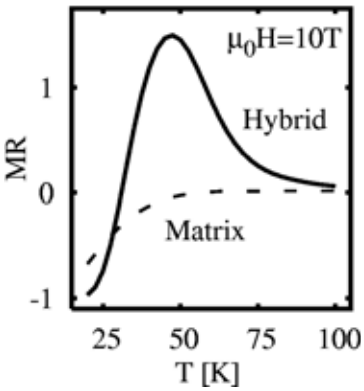

Fig. 5.16. Comparison between the MR at $\mu_0 H = 10\,\mathrm{T}$ of a matrix (dashed line) and a hybrid sample (full line), using $x = 0.08$ and $\mu_0 H_C = 15\,\mathrm{T}$, a magnetic field delocalization of carriers is clearly visible at low T (Parameters as used in Fig. 5.14).

Table 5.1. Model parameters − I matrix parameters

SAMPLE	σ $[meV]$	θ $[meV]$	m_D $[eV]$	n_a $[\frac{1}{cm^3}]$	x_{Mn}	$N_0\beta$ $[eV]$
1	45	0	-1.5	$1.14{\cdot}10^{-18}$	0.008	1.85
2	45	0	-1.5	$1.14{\cdot}10^{-18}$	varied	1.85
3	45	0	-1.5	$1.14{\cdot}10^{-18}$	0.001	1.85
4	45	0	-1.5	$1.14{\cdot}10^{-18}$	varied	1.85
5	45	0	-1.5	$1.14{\cdot}10^{-18}$	0.008	1.85
6	45	0	-1.5	$1.14{\cdot}10^{-18}$	0.008	1.85
7	45	0	-1.5	$1.14{\cdot}10^{-18}$	0.008	1.85
8	45	0	-1.5	$1.14{\cdot}10^{-18}$	0.008	1.85

Table 5.2. Model parameters − II cluster parameters

SAMPLE	x_{Cl}	E_S $[meV]$	E_{AC} $[meV]$	$\mu_0 H_C$ [T]	ρ_{Mac} $[\Omega\ cm]$
1	0.3	0.0	varied	0.0	$2{\cdot}10^{-4}$
2	0.3	0.0	60	varied	$2{\cdot}10^{-4}$
3	0.3	varied	60	0.0	$2{\cdot}10^{-4}$
4	0.3	10.0	60	0.0	$2{\cdot}10^{-4}$
5	varied	0.0	60	0.0	$2{\cdot}10^{-4}$
6	varied	10.0	60	6.0	$2{\cdot}10^{-4}$
7	0.0225	10.0	60	6.0	varied
8	varied	10.0	60	6.0	1.0

5.3 Strong enhancement of MR effects using tailored hybrid nanostructures – a prediction

Theoretical studies (that e.g. show the optimal conditions for strong ferromagnetic coupling in DMS [105, 151, 152, 153], the minimization of clustering tendencies [154] or for the composition of stable ferromagnetic half-metals [155]) are well established tools of condensed matter physics and in particular for spintronic research. Besides this pure theoretical tailoring of microscopic properties to gain insight into the optimized material capacities and to show its principle feasibility, even the effective experimental designing of artificial structures down to nanometer scales has become possible. Such nanostructured materials can show new or enhanced properties compared with their bulk counterparts [156]. The intensive and diversified study of nanostructures was basically enabled by the development of novel lithography techniques [157]. In this context specially magnetic nanostructures have gained attention as they can be considered as basic modules of prospective spintronic devices.

Besides concepts based on the effects related with the intrinsic magnetic properties of magnetic materials and single structures (e.g. high T_C ferromagnetic semiconductors) nanostructures built out of hybrids may offer a promising alternative. In this framework the large magnetoresistance effects of tailored non-magnetic semiconductor-metal hybrid structures the so-called extraordinary magnetoresistance effect (EMR) was in a focus of recent studies [158, 159, 160, 161, 162].

As mentioned previously, another subclass of nanostructures are hybrids formed by ferromagnetic inclusions in a paramagnetic host matrix. In this regard we present here a concept for MnAs/GaAs:Mn ferromagnetic-paramagnetic hybrid-based nanostructures to strongly enhance magnetoresistance effects due to a tailoring of the spatial arrangement of the clusters. On the basis of the model given in section 5.2 the predicted pronounced MR up to several hundred percent can be achieved due to the tailoring of nanostructures simply by a controlled positioning of ferromagnetic MnAs clusters in a paramagnetic GaAs:Mn host matrix.

5.3.1 Remarks on the influence of statistics

The main influence of the effects of a Schottky-barrier formation, of the magnetic field of the cluster and of spin conservation considered in the model for ferromagnetic-paramagnetic hybrid structures have been analyzed in the previous section for a system including a single cluster centered within its host matrix. Here we expand the area of interest to the influence of the spatial

distribution of the ferromagnetic inclusions inside the host matrix. In particular the strong positive MR effect related with spin conservation is based on a local change of the main current path. Thus it is expected that different distributions of clusters (even for the same total amount of cluster cells) will lead to different current paths and to visible differences in the MR data.
Fig. 5.17 displays the calculated MR for different distributions of clusters with a total concentration of cluster cells $x_C = 0.1$, 0.2 and 0.3. For each x_C the figure shows ten different calculated MR for each of the three different sets containing: (1.) three randomly distributed clusters, (2.) five randomly distributed clusters and (3.) forty randomly distributed clusters. It is clearly visible that the MR depends strongly on the position of the cluster cells since the calculated results vary for a fixed value of x_C over a range of (up to) several hundred percent. To illustrate the spatial distribution of clusters related with the results the inset of each graph shows the arrangement of cluster cells which belongs to the largest calculated positive MR (upper inset) and which belongs to the smallest calculated positive MR (lower inset). By studying the insets of the calculations performed with three and five clusters it becomes obvious that a distribution of clusters along the main current direction[12] leads to a strong enhancement of the positive MR effects. A distribution extending perpendicular to the current direction seems to result in a comparatively small positive magnetoresistance. This clarifies that two related but nevertheless different scenarios lead to a strong enhancement of the MR in the spin-conservation regime:

- The increase of the current-path length since the current has to circumfluent the cluster.
- The disappearance of 'quasi' short-circuits since the cluster majority-band does not lead transport anymore.

The first mechanism was described in detail in section 5.2.2. In short, the positive MR results out of the fact that in the presence of a spin dependent splitting of the valence bands of the matrix the carriers cannot flip their spin to pass the cluster in its majority band. The carriers have to circumvent the cluster and the current path gets elongated. In Fig. 5.7 such an elongation of the current path is illustrated. This effect contributes to the positive MR in the regime of spin conservation as long as the cluster's minority band provides a conductivity which is sufficiently smaller than that of the majority band of the matrix. More simplified: As long as the condition[13] (i) $\Delta E_M < E_{AC}$ holds, the elongation of the current path contributes to an enhancement of the resistivity in the regime of spin conservation. ΔE_M represents the activation

[12] In all calculations we use a horizontal current direction from left to right.
[13] For simplicity the influence of different mobilities is not taken into account here.

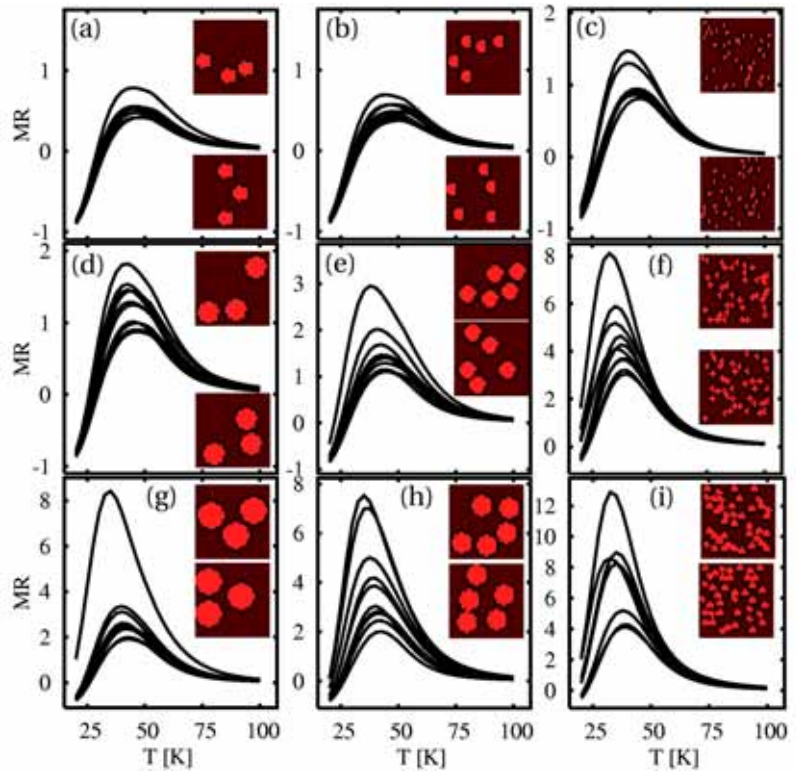

Fig. 5.17. Calculated MR at $\mu_0 H_{ex} = 10\,\mathrm{T}$ versus T for a series of hybrid samples with $x_C = 0.1$ (first row), 0.2 (second row) and 0.3 (third row). The number of clusters increases from 3 (first column) to 5 (second column) up to 40 (third column), the clusters can contact but not overlap each other. Each single graph depicts the results of ten different statistical distributions of clusters and illustrates the influence of the cluster distribution. The insets show the cluster positions of the sample with the largest (upper inset) and the smallest (lower inset) positive MR effect. For remaining parameters see sample No. 6 in Tabs. 5.1, 5.2.

energy of the matrix majority-band.
In addition to (i) the second scenario requires two more conditions to become valid: (ii) The conductivity of the majority band of the cluster has to be much larger than that of the matrix and (iii) it should exist a percolation path through the hybrid system which is remarkably covered by cluster cells. If (ii) is fulfilled[14] the cluster acts as a short-circuit with negligible

[14] This is fulfilled in all calculations so far since $\rho_{Mac} = 2\,10^{-4}\,\Omega\,\mathrm{cm}$.

resistivity (compared to the matrix). With increasing external field and considering the spin-conservation regime, based on (i) the current has to avoid the clusters and the resistivity jumps from (almost) zero (due to iii) to the value corresponding to the matrix majority-band. Under such a condition an elongation of the current path occurs as well. Even if such an increase of the path length was to be neglected, a sufficient increase of the resistivity would occurr. Fig. 5.18 depicts the temperature dependent resistivity at zero field for the two hybrid samples with the largest and smallest positive MR effects of all distributions calculated in Fig. 5.17(g) (The cluster positions of these two distributions are shown in the inset of Fig. 5.17(g).). One distribution is labelled with *across*. This indicates the cluster distribution where the clusters are not aligned with the main current direction. This distribution shows the smallest positive MR effect. In the second sample labelled with *along* are the three clusters almost aligned with the main current direction. This distribution shows the largest positive MR effect. The Arrhenius plot is restricted to elevated temperatures between 40 K and 100 K. In this temperature range the localization of carriers due to the Schottky barrier and the magnetic field of the cluster has been overcome predominantly. At high T even in the case of the *across* distribution the resistivity of the sample gets remarkably reduced due to the cluster incorporation compared with the pure matrix material (shown as a solid line). In the case of the *along* distribution with the clusters roughly oriented along the main current path, the resistivity at high temperatures is even more reduced. A more detailed study of the influence of the effect of metallic quasi short-circuits on the MR is covered by the results given in Fig. 5.19. In Figs. 5.19(a) and (b) the calculated MR and ρ_0 are shown. We assumed different cluster majority-band conductivities for a hybrid structure where a cluster is oriented along the main current direction (as depicted in the inset of (b)). Figs. 5.19(c) and (d) show the results obtained for a sample with a cluster of same size oriented perpendicular to the main current direction (depicted in the inset of (d)). In the first case the cluster serves almost as a short circuit for weak

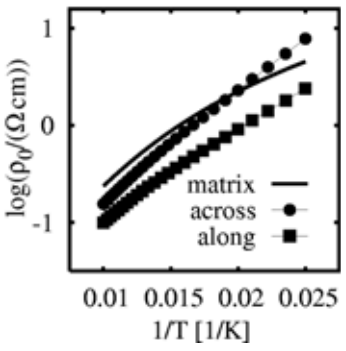

Fig. 5.18. Arrhenius plot of ρ for the hybrid samples given in Fig. 5.17 (g). *along* denotes the sample providing the largest-*across* denotes the sample providing the smallest positive MR. Due to the metallic short circuits the resistivity of both samples is significantly weaker than that of the matrix (solid line).

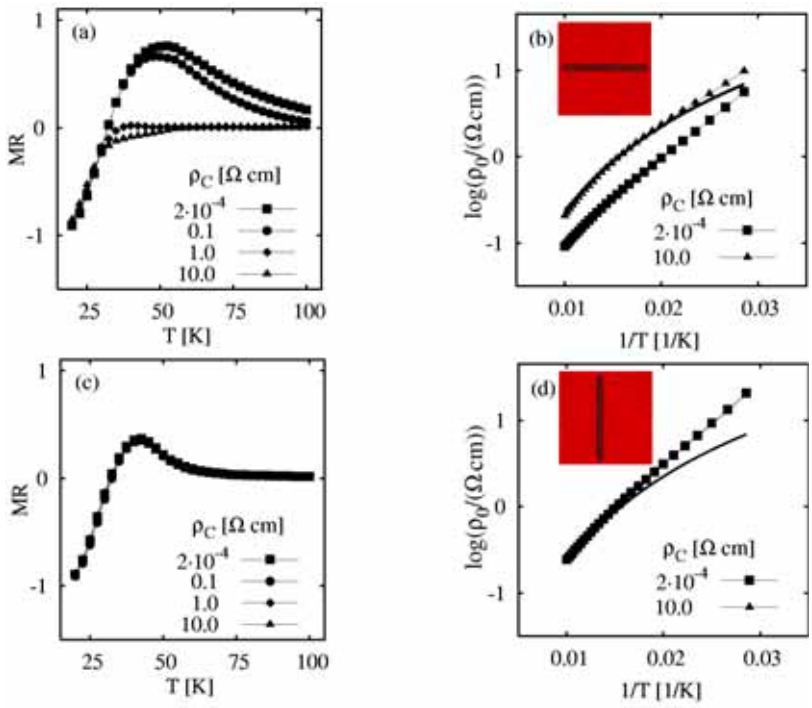

Fig. 5.19. (a) shows the influence of ρ_C on the MR, (b) depicts the corresponding resistivity. Both calculations performed for the cluster configuration given in the inset of (b). For (c) and (d) the cluster configuration given in the inset of (d) is used. (c) shows the influence of ρ_C on the MR while in (d) the influence of ρ_C on the resistivity is shown. Solid lines denote the calculated values of the pure matrix sample. For parameters see sample No. 7 in Tabs. 5.1, 5.2, current from left to right.

values of $\rho_{Mac} = 10^{-4}\,\Omega\,\mathrm{cm}$ and a large positive MR effect is visible. The increase of the current-path length can be neglected for this orientation of the cluster. The lifting of the short circuit due to the external field (in the regime of spin conservation) can be identified definitely as the origin of the strongly enhanced positive MR effect of the hybrid sample. The decrease of the positive MR with decreasing conductivity ρ_{Mac} serves as an additional proof. In (b) the remarkable influence of the cluster oriented along the main current direction on the resistivity in the absence of an external field becomes visible as well. The results of the calculations performed with the second geometry given in Fig. 5.19(c) and (d) show an negligible influence of the variation of ρ_{Mac} on both the MR and $\rho_0(T)$. This is rather expected since the contribu-

tion to the resistivity of a cluster which is oriented perpendicular to the main current path can be neglected.

This detailed analysis of the role of the conductivity of the cluster majority-bands clarifies that the rather trivial mechanism of field induced lifting of short-circuits is not responsible for the observed positive MR effects. The calculated behavior of the resistivity in absence of external fields strongly deviates from the experimental data as e.g. in Fig. 5.2. The experimental data does not support the existence of metallic short-circuits since the measured resistivity of the hybrid samples is not found to be smaller than that of the pure matrix material. As a valuable inference of this analysis it can be summarized that either (i) the density of clusters in the matrix is that low that a percolation path basically connecting metallic clusters does not exist in the samples accessible for experimental characterization so far, or (ii) that the conductivity of the cluster majority band is not sufficiently higher than the conductivity of the matrix. The experimental data given in Ref. [136] in comparison with the calculations shown in Fig. 5.17 may serve as a first hint. In the experimental data a decrease of the cluster size (and therefore an increase of the cluster number) goes along with a decrease of the positive MR effects. The results of the calculations using clusters with very high majority-band conductivity follow from an opposite situation: The positive MR effects increase while the number of cluster cells is increased simply due to the fact that the probability for the formation of short circuits is increased. This comparison is a first, but nevertheless weak, argument against the assumption of a cluster majority-band conductivity which is significantly larger than the average matrix conductivity. Nevertheless these considerations should not hide the wide range of uncertainties concerning the material parameters of the clusters. At this point further measurements of structures including only a few clusters at well defined positions are strongly required.

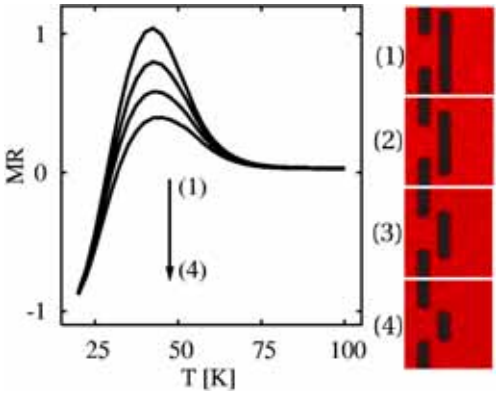

Fig. 5.20. Graph shows the calculated MR versus T at $\mu_0 H = 10\,\mathrm{T}$ for the hybrid structures given right. The concentration of cluster cells is $x_C = 0.15$ (1), 0.13 (2), 0.11 (3), 0.09 (4). For remaining parameters see sample No. 8 in Tabs. 5.1, 5.2.

5.3.2 Examples for optimized hybrid structures

In this section different hybrid structures are shown whose cluster distribution is optimized to provide enhanced magnetoresistance effects. The strong enhancement of the positive MR effect bases on a combination of the spin-conservation mechanism introduced and discussed in detail in section 5.2.2 with tailored hybrid structures. Due to the special choice of cluster positions in these structures they provide a change from a direct to a labyrinth-like current path if an external magnetic field is applied. The conductivity of the majority band of the cluster is set to $\rho_{Mac} = 1.0\Omega\,\mathrm{cm}$ to suppress the influence of cluster built short-circuits as discussed in the previous section 5.3.1. In Fig. 5.20 the MR at $\mu_0 H = 10\mathrm{T}$ versus temperature for a series of tailored hybrids as given in the insets is shown[15]. The sample consists of two clusters forming a gate-like structure while the third cluster is located on the main current path passing this gate. When an external magnetic field is applied, carriers avoid the cluster cells and are passing the matrix gate between the two cluster cells. With increasing size of the two clusters the current density of the matrix cells in the gate increases and the structure acts as a kind of current valve. The third cluster forms an obstacle which the carriers leaving the valve have to evade. This avoiding leads to an increase of the current-path length which is the origin of the observed positive MR. This positive MR scales with the size of the cluster acting as the barrier as given by the calculations presented in Fig. 5.20.

[15] In the images of the hybrid samples of both figures 5.20 and 5.21 only the black area denotes the cluster cells while the surrounding band of cells colored in dark red symbolizes matrix cells which are under the influence of H_C and the Schottky barrier and therefore provide an enhanced density of hole states.

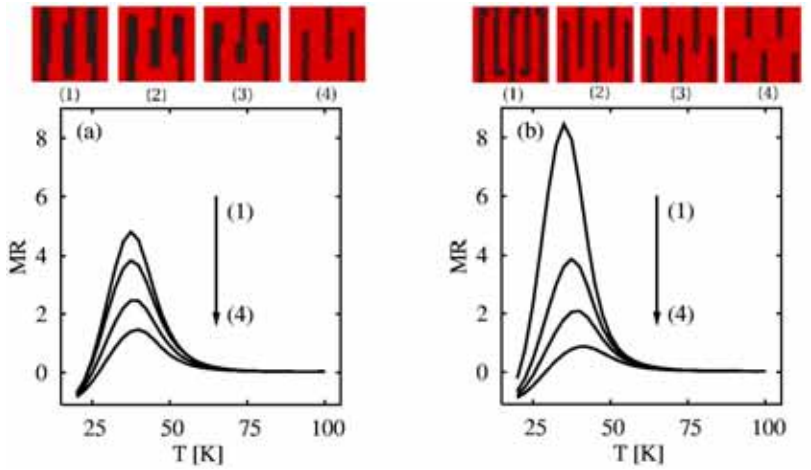

Fig. 5.21. Graphs show the MR versus T at $\mu_0 H = 10\,\mathrm{T}$ in (a) for a series of cluster samples including three clusters as given in the images above and in (b) for a series including five clusters. The concentration of cluster cells decreases from $x_C = 0.1$ (1), 0.15 (2), 0.20 (3), 0.25 (4). For remaining parameters see sample No. 8 in Tabs. 5.1, 5.2.

The second system serving as an example for tailored structures is built by cluster bars forming a sandwich structure oriented perpendicular to the main current direction. Due to the choice of the vertical orientation the bars form a labyrinth-like structure which shows a drastic increase of the current-path length if the carriers cannot pass the cluster cells. The length of the current path increases with increasing number of bars as depicted in Fig. 5.21, where the magnetoresistance is calculated for two different series including three and five bars with increasing concentration of cluster cells. For weak concentrations (e.g. Fig. 5.21b (1)) where the bars located above do not overlap with the bars beneath, the current path is just affected weakly by the spin conservation regime and the MR effects stay comparatively small. With increase of the cluster concentration and according to this with an increase of the overlap of the cluster bars, the current path in the presence of an external field gets elongated and the positive MR reaches values up to about 800 percent (Fig. 5.21b (4)).

5.4 Conclusion

The model was extended to provide a transport description in ferromagnetic/paramagnetic MnAs/GaAs:Mn hybrid structures. In this regard the influence of the formation of a Schottky barrier, the magnetic field of the cluster and a so-called spin-conservation regime were analyzed. This regime accounts for opposite orientations of the matrix and cluster majority bands. On the basis of the modified model the experimentally observed large differences between the magnetotransport properties of hybrids and the paramagnetic host material can be explained at least qualitatively.

In particular it was shown that the effect of spin conservation is responsible for a positive MR in hybrid samples at intermediate temperatures as it is commonly measured. At low temperatures the positive MR attributed to the spin conservation can be compensated. Carriers which are trapped in the vicinity of the cluster due to a cluster field and a Schottky barrier get delocalized when an external magnetic field is applied. An enhancement of the content of magnetically active Mn ions in the matrix material and of H_C can even lead to a low temperature MR of hybrid samples which is below that of the pure matrix material. This finding is again in agreement with experimental data.

The strong increase of the measured resistivity for $H_{ex} = 0$ at low temperatures can also be explained by the interplay of the magnetic field of the cluster with the paramagnetic matrix material. In summary, the influence of the magnetic field of a cluster interacting with a sufficiently large density of Mn ions in the surrounding cells and the assumption of spin conservation can explain the experimentally observed transport as well as magnetotransport effects at least qualitatively.

A closing analysis of the influence of the spatial incorporation of MnAs clusters ends with the prediction of tailored hybrid nanostructures that offer MR effects up to several hundred percent.

6

Conclusion of part I

6.1 Conclusion

A model for the description of the transport and magnetotransport properties of dilute magnetic semiconductors (DMS) and paramagnetic/ferromagnetic semiconductor hybrid-structures was developed.
The macroscopic model provides a description of the transport properties of DMS materials which are beyond the area of validity of the RKKY theories. The approach developed is applicable to a wide range from an almost metallic random alloy in the ferromagnetic phase over paramagnetic semiconductors towards (annealed) samples with non-random incorporation of magnetic ions up to hybrid samples of ferromagnetic clusters embedded in a paramagnetic host matrix. This description may serve as a basis for future microscopic theories.
The model applied is an extension of a network model well established in the description of transport properties in disordered (non-magnetic) semiconductors. It accounts for the material specific properties of DMS such as the magnetic-field induced giant Zeeman splitting of the band states. Alloy disorder is taken into account as well. Many body effects (except the p-d exchange interaction) are neglected.
A first major result is the demonstration that a non-Arrhenius temperature dependence of the resistivity of semiconductors is not indicative for hopping as being the dominant transport mechanism. It is shown that an energetically broad distribution of dopants or band-tail states can cause this non-Arrhenius dependence in the regime of 'usual' activated band-transport. This statement is not limited to the special choice of (dilute) magnetic semiconductors and is in contrast to the widely held belief so far.
The second result is gained by modelling a series of LT MBE grown

$Ga_{1-x}Mn_xAs$ samples annealed at different temperatures. The qualitative description of the experimental results proves that in this regime disorder effects play the dominant role and justifies the neglect of many-body effects as a good approximation. The structural properties of the samples could be condensed into a set of well defined material parameters and the modifications of the transport properties induced by the thermal treatment are connected with changes of these parameters. This treatment allowed first insights into the 'adolescence' of hybrids where segregation sets in and a small fraction of MnAs (micro-) clusters is formed. In this regime the direct influence of these MnAs clusters can be neglected. The transport properties are solely determined by the matrix material which contains a non-random Mn ion incorporation caused by the annealing procedure.
Finally results were obtained for MOVPE grown MnAs/GaAs:Mn hybrid-samples including a high concentration of 'adult' MnAs clusters (with diameters up to 100 nm).
The remarkable discrepancies between the experimental results obtained for (Ga,Mn)As in the paramagnetic phase and ferromagnetic/paramagnetic MnAs/GaAs:Mn hybrids could be explained. The differences were resolved by the assumption of: (a) a Schottky barrier at the interface between cluster and matrix, (b) the influence of the ferromagnetic cluster on the paramagnetic host matrix leading to a giant Zeeman splitting and (c) a spin conservation mechanism using opposite spin orientation of cluster and matrix majority bands. The influence of these three (phenomenological) model ingredients was studied and their order of magnitude could be obtained by numerical simulations and comparison with the measured data. The role of the spatial incorporation of MnAs clusters was analyzed and it was shown that due to tailoring of hybrid nanostructures the MR effects can be enhanced in principle up to several hundred percent. This prediction confirms the auspicious possibilities of hybrids as building blocks of future spintronic devices.

Part II

Spin-dependent charge-carrier recombination

7

Introduction

7.1 Introduction

Recombination of charge carriers belongs to the crucial mechanisms that define the electronic properties of semiconductors. In the following we focus on those recombination paths where the recombination process is determined by the spin state of the involved particles. In the framework of the model developed by Kaplan, Solomon and Mott (KSM) the recombination process is described in terms of so-called intermediate pairs [163]. These intermediate pairs are considered to be the bottle neck of this loss mechanism. Theoretically the evolution of the ensemble of intermediate pairs can be described using the density-matrix formalism, including the fermionic (spin $S = \frac{1}{2}$) character of the pair partners [164]. To investigate the recombination processes via intermediate pairs the pulsed electrically detected magnetic-resonance measurements (pEDMR) had been proven to be a powerful tool [165, 166, 167].

In this work, we apply the most general theoretical concept available for the description of a spin dependent charge-carrier recombination-channel. The concept based on the KSM model contains exchange coupling and disorder effects and can in principle be expanded to describe dipolar coupling. The simulations help to understand the influence of these effects on recombination processes and can provide an interpretation of the experimental results. The insights gained by the simulations may help to provide a better understanding of the recombination process. In the long term the understanding and the possibility of controlling recombination may hopefully lead to an efficiency increase of electronic components where spin-dependent charge-carrier recombination is a major efficiency limiting factor, e.g. solar cells [168].

The hurried reader and those who are solely interested in the simulations may skip the following section, where a very brief overview of the experiments

is given, as well as the introduction sections of chapter 8.1 and continue with 8.3.

7.2 Remarks on the experiments

The time evolution of the density matrix is simulated in the following sections and is used to describe an observable which is obtainable by (pulsed) electrically detected magnetic-resonance experiments (pEDMR). A rather short overview concerning these experiments is given. The basic principles of electrically detected magnetic-resonance experiments are presumed, nevertheless the reading of [169] is warmly recommended.

EDMR is an alternative way to detect electron-spin resonances (ESR) in materials with charge-carrier transport or recombination transitions that are governed by spin-selection rules [170]-[175]. Thus for any EDMR experiment there must be a spin-dependent electronic mechanism which encodes spin-information into electronic transitions which are then detected through charge transport and recombination[1]. This has recently been studied alongside the analysis of recombination processes. This was, in particular, to find potential spin to charge–conversion mechanisms for the electric readout of solid state based spin quantum-computers [166]. The advantage of EDMR, in comparison to the traditional ESR spectroscopy, is the sensitivity of these methods which is typically 6 to 10 orders of magnitude higher [172, 173]. These techniques have become particularly useful for the investigation of paramagnetic centers in highly diluted matrices or low dimensional semiconductor thin film devices, interfaces and point defects [170, 171, 176, 177, 178].

One of the challenges of EDMR spectroscopy is that the information obtained from these experiments is different from the ESR data [179]. The reasons for the discrepancies between ESR and EDMR are mainly due to the two different measurement approaches which imply two different observables: The observable corresponding to ESR experiments will always be spin polarization $\langle \mathcal{P} \rangle = \mathrm{Tr}(\hat{\mathrm{P}}\hat{\rho})$ representing the statistical state of the spin ensemble whereas for indirect detection through spin-dependent transport or recombination, the observables are the permutation-symmetry or -antisymmetry operators represented by the singlet $|S\rangle\langle S|$ or triplet operators $|T_i\rangle\langle T_i|$, respectively [164]. For many experimental EDMR studies (the so-called continuous wave experiments) the difference of the observable in comparison with ESR are not relevant, since these experiments are carried out in the incoherent time regime where only a line shape analysis of the respective spectra is feasible. However,

[1] The influence of spin dependent hopping rates to singly occupied sites on the transport properties is not taken into account.

when coherent effects are studied with a pulsed technique (pEDMR) [165, 180] the interpretation of the experiments strongly relies on the proper theoretical description of spin interaction during coherent microwave excitation [165, 176].

An example of the difference between a pEDMR signal and a pESR signal, which comes from the same spin ensemble, is weak exchange and weak dipolar coupled distant pair states in the band gap of an arbitrary semiconductor material with weak spin-orbit coupling as described analytically by Boehme and Lips [180]. Weak spin-orbit coupling is required in order to ensure a spin-selection rule. When the two pair partners are manipulated (almost) resonantly with a coherent pulse of high field strength B_1 ($(\frac{g\mu_B B_1}{\hbar}) = \gamma B_1 \gg \Delta\omega$ [2] where $\Delta\omega$ denotes the Larmor-frequency difference between the pair partners and $\gamma = \frac{g\mu_B}{\hbar}$ is the gyromagnetic ratio), they undergo a simultaneous spin–Rabi oscillation. With pEDMR, the rate relaxation after the coherent excitation would be integrated reflecting the pair permutation-symmetry within the pairs at the end of the exciting pulse [181]. While both, the pESR and the pEDMR transients (the photoconductivity) would exhibit oscillating signals, the frequency of these oscillations would differ by a factor of 2: The pESR detected nutation frequency $\Omega_{\mathrm{ESR}} = \gamma B_1$ would simply represent the Rabi frequency of an uncoupled spin $S = \frac{1}{2}$, whereas the pEDMR measured oscillation reflects the two-particle character of the system. Using a simple, but nevertheless sustainable model, the oscillations exhibit the frequency at which the identically precessing spins of the two pair partners cross the geometric plane transverse to the direction of the externally applied magnetic field B_0 (the $\hat{x}$-$\hat{y}$ plane) since at these moments the projection of the parallel oriented spins in the $\hat{x}$-$\hat{y}$ plane onto the spin eigenstates with singlet content will be maximized. Since this plane is passed twice per nutation period, the oscillation of the transition rate is twice as high. Note that this frequency discrepancy of the oscillations, between pESR and pEDMR detected transient nutations, is changed as the B_1-field strength becomes weak: When $\gamma B_1 \ll \Delta\omega$, the two-particle character of the system almost vanishes and the system can be considered as a pair of non-interacting particles. Hence, for weak $\mathbf{B_1}$ fields, the nutation frequencies for pESR and pEDMR become equal.

[2] Note that g may be either one of the two pair partners Landé factors g_a or g_b or it may even be assumed to be the free electrons Landé factors $g = g_e$ since the differences between these values compared to their magnitudes is negligible.

8

The model

8.1 Introduction

A central part of the spin-dependent recombination-process, which is discussed in the following, is the creation of a two-particle system called an intermediate pair (IP)[169]. Without external perturbation the system is in a steady state where the creation of IPs equals their annihilation. Annihilation of IPs can be due to recombination or dissociation.

The two annihilation mechanisms are discussed in more detail in section 8.2. If an IP is created once, its probability of being destroyed by recombination is determined by the projection of its actual state onto the eigenstates of the angular-momentum operator $\mathcal{J}$. In the product basis of a two-particle system given by the basis elements $|\uparrow\uparrow\rangle, |\uparrow\downarrow\rangle, |\downarrow\uparrow\rangle, |\downarrow\downarrow\rangle$ these eigenstates are the triplet and singlet states

$$\begin{aligned} |T_+\rangle &= |\uparrow\uparrow\rangle \\ |T_-\rangle &= |\downarrow\downarrow\rangle \\ |T_0\rangle &= \frac{1}{\sqrt{2}}\left(|\uparrow\downarrow\rangle + |\downarrow\uparrow\rangle\right) \\ |S\,\rangle &= \frac{1}{\sqrt{2}}\left(|\uparrow\downarrow\rangle - |\downarrow\uparrow\rangle\right). \end{aligned}$$

While the three triplet states have a small but non-vanishing[1] recombination-rate coefficient r_T the recombination-rate coefficient of the singlet state r_S is about 100 times larger [169]. Thus an IP in a singlet state has a high probability of recombining. Since the triplet states show permutation symmetry while

[1] r_T is non-vanishing in the considered case of small spin-orbit coupling.

the singlet state is antisymmetric, the observable in pEDMR experiments is often referred to as the permutation-symmetry or -antisymmetry operator.

When considering their interaction with an external magnetic field, the two pair partners a and b can be described by using the characteristic Landé g-factors g_a and g_b. The different g-factors represent different local magnetic fields and thus reflect the different characteristic microscopic vicinities of the pair partners. With the application of a constant magnetic field $\mathbf{B_0}$, the spin degeneracy of the eigenstates lifts, resulting in a system with four distinct energy levels. Interpreted in terms of two independent $S = \frac{1}{2}$ particles this scenario becomes more tangible. The energy spacing between each two spin states of the pair partners according to the field $\mathbf{B_0}$ is

$$\hbar\omega_{a(b)} = g_{a(b)}\mu_B B_0 \tag{8.1}$$

where $\omega_{a(b)}$ denotes the Larmor frequency of the pair partners. The recombination rates r_i of the four eigenstates $|i\rangle$ (which are not necessarily eigenstates of the angular-momentum operator $\mathcal{J}$) are given by the projections onto the eigenstates of $\mathcal{J}$ as

$$r_i = r_S \left|\langle i|\ S\rangle\right|^2 + r_T \sum_{j=+,-,0} \left|\langle i|\ T_j\rangle\right|^2 . \tag{8.2}$$

Without any additional disturbance of the system it is in a steady state, where the creation and annihilation of intermediate pairs are in equilibrium. Represented in the density-matrix formalism the time derivative of the diagonal elements ρ_{ii} of the density matrix vanishes in the case $\rho_{ii} = \rho_{ii}^s$ where ρ_{ii}^s denotes the steady-state density-matrix elements. A deviation of the ρ_{ii} from the steady-state value (the accompanying projections onto the eigenvectors of $\mathcal{J}$ change resulting in changing recombination rates) upsets the equilibrium of the IP creation and annihilation. This is reflected in a change of the photoconductivity. The simulated pEDMR experiments based on this feature in particular. In these experiments in addition to the constant $\mathbf{B}_0$ field a time dependent magnetic field $\mathbf{B}_1$ is applied. This $\mathbf{B}_1$ field causes a deviation from the steady state. The change of the photoconductivity obtainable by pEDMR experiments can be simulated if the time evolution of the density-matrix elements is known. In general, an experiment can be described solely by the simulation of the dynamics of a density matrix, representing the statistical state of a four-level system. To do so, the Liouville equation $\frac{d}{dt}\hat{\phi} = i\hbar[\mathcal{H}\hat{\phi}]$ has to be solved. This is done by solving the set of Bloch equations resulting from the commutator in the Liouville equation numerically. Stochastic processes (e.g. the creation of the intermediate pairs) are taken into account as well by resolving the so-called stochastic Liouville equation. Besides the phenomenological treatment of the recombination process described by the

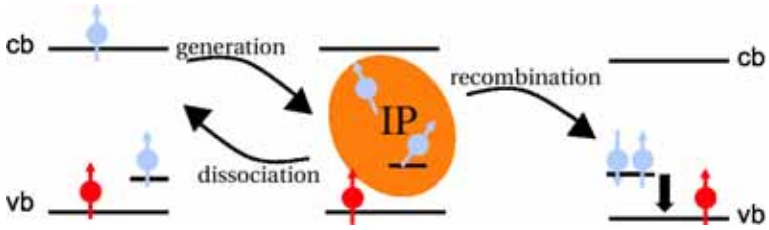

Fig. 8.1. Illustration of a spin dependent recombination process in the KSM picture via a deep level defect as it can happen e.g. at a dangling bond in μc-Si:H. Electrons are colored blue, holes are colored red and the orange area symbolizes the correlated two electron system called an intermediate pair (IP). Arrows indicate the spin of the carriers and cb and vb denote the valence band and conduction band respectively.

recombination rates, further parameters such as the dissociation-rate coefficient d and the generation rate G of the intermediate pairs are taken into account. The description of the dynamics of a four-level system using a Hamilton operator covering the spin-selection rules accounts for all spin dependent system properties. Other descriptions based on the Larmor precession of spins in magnetic fields can be skipped entirely. Thus the rather bulky formalism using sequences of drehoperators can be left out. Apart from that, the given approach fully accounts for the two-particle character which has been proven to be necessary especially in the case of strong light-field coupling as discussed in detail in section 9.2.4.
In summary, applying this approach all relevant (spin-dependent) system information is coded into the energy levels. Out of them all further information can be obtained using an interaction Hamilton-operator which reflects the spin-selection rules. In the framework of this description, taking into account exchange interaction as well as dipolar interaction (covered by the coupling constants J and D^d in Eqn. 9.3) simply leads to a modification of the four energy levels. The whole formalism stays unchanged. As we will show in chapter 11, even an extension to systems containing disorder is possible.

8.2 The intermediate-pair concept, a closer look

The concept of intermediate pairs developed by Kaplan, Solomon and Mott in 1978[2] [163] is a general one, which describes an intermediate step between the charge carriers in independent states and the final recombined state. One example, where this concept can be applied is the recombination at dangling

[2] Referred to as the KSM model

bonds (db) as it takes place e.g. in hydrogenated microcrystalline silicon (μc-Si:H) schematically illustrated in Fig. 8.1. In μc-Si:H this spin dependent recombination 'catalyzed' by dangling bonds is a dominant recombination path [169].

In such a material the generation of an intermediate pair can be interpreted as the process of the localization of a conduction-band electron in proximity of to a db. The localized electron and the electron of the singly occupied (thus neutral and paramagnetic) db form a two-particle system, which is in an excited state. The ground state of this two-particle system is given by the doubly occupied (thus negatively charged) dangling bond. The transition into the ground state is the crucial step that makes this recombination process spin dependent. If an intermediate pair is formed it can only be destroyed by one of the two following mechanisms:
a) *Dissociation* of the IP. Using the example of an IP given above this is a delocalization of the localized electron (e.g. due to thermal fluctuations). This leads to the initial situation of a singly occupied dangling bond and a free conduction-band electron.
b) *Recombination* of the IP. Using the example of an IP given above this is the transition into the ground state of the IP, resulting in the doubly occupied and negatively charged defect state (the dangling bond). This state has a negligible life time, so that one pair partner recombines immediately with a valence-band hole.

8.3 The building blocks of a general model for spin-dependent recombination

Before we start with the detailed theoretical description we give an overview of the assumptions made. They were discussed above and form the general building blocks of the model for the spin-dependent recombination, as primarily given by Boehme [169]:

- Based on the picture of Kaplan, Solomon and Mott, the intermediate pair is the bottle neck through which every recombination process discussed in the following has to pass.
- An intermediate pair is formed by two particles, each with spin $S = \frac{1}{2}$. The resulting two particle system has four eigenstates with respect to the Hamilton operator.
- The density of intermediate pairs is so weak compared with the density of carriers that effects of higher order can be neglected, i. e. a (coherent) manipulation of the recombination process resulting in a change of the carrier density does not affect the generation rate of intermediate pairs.

- If an intermediate pair is created, it can (a) be destroyed due to recombination or it can (b) be destroyed due to pair dissociation. The creation as well as the two different mechanisms to destroy an intermediate pair are taken into account in the calculations in a parameterized form. These parameters are inputs to the calculations rather than being calculated therein.
- The spin-orbit coupling of the discussed system is so weak that the spin of the two-particle system is almost conserved and so the recombination becomes spin-dependent. Nevertheless a non-vanishing triplet recombination probability has to be taken into account.
- The interactions between the two pair partners such as spin-exchange interaction and spin-dipole interactions are possible and can modify the recombination properties. If such interactions are taken into account in the model, this is solely done by the introduction of parameters such as the strength of the exchange integral J.
- The interaction of a spin pair with its environment (spin-lattice or spin-spin relaxation) can destroy the correlation of the spin pair.

8.4 The observable

The observable usually measured when performing a pEDMR experiment[3] is the change of the photoconductivity $\Delta\sigma(t)$. The photoconductivity is given by

$$\sigma = \mu_e e n_e + \mu_h e n_h \tag{8.3}$$

with the electron charge e, mobility $\mu_{e(h)}$ for the electron and hole respectively and the electron (hole) density $n_{e(h)}$. The observable is given by

$$\Delta\sigma(t) = e\left(\mu_e \Delta n_e(t) + \mu_h \Delta n_h(t)\right) \tag{8.4}$$

with

$$\Delta n_{e(h)} = n_{e(h)}(t) - n^s_{e(h)} \tag{8.5}$$

with the steady-state electron (hole) density $n^s_{e(h)}$. The steady-state electron density is

$$n^s_e = \tau_l \left(-G^s + d \sum_i \rho^s_{ii} + G^* \right) \tag{8.6}$$

where ρ^s_{ii} are the (diagonal) elements of the steady-state density matrix, G^s is the (steady-state) intermediate-pair generation rate, d is the dissociation-rate coefficient of the spin pairs and G^* is the constant electron-hole pair generation-rate due to the continuous wave light-field source. The lifetime τ_l is the averaged carrier lifetime. The different signs of the expressions for the pair generation and the pair dissociation represent the different influence of both processes on the density of electrons: The generation of an intermediate pair takes an electron from the conduction band. The dissociation, which depends on the density of intermediate pairs in the steady state ($\mathrm{Tr}\hat{\rho}^s$), destroys an IP and thus adds an electron to the conduction band.
The steady-state hole-density is mainly determined by the recombination process

$$n^s_h = \tau_l \left(-\sum_i r_i \rho^s_{ii} + G^* \right) \tag{8.7}$$

where r_i are the recombination-rate coefficients.

[3] For a detailed description of the experiments see [169].

The electron (hole) density at time t is basically given by the time evolution of the density matrix[4]

$$n_e(t) = \tau_l \left(-G(t) + d \sum_i \rho_{ii}(t) + G^* \right) \tag{8.8}$$

$$n_h(t) = \tau_l \left(-\sum_i r_i \rho_{ii}(t) + G^* \right). \tag{8.9}$$

According to Sect. 8.3 the generation rate of spin pairs is considered as constant ($G(\mathrm{t}) = G^s{=}G$). Although the generation rate of the spin pairs depends on the density of carriers this assumption is justified to first order[5]. By use of Eqns. 8.6, 8.7, 8.8, 8.9 and Eqn. 8.5 one gets

$$\Delta n_e(t) = \tau_l d \left(\sum_i \left(\rho_{ii}(t) - \rho_{ii}^s \right) \right) \tag{8.10}$$

$$\Delta n_h(t) = \tau_l \left(\sum_i r_i \left(\rho_{ii}^s - \rho_{ii}(t) \right) \right). \tag{8.11}$$

Finally the equation for the change of the photoconductivity (Eqn. 8.4) becomes

$$\begin{aligned} \Delta\sigma(t) &= \tau_l e \left(\mu_e d \sum_{i=1}^{4} (\rho_{ii} - \rho_{ii}^S) + \mu_h \sum_{i=1}^{4} r_i (\rho_{ii}^S - \rho_{ii}) \right) \\ &= \tau_l e \sum_{i=1}^{4} (\rho_{ii} - \rho_{ii}^s) \left(\mu_e d - \mu_h r_i \right) \\ &= \tau_l e \mu_e d \sum_{i=1}^{4} (\rho_{ii} - \rho_{ii}^s) \left(1 - \frac{r_i}{d} \frac{\mu_h}{\mu_e} \right). \end{aligned} \tag{8.12}$$

Thus Eqn. 8.12 provides a connection between the macroscopic change of the photoconductivity $\Delta\sigma(t)$ and the microscopic spin-dependent dynamics of an ensemble of intermediate-pair states. This change $\Delta\sigma(t)$ can be positive (enhancement of the conductivity) or negative (quenching of the conductivity), depending on the difference of the diagonal elements of $\rho(t)$ and their steady-state value as well as on the recombination rates.

[4] It should be noted, that the trace of the density matrix is not necessarily conserved during the excitation.

[5] The relative charge-carrier density-changes usually obtained in the experiments are of less than 10^{-3} [169]

9

Theoretical description

9.1 General description — the stochastic Liouville equation

The general problem examined here is the solution of a stochastic Liouville equation [164]

$$\frac{d}{dt}\hat{\rho} = \frac{i}{\hbar}\left[\hat{\rho}, \mathcal{H}\right]^{-} + \mathcal{S}[\hat{\rho}] + \mathcal{R}[\hat{\rho} - \hat{\rho}^{\mathrm{s}}] \tag{9.1}$$

where $\hat{\rho}^{(s)}$ is the (steady-state) density operator and $\mathcal{H}$ is given as the sum of a time-independent and a time-dependent part

$$\mathcal{H} = \mathcal{H}_0 + \mathcal{H}_1(t) \tag{9.2}$$

$\mathcal{S}$ is a stochastic operator describing recombination, dissociation and generation of the pairs while $\mathcal{R}$ is the so-called Redfield operator describing the interaction with a bath [182, 183].

9.2 Basic equations and conventions

The starting point of the description is the Hamilton operator $\mathcal{H}_0$ as it is given in Eqn. 3.5 in [169][1]

$$\mathcal{H}_0 = \underbrace{\frac{\mu_B g_a}{\hbar}\mathcal{S}_a \cdot \mathbf{B}_0 + \frac{\mu_B g_b}{\hbar}\mathcal{S}_b \cdot \mathbf{B}_0}_{I} - \underbrace{\tilde{J}\mathcal{S}_a \cdot \mathcal{S}_b}_{II} - \underbrace{\tilde{D^d}\left[3\mathcal{S}_a^z\mathcal{S}_b^z - \mathcal{S}_a \cdot \mathcal{S}_b\right]}_{III}. \quad (9.3)$$

Part I of the Hamilton operator describes the usual Zeeman splitting of the two particles due to the (time independent) external magnetic field while II and III account for the interactions of the pair partners (exchange interaction as well as the dipolar interaction in the high-field approximation ($\mid D^d \mid \ll g\mu_{\mathrm{B}}B_0$)). The constant external magnetic field $\mathbf{B_0}$ is given as

$$\mathbf{B_0} = (0, 0, B_0).$$

The matrix representation of $\mathcal{H}_0$ in the product base is given by

$$\hat{H}_0 = \begin{pmatrix} \frac{\hbar}{2}\omega_0 - I_I & 0 & 0 & 0 \\ 0 & \frac{\hbar}{2}\Delta\omega + I_I & -J\frac{1}{2} + D^d\frac{1}{2} & 0 \\ 0 & -J\frac{1}{2} + D^d\frac{1}{2} & -\frac{\hbar}{2}\Delta\omega + I_I & 0 \\ 0 & 0 & 0 & -\frac{\hbar}{2}\omega_0 - I_I \end{pmatrix}$$

with $\omega_0 = \omega_a + \omega_b$ and using the abbreviation $I_I = J\frac{1}{4} + D^d\frac{1}{2}$. With the introduction of the time dependent magnetic field $\mathbf{B_1(t)} = (B_1\cos(\omega t), 0, 0)$ the matrix representation of the interaction Hamilton-operator $\mathcal{H}_1$ is given following [169] as

$$\hat{H}_1(t) = \frac{1}{2}\mu_B B_1 \cos(\omega t) \begin{pmatrix} 0 & g_a & g_b & 0 \\ g_a & 0 & 0 & g_b \\ g_b & 0 & 0 & g_a \\ 0 & g_b & g_a & 0 \end{pmatrix}.$$

The Hamilton operator $\mathcal{H}_1$ accounts for the spin conservation of the discussed weakly spin-orbit coupled system. In the regime of weak spin-orbit coupling the spin-dependent transitions are governed by spin-selection rules. These spin-selection rules are coded into the matrix elements of $\mathcal{H}_1$ and thus determine the allowed transitions.

[1] In contrast to [169] the eigenvalues of $\mathcal{S}_z$ are set to $\pm\frac{\hbar}{2}$, so the exchange integral and the dipolar coupling constant have been rewritten as $\tilde{J} = \frac{J}{\hbar^2}$, $\tilde{D^d} = \frac{D^d}{\hbar^2}$, where J and D^d have unit energy.

Since the derivation of the product-base representation of both parts of the Hamilton operator is a rather lengthy procedure, it is not performed here. The interested reader is recommended to study appendix E where the derivation is given in detail.
Usually (whenever $D^d - J \neq 0$), $\hat{H}_0$ has no diagonal form in the product-basis representation. $\hat{H}_0$ can be diagonalized by the transformation $\hat{H}_{dia} = \tilde{U}\hat{H}_0\tilde{U}^{-1}$. The transformation matrix $\tilde{U}$ is given as

$$\tilde{U} = \begin{pmatrix} 1 & 0 & 0 & 0 \\ 0 & A & B & 0 \\ 0 & C & D & 0 \\ 0 & 0 & 0 & 1 \end{pmatrix}, \tag{9.4}$$

with the entries:

$$A := \frac{\hbar\Delta\omega - \sqrt{(D^d - J)^2 + \hbar^2\Delta\omega^2}}{(D^d - J)\sqrt{2 - \frac{2\hbar\Delta\omega}{\hbar\Delta\omega + \sqrt{(D^d - J)^2 + \hbar^2\Delta\omega^2}}}},$$

$$B := \frac{\hbar\Delta\omega + \sqrt{(D^d - J)^2 + \hbar^2\Delta\omega^2}}{(D^d - J)\sqrt{2 + \frac{2\Delta\omega\left(\hbar\Delta\omega + \sqrt{(D^d - J)^2 + \hbar^2\Delta\omega^2}\right)}{(D^d - J)^2/\hbar}}},$$

$$C := \frac{1}{(D^d - J)\sqrt{2 - \frac{2\hbar\Delta\omega}{\hbar\Delta\omega + \sqrt{(D^d - J)^2 + \hbar^2\Delta\omega^2}}}},$$

$$D := \frac{1}{(D^d - J)\sqrt{2 + \frac{2\Delta\omega\left(\hbar\Delta\omega + \sqrt{(D^d - J)^2 + \hbar^2\Delta\omega^2}\right)}{(D^d - J)^2/\hbar}}}.$$

Hence the normalized eigenbasis of the free Hamilton operator $\mathcal{H}_0$ in the representation of the product basis becomes

$$
\begin{aligned}
|1\rangle = |T_+\rangle &= \begin{pmatrix} 1 \\ 0 \\ 0 \\ 0 \end{pmatrix}, \\
|2\rangle &= \begin{pmatrix} 0 \\ \dfrac{\hbar\Delta\omega - \sqrt{(D^d-J)^2+\hbar^2\Delta\omega^2}}{(D^d-J)\sqrt{2-\frac{2\hbar\Delta\omega}{\hbar\Delta\omega+\sqrt{(D^d-J)^2+\hbar^2\Delta\omega^2}}}} \\ \dfrac{1}{(D^d-J)\sqrt{2-\frac{2\hbar\Delta\omega}{\hbar\Delta\omega+\sqrt{(D^d-J)^2+\hbar^2\Delta\omega^2}}}} \\ 0 \end{pmatrix}, \qquad (9.5) \\
|3\rangle &= \begin{pmatrix} 0 \\ \dfrac{\hbar\Delta\omega + \sqrt{(D^d-J)^2+\hbar^2\Delta\omega^2}}{(D^d-J)\sqrt{2+\frac{2\Delta\omega\left(\hbar\Delta\omega+\sqrt{(D^d-J)^2+\hbar^2\Delta\omega^2}\right)}{(D^d-J)^2/\hbar}}} \\ \dfrac{1}{(D^d-J)\sqrt{2+\frac{2\Delta\omega\left(\hbar\Delta\omega+\sqrt{(D^d-J)^2+\hbar^2\Delta\omega^2}\right)}{(D^d-J)^2/\hbar}}} \\ 0 \end{pmatrix}, \qquad (9.6) \\
|4\rangle = |T_-\rangle &= \begin{pmatrix} 0 \\ 0 \\ 0 \\ 1 \end{pmatrix}.
\end{aligned}
$$

It is obvious that the triplet-plus state $|T_+\rangle$ and the triplet-minus state $|T_-\rangle$ are still members of the eigenbasis but it should be noted that $|2\rangle$ and $|3\rangle$ are usually not elements of the triplet-singlet basis. The eigenbasis vectors $|2\rangle$ and $|3\rangle$ are mixed states built out of linear combinations of the triplet zero and the singlet state. It can be anticipated here that for high values of J (while D^d=0) the state $|2\rangle$ almost only has triplet contributions and the state $|3\rangle$ only singlet contributions.

The matrix representation of the free Hamilton operator $\mathcal{H}_0$ in its eigenbasis is given as

$$
\hat{H}_0 = \frac{1}{4}\begin{pmatrix} -W+2\hbar\omega_0 & 0 & 0 & 0 \\ 0 & W-2V & 0 & 0 \\ 0 & 0 & W+2V & 0 \\ 0 & 0 & 0 & -W-2\hbar\omega_0 \end{pmatrix} \qquad (9.7)
$$

with $V = \sqrt{(D^d-J)^2+\hbar^2\Delta\omega^2}$ and $W := 2D^d + J$.

The matrix representation of the interaction Hamilton operator $\mathcal{H}_1$ in its eigenbasis is given as

$$\hat{H}_I = \frac{1}{2}\mu_B B_1 \cos\omega t \begin{pmatrix} 0 & g_a A + g_b C & g_a B + g_b D & 0 \\ g_a A + g_b B & 0 & 0 & g_a C + g_b A \\ g_a B + g_b D & 0 & 0 & g_a D + g_b B \\ 0 & g_a B + g_b A & g_a D + g_b B & 0 \end{pmatrix}.$$

9.2.1 Remarks on incoherent phenomena

The commutator in Eqn. 9.1 describes the evolution of a closed system characterized by $\mathcal{H}_0$ interacting with $\mathbf{B_1}$. The last two terms, $\mathcal{S}$ and $\mathcal{R}$, describe the interaction with the environment. While $\mathcal{S}$ describes stochastic processes, due to the many-particle character of the system, $\mathcal{R}$ represents the resulting influence of a bath. While the stochastic processes will be called *generation* (pair creation), *dissociation* (dissociation of a pair) and *recombination* (pair-partners recombine), we will call the bath influence *relaxation*. The influence of relaxation which can be described by the Redfield-operator as given in Eqn. 9.1 is neglected in all further calculations. The following assumptions about the stochastic processes are made:

- Without a $\mathbf{B_1}$ field the photoconductivity is constant, i.e. the generation is in equilibrium with the dissociation and recombination.
- The generation is independent of the $\mathbf{B_1}$ field. It depends only on the constant reservoir of free carriers and defects. It is assumed that small changes of the carrier density, due to a change of the recombination, have no effect on the generation since the ratio between pairs and carriers is small.
- Dissociation and recombination affect not only the populations (diagonal elements of $\hat{\rho}$) but also the polarizations (the off-diagonal elements of $\hat{\rho}$).
- The $\mathbf{B_1}$ field manipulates the populations, therefore the equilibrium of generation, dissociation and recombination is perturbed.

It should be noted that based on these assumptions, the norm of the density matrix is not necessarily conserved during excitation with the $\mathbf{B_1}$ field.

9.2.2 Generation and recombination

As is briefly stated in Sect. 8.1 the recombination rates of the eigenstates $|i\rangle$ of $\mathcal{H}_0$ are given by their projections on the eigenvectors of the angular-momentum operator $\mathcal{J}$

$$
\begin{aligned}
r_1 &= r_{T_+} = r_T, \qquad (9.8)\\
r_2 &= r_S \left|\langle 2|\ S\rangle\right|^2 + r_T \left|\langle 2|\ T_0\rangle\right|^2\\
&= \frac{r_S}{2}\left(\frac{\hbar^2\Delta\omega^2}{\sqrt{(D^d-J)^2+\hbar^2\Delta\omega^2}\left(-(D^d-J)+\sqrt{(D^d-J)^2+\hbar^2\Delta\omega^2}\right)}\right)\\
&\quad + \frac{r_T}{2}\left(\frac{\hbar^2\Delta\omega^2}{\sqrt{(D^d-J)^2+\hbar^2\Delta\omega^2}\left((D^d-J)+\sqrt{(D^d-J)^2+\hbar^2\Delta\omega^2}\right)}\right),\\
r_3 &= r_S \left|\langle 3|\ S\rangle\right|^2 + r_T \left|\langle 3|\ T_0\rangle\right|^2\\
&= \frac{r_S}{2}\left(\frac{\hbar^2\Delta\omega^2}{\hbar^2\Delta\omega^2+(D^d-J)\left((D^d-J)+\sqrt{(D^d-J)^2+\hbar^2\Delta\omega^2}\right)}\right)\\
&\quad + \frac{r_T}{2}\left(\frac{\hbar^2\Delta\omega^2}{\hbar^2\Delta\omega^2-(D^d-J)\left(-(D^d-J)+\sqrt{(D^d-J)^2+\hbar^2\Delta\omega^2}\right)}\right),\\
r_4 &= r_{T_-} = r_T.
\end{aligned}
$$

Now all the necessary ingredients for the presentation of the matrix elements for the stochastic operator $\mathcal{S}$ (as introduced by Haberkorn and Dietz [164]), are well defined as

$$\mathcal{S}\left[\rho(t)\right] = \mathcal{S}_{an}[\rho(t)] + \mathcal{S}_{cr}[\rho(t)], \qquad (9.9)$$

$$\left\{\mathcal{S}_{an}[\rho(t)]\right\}_{ij} = (r_i + r_j + d)\frac{\rho_{ij}}{2}, \qquad (9.10)$$

$$\left\{\mathcal{S}_{cr}[\rho(t)]\right\}_{ij} = \delta_{ij}G_i, \;\; i,j \in 1,2,3,4 \qquad (9.11)$$

where G_i are the generation rates of the four diagonal elements of $\hat{\rho}$, for simplicity taken here as $G_i = \frac{G}{4}$, the $r_{i(j)}$ are the recombination rate coefficients as given by Eqn. 9.8 and d is the dissociation rate coefficient.

9.2.3 The Bloch equations

With use of the density matrix $\hat{\rho}$

$$\hat{\rho}(t) = \begin{pmatrix} \rho_{11} & \rho_{12} & \rho_{13} & \rho_{14} \\ \rho_{21} & \rho_{22} & \rho_{23} & \rho_{24} \\ \rho_{31} & \rho_{32} & \rho_{33} & \rho_{34} \\ \rho_{41} & \rho_{42} & \rho_{43} & \rho_{44} \end{pmatrix}$$

the commutator $[\hat{\rho}, \mathcal{H}]^-$ appearing in Eqn. 9.1 can be evaluated. The resulting Bloch equations are a set of 16 coupled differential equations which represent the interaction of a four-level system (the eigenstates of $\mathcal{H}_0$) with a coherent excitation (given by $\mathcal{H}_1$). They can be found in appendix F.

9.2.4 The regimes of different light-field coupling

The Bloch equations resulting from $[\hat{\rho}, \mathcal{H}]^-$ serve as the most general description of the dynamics of the discussed two-particle system and can be solved numerically. However, an interpretation of the results using these differential equations turns out to be rather difficult and simply inappropriate. The picture of two spin-$\frac{1}{2}$ particles with Larmor frequencies $\omega_{a(b)}$ that precess around the $\mathbf{B}_0$ field is commonly used and has turned out to be a helpful interpretation tool. Needless to say that such a model based on single-particle quantities is not able to explain the quantum-mechanical two-particle character of the system. In the same way it is questionable to draw conclusions and to make predictions about experiments based solely on such a simple picture. Nevertheless it can help to interpret borderline cases of the two-particle system in which the single-particle signatures appear dominantly.
A quantity which can be used to distinguish between different intermediate-pair regimes which can be observed by e.g. pEDMR is the coupling strength of the $\mathbf{B}_1$ field. The parameter that separates the system into weak, medium and strong $\mathbf{B}_1$ field coupling is the ratio between the amplitude of the $\mathbf{B}_1$ field and the pair partners Larmor-frequency difference $\Delta\omega$. We concentrate on the two extreme cases: If $\gamma B_1 << \Delta\omega$ the system is said to be weakly light-field coupled[2]. This means that the system can be considered in a first approximation to decompose into two one-particle systems. Each of these one-particle systems can be characterized by its Larmor frequency $\omega_{a(b)}$. If $\gamma B_1 << \Delta\omega$ and e.g. the $\mathbf{B}_1$ field is in resonance with the two-level system of particle a ($\omega = \omega_a$) almost no transitions with transition frequency ω_b are induced between the two states of particle b. In other words, the spins can be considered

[2] The terms weak (strong) light-field coupling or large (small) Larmor separation are used synonymously in the following.

to precess independently of each other with their Larmor frequencies. Both spins are considered to be distinguishable.

In general the Rabi frequency Ω of transitions between two states with transition (Larmor) frequency ω_{L} excited by an external field $\mathbf{B}_1$ of strength B_1 and frequency ω is given by

$$\Omega = \sqrt{(\gamma B_1)^2 + (\omega - \omega_{\mathrm{L}})^2}. \tag{9.12}$$

The analytic expression of the relative change of the density matrix elements[3] $\Delta(\tau)$ of a weakly light-field coupled pair, as derived in [169], becomes

$$\Delta(\tau) = \frac{1}{2}\frac{\gamma^2 B_1^2}{\Omega_{a(b)}^2}[1 - \cos(\Omega_{a(b)}\tau)]. \tag{9.13}$$

This dependence of $\Delta(\tau)$ on the single-particle Rabi-frequencies confirms the assumption that the two-particle system can be considered in a first approximation as two one-particle systems as soon as the light-field coupling is sufficiently small. Thus, the two signals appearing in the calculations of $\Omega = \mathrm{FT}(\Delta\sigma(t))$ versus excitation frequency ω (in the regime of weak light-field coupling), which reach their maximum intensities at $\Omega = \gamma B_1$ for $\omega = w_{a(b)}$, are called the spin-$\frac{1}{2}$ contributions $S_{\frac{1}{2}}$.

The other extreme scenario is the regime of so-called strong light-field coupling (weak Larmor separation) fulfilling $\gamma B_1 >> \Delta\omega$. In this case the separation of the two Larmor frequencies is small compared to their absolute values. In the picture of spins exposed to external magnetic fields this can be interpreted as a precession of the two pair partners across the geometric plane, transverse to the field direction of the externally applied magnetic field B_0 (the **x**-**y**-plane). At these moments the projection of the parallel oriented spins in the **x**-**y**-plane onto the spin eigenstates with singlet content will be maximized. Since this plane is passed twice per nutation period, the oscillation frequency of the transition rate is twice as high as that of an uncoupled spin $S = \frac{1}{2}$. This can alternatively be represented as one system with spin $S = 1$, with a Rabi frequency which is twice that of a single pair partner with $S = \frac{1}{2}$. Thus for $\gamma B_1 >> \Delta\omega$ the signal appearing in the calculation of $\Omega = \mathrm{FT}(\Delta\sigma(t))$ versus excitation frequency ω which reaches its maximum intensity at $\Omega = 2\gamma B_1$ for $\omega = w_a \simeq w_b$ will be called the spin-1 contribution S_1. The analytic expression of $\Delta(\tau)$ in the regime of strong light-field coupling as given by [169] is

$$\Delta(\tau) = \frac{1}{2}\frac{\gamma^2 B_1^2}{\Omega_{a(b)}^2}[1 - \cos(2\Omega_{a(b)}\tau)] \tag{9.14}$$

[3] Since the observable is a linear combination of the density matrix elements the frequency components of $\Delta(\tau)$ are found in the Fourier transformation of $\Delta\sigma(t)$. In this framework τ indicates the length of the pulse.

with a Rabi frequency of the two almost resonantly excited spins which is twice the single-particle Rabi-frequency. This can be seen as a beat oscillation of the two simultaneously excited spin states and is usually called a *Rabi beat-oscillation* [169].

Besides these two extreme cases there in no known analytic expression of $\Delta(\tau)$ in the case of the remaining regime of intermediate light-field coupling. In addition to the work of Rajevac et al. ([184]), where the Liouville equation (9.1) was solved without the stochastic contribution[4], in the following chapter the first calculations of this intermediate case are shown.

[4] And without the Redfield operator $\mathcal{R}$ which is skipped in this work as well.

10

Results in absence of disorder

10.1 Recombination through pairs without exchange coupling

In this section the results of the calculations of the change of the photoconductivity $\Delta\sigma(t)$ for a system of localized identical spin pairs in semiconductors during coherent spin excitation are shown. The accompanying set of Bloch equations given in appendix F was solved numerically using a standard Runge-Kutta algorithm.

In all calculations we use $J = 0$ and $D^d = 0$. For the illustration of all calculated results, shown in this work, the units of the intensity are arbitrary.[1] The relevant information contained in the calculated transients $\Delta(\tau)$ which appear in the observable $\Delta\sigma(t)$ are the frequencies as well as the amplitudes of the transitions (nutation components). Thus, from the solutions of $\Delta\sigma(t)$ the Fourier transform (FT) was calculated in order to analyze the various frequencies contained therein.[2]

Figure 10.1 displays $\Omega = \mathrm{FT}(\Delta\sigma(t))$ versus ω (the frequency of the B_1 field) obtained by the solution of Eqn. 9.1 for spin pairs with four different Larmor separations ($\frac{\Delta\omega}{2\pi} = 1\,\mathrm{MHz},\ 5\,\mathrm{MHz},\ 20\,\mathrm{MHz},\ 40\,\mathrm{MHz}$) for microwave excitation frequencies of $9.95\,\mathrm{GHz} \leq \nu = \frac{\omega}{2\pi} \leq 10.05\,\mathrm{GHz}$ with a given $\mathbf{B_1}$

[1] Since the chosen absolute values of the scale are defined with respect to the maximum intensity of a data set which often lies in the data offset (not shown) originating in numerical artifacts, a comparison of the given intensities of the signals between different figures will often be misleading.

[2] The time scale for the time domain simulation and, therefore, the Fourier integration was chosen to be 5μs long.

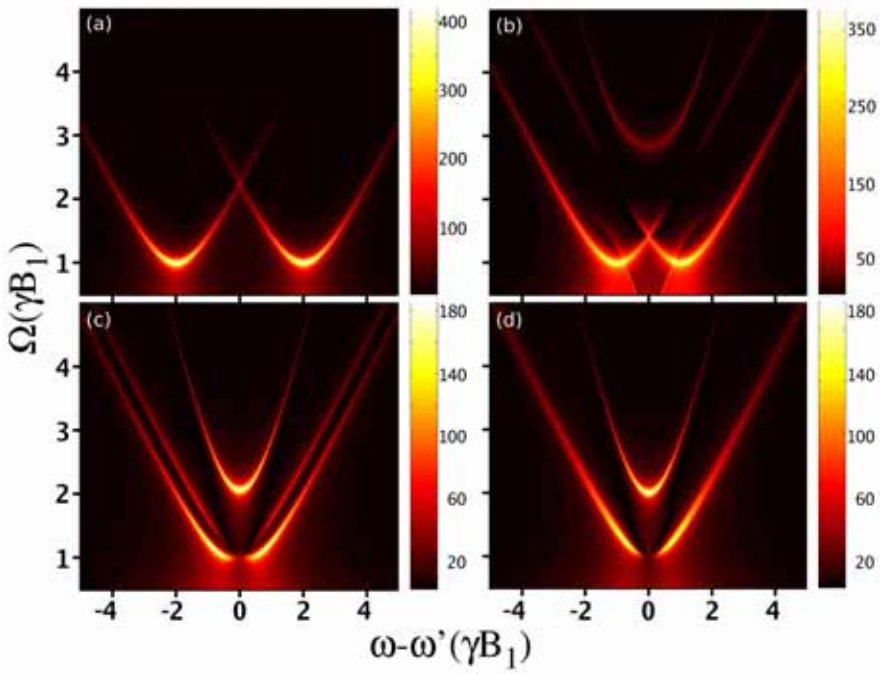

Fig. 10.1. Three-dimensional color plot of the calculated $\Omega = \mathrm{FT}(\Delta\sigma(t))$ as a function of the excitation frequency ω scaled in units of γB_1 as the difference between ω and the average of the Larmor frequencies of the two pair partners $\omega' = \frac{1}{2}(\omega_a + \omega_b)$ and the Rabi frequency Ω in units of γB_1. For all plots $\frac{\gamma}{2\pi}B_1 = 10$ MHz and $\frac{\omega'}{2\pi} = 10$ GHz. The Larmor-frequency separation of the pair partners decreases from (a) to (d): (a) 40 MHz, (b) 20 Mhz, (c) 5 MHz and (d) 1 MHz.

field-strength of $\frac{\gamma B_1}{2\pi} = 10$ MHz.[3] It should be noted that the scaling of the color code was normalized for all figures to the maximum for each graph in order to achieve sufficient contrast. While the plots (a) and (d) fulfill the

[3] It should be noted that in this work the magnetic fields $\mathbf{B}_0$ and $\mathbf{B}_1$ are considered to be linearly polarized. As long as the absolute value of the magnetic field-strength is transformed out, as it is done here by use of the unit γB_1, the distinction between different definitions of a magnetic field becomes unimportant. The situation changes when comparing the absolute values of the Rabi frequency depending on the strength of variously defined magnetic fields $\mathbf{B}_1$ (e.g. comparing [180] and [184]). A diagram of how to transform the field strength between the different frames is given in G.

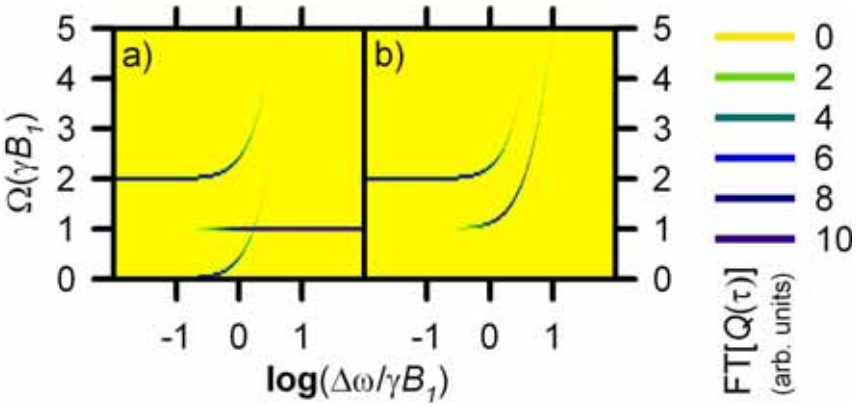

Fig. 10.2. Color plot of the Rabi-frequency components $\Omega = \mathrm{FT}(\Delta\sigma(t))$ as function of $\log(\frac{\Delta\omega}{\gamma B_1})$ for an excitation frequency (a) $\omega = \omega_{a,b}$ on resonance with one of the pair partners and (b) $\omega = \omega'$ on resonance with the average ω' of the pair partners Larmor frequencies.[184] Note that the results are obtained for calculations neglecting $\mathcal{S}$ in Eqn. 9.1.

extreme cases of small and large Larmor separation, respectively, the plots (b) and (c) describe two intermediate cases with $\gamma B_1 \approx \Delta\omega$.

The four different scenarios displayed in Fig. 10.1 confirm the hyperbolic increase of the Rabi frequency $\Omega = \sqrt{(\gamma B_1)^2 + (\omega - \omega_{a,b})^2}$ as the microwave frequency is shifted out of resonance. For the two extreme cases $\Omega = \gamma B_1$ for large Larmor separation and $\Omega = 2\gamma B_1$ for small Larmor separation the results shown in Fig. 10.1(a) and (d) show only one frequency component, which confirms the analytical results of Ref. [180]. Outside of the resonances ($\omega \neq \omega_{a,b}$), the oscillation splits into two components for the extreme cases and in the general intermediate cases, there are up to four different nutation frequencies visible as known from [184]. The main result is that the calculations justify the approach of Rajevac et al. where incoherence was not taken into account. By comparison with their results it becomes clear, that under the assumption of realistic recombination rate-coefficients the influence of $\mathcal{S}$ is negligible in a first approximation.

Thus the essential point in [184] remains valid: In the simulations of the spin-Rabi oscillation the doubling of the dominant frequency component from $\Omega = \gamma B_1$ to $\Omega = 2\gamma B_1$ appears 'abruptly' with increasing strength of the $\mathbf{B}_1$ field. A visualization of this behavior is shown in Fig. 10.2. This signature at $\Omega = 2\gamma B_1$ does not increase continuously out of the $S_{\frac{1}{2}}$ resonance. It evolves at higher Rabi frequencies and converges with increasing strength of the light-field coupling down to its minimum value $\Omega = 2\gamma B_1$.

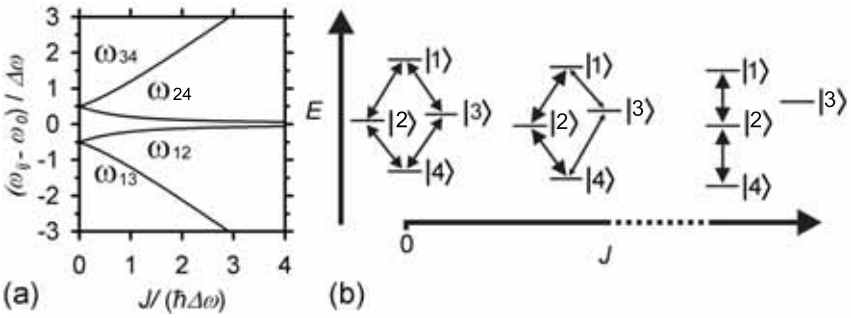

Fig. 10.3. (a) Plot of the ESR allowed transition frequencies $\omega_{ij} = \frac{1}{\hbar}(E_i - E_j)$ with $(ij) \in \{12, 13, 24, 34\}$ as function of J. Transitions indicated by ω_{13} and ω_{34} involve the state $|3\rangle$ with high projection on the singlet state for large values of J. For the plot, Larmor frequencies of $\omega_{a,b} = 10 \pm 0.01$GHz have been assumed. (b) Schematic illustration of the transition probabilities between the four states depending on the strength of J. The probability of transitions involving $|3\rangle$ (indicated by the thickness of the arrows) decreases with increasing J. Note that the position of the energy levels of the four states is not true to scale.

10.2 Recombination through exchange-coupled pairs

In the following a numerical study of transport and recombination through localized exchange coupled identical spin pairs during coherent excitation is presented. One purpose is to elucidate differences between transient nutation experiments on exchange-coupled radical pairs detected by pESR in contrast to the detection by pEDMR. In particular we focus on when the observed spin pairs can be approximated as two one-particle systems or show the full characteristics of a two-particle system. This has turned out to be one of the key differences for pESR- and pEDMR- detected transient nutation of weakly coupled spin pairs. Another question that is discussed is whether magnetic resonance induced triplet–singlet transitions, which become increasingly forbidden with increasing exchange coupling (see Fig. 10.3(b)), will reduce the observed signal intensities. It shall be pointed out here that the focus of this study deals solely with electronic transitions, based on spin–selection rules, between paramagnetic states in weakly spin–orbital coupled systems. Besides the applicability of the model on IPs, formed by a singly charged dangling bond and an electron localized in its vicinity, typical examples would be charge carrier pairs in semiconductors such as electron–hole or polaron pairs [185], defect pairs such as donor–acceptor pairs [186, 187] or radical pairs [188] in molecular systems or solid state host environments [189].

In summary the key problem that should be resolved by the calculations is the following: What are the features of the studied quantity $\Omega = \mathrm{FT}(\Delta\sigma(t))$

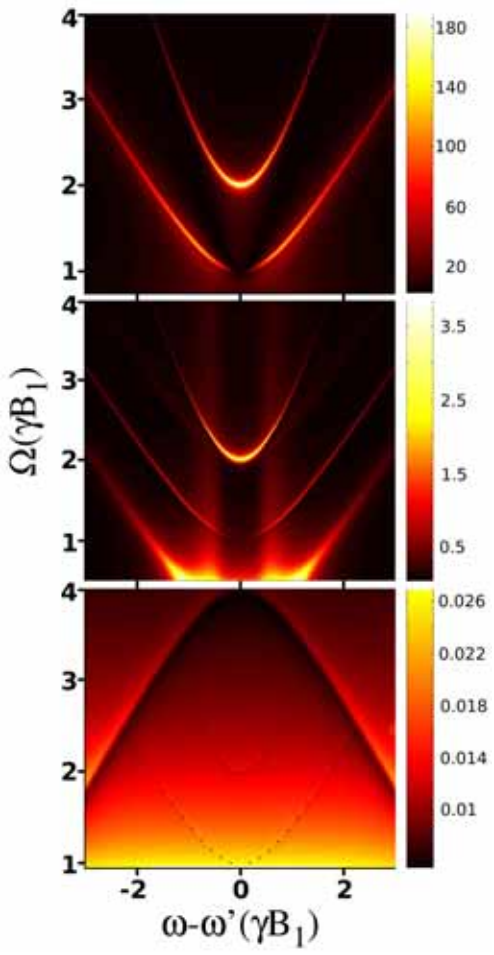

Fig. 10.4. Three-dimensional color plot of the calculated $\Omega = \mathrm{FT}(\Delta\sigma(t))$ as a function of the excitation frequency ω scaled in units of γB_1 as the difference between ω and the average of the Larmor frequencies of the two pair partners $\omega' = \frac{1}{2}(\omega_a + \omega_b)$ and the Rabi frequency Ω in units of γB_1. For all plots $\frac{\gamma}{2\pi}B_1 = 10\,\mathrm{MHz}$ and $\frac{\omega'}{2\pi} = 10\,\mathrm{GHz}$. Shown here for strong light-field coupling with $\frac{\Delta\omega}{2\pi} = 1\,\mathrm{MHz}$, for medium and small light-field coupling see Fig. 10.5. For proper illustration the barely visible resonances in (c) are marked with black dots. The strength of the J-coupling used in the calculations increases from top to bottom: $\frac{1}{2\pi}J = 1\,\mathrm{MHz}$ (a), 10 MHz (b), 50 MHz (c).

that are affected by changing the coupling strength J in spin pairs responsible for carrier recombination and how do these features depend on the strength of the light field B_1 ? Furthermore, it should become clear whether one could distinguish experimentally between the cases of strong and weak exchange coupling[4] between the pair partners at different microwave fields.

The theoretical model we use here has been described in detail in chapter 9. The time-independent Hamiltonian $\mathcal{H}_0$ including part I and II as given by Eqn. 9.3 has the eigenvalues

[4] 'Weak' and 'strong' are defined in comparison with $\Delta\omega$.

$$E_{1,4}(J) = -\frac{1}{4}J \pm \frac{1}{2}\hbar\omega_0, \qquad (10.1)$$
$$E_{2,3}(J) = \frac{1}{4}J \mp \frac{1}{2}\sqrt{J^2 + \hbar^2 \Delta\omega^2}$$

where $\omega_{a,b}$ are the Larmor frequencies of the pair partners while $\omega_0 = \omega_a + \omega_b$ and $\Delta\omega = \omega_a - \omega_b$ are the sum and the difference of the Larmor frequencies within the pair. As expected for a two-particle system the energy eigenvalues represent a four–level system and, as long as only single-photon processes are concerned, there are four allowed transitions as is well known from conventional ESR spectroscopy. Fig. 10.3(a) shows the transition frequencies of all four transitions as a function of the exchange coupling strength J. One can see that with increasing exchange, the $|1\rangle \leftrightsquigarrow |2\rangle$ and the $|2\rangle \leftrightsquigarrow |4\rangle$ transitions (which are the transitions between the triplet states) will gradually reach the same transition-frequency $\frac{\omega_0}{2}$. The transition frequencies of the two transitions involving the mixed state $|3\rangle$, which has high singlet content for increasing exchange coupling, will develop almost proportionally with J. In the case of strong exchange coupling ($J \gg \Delta\omega$), the transition strength into state $|3\rangle$ (State $|3\rangle$ shows an increasing projection on the singlet state with an increase of J.) will decrease and vanish entirely for infinite strength of J. This dependence of the transition strength on the exchange coupling constant J is schematically shown in Fig. 10.3(b)[5]. The results of the simulations of $\Omega = \mathrm{FT}(\Delta\sigma(t))$ versus excitation frequency ω for various exchange-coupling strengths are shown in Fig. 10.4 for a system with strong light-field coupling and in 10.5 for the medium and weak light-field coupling regimes.

We start our discussion from the results of the calculation in the case of a weak light field B_1 shown in Fig. 10.5(d-f). The curves presented in (d) and (e) of this figure obtained for small and moderate exchange couplings J can be well understood using the resonant frequencies shown in Fig. 10.3(a). In particular, the resonant frequencies Ω belonging to the transitions between states involving singlet projections, (the transitions between states $|1\rangle$ and $|3\rangle$ and between states $|3\rangle$ and $|4\rangle$) shift away from the reference point and correspond to nutations with smaller Rabi frequencies with increasing J. The data shown in part (e) of this figure shows a new pronounced resonance at $\Omega \approx 2\gamma B_1$ which continually develops from resonances in parts (a) and (b). In the calculations shown in Fig. 10.1 as well as in Ref. [184] a very similar resonance was obtained at the very same Rabi frequency $\Omega = 2\gamma B_1$ for the case of strong light-field coupling and zero exchange coupling ($J = 0$). In the latter

[5] This is the reason why ESR spectroscopy of strongly coupled pairs is typically a triplet spectroscopy.

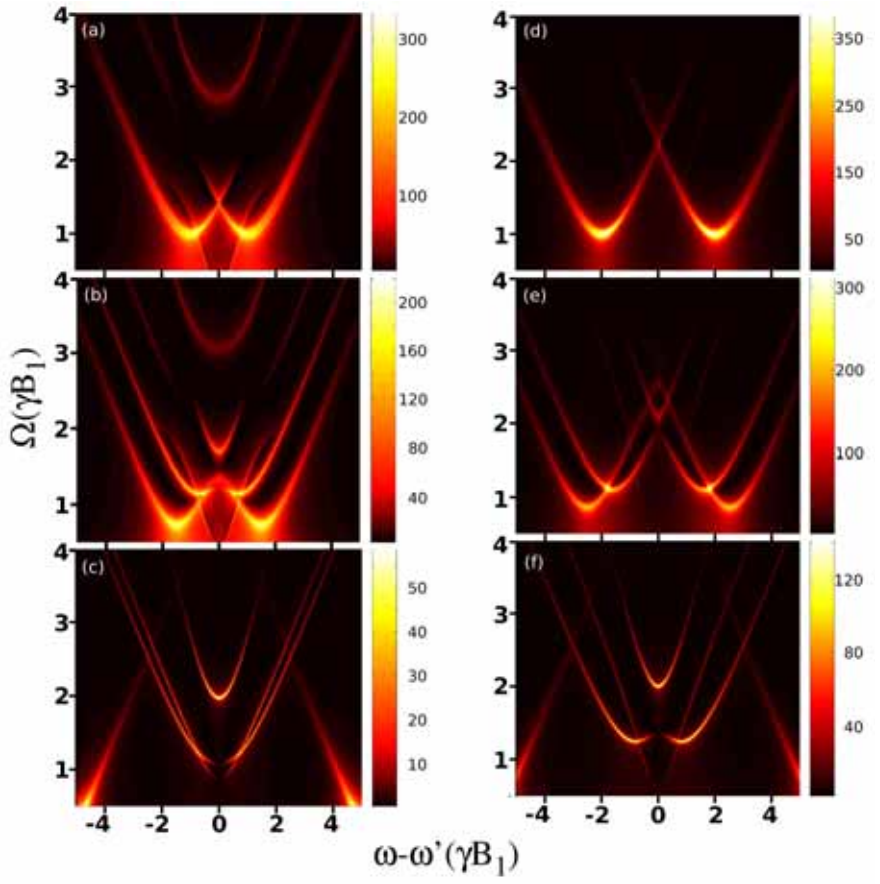

Fig. 10.5. Three-dimensional color plot of the calculated $\Omega = \mathrm{FT}(\Delta\sigma(t))$ as a function of the excitation frequency ω scaled in units of γB_1 as the difference between ω and the average of the Larmor frequencies of the two pair partners $\omega' = \frac{1}{2}(\omega_a + \omega_b)$ and the Rabi frequency Ω in units of γB_1. Data shown for intermediate light-field coupling $\frac{\Delta\omega}{2\pi}$=20 MHz (left) and weak light-field coupling $\frac{\Delta\omega}{2\pi}$=40 MHz (right). The strength of the J coupling used in the calculations increases from top to bottom: $\frac{1}{2\pi}J = 1$ MHz (a) and (d), 10 Mhz (b) and (e), 50 MHz (c) and (f). For remaining parameters see caption of Fig. 10.4.

case, however, this resonance arises 'abruptly'[6] with increasing B_1. In the case discussed here with finite exchange coupling between spin constituents of the

[6] 'abruptly' in the sense that it does not evolve out of the single particle $S_{\frac{1}{2}}$ resonances with increasing light-field coupling.

pair this resonance evolves continuously with increasing J out of resonances caused by transitions between the states $|1\rangle$ and $|3\rangle$ and states $|3\rangle$ and $|4\rangle$ shown in (e) and (f) of Fig. 10.5. In Ref.[184] as well as in section 10.1 the abruptly arising resonance at $\Omega = 2\gamma B_1$ was interpreted as Rabi oscillations of a spin-1 system, since the two spin-$\frac{1}{2}$ particles are excited simultaneously being coupled by the strong light field B_1. The resonance at $\Omega = 2\gamma B_1$ arising smoothly in Fig. 10.5 with increasing exchange coupling J has however a completely different nature as we show below. Therefore this resonance cannot be interpreted as formation of a spin-1 system.

Let us consider the results obtained for the calculation of $\Omega = \mathrm{FT}(\Delta\sigma(t))$ versus excitation frequency ω in the medium light-field coupling regime shown in Fig. 10.5(a-c). Besides the splitting of one transition frequency into two separate transition-frequency signals due to the J-coupling (discussed already with respect to Fig. 10.5(d-f)), one can recognize in part (a) of Fig. 10.5 a weak resonance at higher Rabi frequency $\Omega \approx 3\gamma B_1$. This corresponds to the two spin-$\frac{1}{2}$ particles coupled into an effective spin-1 system due to the coupling of spins by the microwave field [184]. Following the development of the observable $(\mathrm{FT}(\Delta\sigma(t)))$ in Fig. 10.5 (b) with increasing J the intensity of this resonance decreases and is not visible anymore. Nevertheless this is a problem of the choice of depiction. Out of the calculated data it can be concluded that the resonance shifts towards higher Rabi frequencies with increase of J. Instead a new resonance clearly seen at $\Omega = 2\gamma B_1$ in part (c) of Fig. 10.5 evolves gradually with increasing J similar to the case shown in parts (e)−(f). Therefore this resonance cannot be interpreted as belonging to a spin-1 system created by coupling of the pair partners due to the light field B_1. Instead this resonance is caused by the strong spin-exchange coupling. In the case of the strongest J coupling shown in parts (c) and (f) additional prominent resonances appear at very low Ω whose minimum Rabi frequency is reached at increasing $\mid \omega - \omega' \mid$ with increasing light-field coupling. This rather unexpected high intensity of resonances involving transitions with participation of $|3\rangle$ (since $|3\rangle$ is the state with high projection on the singlet state for large values of J, the signals of transitions involving $|3\rangle$ are referred to in the following as 'singlet' signatures (resonances)) becomes most intensive in the case of a strong light field shown in Fig. 10.4. In this case the previously discussed signal at $\Omega = 2\gamma B_1$ is barely visible due to its weak intensity in comparison with the 'singlet' signatures. So far these 'forbidden' transitions including $|3\rangle$ have been considered (at least in the ESR literature) as negligible. While the curves in part (a) of Fig. 10.4 coincide with the results obtained for non-interacting pair partners given in Fig. 10.1 and [184], the increase of the exchange interaction between the spins in the pair creates pronounced resonances with very high intensity at very low Rabi frequencies as shown in

part (b) and (c) of Fig. 10.4 and shift with increasing J far apart. The intensity becomes so strong that the depicted frequency range had to be reduced in order to avoid the maximum intensity of these signatures to keep the other comparatively weak resonances visible. These dominant 'singlet' resonances arise solely due to the exchange interaction. Looking at Fig. 10.3 one can recognize that such behavior is to be expected for transitions with frequencies ω_{13} and ω_{34} involving state $|3\rangle$. Therefore we conclude that state $|3\rangle$ which has a large projection on the singlet state (in comparison with the projection on the singlet state of state $|2\rangle$.) plays an essential role in the regime of strong spin coupling via the light field and via exchange interactions. This pronounced role of states with considerable singlet projection in the coherent dynamics of spin pairs was unexpected. With rising exchange-coupling constant J the states $|2\rangle$ and $|3\rangle$ evolve from the mixed states with equal singlet and triplet contents into almost pure singlet and triplet states, respectively. Matrix elements involving transitions to/from state $|3\rangle$ almost vanish with rising J as the interaction Hamilton operator fully accounts for the spin selection-rules. However the huge recombination rate of the singlet state r_s as compared to the recombination rate of the triplet state r_t makes the contribution of transitions involving $|3\rangle$ into the observable ($\mathrm{FT}(\Delta\sigma(t))$) given by Eqn. 8.12 essential. In other words: The contribution of 'forbidden' transitions involving the state with the large singlet projection (for sufficient values of J) arises due to the fact that we consider those spin pairs which strongly affect the transport and recombination processes. A second major result of this study is almost covered by the effects discussed so far. Under experimental conditions the systems of strong light-field coupled pairs without exchange interaction (Fig. 10.1(c)) and systems with strong exchange interaction (Fig. 10.4(c)) are almost indistinguishable. The strong intensity differences between both cases are not present when performing such experiments on a material sample. As soon as the experiment is not performed such that one can assure that resonances related with transitions incorporating 'singlet' states can be detected, the two different regimes stay indistinguishable.

11

Influence of disorder

11.1 Introduction

The rich structure of the simulation results, as it has been shown in section 10.1 as well as in [184] is mostly invisible in the experimental results as e.g. Fig. 11.1. The prominent peak in the case of a system with strong light-field coupling, is the spin-1 contribution S_1, while the $S_{\frac{1}{2}}$ resonance is barely visible. In Fig. 10.1(d) the branches of the $S_{\frac{1}{2}}$ contributions in the simulations of one system without exchange coupling are clearly of the same intensity as the S_1 peak shows at $\omega = \frac{\omega_0}{2}$. The introduction of exchange coupling does not resolve this disagreement between the simulations and the experimental data (see Fig. 10.4). In the following a rather simple extension of the previously introduced theoretical model on ensembles of unequal intermediate pairs is presented. It is shown that by taking disorder into account, namely a distribution of pair-partner g-factors, the deviation between theoretical and experimental results can be remedied. Following to this a qualitative interpretation of the g-factor disorder is given which may allow us to obtain further insights into the material properties. In this framework a detailed model study of the influence of differently distributed pair-partner g-factors on the observable is presented.

11.2 Ensembles of unequal pairs − the regime of strong light-field coupling

The spin dependent recombination process which was simulated in the previous chapter is supposed to happen only within intermediate pairs, formed, for example, by a dangling-bond electron and a conduction band electron weakly

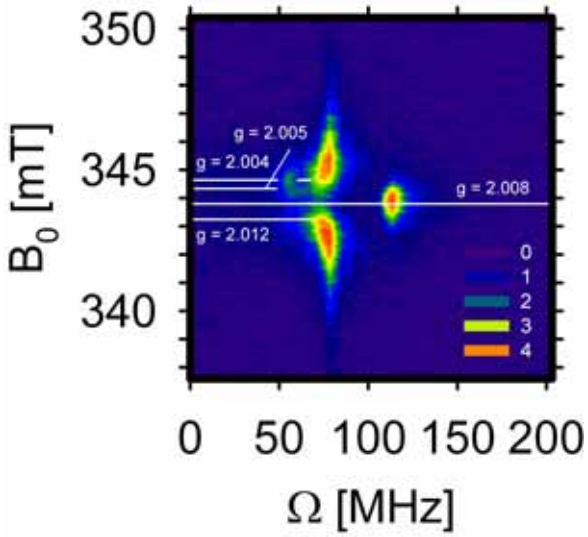

Fig. 11.1. An example for experimental data obtained by pODMR on a-Si:H. The signal at $\Omega \approx 2\gamma B_1 \approx 60\,\mathrm{MHz}$ is indicative for strongly (light-field) coupled systems, the signal at $\Omega \approx 40\,\mathrm{MHz}$ has a different origin and is not discussed here. For a detailed description and remaining parameters see [190].

localized in its vicinity. The model is in principle applicable to intermediate pairs built out of other pair partners which are not discussed here. Since the pair partners are considered to have characteristic local properties on a microscopic scale, resulting in specific internal magnetic fields, the effective magnetic field for both partners differs and has characteristic values for each of them. This difference of the effective magnetic field can be represented by use of two different characteristic average g-factors, $\bar{g_a}$ and $\bar{g_b}$ e.g. for the weakly localized electron and for the dangling-bond electron, respectively. All local modifications of the external magnetic field due to the interaction with the magnetic moments present in characteristic environment in the sample (e.g. the magnetic moments of the atomic nuclei) are coded into these effective parameters. For an ensemble of identical recombination centers[1] the g-factor distribution is shown in Fig.11.2(a). Nevertheless one can claim that the recombination centers are not all identical since deviations from a perfect crystal structure can never be avoided. Due to the fact that the local environment for both pair partners change within the crystal, both pair partner g-factors will reflect this change of local environment and will fluctuate around their mean values. On the basis of the assumptions made (in comparison with the microscopic g-factor change discussed above) this fluctuation of the effective magnetic field on a mesoscopic length-scale is described by a Gaussian distribution for both pair-partner electrons. The probability of a certain g_a (g_b) is

[1] As taken into account in the calculations presented so far.

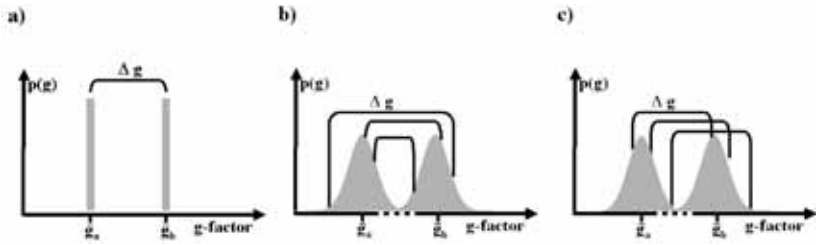

Fig. 11.2. The graphs show the probability-density distribution of the intermediate-pair partners g-factors (g_a and g_b) for different correlations between the pairs. In case a) the g-factors g_a and g_b of each IP are distributed δ-like at their corresponding mean values $\bar{g_a}$ and $\bar{g_b}$. Due to this the ensemble of intermediate pairs consists of equal ones. The g-factor difference Δg of the pair partners of an intermediate pair is constant for all pairs. In b) and c) the distributions of the g-factors are given by Gaussian distributions around $\bar{g_a}$ and $\bar{g_b}$ with a standard deviation δ. In b) Δg varies and the ensemble consists of pairs with all possible combinations of values of g_a and g_b. This results in an ensemble of intermediate pairs, whose pair partner g-factors are not correlated. In c) Δg is constant with $\Delta g = \bar{g_b} - \bar{g_a}$, and the ensemble consists of pairs with all combinations of values of g_a and g_b fulfilling the condition for Δg. This results in an ensemble of intermediate pairs, whose pair partner g-factors are correlated. Note that in this depiction the ratio of $\frac{\delta}{\Delta g}$ is strongly decreased in comparison with the values used for the calculations in order to provide a proper illustration of both types of g-factor distributions.

given by

$$p(g_{a(b)}) = \frac{1}{\sqrt{2\pi\delta}} e^{-\frac{(g_{a(b)} - \bar{g}_{a(b)})^2}{2\delta^2}}. \tag{11.1}$$

For simplicity the standard deviation δ is assumed to be the same for the distributions of g_a and g_b.

We take into account an ensemble of M non-interacting intermediate pairs whose members are numbered by the index i. Each pair is characterized by its two g-factors g_a^i and g_b^i. This corresponds to the Larmor frequencies $\omega_a^i = \frac{1}{\hbar} g_a^i \mu_B B_0$ and $\omega_b^i = \frac{1}{\hbar} g_b^i \mu_B B_0$ with $\omega_0^i = \omega_a^i + \omega_b^i$ and $\Delta\omega^i = \omega_a^i - \omega_b^i$

With the Hamilton operator given in Eqn. 9.7 and with use of $J = 0$ and $D^d = 0$ one gets the energy levels

$$E_1^i = \frac{1}{2}\hbar\omega_0^i,$$
$$E_2^i = -\frac{1}{2}\hbar\Delta\omega^i,$$
$$E_3^i = \frac{1}{2}\hbar\Delta\omega^i,$$
$$E_4^i = -\frac{1}{2}\hbar\omega_0^i.$$

The fluctuation of the local magnetic field[2] represented by the g-factor distributions given in Eqn. 11.1 is supposed to take place on a characteristic length-scale L_B as illustrated in Fig. 11.3(b). This length-scale depends on the specific properties of the sample material[3]. In the case that the localization radius L of the two-particle system (consisting of the electron on the dangling bond and its pair partner localized around it) as shown in Fig. 11.3(a), for example, is large compared to L_B one has to consider that the values of the local magnetic fields felt by the pair partners will not be correlated. Due to this, the non-correlated g-factor distribution shown in Fig. 11.2(b) is the correct way to model such a scenario. For the members of the ensemble of intermediate pairs all combinations of g_a and g_b are possible and thus such a distribution of g-factors is referred in the following as *non-correlated*. In this case the difference between the pair partners' g-factors Δg will not be constant for all members of the ensemble of IPs.

In the opposite case, when the localization radius L of the two-particle system is small compared to L_B, the value of the local magnetic field, felt by the pair partners, can be considered to be almost equal. This results in a so-called *correlated* distribution of g-factors. For example a pair state whose g_a is below its mean value g_b will be below its mean value and vice versa. According to this the g-factor difference Δg within each pair is the same for all members of the ensemble of intermediate pairs (see Fig. 11.2).

Remarks on the length-scale of an IP

So far the value of L was treated as a free, but almost constant, value. The question arises whether it has to be considered distributed, and if so, whether a distribution involving all possible length-scales L_i will have a crucial influence

[2] Local magnetic field means, in this context, the position-dependent magnetic field resulting from the interactions of the external magnetic field with the entire system of magnetic moments of the atomic cores in the material.

[3] It should be noted that we consider only an isotropic material in this simple model.

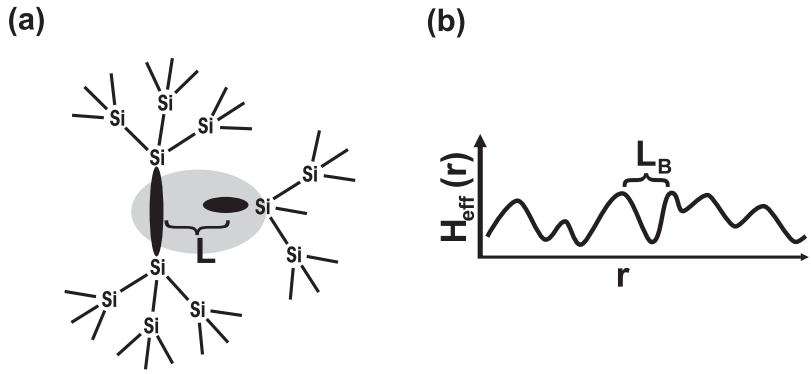

Fig. 11.3. (a) Illustration of the length-scale L of an intermediate pair with the example of an IP formed by a dangling-bond electron and an electron weakly localized in its vicinity, (b) Illustration of the fluctuation of the strength of the inner (effective) magnetic field $\mathbf{H}_{\text{eff}}$ on a characteristic lenght scale L_B.

on the results. Such a case describes an ensemble of IPs where all combinations of the ratio between L_i and L_B and between $L_i \ll L_B$ and $L_i \gg L_B$ have to be considered and the assumption of an either totally correlated or totally non-correlated g-factor distribution is not valid anymore. At this point one has to place emphasis on the KSM model which justifies the assumption taken previously. The recombination can only take place out of an IP. Not all possible combinations of a conduction-band electron and a singly charged dangling bond with, for example, the corresponding spatial separation of the length L_i can be considered as an IP, since the formation of an IP is equivalent to a spatial localization of the electron in the vicinity of the impurity. Thus recombination will only take place as combinations of, for example, a conduction-band electron and a singly charged dangling bond if their spatial separation L_I is smaller than a certain maximum value $L_M = L$. This length-scale L can be seen as the natural upper boundary of the localization length of an IP. So if $L_B \gg L$ (the correlated case) the system is modelled correctly by use of this upper bond L as $L_i \leq L \ll L_B$ and all members of the ensemble are correlated. On the other hand if $L_B \ll L$ (the non-correlated case) the real system will not consist of non-correlated pairs only, since with $L_i \leq L$ the amount of pairs with smaller localization length fulfill the condition $L_B > L_i \leq L$ and are thus correlated. Their effect is neglected when simulating the non-correlated ensemble.

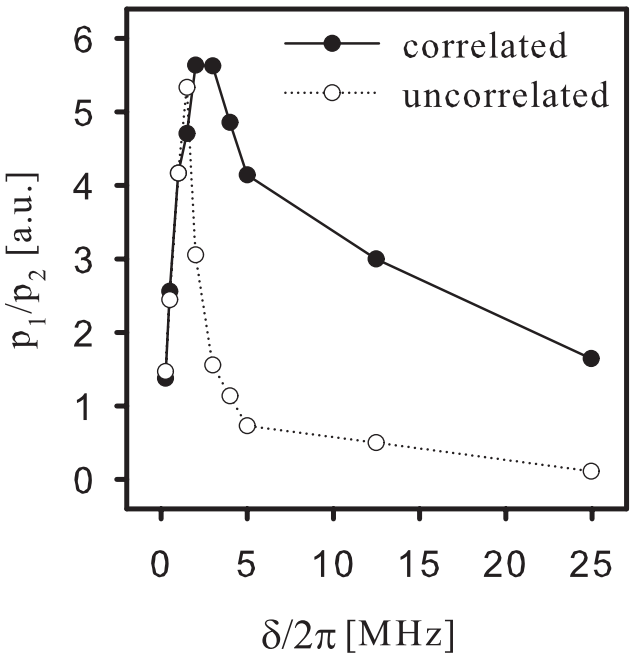

Fig. 11.4. Ratios between the intensity of the calculated $\Omega = \mathrm{FT}(\Delta\sigma(t))$ as a function of the excitation frequency ω at $\Omega = 2\gamma B_1$ (the $S = 1$ signature), p_1 and the maximum value of the intensity of the $S = \frac{1}{2}$ component p_2 against the standard deviation δ of the g-factor distribution for correlated and non-correlated distributions of 81 intermediate pairs. For parameters see text.

11.2.1 Discussion of the results

In the following the mobility of holes and electrons are assumed to be equal ($\mu_e = \mu_h$) for simplicity. Furthermore, in all simulations, including the stochastic contribution, it holds for the dissociation-rate coefficient $\frac{d}{ns} = 10^{-6}$, the triplet recombination-rate coefficient $\frac{r_T}{ns} = 10^{-5}$ and the singlet recombination-rate coefficient $\frac{r_S}{ns} = 10^{-3}$.

In Fig. 11.4 the ratio between the $\Omega = 2\gamma B_1$ amplitude and the largest amplitude of the $\Omega = 1\gamma B_1$ frequency component from the FT of $\Delta\sigma(t)$ is plotted against the standard deviation δ of the g-factor distribution for the correlated and the non-correlated case. The parameters are: $\frac{\gamma B_1}{2\pi} = 10\,\mathrm{MHz}$, $M = 81$, $\Delta\omega = 0.2\,\mathrm{MHz}$. The influence of the stochastic part in Eqn. 9.1 was neglected here. Since for very small δ the ratios are almost equal, the ratio for the non-correlated distribution breaks down with increasing δ and is even smaller than 1 for standard deviations larger than $\frac{\delta}{2\pi} = 5\,\mathrm{MHz}$. For the correlated case the ratio decreases with increasing δ after a maximum slightly below 5 MHz, but even for large standard deviations as 25 MHz the $\Omega = 2\gamma B_1$ signal is twice as large as the $\Omega = 1\gamma B_1$ signal.

In Fig. 11.5 two 3-d plots[4] of the calculated FT($\Delta\sigma(t)$) are shown[5]. The plots are shown in this manner to illustrate the peak ratio between the $S_{\frac{1}{2}}$ and the S_1 resonance. The calculations were performed for an ensemble of $M = 81$ IPs, for a correlated g-factor distribution and a standard deviation $\frac{\delta}{2\pi} = 3$ MHz, corresponding to the maximum ratio between the S_1 and the $S_{\frac{1}{2}}$ according to Fig. 11.4. In (a) the observable was calculated by solving the Liouville equation via use of the Hamilton operator given in Eqn. 9.1 without a stochastic term. In (b) it is calculated including the stochastic term representing incoherent processes such as recombination, dissociation and generation of pairs as covered by Eqn. 9.1. Both calculations show a dominant S_1 contribution at a Rabi frequency of $\Omega = 2\gamma B_1$ as obtained by the experimental results. The differences between these results is rather small. The stochastic term causes only a slight broadening of the 'U'-structure which is centered at $(0,\gamma B_1)$ in the $(\omega - \omega', \Omega)$-sphere. This is the plane relates increase of the Rabi frequency to increase of detuning in the two non-interacting $S_{\frac{1}{2}}$ systems.

The strong deviation of those results which depend on ones choice of g-factor distribution can be explained geometrically. For example the prominent dot-like signal of the S_1-resonance, appearing under the assumption of a correlated g-factor distribution, evolves due to the overlapping centers of the U structures while the arms of the Us don't sum up. A detailed discussion of this explanation is given in Sect. H.

A dulcet note

This simple geometric description reflects the information contained in the Fourier transformed signals due to simple additions of single-pair results. Interactions between the different pairs are not taken into account in the calculations. Signal interference effects of a single system in the time domain must lead to the Fourier transformed plots, considered here, and do not contain other information.

[4] Due to the symmetry of the 3-d plots (and thus without loss of information) the results shown in this section display only a cutout of the (Ω, ω)-sphere shown. Fig. 10.4 is a good example of this.

[5] The calculation was made with 1000 steps per nanosecond in a time range of 6 micro seconds

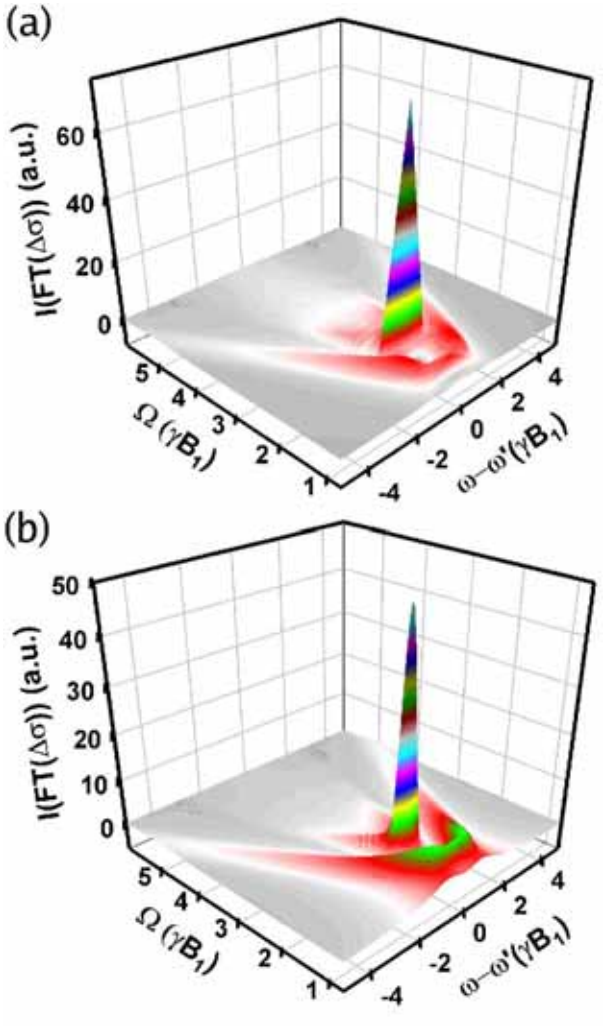

Fig. 11.5. Three-dimensional color plot shows the intensity I of the calculated FT($(\Delta\sigma(t))$ as a function of the excitation frequency ω, scaled in units of γB_1 as the difference between ω and the average of the Larmor frequencies of the two pair partners $\omega' = \frac{1}{2}(\omega_a + \omega_b)$, and the Rabi frequency Ω in units of γB_1 for a system of 81 intermediate pairs with a correlated g-factor distribution ($\frac{\delta}{2\pi} = 3\,\mathrm{MHz}$). The used parameters are $\frac{\gamma}{2\pi}B_1 = 10\,\mathrm{MHz}$, $\frac{\omega_0}{2\pi} = 10\,\mathrm{GHz}$, and $\frac{\Delta\omega}{2\pi} = 0.2\,\mathrm{MHz}$. In (a) Eqn. 9.1 was solved without the stochastic part $\mathcal{S}$, in (b) the dissociation rate-coefficient $\frac{d}{\mathrm{ns}} = 10^{-6}$, the triplet recombination rate-coefficient $\frac{r_t}{\mathrm{ns}} = 10^{-5}$, the singlet recombination rate-coefficient $\frac{r_s}{\mathrm{ns}} = 10^{-3}$ and the pair generation-rate $\frac{G}{\mathrm{ns}} = 2.1\ 10^{-4}$ were used. For this parameter set the influence of $\mathcal{S}$ is weak as the graphs show marginal differences.

11.3 Ensembles of unequal pairs — the regime of weak light-field coupling

After analyzing the influence that a g-factor distribution has on the FT($\Delta\sigma(t)$) of a collection of intermediate pairs in the strong light-field coupling regime we

now discuss the influence of such a distribution on a collection in the regime of weak light-field coupling. Therein we use the parameters given in [184] $\frac{w_a}{2\pi}$= 9.98 GHz, $\frac{w_b}{2\pi} = 10.02$ GHz, $\frac{\Delta\omega}{2\pi} = 40$ MHz and $\frac{\gamma B_1}{2\pi}$= 10 MHz.

11.3.1 Influence of system size

The introduction of g-factor disorder in the (Ω, ω)-sphere is assumed to lead the U-like structures of the $S_{\frac{1}{2}}$ resonance to vanish and point-like signatures to develop. This can be predicted for the strong light-field coupling regime since the mechanism applied to explain the change in the S_1 signature induced by the disorder, which is given above, remains applicable. The two different distributions of the pair partner g-factors are modelled as in the previous section. On initial inspection the choice of g-factor distribution, either a correlated or an non-correlated distribution should play no role in the regimes of weak light-field coupling, since the strength of the $\mathbf{B}_1$ field is so weak, that both pair partners get excited independently of each other. In other words the calculated Rabi-frequency signal of the pair partner whose resonance (Larmor-) frequency is, for example, $\frac{w_a}{2\pi} = (10.02 + \delta)$ GHz (where δ is the standard deviation of g-factor distribution) will not change if the corresponding resonance (Larmor)-frequency w_b of its pair partner is located at $\frac{w_b}{2\pi} = (9.98 + \delta)$ GHz (as is assumed of a correlated g-factor distribution). Neither will it change if it is located at a random position within the interval $[w_b - 2\delta, w_b + 2\delta]$.

The large deviations between the calculated $\Omega = \mathrm{FT}(\Delta\sigma(t))$ as a function of ω for a correlated and a non-correlated ensemble with 9 times 9 intermediate pairs each, can be found by a comparison of Fig. 11.6(a) and Fig. 11.7(b). These deviations result in the fact, that for a correlated g-factor distribution the 81 different resonance signatures of one of the pair partners with e.g. index b are distributed over the interval $[w_b - 2\delta, w_b + 2\delta]$ in the (Ω, ω)-sphere. In the case of the non-correlated distribution only 9 different resonances are distributed over the same interval. In this situation the total sum of 81 ensemble members results out of all combinations between the 9 resonances given for ω_a with all 9 resonances given for ω_b as discussed in more detail in Appendix H. Thus the pair partner (Larmor)-frequency resonances of a correlated g-factor distribution are almost continuously distributed while for a non-correlated g-factor distribution they are discretely distributed. In other words, the differences between the calculated results for ensembles of correlated and non-correlated g-factor distributions for a system with weak light-field coupling arise solely due to the special choice of modelling the different distributions. Fig. 11.6 bears this point out where $\Omega = \mathrm{FT}(\Delta\sigma(t))$ as a function of the excitation frequency ω is shown for different distributions and numbers of ensemble members but for the same density of resonances. In (a)

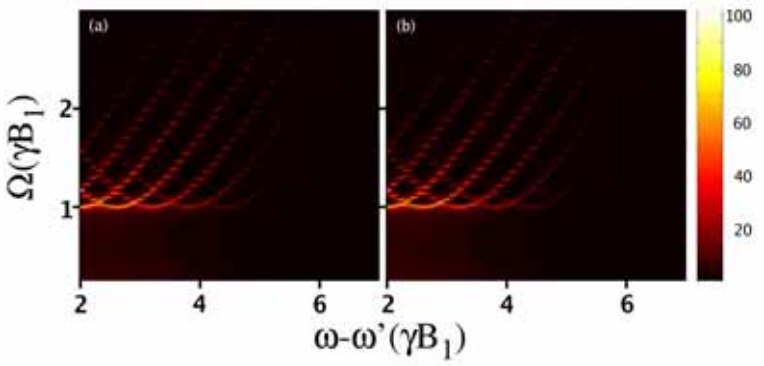

Fig. 11.6. Three-dimensional color plot of the calculated $\Omega = \mathrm{FT}(\Delta\sigma(t))$ as a function of the excitation frequency ω. It is scaled in units of γB_1 as the difference between ω and the two pair partners $\omega' = \frac{1}{2}(\omega_a + \omega_b)$ average Larmor frequencies and the Rabi frequency Ω in units of γB_1. (a) for a system of $9 \cdot 9$ IPs with a non-correlated g-factor distribution, (b) for a system of $3 \cdot 3$ IPs with a correlated g-factor distribution. The two results for the weakly light-field coupled systems displayed in (a) and (b) are identical. The standard deviation is $\frac{\delta}{2\pi} = 12\,\mathrm{MHz}$. Other parameters are used as for the calculation shown in Fig. 10.1(a).

$\Omega = \mathrm{FT}(\Delta\sigma(t))$ as a function of ω is shown for a system of $9 \cdot 9$ IPs with an non-correlated distribution, while in (b) $\Omega = \mathrm{FT}(\Delta\sigma(t))$ as a function of ω is shown for a system of $3 \cdot 3$ IPs with a correlated distribution; all further parameters are identical. As expected the plots shown in Fig. 11.6(a) and (b) are equal.

As one can clearly see in Fig. 11.6(b) at very low densities of different (single-particle) resonance signatures the resonance of each single system becomes visible and the resulting plot is the same as in Fig. 11.6(a) in the case of the non-correlated system with $9 \cdot 9$ members. Herewith it has been shown that due to the special choice of the model parameters the ensemble size used to calculate a system of weakly coupled spin pairs with a non-correlated g-factor distribution has to be significantly larger than that used for the corresponding system with a correlated g-factor distribution. Therefore we come to the conclusion that in the regime of weak light-field coupling, a system with a non-correlated g-factor distribution and a system with a correlated g-factor distribution are indistinguishable and show equal results.

Fig. 11.7 shows the calculation of $\Omega = \mathrm{FT}(\Delta\sigma(t))$ versus excitation frequency ω for a system of $9 \cdot 9$ IPs with weak light-field coupling for three different standard deviations (a) $\frac{\delta}{2\pi} = 5\,\mathrm{MHz}$, (b) $\frac{\delta}{2\pi} = 12\,\mathrm{MHz}$ and (c) $\frac{\delta}{2\pi} = 25\,\mathrm{MHz}$. It is obvious by comparison of the three graphs that the width

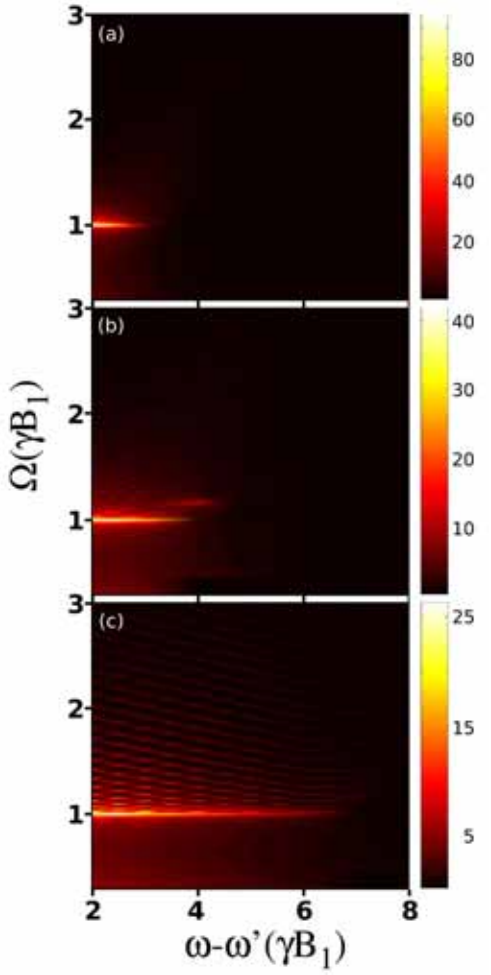

Fig. 11.7. Three-dimensional color plot of the calculated $\Omega = \mathrm{FT}(\Delta\sigma(t))$ as a function of the excitation frequency ω scaled in units of γB_1 as the difference between ω and the average of the Larmor frequencies of the two pair partners $\omega' = \frac{1}{2}(\omega_a + \omega_b)$ and the Rabi frequency Ω in units of γB_1 for a system of 81 intermediate pairs with a correlated g-factor distribution. The standard deviation of the distribution ranges from $\frac{\delta}{2\pi} = 5\,\mathrm{MHz}$ in (a), over $\frac{\delta}{2\pi} = 12\,\mathrm{MHz}$ in (b) to $\frac{\delta}{2\pi} = 25\,\mathrm{MHz}$ in (c). As used for the calculation in Fig. 10.1(a) $\frac{\gamma}{2\pi}B_1 = 10$ MHz, $\frac{\omega'}{2\pi} = 10\,\mathrm{GHz}$ and the Larmor-frequency separation of the pair partners is 40 MHz.

of the $S_{\frac{1}{2}}$ resonance gets broadened with increasing δ. Fig. 11.8 shows the intensity of the calculated Rabi frequency at $\frac{\Omega}{2\pi} = \frac{\gamma B_1}{2\pi} = 0.01\,\mathrm{GHz}$ versus the excitation frequency ω for three ensembles of 81 pairs with different standard deviations $\frac{\delta}{2\pi} = 5\,\mathrm{MHz}$, 12 MHz and 25 MHz.

The small oscillation visible in the depicted data belonging to the ensemble with the largest value of δ results in the fact that for large standard deviations the separation of different pair partner's g-factors becomes so large, that signatures of single intermediate-pair partners become visible. Such oscillations vanish with increasing number of ensemble members and therefore represent

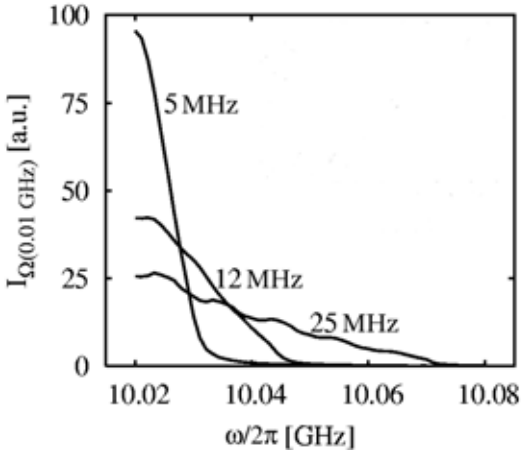

Fig. 11.8. Intensity I of the calculated $\Omega = \mathrm{FT}(\Delta\sigma(t))$ at $\frac{\Omega}{2\pi} = 0.01\,\mathrm{GHz}$ versus excitation frequency ω for ensembles with 9x9 correlated intermediate pairs, distributed with three different standard deviations δ as indicated in the figure. For remaining parameters see caption of Fig. 11.6.

no general restrictions of the model. It can be concluded apparently that based on the discussed model the magnitude of disorder of the g-factor distribution (represented by the value of δ in our calculations), should be indicated by the width of the measured spin-$\frac{1}{2}$ resonances in the regime of weak light-field coupling.

In summary taking into account disorder via the introduction of an ensemble of pairs with distributed g-factors for a weak light-field coupled regime, leads to vanishing "U"-like structures in the 3-d plots of Ω versus ω and appearance of "dot"-like structures. This effect is similar to the case of strong light-field coupling. The width of a resonance in the ω-sphere scales with the size of δ. On the basis of the given model, the extraction of this width in the ω-sphere out of experimental data may allow a conclusion about the g-factor disorder in the system to be made.

12

Conclusion of part II

12.1 Conclusion

In summary, the response of charge-carrier transport and recombination rates through localized electronic states in semiconductors to a coherent manipulation by magnetic resonance were simulated as they would be expected in pEDMR/pODMR experiments on, for example, μc-Si:H. The transient response was calculated with the spin excitation present for different excitation fields and frequencies as well as different Larmor separations within the pairs. Firstly it was assumed that exchange and dipolar interaction were weak. Incoherence due to the electronic transitions or spin-relaxation was taken into account. The results were obtained by the numerical solution of the stochastic Liouville equation. The results show that four qualitatively distinguishable nutation processes influence the oscillation of the transition rates which reduce to one significant contribution in the cases of large and small Larmor separations. The presence of the four oscillation processes implies that changing the Larmor separation or the applied excitation field leads to an 'abrupt' and non-continuous change of the observed signal frequencies.

In the second part we have studied the effect of the exchange interaction. The study was carried out for different coupling strengths between the intermediate pair and the microwave field. At weak and moderate spin couplings induced by the light field a new resonance has been found in the photoconductivity response. This resonance is clearly distinguished from the one arising in the absence of the exchange interaction. At strong light-field coupling the contribution of singlet states plays an essential role even at strong exchange coupling. Such contributions were not discussed so far. Furthermore it is shown that only if signals of transitions incorporating singlet states can be detected experimentally a distinction between the following two scenarios of

strong light-field coupled pairs is possible:(a) Strong exchange coupling and (b) Weak exchange coupling.
The results of the last chapter eliminate the crucial discrepancy between all existing theoretical predictions and the experimental data. Disorder in terms of a distribution of the pair partners g-factors is responsible for the primarily reproduction of essential measured characteristics. By a comparison between experimental and theoretical results other distributions, except one with correlated pair partner g-factors, can be excluded. The length-scale of the g-factor disorder can be obtained by a comparison between simulation and experimental results. This hopefully provides new insight into the characteristics of the recombining pairs in the future. In addition the assumption of pair-partner g-factor distributions of different width provides a promising interpretation of 'non-symmetric' (in the Ω-ω-plane) experimental results which remain unexplained so far.
The influence of the simulated disorder related effects can be understood on the basis of the given model by simple geometrical considerations applied on the Fourier transformed results.

A

The network model

The starting point of the resistor network model is a system of K^2 cubes of same size l^3 which are arranged as a quadratic slice of single-cube thickness. The resistivity (resistance respectively) of each cube is known and may depend e.g. on temperature or magnetic field. The resistivity can differ from cell to cell depending on the nature of the underlying material. Fig. 1.4 depicts an arrangement of cubes with different resistivity serving as the basis of the network model. Each cube is connected with its neighbor cubes, only connections between side surfaces are allowed. The inner cubes are connected with four other cubes each and cubes at the surface of the system are connected with just two other neighbors. The number of cubes which are connected with an inner cube is called the coordination number. A network which is built up in the described way is said to be fourfold coordinated. In the used fourfold coordinated network for each cube exists only one possible connection with a neighbor cube which allows a current in the direction of the main current. This value changes if the coordination number of the network is changed.
Independently from the coordination number the network needs to be able to describe the trivial system of cubes of the same type, resulting in a total resistivity which is the same as that of each of the cubes. This characterization of a minimal condition for a transport network is naturally fulfilled in the case of the present model.
The network is built out of knots and paths. The knots are centered in the cubes and the paths represent the resistors between them.[1] The current between two knots k_i and k_j passes half the cube i and half the cube j. Therefore the resistance $R_{(i,j)}$ representing the path between the knots i and j is given as

[1] For simplicity and without any general restriction we use resistors instead of resistivity here.

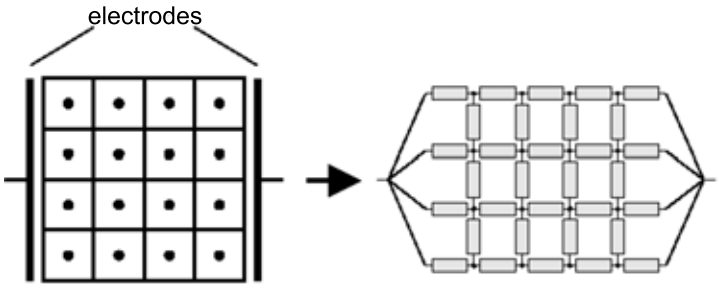

Fig. A.1. Model of a 2-dimensional network with coordination number 4 consisting of 16 cubes and the corresponding 16 + 2 knots. Left side shows the sample of cubes right side the corresponding resistor network.

$$R_{i,j} = \frac{1}{2}\left(R_i + R_j\right) \tag{A.1}$$

where R_i and R_j are the resistors of the cubes i and j which have to be known. With the knowledge of the resistors given by each cube and the application of Kirchhoff's laws (in our case the knot law) as well as Ohm's law the total resistor given by such a network of resistors can be derived.

Every knot is unable to store carriers. Hence the sum of current passing into a knot and out of it has to be zero

$$\sum_{l=1}^{4} I_i^l = 0, \tag{A.2}$$

I_i^l represent the four currents flowing from knot i into the four neighbor knots or flowing into knot i. By use of Eqn. A.2 the Kirchhoff knot-law is described for a fourfold coordinate network. Furthermore the connection between the voltage and the current between two knots is required. This is provided by Ohm's law which is formulated for each pair of cubes k_n and k_m

$$U_{(n,m)} = R_{(n,m)} \cdot I_{(n,m)} \tag{A.3}$$

with voltages $U_{(n,m)}$ and the the resistance and current between knots n and m $R_{(n,m)}$ and $I_{(n,m)}$. The network that is required for the description of the system formed by K^2 cubes consists of one knot centered in each cube and two additional knots representing the two electrodes. Fig. A.1 displays a two dimensional system of $4 \cdot 4$ cubes with both electrodes and the corresponding resistor network built out of $16 + 2$ resistors.

A possible treatment to solve such a system of equations is the so-called knot analysis [195, 196]. First of all every knot k_i gets allocated a potential

ϕ_i. After the potential of one of the K^2+2 knots is fixed as a reference value (a simple calibration of the potential capacity) K^2+1 knot potentials are left to be defined.
For each of the K^2+2 knots the Kirchohoff knot-law is written as

$$\sum_{\substack{i=0\\ i\neq j}}^{K^2+1} (\phi_j - \phi_i) G_{(ij)} = i_j \tag{A.4}$$

where i_j is the current induced extraneously into knot j and $G_{(ij)}$ denotes the reciprocal resistance of the path between the knots i and j. For the taken assumptions for all knots which are not connected directly by a path it holds that $G_{(ij)} = 0$. By rewriting Eqn. A.4 one gets

$$\phi_j \sum_{\substack{i=0\\ i\neq j}}^{K^2+1} G_{(ij)} - \sum_{\substack{i=0\\ i\neq j}}^{K^2+1} \phi_i G_{(ij)} = i_j. \tag{A.5}$$

The sum over all four reciprocal resistances connected with a knot j gets written as $G_{(jj)}$ and Eqn A.5 becomes

$$\phi_j G_{(jj)} - \sum_{\substack{i=0\\ i\neq j}}^{K^2+1} \phi_i G_{(ij)} = i_j. \tag{A.6}$$

Such an equation can be set up for all knots and the resulting K^2+2 equations can be represented by a linear system of equations

$$\hat{A}\boldsymbol{\phi} = \mathbf{i} \tag{A.7}$$

where
i_j is the current induced extraneously into knot j for $1 \leq j \leq K^2+2$,
ϕ_i is the potential of the knot i for $1 \leq j \leq K^2+2$
and

$$A_{ij} = \begin{cases} 0 & : \ i \neq j \text{ and } k_i,k_j \text{ not connected directly} \\ \sum\limits_{\left(\text{for all } k \text{ neighboring } i\right)}^{k} G_{(kk)} & : \ \text{if } i = j \\ -G_{(ij)} & : \ \text{else.} \end{cases}$$

The resulting symmetric $(K^2+2)\cdot(K^2+2)$ matrix $\hat{A}$ with the entries A_{ij} is called the conductivity matrix. Since not the absolute values but only the potential differences are of interest, one potential ϕ_i can be chosen freely as a

Fig. A.2. Scheme of a network with $3 \cdot 3 + 2$ knots which is described by Eqn. A.8

calibration.[2] By use of this simple physical argument it is illustrated that the rank of this matrix is $K^2 + 1$. After this calibration the technical challenge is to find the subsystem of $K^2 + 1$ linear independent row- and column-vectors of $\hat{A}$ to gain an uniquely solvable set of equations. The solution of this set of equations is done numerically by use of the Bi-CGSTAB method [197]. An example of a network and the corresponding set of equations is given in Fig. A.2, where a network of $3 \cdot 3 + 2$ knots is shown, that is described by the linear equation system given in Eqn. A.8. In this equation it holds for all matrix entries that $A_{ij} \neq 0$ for matrix elements which are labelled by $+$. After the calibration $\phi_0 = 0$ the first row of the equation system was added to the last and by omitting the first row and column the equation set was reduced down to

$$\begin{pmatrix} + & + & 0 & + & 0 & 0 & 0 & 0 & 0 & 0 \\ + & + & + & 0 & + & 0 & 0 & 0 & 0 & 0 \\ 0 & + & + & 0 & 0 & + & 0 & 0 & 0 & 0 \\ + & 0 & 0 & + & + & 0 & + & 0 & 0 & 0 \\ 0 & + & 0 & + & + & + & 0 & + & 0 & 0 \\ 0 & 0 & + & 0 & + & + & 0 & 0 & + & 0 \\ 0 & 0 & 0 & + & 0 & 0 & + & + & 0 & + \\ 0 & 0 & 0 & 0 & + & 0 & + & + & + & 0 \\ 0 & 0 & 0 & 0 & 0 & + & 0 & + & + & 0 \\ + & + & + & 0 & 0 & 0 & + & 0 & 0 & + \end{pmatrix} \cdot \begin{pmatrix} \phi_1 \\ \phi_2 \\ \phi_3 \\ \phi_4 \\ \phi_5 \\ \phi_6 \\ \phi_7 \\ \phi_8 \\ \phi_9 \\ \phi_{10} \end{pmatrix} = \begin{pmatrix} 0 \\ 0 \\ 0 \\ 0 \\ 0 \\ 0 \\ 0 \\ 0 \\ 0 \\ + \end{pmatrix} . \tag{A.8}$$

[2] The solution space of dimension $K^2 + 1$ gets subtended with the 1-dimensional kernel, which makes the solution unique.

B

Dependence of the potential fluctuations on the choice of l

To assure a short motivation how the length-scale l of the network influences the amplitude of the (valence-band) subband fluctuations we consider a DMS with a density of lattice points d. The interaction with an external magnetic field may be described according to Eqn. 1.11. The valence-band edge E_V^{m,j_z} of a subband of a cell with index m is given by

$$E_V^{m,j_z} = E_0 - \frac{1}{3} N_0 \beta \cdot \delta x \cdot < S_z > j_z \tag{B.1}$$

where E_0 denotes the valence-band split related with the average Mn ion concentration $E_0 = E_V^{m,j_z}(x)$ and $\delta x = x_{loc} - x$ is the deviation of the local Mn concentration from the mean value. The deviation δE_V of E_V^{m,j_z} from the average value of the local valence-band edges is given by[1] $\delta E_V = E_V^m - E_0$. With the derivative $\frac{dE_V^{m,j_z}}{dx} = \Gamma$ it yields

$$\Gamma \cdot \delta x = \delta E_V . \tag{B.2}$$

A spatial normal distribution of the Mn ions over the cells of the network is assumed. Following Gaussian statistics this leads to the standard deviation of the local Mn concentration

$$\bar{\delta x} = \frac{\sqrt{x \cdot d \cdot l^3}}{d \cdot l^3}. \tag{B.3}$$

The average deviation of the shift of the valence-band edge from its mean value is given by

[1] For simplification and without loss of generality j_z is considered as fixed.

$$\delta\bar{E}_V = \Gamma \cdot \bar{\delta x} \tag{B.4}$$

$$= \Gamma \frac{\sqrt{x}}{\sqrt{d} \cdot l^{\frac{3}{2}}}. \tag{B.5}$$

Thus Eqn. B.5 provides the average deviation of the shift of the valence-band edge from its mean value. This characterizes the potential fluctuations and the disorder is scaled with the choice of l as

$$\delta\bar{E}_V \propto l^{\frac{3}{2}}. \tag{B.6}$$

This illustrates that the model parameter l influences the amount of disorder which is taken into account when modelling the sample.

C

The thermal average of S_z

The (normalized) thermal average $\frac{<S_z>}{S}$ of the spin component S_z of a particle with S = $\frac{5}{2}$ in the presence of an external magnetic field **H** = (0,0,H) oriented in the z-direction is given by

$$\frac{< S_z >}{S} = \frac{1}{S} \sum_i \rho(S_i) \cdot S_i \tag{C.1}$$

where the summation has to be performed over all possible values of S_i while $\rho(S_i)$ is the probability that the particle has the eigenvalue S_i of the operator $\mathcal{S}_z$. Eqn. C.1 can be rewritten as

$$\frac{< S_z >}{S} = \frac{1}{S} \sum_i \frac{1}{Z} e^{\left(-\frac{E_i}{k_B T}\right)} \cdot S_i \tag{C.2}$$

with $E_i = g' \mu_B \mu_0 H S_i$ as given by the Hamilton operator in Eqn. 1.8 and the canonical partition function

$$Z = \sum_i e^{\left(-\frac{E_i}{k_B T}\right)}. \tag{C.3}$$

By use of $y = \frac{g' \mu_B \mu_0 H S}{k_B T}$ the partition function Z can be rewritten as

$$\begin{aligned} Z &= \underbrace{e^{-\frac{y}{S}S} + e^{-\frac{y}{S}(S-1)} + ... + e^{\frac{y}{S}(S)}}_{2S+1} \\ &= e^{-\frac{y}{S}S} \frac{\left(1 - e^{\frac{y}{S}(2S+1)}\right)}{1 - e^{yS}} \\ &= \frac{\sinh\left(\frac{2S+1}{S} y\right)}{\sinh\left(\frac{y}{2S}\right)}. \end{aligned} \tag{C.4}$$

Now employing both Eqn. C.2 and Eqn. C.4 one gets

$$\begin{aligned}\frac{< S_z >}{S} &= \frac{d}{dy}\ln Z \\ &= \frac{2S+1}{2S}\coth\left(\frac{2S+1}{2S}y\right) - \frac{1}{2S}\coth\left(\frac{y}{2S}\right) \\ &= \mathrm{B}_f(y) \end{aligned} \tag{C.5}$$

where $\mathrm{B}_f(y)$ is called the Brillouin function.

D

Temperature dependence of the spontaneous magnetization – a simple molecular-field approach

An extension of the theory of paramagnetism basing on P. Weiß (1907) is the most simple description of ferromagnetic ordering below T_{C}. Only a short overview over the used equations is given here. For a detailed description see e.g. [198].

One starts with the assumption of an inner magnetic field[1] H_i, named molecular field, which has to be proportional to the magnetization. The origin of this field is not further discussed here. This inner magnetic field represented by $H_i = WM$, where W is the so-called molecular-field constant, is added to the external field H inside the Brillouin function

$$M = Ng\mu_{\mathrm{B}} J \mathrm{B}_f \left(\frac{g\mu_{\mathrm{B}} J \mu_0}{k_{\mathrm{B}} T} (H + WM) \right). \tag{D.1}$$

The saturation value of the magnetization $M_0 = Ng\mu_{\mathrm{B}} J$ is the maximum magnetization. The external magnetic field is set to zero and with $H = 0$ Eqn. D.1 becomes

$$\frac{M}{M_0} = \mathrm{B}_f \left(\frac{g\mu_{\mathrm{B}} J \mu_0 WM}{k_{\mathrm{B}} T} \right). \tag{D.2}$$

Rewriting the left side in terms of the argument $a = \frac{g\mu_{\mathrm{B}} J \mu_0 WM}{k_{\mathrm{B}} T}$ of the Brillouin function one gets

$$a \frac{k_{\mathrm{B}} T}{g\mu_{\mathrm{B}} J \mu_0 W M_0} = \mathrm{B}_f(a). \tag{D.3}$$

On the left side of Eqn. D.3 one finds a linear function whose slope depends on T. For small enough temperatures this linear function intersects the Brillouin

[1] We use the scalar values of the magnetic fields in this section instead of the vectors since the vector character is neglected when incorporating the Weißmolecular-field into our model.

function on the right side and thus for such a temperature the equation has a solution. With increasing temperatures the value of M belonging to the intersection point decreases until it vanishes at the Curie temperature T_C. For temperatures above T_C Eqn. D.3 has no solution and no magnetic ordering is present.

Expanding $\mathrm{B}_f(a)$ for small values of a leads to

$$\mathrm{B}_f(a) \approx \frac{J+1}{3J} a. \tag{D.4}$$

Equating the derivatives with respect to a of Eqn. D.3 and Eqn. D.4 leads to a representation of the molecular-field constant

$$W = \frac{T_\mathrm{C}}{N g^2 {\mu_\mathrm{B}}^2 \mu_0} \frac{3k_\mathrm{B}}{J(J+1)}. \tag{D.5}$$

Inserting W into Eqn. D.2 one ends up with an implicit equation of the magnetization M depending on $\frac{T_\mathrm{C}}{T}$ as an input parameter

$$\frac{M}{M_0} = \mathrm{B}_f \left(\frac{3M}{N g \mu_\mathrm{B} (J+1)} \frac{T_\mathrm{C}}{T} \right). \tag{D.6}$$

This equation can be solved numerically and thus the molecular field WM can be derived.

E

The product-basis representation of $\mathcal{H}_0$

Here we give a detailed derivation of the product-basis representation of the free Hamilton operator $\mathcal{H}_0$ as introduced in section 9.2.

Using the two spaces of the electrons with index a, $\mathcal{H}_a$ and with index b, $\mathcal{H}_b$, respectively, all two-particle operators act in the Hilbert space

$$\mathcal{H} = \mathcal{H}_a \otimes \mathcal{H}_b.$$

The spin operators $\mathcal{S}_a$ and $\mathcal{S}_b$ act on the particles a and b. We will use the abbreviations

$$\begin{aligned} \mathcal{S}_a &= \mathcal{S}'_a \otimes \mathcal{I}_b, \\ \mathcal{S}_b &= \mathcal{I}_a \otimes \mathcal{S}'_b \end{aligned}$$

where $\mathcal{I}_{a(b)}$ is the identity. In that spirit we can represent them as

$$\mathcal{S}_a = (S_a^x, S_a^y, S_a^z),$$

$$\mathcal{S}_b = (S_b^x S_b^y, S_b^z).$$

The normalized eigenbasis of $\mathcal{S}^2$ and $\mathcal{S}_z$ will be written as

$$\begin{aligned} |\uparrow\rangle &= (1,0), \\ |\downarrow\rangle &= (0,1). \end{aligned}$$

The single-particle Pauli matrices are given in this basis as

$$S_{a(b)}^{\hat{x}} = \frac{\hbar}{2}\begin{pmatrix} 0 & 1 \\ 1 & 0 \end{pmatrix}, \quad S_{a(b)}^{\hat{y}} = \frac{\hbar}{2}\begin{pmatrix} 0 & -i \\ i & 0 \end{pmatrix}, \quad S_{a(b)}^{\hat{z}} = \frac{\hbar}{2}\begin{pmatrix} 1 & 0 \\ 0 & -1 \end{pmatrix}.$$

In the following we will use

$$\begin{aligned} |\mu\nu\rangle &= |\mu\rangle \otimes |\nu\rangle \;\text{ with } \mu,\nu \in \{\uparrow,\downarrow\}\,, \\ \langle\mu\nu|\;\mu'\nu'\rangle &= \delta_{\mu\mu'}\delta_{\nu\nu'} \end{aligned} \tag{E.1}$$

to represent two-particle states and the orthogonality relation between the elements of the basis.

Using the conventions defined so far the spin operators given in Eqn. 9.3 act on the two-particle basis as

$$\mathcal{S}_{a(b)} \cdot \mathbf{B_0} = B_0 S^{\hat{z}}_{a(b)} = B_0 \frac{\hbar}{2} \begin{pmatrix} 1 & 0 \\ 0 & -1 \end{pmatrix},$$

$$\begin{aligned} \mathcal{S}_a \cdot \mathcal{S}_b \;&= \mathcal{S}^x_a \mathcal{S}^x_b + \mathcal{S}^y_a \mathcal{S}^y_b + \mathcal{S}^z_a \mathcal{S}^z_b \\ \Rightarrow \mathcal{S}_a \cdot \mathcal{S}_b \,|\uparrow\uparrow\rangle &= \frac{\hbar^2}{4}\,|\uparrow\uparrow\rangle\,, \\ \mathcal{S}_a \cdot \mathcal{S}_b \,|\uparrow\downarrow\rangle &= \frac{\hbar^2}{4}\,(2\,|\downarrow\uparrow\rangle - |\uparrow\downarrow\rangle)\,, \\ \mathcal{S}_a \cdot \mathcal{S}_b \,|\downarrow\uparrow\rangle &= \frac{\hbar^2}{4}\,(2\,|\uparrow\downarrow\rangle - |\downarrow\uparrow\rangle)\,, \\ \mathcal{S}_a \cdot \mathcal{S}_b \,|\downarrow\downarrow\rangle &= \frac{\hbar^2}{4}\,|\downarrow\downarrow\rangle\,, \end{aligned}$$

$$\begin{aligned} \mathcal{S}^z_a \mathcal{S}^z_b \,|\uparrow\uparrow\rangle &= \frac{\hbar^2}{4}\,|\uparrow\uparrow\rangle\,, \\ \mathcal{S}^z_a \mathcal{S}^z_b \,|\uparrow\downarrow\rangle &= -\frac{\hbar^2}{4}\,|\uparrow\downarrow\rangle\,, \\ \mathcal{S}^z_a \mathcal{S}^z_b \,|\downarrow\uparrow\rangle &= -\frac{\hbar^2}{4}\,|\downarrow\uparrow\rangle\,, \\ \mathcal{S}^z_a \mathcal{S}^z_b \,|\downarrow\downarrow\rangle &= \frac{\hbar^2}{4}\,|\downarrow\downarrow\rangle\,. \end{aligned}$$

With the definition of the product basis

$$\begin{aligned} |\uparrow\rangle_a \otimes |\uparrow\rangle_b &= |\uparrow\uparrow\rangle = |1\prime\rangle\,, \\ |\uparrow\rangle_a \otimes |\downarrow\rangle_b &= |\uparrow\downarrow\rangle = |2\prime\rangle\,, \\ |\downarrow\rangle_a \otimes |\uparrow\rangle_b &= |\downarrow\uparrow\rangle = |3\prime\rangle\,, \\ |\downarrow\rangle_a \otimes |\downarrow\rangle_b &= |\downarrow\downarrow\rangle = |4\prime\rangle \end{aligned} \tag{E.2}$$

and the abbreviations:

$$\begin{aligned}\omega_{a(b)} &= g_{a(b)}\mu_B B_0,\\ \omega_0 &= \omega_a + \omega_b, \qquad \text{(E.3)}\\ \Delta\omega &= \omega_a - \omega_b \qquad \text{(E.4)}\end{aligned}$$

the matrix elements of the time independent Hamilton operator $\mathcal{H}_0$ as given by Eqn. 9.3 can be calculated in the product-basis representation

$$\begin{aligned}\langle 1\prime|\,\hat{H}_0\,|1\prime\rangle &= \frac{\hbar}{2}\omega_0 - J\frac{1}{4} - D^d\frac{1}{2},\\ \langle 2\prime|\,\hat{H}_0\,|2\prime\rangle &= \frac{\hbar}{2}\Delta\omega + J\frac{1}{4} + D^d\frac{1}{2},\\ \langle 2\prime|\,\hat{H}_0\,|3\prime\rangle &= -J\frac{1}{2} + D^d\frac{1}{2},\\ \langle 3\prime|\,\hat{H}_0\,|2\prime\rangle &= -J\frac{\hbar^2}{2} + D^d\frac{1}{2},\\ \langle 3\prime|\,\hat{H}_0\,|3\prime\rangle &= -\frac{\hbar}{2}\Delta\omega + J\frac{1}{4} + D^d\frac{1}{2},\\ \langle 4\prime|\,\hat{H}_0\,|4\prime\rangle &= -\frac{\hbar}{2}\omega_0 - J\frac{1}{4} - D^d\frac{1}{2},\\ \text{rest} &= 0.\end{aligned}$$

Using the abbreviation $I = J\frac{1}{4} + D^d\frac{1}{2}$ the matrix representation of $\mathcal{H}_0$ in the product basis is given by:

$$\hat{H_0} = \begin{pmatrix} \frac{\hbar}{2}\omega_0 - I & 0 & 0 & 0\\ 0 & \frac{\hbar}{2}\Delta\omega + I & -J\frac{1}{2} + D^d\frac{1}{2} & 0\\ 0 & -J\frac{1}{2} + D^d\frac{1}{2} & -\frac{\hbar}{2}\Delta\omega + I & 0\\ 0 & 0 & 0 & -\frac{\hbar}{2}\omega_0 - I \end{pmatrix}. \qquad \text{(E.5)}$$

In the same way the time dependent part $\mathcal{H}_1$ of the Hamilton operator in Eqn. 9.2 describing the interaction with an external field gets rewritten. Starting from

$$\mathcal{H}_1 = \frac{g_a\mu_B}{\hbar}\mathcal{S}_a \cdot \mathbf{B_1} + \frac{g_b\mu_B}{\hbar}\mathcal{S}_b \cdot \mathbf{B_1} \qquad \text{(E.6)}$$

this leads to the expression

$$\begin{aligned}\mathcal{H}_1 &= \frac{g_a\mu_B}{\hbar}B_1\mathcal{S}_a^x + \frac{g_b\mu_B}{\hbar}B_1\mathcal{S}_b^x\\ &= \frac{g_a\mu_B}{\hbar}B_1\frac{\hbar}{2}\begin{pmatrix}0&1\\1&0\end{pmatrix}_a \otimes \mathcal{I}_b + \frac{g_b\mu_B}{\hbar}B_1\frac{\hbar}{2}\mathcal{I}_a \otimes \begin{pmatrix}0&1\\1&0\end{pmatrix}_b.\end{aligned}$$

This is used to calculate the non-vanishing matrix elements of the interaction Hamiltonian $\mathcal{H}_1$ in the product basis

$$\begin{aligned}
\langle 1\prime|\,\hat{H}_1\,|2\prime\rangle &= \frac{1}{2}g_a\mu_B B_1,\\
\langle 1\prime|\,\hat{H}_1\,|3\prime\rangle &= \frac{1}{2}g_b\mu_B B_1,\\
\langle 2\prime|\,\hat{H}_1\,|1\prime\rangle &= \frac{1}{2}g_a\mu_B B_1,\\
\langle 2\prime|\,\hat{H}_1\,|4\prime\rangle &= \frac{1}{2}g_b\mu_B B_1,\\
\langle 3\prime|\,\hat{H}_1\,|1\prime\rangle &= \frac{1}{2}g_b\mu_B B_1,\\
\langle 3\prime|\,\hat{H}_1\,|4\prime\rangle &= \frac{1}{2}g_a\mu_B B_1,\\
\langle 4\prime|\,\hat{H}_1\,|2\prime\rangle &= \frac{1}{2}g_b\mu_B B_1,\\
\langle 4\prime|\,\hat{H}_1\,|3\prime\rangle &= \frac{1}{2}g_a\mu_B B_1.
\end{aligned}$$

With the same definitions as used previously we come to the following matrix representation of the interaction Hamiltonian in the product basis:

$$\mathcal{H}_1(t) = \frac{1}{2}\mu_B B_1 cos(\omega t)\begin{pmatrix} 0 & g_a & g_b & 0\\ g_a & 0 & 0 & g_b\\ g_b & 0 & 0 & g_a\\ 0 & g_b & g_a & 0 \end{pmatrix}.$$

Here the time dependent magnetic field $\mathbf{B}_1(t) = (B_1 cos(\omega t), 0, 0)$ is introduced.

F

The Bloch equations

The calculation of the commutator $[\hat{\rho}, \hat{\mathcal{H}}]^-$ given in Eqn. 9.1, leads to the Bloch equations

$$\partial_t \rho_{11} = \frac{i}{\hbar}\frac{1}{2}\mu_B B_1 \cos\omega t\left((g_a A + g_b B)\rho_{12} + (g_a B + g_b D)\rho_{13} - (g_a A + g_b C)\rho_{21} - (g_a B + g_b D)\rho_{31}\right)$$

$$\partial_t \rho_{12} = i\omega_{21}\rho_{12} + \frac{i}{\hbar}\frac{1}{2}\mu_B B_1 \cos\omega t\left((g_a B + g_b A)\rho_{14} + (g_a A + g_b C)(\rho_{11} - \rho_{22}) - (g_a B + g_b D)\rho_{32}\right)$$

$$\partial_t \rho_{13} = i\omega_{31}\rho_{13} + \frac{i}{\hbar}\frac{1}{2}\mu_B B_1 \cos\omega t\left((g_a D + g_b B)\rho_{14} - (g_a A + g_b C)\rho_{23} + (g_a B + g_b D)(\rho_{11} - \rho_{33})\right)$$

$$\partial_t \rho_{14} = i\omega_{41}\rho_{14} + \frac{i}{\hbar}\frac{1}{2}\mu_B B_1 \cos\omega t\left((g_a C + g_b A)\rho_{12} + (g_a D + g_b B)\rho_{13} - (g_a A + g_b C)\rho_{24} - (g_a B + g_b D)\rho_{34}\right)$$

$$\partial_t \rho_{21} = i\omega_{12}\rho_{21} + \frac{i}{\hbar}\frac{1}{2}\mu_B B_1 \cos\omega t\left((g_a A + g_b B)(-\rho_{11} + \rho_{22}) + (g_a B + g_b D)\rho_{23} - (g_a C + g_b A)\rho_{41}\right)$$

$$\partial_t \rho_{22} = \frac{i}{\hbar}\frac{1}{2}\mu_B B_1 \cos\omega t\left((g_a A + g_b C)\rho_{21} - (g_a A + g_b B)\rho_{12} + (g_a B + g_b A)\rho_{24} - (g_a C + g_b A)\rho_{42}\right)$$

$$\partial_t \rho_{23} = i\omega_{32}\rho_{23} + \frac{i}{\hbar}\frac{1}{2}\mu_B B_1 \cos\omega t\left((g_a B + g_b D)\rho_{21} - (g_a A + g_b B)\rho_{13} + (g_a D + g_b B)\rho_{24} - (g_a C + g_b A)\rho_{43}\right)$$

$$\partial_t \rho_{24} = i\omega_{42}\rho_{24} + \frac{i}{\hbar}\frac{1}{2}\mu_B B_1 \cos\omega t\left((g_a D + g_b B)\rho_{23} - (g_a A + g_b B)\rho_{14} + (g_a C + g_b A)(\rho_{22} - \rho_{44})\right)$$

$$\partial_t \rho_{31} = i\omega_{13}\rho_{31} + \frac{i}{\hbar}\frac{1}{2}\mu_B B_1 \cos\omega t\left((g_a A + g_b B)\rho_{32} + (g_a B + g_b D)(-\rho_{11} + \rho_{33}) - (g_a D + g_b B)\rho_{41}\right)$$

$$\partial_t \rho_{32} = i\omega_{23}\rho_{32} + \frac{i}{\hbar}\frac{1}{2}\mu_B B_1 \cos\omega t\left((g_a A + g_b C)\rho_{31} - (g_a B + g_b D)\rho_{12} + (g_a B + g_b A)\rho_{34} - (g_a D + g_b B)\rho_{42}\right)$$

$$\partial_t \rho_{33} = \frac{i}{\hbar}\frac{1}{2}\mu_B B_1 \cos\omega t\left((g_a B + g_b D)\rho_{31} - (g_a B + g_b D)\rho_{13} + (g_a D + g_b B)\rho_{34} - (g_a D + g_b B)\rho_{43}\right)$$

$$\partial_t \rho_{34} = i\omega_{43}\rho_{34} + \frac{i}{\hbar}\frac{1}{2}\mu_B B_1 \cos\omega t\left((g_a C + g_b A)\rho_{32} - (g_a B + g_b D)\rho_{14} + (g_a D + g_b B)\rho_{33} - (g_a D + g_b B)\rho_{44}\right)$$

$$\partial_t \rho_{41} = i\omega_{14}\rho_{41} + \frac{i}{\hbar}\frac{1}{2}\mu_B B_1 \cos\omega t\left((g_a A + g_b B)\rho_{42} - (g_a B + g_b A)\rho_{21} - (g_a D + g_b B)\rho_{31} + (g_a B + g_b D)\rho_{43}\right)$$

$$\partial_t \rho_{42} = i\omega_{24}\rho_{42} + \frac{i}{\hbar}\frac{1}{2}\mu_B B_1 \cos\omega t\left((g_a A + g_b C)\rho_{41} - (g_a D + g_b B)\rho_{32} + (g_a B + g_b A)(\rho_{44} - \rho_{22})\right)$$

$$\partial_t \rho_{43} = i\omega_{34}\rho_{43} + \frac{i}{\hbar}\frac{1}{2}\mu_B B_1 \cos\omega t\left((g_a B + g_b D)\rho_{41} - (g_a B + g_b A)\rho_{23} + (g_a D + g_b B)(\rho_{44} - \rho_{33})\right)$$

$$\partial_t \rho_{44} = \frac{i}{\hbar}\frac{1}{2}\mu_B B_1 \cos\omega t\left((g_a C + g_b A)\rho_{42} - (g_a B + g_b A)\rho_{24} - (g_a D + g_b B)\rho_{34} + (g_a D + g_b B)\rho_{43}\right)$$

with $\omega_{ij} := \frac{h_{ii} - h_{jj}}{\hbar}$.

G

On the definition of the magnetic-field strength

A light field which is linearly polarized in the **x** direction, is given as

$$\mathbf{B_1} = (B_1 \cos(\omega t), 0, 0). \tag{G.1}$$

With this definition, the amplitude of the light field is B_1. It can be rewritten in a complex notation

$$(B_1 \cos(\omega t), 0, 0) = (B_1'(e^{i\omega t} + e^{-i\omega t}), 0, 0) \tag{G.2}$$

with the relation between the *new* amplitude B_1' and the *old* one

$$B_1 = 2B_1'.$$

A circularly polarized wave (in the $\mathbf{x}, \mathbf{y}$-plane) is given as

$$\mathbf{B}_1 = B_1(\cos\omega t, \sin\omega t, 0) \text{ anticlockwise}, \tag{G.3}$$
$$\mathbf{B}_1 = B_1(\cos\omega t, -\sin\omega t, 0) \text{ clockwise}. \tag{G.4}$$

A linear polarized wave can always be seen as the superposition of two circular polarized waves

$$(B_1 \cos(\omega t), 0, 0) = B_1''(\cos(\omega t), \sin(\omega t), 0) + B_1''(\cos(\omega t), -\sin(\omega t), 0) \tag{G.5}$$

with the relation

$$B_1 = 2B_1'' \tag{G.6}$$

between the amplitudes. Representing the linearly polarized wave in its complex representation (G.2) in terms of circularly polarized waves (G.5) leads to

$$\begin{aligned}(B_1\cos(\omega t),0,0) &= (B_1'(e^{i\omega t}+e^{-i\omega t}),0,0)\\ &= B_1'''((e^{i\omega t}+e^{-i\omega t}))((1,i,0)+(1,-i,0))\end{aligned}$$

with the relation

$$B_1 = 2B_1' = 4B_1'''$$

between the amplitudes The following scheme illustrates how to transform the field strength depending on the definition of the magnetic field:

$$\begin{array}{rcl} B_1\ complex & \longrightarrow & B_1' = \dfrac{B_1}{2} \\ circular\downarrow & & circular\downarrow \\ B_1'' = \dfrac{B_1}{2}\ complex & \longrightarrow & B_1''' = \dfrac{B_1}{4} \end{array}$$

In this work we use B_1.

H

Influence of the g-factor distribution of an ensemble of intermediate pairs

H.0.1 Open questions so far

In this chapter we show that the deviations between the calculated $\Omega = \mathrm{FT}(\Delta\sigma(t))$ versus excitation frequency ω for ensembles with different g-factor correlations (δ-like, correlated and non-correlated) can be understood using a rather simple geometrical model. As a fundament of further considerations we present briefly the essential points visualized in Figs. 11.4, 11.5 and H.2 which will directly lead to the questions given below: (a) In the case of a δ-like g-factor distribution, i.e. $\omega^i_{a(b)} = \text{constant}\ \forall i$, all pairs are identical with $\omega^i_a - \omega^i_b = \Delta\omega$. The results of the calculated $\Omega = \mathrm{FT}(\Delta\sigma(t))$ versus excitation frequency ω shown first in [184] are almost similar to the calculated results including the stochastic term as given by Fig. 11.5. (b) In the calculations of $\Omega = \mathrm{FT}(\Delta\sigma(t))$ versus excitation frequency ω of an ensemble with a correlated g-factor distribution (the Larmor separation $\Delta\omega^i = \Delta\omega = \text{constant}\ \forall i$) the S_1 contribution showing a sharp resonance at $\Omega = 2\gamma B_1$ is the dominant peak. Its U-like structure vanishes since the intensity of the U's arms drops rapidly with off-resonant excitation. (c) In the case of a non-correlated g-factor distribution the ratio between the intensity of the S_1 signal at $\Omega = 2\gamma B_1$ and the maximum $S_{\frac{1}{2}}$ signal becomes smaller compared to the result calculated by use of a correlated distribution (e.g. see Fig. 11.4).

While the main result shown in Figs. 11.5 and H.2 is clear, namely that due to the introduction of a correlated g-factor distribution, the experimental data e.g. shown in Fig. 11.1 can be reproduced. Two major questions for the reasons of this behavior arise:

- How can a correlated distribution of g-factors lead to a dominant S_1 resonance while a non-correlated distribution does not?

- Why do the 'arms' of the dominant S_1 resonance disappear stronger (see Fig. 11.5) as compared to a system with a δ-like distribution of g-factors (e.g. Fig. 10.1(d))?

The starting points for the answers of both questions are the following definitions serving as the basis of all further considerations: We take into account an ensemble G of non-interacting[1] intermediate pairs P_i. The Larmor frequencies of the pair partners are ω_a^i and ω_b^i. A detailed look at the modelling of the different distributions is required. The order of magnitude of the involved quantities and the special choice of the distributions play an important role for the interpretation of the results. The average values of the g-factors are $\bar{g}_{a(b)}$. For simplification the standard deviations $\delta_{a(b)}$ of both the Gaussian distribution of g_a^i and g_b^i are assumed to be equal: ($\delta_a = \delta_b = \delta$). The Larmor frequencies of the pair partners result directly out of the g-factors by: $\omega_{a(b)}^i = \frac{1}{\hbar} g_{a(b)}^i \mu_B B_0$.

Modelling a correlated g-factor distribution

The method, used here, for modelling an ensemble of n^2 intermediate pairs with correlated g-factors is as follows: Using $\bar{g}_a - \bar{g}_b = \Delta g$ the g-factor difference for all pairs is given (w.l.o.g. we assume here $\bar{g}_a < \bar{g}_b$). We take the interval $[\bar{g}_a - 2\delta, \quad \bar{g}_a + 2\delta]$ and distribute the g_a^i equally over it: $g_a^i = \bar{g}_a - 2\delta + i \cdot \frac{4\delta}{n^2} \ \forall i \in \left\{0, n^2 - 1\right\}$ The corresponding pair partners g-factor is given by: $g_b^i = g_a^i + \Delta g \ \forall i$. Using these definitions for all n^2 pairs the g-factor differences Δg^i and thus all Larmor-frequency separations $\Delta\omega^i$ are the same. For each one of these pairs, characterized by the tuple $\left(g_a^i, g_b^i\right)$, the observable $\Delta\sigma(t)$ is calculated, weighted with a Gaussian distribution $G(g_a^i)$ with mean value $\bar{g}_a$ and standard deviation δ and all signals are summed.

Modelling a non-correlated g-factor distribution

The method, used here, for modelling an ensemble of n^2 intermediate pairs with non-correlated g-factors is as follows: The intervals $\left[\bar{g}_{a(b)} - 2\delta, \quad \bar{g}_{a(b)} + 2\delta\right]$ are taken and at any one time the $g_{a(b)}^i$ are equally distributed over them: $g_{a(b)}^i = \bar{g}_{a(b)} - 2\delta + i \cdot \frac{4\delta}{n} \ \forall i \in \{0, n-1\}$. The resulting n^2 pairs are constructed out of all possible combinations of n g_a^i with n g_b^j ending up with tuples $\left(g_a^i, g_b^j\right)$ whose pair partner g-factor difference Δg^{ij} is not constant. This results in Larmor-frequency differences $\Delta\omega^{ij} \in [\Delta g - 4\delta, \quad 4\delta + \Delta g]$ for $\Delta g > 4\delta$ and $\Delta\omega^{ij} \in [0 \quad 4\delta + \Delta g]$ in the case that

[1] Non interacting means the intermediate pairs do not interact with each other.

$\Delta g \leq 2\delta$. For each one of these pairs characterized by the tuple $\left(g_a^i, g_b^j\right)$ the observable is calculated, weighted with $G_a(g_a^i) \cdot G_b(g_b^j)$ where $G_{a(b)}$ are Gaussian distributions with standard deviation δ around the mean value g_a and g_b respectively. After this had been done, the observables for each IP get summed and a Fourier transformation is taken. [2]

Influence of the g-factor correlation of an ensemble of IPs on the FT($\Delta\sigma(t)$)

First of all it should be mentioned that the calculated signal of the S_1 resonance is visible only for middle ($\Delta\omega/\gamma B_1 \approx 1$ and strong ($\Delta\omega \ll \gamma B_1$) light-field coupling as shown in Fig. 10.1 and [184] Fig. 3. We remind the reader that with decreasing value of $\frac{\Delta\omega}{\gamma B_1}$ the Rabi frequency Ω of the S_1 resonance reaches its minimum at $\Omega = 2\gamma B_1$. With increasing ratio $\frac{\Delta\omega}{\gamma B_1}$ the Rabi frequency shifts towards larger values with strongly decreasing intensity (see again Fig. 10.1 as well as [184] Fig. 3). The strong signal of the S_1 resonance at $2\gamma B_1$ in the case of a correlated g-factor distribution, shown in Fig. 11.5, can be understood since with $\gamma B_1 \gg \Delta\omega^i = \text{constant}\ \forall i$ all pairs are strongly coupled, have the same (minimum) Rabi frequency and are distributed almost 1-dimensionally in the (Ω, ω)-sphere parallel to the ω-axis with a high density of n^2 distinct resonances distributed over the interval $\left[\omega_a + \frac{\Delta\omega}{2} - 2\delta, \quad \omega_b - \frac{\Delta\omega}{2} + 2\delta\right]$. Therefore the average density[3] of resonances in the 1-dimensional ω-sphere is $\frac{n^2}{4\delta - \Delta\omega}$. Now we come to the crucial point whether the weaker signal of the S_1 resonance in the case of a non-correlated ensemble can be understood on the basis of the given assumptions. We give two major reasons:

- Since all possible combinations of ω_a^i and ω_b^i appear in the non-correlated ensemble, depending on the choice of parameters, not all pairs fulfill the condition for strong light-field coupling $\Delta\omega \ll \gamma B_1$. For the amount of pairs with weaker light-field coupling the Rabi frequency of the S_1 resonance shifts towards higher Ω values and looses intensity. The amount of pairs with increased strength of the light-field coupling due to a decrease of $\Delta\omega^i$ is not able to compensate for this, since the Rabi frequency converges

[2] For simplicity we do not take into account the g-factor differences and distributions for the definition of γ since they play a minor role and can be neglected in the description of the interaction Hamiltonian (see [169] page 14), nevertheless these g-factor differences were taken into account in the derivation of the interaction Hamilton operator.

[3] This is an average density, the density at intervals around ω' increases with reduction of the width of the interval since the Gaussian weighting of the single resonances is not taken into account in this estimation.

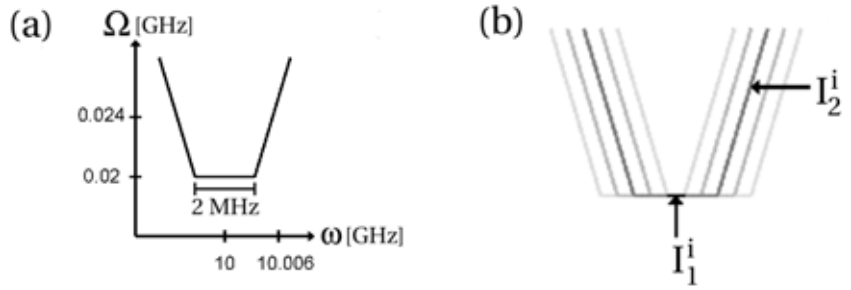

Fig. H.1. (a) shows the approximation of the calculated $\Omega = \mathrm{FT}(\Delta\sigma(t))$ versus excitation frequency ω for a pair in the strong light-field coupling regime with $\frac{2\gamma B_1}{2\pi} = 0.02\,\mathrm{GHz}$ and $\frac{\omega'}{2\pi} = 10\,\mathrm{GHz}$ due to a 'U'-like structure. In (b) the addition of different U-structured resonances in the Ω, ω-plane of pairs of a correlated ensemble is illustrated resulting in a strongly enhanced intensity I_1^i.

with increasing strength of the light-field coupling against $2\gamma B_1$. Taking this into account the center of the calculated U-shaped resonances in the (Ω, ω)-sphere are not only distributed over a one dimensional space (as in the correlated case) but over a 2-dimensional plain. Therefore the density of overlapping Us is reduced.

- Even the pairs with strong light-field coupling do not contribute to the S_1 signal as strongly as in the calculations for a correlated ensemble, since they are distributed over a wider range. Namely an interval of width 4δ.

As a short illustration may serve the following estimation using an non-correlated distribution and the parameters given in the caption of Fig. 11.5: The step-width s_i between ω_a^i for different i is $s_i = 4\delta n = \frac{12/2\pi\mathrm{MHz}}{9} = 1.33/2\pi\mathrm{MHz}$. This makes clear that in almost $\frac{8}{9}$ of all possible combinations of ω_a^i and ω_b^i the $\Delta\omega$ is more than 6 times larger than in the case of a correlated distribution.

The 'U'-shape of the calculated FT($\Delta\sigma(t)$) depending on ω.

To answer the second question one can again use a geometrical explanation. For simplicity we approximate the parabolic form of the S_1 resonance by a U-form (see Fig. H.1(a)). Also for simplicity we suppose a width of the bottom of $\frac{2}{2\pi}$ MHz. The point of intersection between the axis of symmetry and the bottom of the U will be called the *symmetry point* p_s. For one system this symmetry point is located at a microwave frequency $\frac{\omega}{2\pi} = \frac{\omega'}{2\pi} = 10\,\mathrm{GHz}$ and a Rabi frequency $\frac{\Omega}{2\pi} = \frac{2\gamma B_1}{2\pi} = 0.02\,\mathrm{GHz}$ (from now on we will note points by giving their coordinates (ω, Ω), i.e. p_s is located at $(10, 0.02)$). In

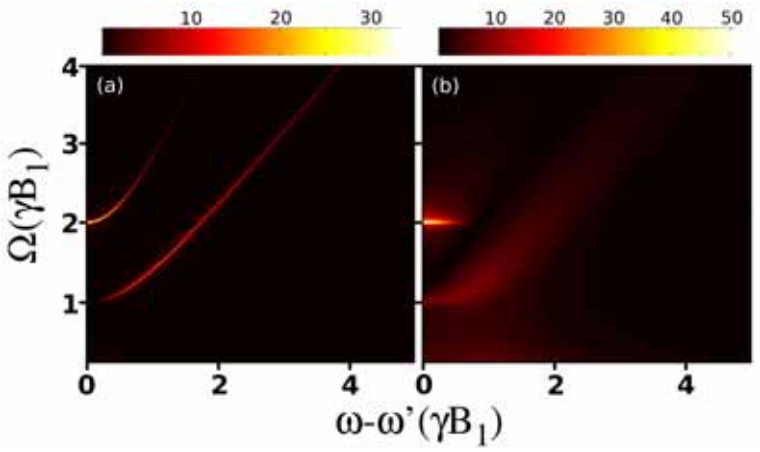

Fig. H.2. Three-dimensional color plot of the calculated $\Omega = \mathrm{FT}(\Delta\sigma(t))$as a function of the excitation frequency ω scaled in units of γB_1 as the difference between ω and the average of the Larmor frequencies of the two pair partners $\omega' = \frac{1}{2}(\omega_a + \omega_b)$ and the Rabi frequency Ω in units of γB_1 for two systems with strong light-field coupling. In (a) the result is shown for the calculation of a single pair ($\cong$ δ-like g-factor distribution), in (b) for an ensemble of 81 correlated pairs. Eqn. 9.1 was solved without the stochastic operator $\mathcal{S}$, $\frac{\delta}{2\pi} = 3\,\mathrm{MHz}$, the remaining parameters are given in the caption of Fig. 11.5.

all calculations this symmetry point is the area of the highest intensity in the 3-d plots. To investigate the ratio of the intensity between p_s and the arms, we have chosen $(10.006, 0.024)$ as a reference point inside the arm of the resonance. The corresponding intensities will be labelled with I_1^i for that of p_s and I_2^i for the arm, the upper index i labels the number of pairs used in the calculation. For one system one gets $I_1^1 = 16500$ and $I_2^1 = 7000$ (both in arbitrary units). This results in a ratio $\frac{I_1^1}{I_1^1} \approx 2.35$.

The distribution of Us

For an ensemble with a correlated g-factor distribution the Larmor-frequency difference $\Delta\omega$ is the same for all intermediate pairs. The geometric translation is the following: The symmetry point is shifted in ω-direction, but its Ω-coordinate stays constant. This is rather obvious since by change of $\omega_{a(b)}$ the frequency of the resonant excitation changes but the value of the Rabi- frequency stays constant as long as the regime of strong light-field coupling is not left. The g-factor distribution leads to a distribution of Us which is schematically shown in

Fig. H.1(b). It is obvious, that only Us contribute to the intensity at (10,0.02) that have their s_p within the interval $W = [9.999, 10.001]$ with width $h = \frac{2}{2\pi}$ MHz. The simulated data shown in Fig. H.2(a)[4] was achieved by considering a single pair only that corresponds to an ensemble with the δ-like g-factor distribution shown in Fig. 11.2(a). While Fig. H.2(b) was simulated using an ensemble of i = 81 pairs and Gaussian g-factor distribution with a standard deviation of $\frac{\delta}{2\pi} = 3$ MHz. We have distributed the g-factors of the pair partners evenly over a range with the width of 4δ. The number f of systems whose U-signature in the $\Omega - \omega$-plane overlaps with the point (10,0.02) is

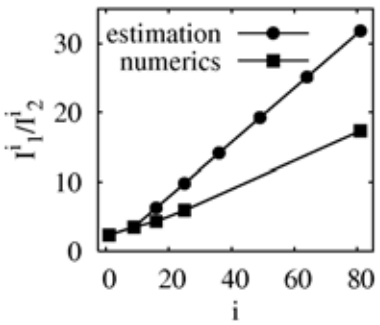

Fig. H.3. Ratio of I_1^i/I_2^i against the number of pairs i estimated as given in the text and obtained by the numerical calculations.

$$f_i = i\frac{h}{4\delta}$$

Thus for the calculation of the number of system signals contributing to the sharp S_1 signature displayed in Fig. H.2(b), we get

$$f_{81} = 81\frac{2\text{MHz}}{12\text{MHz}} = 13.5$$

that denotes the factor between $\frac{I_1^1}{I_2^1}$ and $\frac{I_1^{81}}{I_2^{81}}$. To summarize the given simple geometric explanation for the origin of this increase of f_i with increasing i for the discussed scenario is:

- The centers of the S_1-resonance sum up at $(\omega_0, 2\gamma B_1)$.
- The arms of the S_1-resonance do not sum up, as they stay parallel.

We have to mention that so far we have neglected in the discussion the Gaussian distribution of the U's intensities: i.e. the system with p_s at (10, 0.02) has the maximum intensity, while a system located outside with a symmetry point at $(10 + 2\delta,\ 0.02)$ is almost not visible anymore. For simplicity we assume that all systems within the interval W with width h centered around $\frac{\omega}{2\pi} = 0.02$ GHz have the same weight factor, i.e. the same intensity. Thus

[4] Due to the symmetry of the 3-d plots (and thus without loss of information) the results shown in this section display only about $\frac{1}{4}$ of the (Ω, ω) plane shown e.g. in Fig. 10.4.

we substitute the Gaussian distribution with a constant. This leads to the intensity at (10, 0.02) of $I_1^i \propto f_i I_1^1$ while the largest intensity in the region of the arms is the one of the system whose p_s is at (10, 0.02), i.e. will be $I_2^i \propto I_2^1$. Herewith one gets the ratio between peak and arm intensities of the S_1 resonance depending on the system number i

$$\frac{I_1^i}{I_2^i} = f_i \frac{I_1^1}{I_2^1}. \tag{H.1}$$

This leads in the case of $9 \cdot 9 = 81$ pairs to the ratio between the bottom and the reference point of the arm

$$\frac{I_1^{81}}{I_2^{81}} = 13.5 \cdot 2.35 \approx 32.$$

In Fig. H.3 we have compared the result of the theoretical estimation using Eqn. H.1 with the numerical values obtained by an extraction of the peak intensities out of the calculated data. The fact that the numerical values are smaller than the predicted ones is not surprising. Calculated signals do not have exact U-form which leads to an overestimation of the number f of systems overlapping in (10, 0.02) when deriving f_i in comparison with the reality. Furthermore, taking into account the Gaussian distribution leads to smaller contributions of the *outer* systems to the peak.

A comment on the the spin $\frac{1}{2}$ peak

The question, whether the $S_{\frac{1}{2}}$ resonance does not show a behavior similar to the S_1 resonance, can also be understood easily on the basis of the given simple geometric explanation. One can suppose a U-form again, but the bottom has a hole as depicted in, for example, Fig. 11.5(d). Therefore the influence of the summation of different Us becomes much weaker in their middle point. On the other hand this hole in the U structure seen in the calculations of $\Omega = \mathrm{FT}(\Delta\sigma(t))$ versus ω for a single pair in the regime of strong light-field coupling disappears as the shifted holey Us overlap with the parts of U structures of other ensemble members.

References

1. G. A. Prinz, Science **250**, 1092 (1990).
2. S. Das Sarma, Am. Sci. **89**, 516 (2001).
3. F. Matsukura, H. Ohno, A. Shen, and Y. Sugawara, Phys. Rev. B **57**, R2037 (1998).
4. J. Sadowski, R. Mathieu, P. Svedlindh, J. Z. Domanga, J. Bak-Misiuk, K. Swiatek, M. Karlsteen, K. Kanski, H. Åsklund, and U. Södervall, Appl. Phys. Lett. **78**, 3271 (2001).
5. M. Csontos, T. Wojtowicz, X. Liu, M. D. B. Janko, J. K. Furdyna, G. Mihaly, Phys. Rev. Lett. **95**, 22 (2005).
6. M. Yokoyama, Y. Yamaguchi, T. Ogawa, and M. Tanaka, J. Appl. Phys. **97**, 10D3171 (2005).
7. P. B. Parchinskiy, F. C. Yu, S. Y. Jeong, C. Gao, D. Kim, H. Kim, and Y. E. Ihm, Appl. Surf. Sci. **253**, 515 (2006).
8. P. B. Parchinskiy, F. C. Yu, C. Gao, S. W. Lee, D. Kim, H. Kim, and Y. E. Ihm, J. Electroceram. **17**, 1047 (2006).
9. A. Kwiatkowski, D. Wasik, M, Kamińska, R. Bożek, J. Szczytko, A. Twardowski, J. Borysiuk, J. Sadowski, and J. Gosk, J. Appl. Phys. **101**, 113912 (2007).
10. C. Michel, P. J. Klar, S. D. Baranovskii and P. Thomas, Phys. Rev. B **69**, 165211 (2004).
11. K. T. Nam, N. Watanabe, S. Kuroda and K. Takita, J. Superconductivity: Incorporating Novel Magnetism **16**, 335 (2003).
12. S. Ye, P. J. Klar, T. Henning, M. Lampalzer, W. Stolz and W. Heimbrodt, J. Superconductivity: Incorporating Novel Magnetism **16**, 159 (2003).
13. H. Ohno, F. Matsukura and Y. Ohno, Solid State Commun. **119**, 281 (2001).
14. O. Goede and W. Heimbrodt, Phys. Stat. Sol. B **146**, 11 (1988).
15. J. K. Furdyna, J. Appl. Phys. **64**, R29 (1988).
16. H. Ohno, J. Magn. Magn. Mater. **200**, 110 (1999).
17. T. Dietl, Physica E **10**, 120 (2001).
18. T. Omiya, F. Matsukura, A. Shen, Y. Ohno, H. Ohno, Physica E **10**, 206 (2001).
19. S. Wolff, D. D. Awschalom, R. A. Buhrmann, J. M. Daughton, S. von Molnar, M. L. Roukes, A. Y. Chtchelkanova, D. M. Treger, Science **294**, 1488 (2001).

20. J. Schneider, U. Kaufmann, W. Wilkening, M. Baeumler, and F. Köhl, Phys. Rev. B **59**, 240 (1987).
21. C. L. Chan, J. Electron. Mater **22**, 1413 (1993).
22. T. Dietl, A. Haury, Y. Merle d' Aubigné, Phys. Rev. B **55**, 3347 (1997).
23. B. Grandidier, J. P. Nys, C. Delerue, D. Stievenard, Y. Higo and M. Tanaka, Appl. Phys. Lett. **77**, 4001 (2000).
24. T. Dietl, H. Ohno, and F. Matsukura, Phys. Rev. B **63**, 195205 (2001).
25. M. Abolfath, T. Jungwirth, J. Brum, and A. H. MacDonald, Phys. Rev. B **63**, 054418 (2001).
26. T. Dietl, H. Ohno, F. Matsukura, J. Cibert, and D. Ferrand, Science **287**, 1019 (2000).
27. T. Jungwirth, J. König, J. Sinova, J. Kucera, and A. H. MacDonald, Phys. Rev. B **66**, 012402 (2002).
28. K. Y. Wang, R. P. Campion, K. W. Edmonds, M. Sawicki, T. Dietl, C. T. Foxon, and B. L. Gallagher, AIP Conf. Proc. **772**, 333 (2005).
29. H. Sauvage, J. J. Rhyne, R. Holm, J. R. Cullen, C. E. Carroll, and E. P. Wohlfarth, phys. stat. sol. **58**, 658 (1937).
30. S. Nagata, R.R. Galazka, D.P. Mullin, H. Akbarzadeh, G.D. Khattak, J. K. Furdyna and P.H. Keesom, Phys. Rev. B **22**, 3331 (1980).
31. R. R. Galazka, S. Nagata and P. H. Keesom, Phys. Rev. B **22**, 3344 (1980).
32. J. K. Furdyna, J. Appl. Phys. **53**, 7637 (1982).
33. Y. Q. Yang, P.H. Keesom, J. K. Furdyna, and W. Giriat, J. Solid State Chem. **49**, 20 (1983).
34. B. T. Jonker, Y. D. Park, B. R. Bennett, H. D. Cheong, G. Kioseoglou, and A. Petrou, Phys. Rev. B **62**, 8180 (2000).
35. R. Fiederling, M. Keim, G. Reuscher, W. Ossau, G. Schmidt, A. Waag, L. W. Molenkamp, Nature (London) **402**, 787 (1999).
36. M. Oestreich, J. Hübner, D. Hägele, P. J. Klar, W. Heimbrodt, W. W. Rühle, D. E. Ashenford, and B. Lunn, Appl. Phys. Lett. **74**, 1251 (1999).
37. G. Schmidt, G. Richter, P. Grabs, C. Gould, D. Ferrand, and L.W. Molenkamp, Phys. Rev. Lett. **87**, 227203 (2001).
38. M. Tanaka, Semicond. Sci. Technol. **17**, 327 (2002).
39. P. J. Wellmann, J. M. Garcia, J. L. Feng, and P. M. Petroff, Appl. Phys. Lett. **73**, 3291 (1998).
40. H. Akinaga, J. De Boeck, G. Borghs, S. Miyanishi, A. Asamitsu, W. Van Roy, Y. Tomioka, and L.H. Kuo, Appl. Phys. Lett. **72**, 3368 (1998).
41. S. Ye, P. J. Klar, T. Hartmann, W. Heimbrodt, M. Lampalzer, S. Nau, T. Torunski, W. Stolz, T. Kurz, H. A. Krug von Nidda and A. Loidl, Appl. Phys. Lett. **83**, 3927 (2003).
42. D. R. Schmidt, A. G. Petukhov, M. Foygel, J. P. Ibbetson and S. J. Allen, Phys. Rev. Lett. **82**, 823 (1999).
43. M. Mizuguchi, H. Akinaga, K. Ono and M. Oshima, J. Appl. Phys. **87**, 5639 (2000).
44. H. Akinaga, S. Miyanishi, K. Tanaka, W. Van Roy and K. Onodera, Appl. Phys. Lett. **76**, 97 (2000).

45. Y. D. Park, A. Wilson, A. T. Hanbicki, J. E. Mattson, T. Ambrose, G. Spanos and B. T. Jonker, Appl. Phys. Lett. **78**, 2739 (2001).
46. Y. Shapira, N. F. Oliveira Jr, P. Becla and T. Q. Vu, Phys. Rev. B **41**, 5931 (1990).
47. Y. Shapira, D. H. Ridgley, K. Dwight, A. Wold, K. P. Martin and J. S. Brooks, J. Appl. Phys **57**, 3210 (1985).
48. Y. Shapira, N.F. Oliveira Jr., D.H. Ridgley, R. Kershaw, K. Dwight, and A. Wold, Phys. Rev. B **34**, 4187 (1986).
49. C. Haas, Phys. Rev. **168**, 531 (1968).
50. M. Sawicki, T. Dietl, J. Kossut, J. Igalson, T. Wojtowicz, and W. Plesiewicz, Phys. Rev. Lett. **56**, 508 (1986).
51. J. Stankiewicz, S. von Molnar, and W. Giriat, Phys. Rev. B **33**, 3573 (1986).
52. Y. Ono and J. Kossut, J. Phys. Soc. Jpn **53**, 1128 (1984).
53. T. Wojtowicz, T. Dietl, M. Sawicki, W. Plesiewicz, and J. Jaroszynski, Phys. Rev. Lett. **56**, 2419 (1986).
54. T. Dietl, J. Antoszewski, and L. Swierkowski, Physica B **117&118**, 491 (1983).
55. S.M. Ryabchenko, Y. G. Semenov, and O. V. Terletskii, Sov. Physics: Solid State **27**, 1746 (1985).
56. S. A. Crooker, D. G. Rickel, S. K. Lyo, N. Samarth, and D. D. Awschalom, Phys. Rev. B **60**, R2173 (1999).
57. H. Falk, P. J. Klar and W. Heimbrodt, Thin Solid Films **380**, 215 (2000).
58. P. J. Klar, H. Falk and W. Heimbrodt, Solid State Commun. **116**, 125 (2000).
59. H. Overhof, P. Thomas, *Electronic Transport in Hydrogenated Amorphous Semiconductors*, Springer Tracts in Modern Physics **Vol. 114**, (1989).
60. B. I. Shklovskii and A. L. Efros, *Electronic properties of doped semicodnuctors* (Springer, Heidelberg, 1984).
61. A. I. Efros and M. E. Raikh, *Effects of Composition Disorder on the Electronic Properties of Semiconducting Mixed Crystals* in *Optical Properties of Mixed Crystals*, edited by R.J. Elliott and I.P. Ipatova (Elsevier, New York, 1988).
62. D. Aerts *The One and the Many: Towards a Unification of the Quantum and the Classical Description of One and Many Physical Entities*, Doctoral Thesis, Brussels Free University, (1981).
63. D. Aerts and F. Valckenborgh, International Journal of Theoretical Physics **43**, 251 (2004).
64. A. Gliesche, private communication, (2007).
65. Lautenschläger, P. Garriga, M. Logothetidis, S. Cardona, M. Phys. Rev. B **35**, (1987) 9174.
66. O. Madelung, Semiconductors - Basic data, 2nd revised Edition (Springer, Berlin, 1996).
67. H. Overhof, M. Otte, M. Schmidtke, U. Backhausen and R. Carius, J. Non-Cryst. Sol. **230**, 992 (1998).
68. H. Overhof, M. Schmidtke, Phys. Rev. B **61**, 12977 (2000).
69. H. Overhof, W. Beyer, Phil. Mag. B **43**, 433 (1981).
70. P. W. Anderson, Phys. Rev. **109**, 1492 (1958).
71. A. G. Petukhov and M. Foygel, Phys. Rev. B **62**, 520 (2000).
72. M. Foygel, R. D. Morris and A. G. Petukhov, Phys. Rev. B **67**, 134204 (2003).

73. M. Umehara, Phys. Rev. B **67**, 035201 (2003).
74. J. H. Harris and A. V. Nurmikko, Phys. Rev. Lett. **51**, 1472 (1983).
75. A. Kaminski and S. Das Sarma, Phys. Rev. Lett. **88**, 247202 (2002).
76. P. A. Wolff, R. N. Bhatt and A. C. Durst, J. Appl. Phys. **79**, 5196 (1996).
77. P. A. Wolff and J. Warnock, J. Appl. Phys. **55**, 2300 (1984).
78. N. F. Mott, Phys. Rev. Lett. **31**, 466 (1973).
79. J. S. Blakemore, *Semiconductor Statistics* (Dover, Mineola, 1987).
80. S. Bhattacharyya, Phys. Rev. B **70**, 125412 (2004).
81. A. Narsale, Y. P. Ali, U. Bhambhani, V. P. Salvi, B. M. Arora, D. Kanjilal, G. K. Mehta, J. Appl. Phys. **82**, 4228 (1997).
82. A. Dussan, R. H. Buitrago, J. Appl. Phys. **97**, 043711 (2005).
83. J. Betko, M. Morovic, J. Novak, A. Förster, P. Kordos, J. Appl. Phys. **86**, 6234 (1999).
84. G. E. Stillman, C. M. Wolfe, and J. O. Dimmock, J. Phys. Chem. Solids **31**, 1199 (1970).
85. L. Bergqvist, O. Eriksson, J. Kudrnovsky, V. Drchal, P. Korzhavyi, and I. Turek, Phys. Rev. Lett. **93**, 137202 (2004).
86. L. Bergqvist, O. Eriksson, J. Kudrnovsky, V. Drchal, A. Bergman, L. Nordström, and I. Turek, Phys. Rev. B **72**, 195210 (2005).
87. M. Abolfarth, T. Jungwirth, A. H. MacDonald, Physica E **10**, 161 (2001).
88. T. Jungwirth, W. A. Atkinson, B. H. Lee, A. H. MacDonald, Physica E **6**, 794 (2000).
89. T. Jungwirth, B. Lee, and A. H. MacDonald, Physica E **10**, 153 (2001).
90. T. Jungwirth, K. Y. Wang, J. Masek, K. W. Edmonds, J. König, J. Sinova, M. Polini, N. A. Goncharuk, A. H. MacDonald, M. Sawicki, A. W. Rushforth, R. P. Campion, L. X. Zhao, C. T. Foxon, and B. L. Gallagher, Phys. Rev. B **72**, 165204 (2005).
91. T. Jungwirth,J. Masek, K. Y. Wang, K. W. Edmonds, M. Sawicki, M. Polini, J. Sinova, A. H. MacDonald, R. P. Campion, L. X. Zhao, N. R. S. Farley, T. K. Johal, G. van der Laan, C. T. Foxon, and B. L. Gallagher, Phys. Rev. B **73**, 165205 (2006).
92. T. Dietl, F. Matsukura, and H. Ohno, Phys. Rev. B **66**, 033203 (2002).
93. T. Dietl, J. König, and A. H. MacDonald, Phys. Rev. B **64**, R241201 (2000).
94. D. Chiba, Y. Nishitani, F. Matsukura, and H. Ohno, Appl. Phys. Lett. **90**, 122503 (2007).
95. T. Omiya, F. Matsukura, T. Dietl, Y. Ohno, T. Sakon, M. Motokawa and H. Ohno, Physica E **7**, 976 (2000).
96. M. Lampalzer, K. Volz, W. Treutmann, S. Nau, T. Torunski, M. Megges, J. Lorberth, and W. Stolz, J. Cryst. Growth **248**, 474 (2003).
97. J. Sadowski, J. Z. Domagala, J. Bak-Misiuk, S. Kolesnik, M. Sawicki, K. Swiatek, J. Kanski, L. Ilver, and V. Ström, J. Vac. Sci. Technol. B **18**, 1697 (2000).
98. A. Van Esch, L. Van Bockstal, J. de Boeck, G. Verbanck, A. S. van Steenbergen, P. J. Wellmann, B. Grietens, R. Bogaerts, F. Herlach, and G. Borghs, Phys. Rev. B **56**, 13103 (1997).
99. K. W. Edmonds, K. Y. Wang, R. P. Campion, A. C. Neumann, N. R. S. Farley, B. L. Gallagher, and C. T. Foxon, Appl. Phys. Lett. **81**, 4991 (2002).

100. F. Tuomisto, K. Pennanen, K. Saarinen, and J. Sadowski, Phys. Rev. Lett. **93**, 55505 (2004).
101. F. Glas, G. Patriarche, L. Largeau, and A. Lemaitre, Phys. Rev. Lett. **93**, 86107 (2004).
102. G. Bouzerar, T. Ziman, and J. Kudrnovsky, Phys. Rev. B **72**, 1252071 (2005).
103. A. Wolos, M. Kaminska, M. Palczewska, A. Twardowski, X. Liu, T. Wojtowicz and J. K. Furdyna, J. Appl. Phys. **96**, 530 (2004).
104. K. Y. Wang, K. W. Edmonds, R. P. Campion, B. L. Gallagher, N. R. S. Farley, M. Sawicki, P. Boguslawski, and T. Dietl, J. Appl. Phys. **95**, 6512 (2004).
105. P. Mahadevan and A. Zunger, Phys. Rev. B **68**, 75202 (2003).
106. T. Hayashi, Y. Hashimoto, S. Katsumoto and Y. Iye, Appl. Phys. Lett. **78**, 1691 (2001).
107. K. C. Ku, S. J. Potashnik, R. F. Wang, S. H. Chun, P. Schiffer, N. Samarth, M. J. Seong, A. Mascarenhas, E. Johnston-Halperin, R. C. Myers, A. C. Gossard, and D. D. Awschalom, Appl. Phys. Lett. **82**, 2302 (2003).
108. B. S. Sorensen, P. E. Lindelof, J. Sadowski, R. Mathieu and P. Svedlindh, Appl. Phys. Lett. **82**, 2287 (2003).
109. K. M. Yu and W. Walukiewicz, T. Wojtowicz, I. Kuryliszyn, X. Liu, Y. Sasaki and J. K. Furdyna, Phys. Rev. B **65**, 201303 (2002).
110. S. J. Potashnik, K. C. Ku, S. H. Chun, J. J. Berry, N. Samarth, and P. Schiffer, Appl. Phys. Lett. **79**, 1495 (2001).
111. B. J. Kirby, J. A.Borchers, J. J. Rhyne, K. V. O'Donovan, T. Wojtowicz, X. Liu, Z. Ge, S. Shen and J. K. Furdyna, Appl. Phys. Lett. **86**, 72506 (2005).
112. K. W. Edmonds, P. Boduslawski, K. Y. Wang, R. P. Campion, S. N. Novikow, N. R. S. Farley, B. L. Gallagher, C. T. Foxon, M. Sawicki, T. Dietl, M. Buongiorno Nardelli, and J. Bernhole, Phys. Rev. Lett. **92**, 372011 (2004).
113. D. E. Bliss, W. Walukiewicz, J. W. Ager, E. E. Haller, K. T. Chan, and S. Tanigawa, J. Appl. Phys. **71**, 1699 (1992).
114. C. Michel, S. D. Baranovskii, P. Thomas, W. Heimbrodt, M. T. Elm, P. J. Klar, B. Goldlücke, U. Wurstbauer, M. Reinwald, W. Wegscheider, J. Appl. Phys. **102**, 073712 (2007).
115. C. Michel, M. T. Elm, S. D. Baranovskii, P. Thomas, W. Heimbrodt, B. Goldlücke, P. J. Klar, Phys. Stat. Sol., accepted (2007).
116. V. V. Ryl'kov, B. A. Aronzon, Yu. A. Danilov, Yu. N. Drozdov, V. P. Lesnikov, K. I. Maslakov and V. V. Polol'skii, JETP **100**, 742 (2005).
117. A. Pross, S. Bending, K. Edmonds, R. P. Campion, C. T. Foxon, and B. Gallagher, J. Appl. Phys. **95**, 3225 (2004).
118. A. Pross, S. Bending, K. Edmonds, R. P. Campion, C. T. Foxon, and B. Gallagher, J. Appl. Phys. **95**, 7399 (2004).
119. A. Pross, S. J. Bending, K. W. Edmonds, R. P. Campion, C. T. Foxon, B. Gallagher, and M. Sawicki, J. Appl. Phys. **99**, 939081 (2006).
120. K. W. Edmonds, K. Y. Wang, R. P. Campion, A. C. Neumann, C. T. Foxon, B. L. Gallagher, and P. C. Main, Appl. Phys. Lett. **81**, 3010 (2002).
121. J. Schliemann, J. König, H. H. Lin, and A. H. MacDonald, Appl. Phys. Lett. **78**, 1550 (2001).
122. M. P. Kennett, M. Berciu, and R. N. Bhatt, Phys. Rev. B **65**, 115308 (2002).

123. T. Hartmann, S. Ye, P. J. Klar, W. Heimbrodt, M. Lampalzer, W. Stolz, T. Kurz, A. Loidl, H. A. Krug von Nidda, D. Wolverson, J. J. Davies, and H. Overhof, Phys. Rev. B **70**, 233201 (2004).
124. J. Okabayashi, A. Kimura, O. Rader, T. Mizokawa, A. Fujimori, T. Hayashi, M. Tanaka, Phys. Rev. B **58**, R4211 (1998).
125. Y. Satoh, D. Okazawa, A. Nagashima, J. Yoshino, Physica E **10**, 196 (2001).
126. T. C. Lee and W. W. Anderson, Solid State Commun. **2**, 265 (1964).
127. W. Schairer and M. Schmidt, Phys. Rev. B **10**, 2501 (1974).
128. R. A. Chapman and W. G. Hutchinson, Phys. Rev. Lett. **18**, 445 (1967).
129. C. Michel, S. D. Baranovskii, P. J. Klar, P. Thomas and B. Goldlücke, Appl. Phys. Lett. **89**, 112116 (2006).
130. K. Y. Wang, K. W. Edmonds, R. P. Campion, L. X. Zhao, C. T. Foxon, and B. L. Gallagher, Phys. Rev. B **72**, 085201 (2005).
131. H. A. Krug von Nidda, T. Kurz, A. Loidl, T. Hartmann, P. J. Klar, W. Heimbrodt, M. Lampalzer, K. Volz, and W. Stolz, J. Phys. Cond. Mat. **18**, 6071 (2006).
132. C. Michel, C. H. Thien, S. Ye, P. J. Klar, W. Heimbrodt, S. D. Baranovskii, P. Thomas, M. Lampalzer, K. Volz, W. Stolz, and B. Goldlücke, Superlatt. & Microstruct. **37**, 321 (2005).
133. W. Heimbrodt, P. J. Klar, S. Ye, M. Lampalzer, C. Michel, S. D. Baranovskii, P. Thomas, and W. Stolz, J. Supercond. **18**, 315 (2005).
134. M. Fischer and J. S. Langer, Phys. Rev. Lett. **20**, 665 (1968).
135. C. Timm, M. E. Raikh, and F. von Oppen, Phys. Rev. Lett. **94**, 36602 (2005).
136. S. Ye, *Magnetotransport in (Ga,Mn)As alloys and hybrids*, Philipps-Universität Marburg, Dissertation (2005).
137. G. Alvarez, E. Dagotto, J. Magn. Magn. Mater. **272**, 15 (2004).
138. J. Sadowski, E. Janik, E. Jusakowska, J. Z. Domagala, S. Kret, P. Diluzewski, M. Adell, J. Kanski, L. Ilver, R. Brucas, an M. Hanson, Appl. Phys. Let.**87**, 263114 (2005).
139. S. J. Potashnik, K. C. Ku, R. Mahendrian, S. H. Chun, R. F. Wang, N. Samarth, and P. Schiffer, Phys. Rev. B **66**, 012408 (2002).
140. T. Wojtowicz, J. K. Furdyna, X. Liu, K.M. Yu, and W. Walukiewicz, Physica E **25**, 171 (2004).
141. O. D. D. Couto, Jr. M. J. S. P. Brasil, F. Likawa, C. Giles, C. Adriano, J. R. R. Bortoleto, M. A. A. Pudenzi, and H. R. Gutierrez, Appl. Phys. Lett. **86**, 071906 (2005).
142. M. Moreno, B. Jenichen, I. Däwenitz. and K. H. Ploog, J. Appl. Phys. **92**, 4672 (2002).
143. J. De Boeck, R. Oesterholt, A. Van Esch, H. Bender, C. Bruynseraede, C. Van Hoof, and G. Borghs, Appl. Phys. Lett. **68**, 2744 (1996).
144. I. Galanakis and P. Mavropoulos, Phys. Rev. B **67**, 104417 (2003).
145. M. C. Qian, C. Y. Fong, W. E. Pickett, H. Y. Wang, J. Appl. Phys. **95**, 7459 (2004).
146. S. Sanvito, G. Theurich, N. A. Hill, J. Supercond. **15**, 85 (2002).
147. A. Continenza, S. Picozzi, W. T. Geng, A. J. Feeman, Phys. Rev. B **64**, 085204 (2001).

148. B. Sanyal, L. Bergqvist and O. Eriksson, Phys. Rev. B **68**, 054417 (2003).
149. A. Janotti, S-H. Wei, L. Bellaiche, Appl. Phys. Lett. **82**, 766 (2002).
150. E. H. Rhoderick and R. H. Williams, *Metal-Semiconductor Contacts*, (Oxford Science Publications, New York, 1988).
151. P. Mahadevan, A. Zunger and D. Das Sarma, Phys. Rev. Lett. **93**, 177201 (2004).
152. Y. J. Zhao, P. Mahadevan and A. Zunger, Appl. Phys. Lett. **84**, 3753 (2004).
153. T. Dietl, Physica E **10**, 120 (2001).
154. P. Mahadevan, J. M. Osorio-Guillen and A. Zunger, Appl. Phys. Lett. **86**, 172504 (2005).
155. Y. J. Zhao and A. Zunger, Phys. Rev. B **71**, 132403 (2005).
156. C. B. Murray, C. R. Kagan, and M. G. Bawendi, Annu. Rev. Mater. Sci. **30**, 545 (2000).
157. J. I. Martin, J. Nogues, K. Liu, J. L. Vincent, and I. K. Schuller, J. Magn. Magn. Mater. **256**, 449 (2003).
158. S. A. Solin, T. Thio, D. R. Hines, J. J. Heremans, Science **289**, 1530 (2000).
159. J. Moussa, L. R. Ram-Mohan, J. Sullivan, T. Zhou, D. R. Hines, and S. A. Solin, Phys. Rev. B **64**, 184410 (2001).
160. A. C. H. Rowe and S. A. Solin, Phys. Rev. B **71**, 235323 (2005).
161. M. Holz, O. Kronenwerth, and D. Grundler, Appl. Phys. Lett. **86**, 072513 (2005).
162. M. Holz, O. Kronenwerth, and D. Grundler, Appl. Phys. Lett. **87**, 172501 (2005).
163. D. Kaplan, I. Solomon, and N. F. Mott, J. Phys. (Paris) – Lettres **39**, L51 (1978).
164. R. Haberkorn and W. Dietz, Solid State Commun. **35**, 505 (1980).
165. C. Boehme and K. Lips, Phys. Rev. Lett. **91**, 246603 (2003).
166. A. R. Stegner, C. Boehme, H. Huebl, M. Stutzmann, K. Lips and M. S. Brandt, Nature Physics **2**, 835 (2006).
167. F. H. L. Koppens, C. Buizert, K. J. Tielrooij, I. T. Vink, K. C. Nowack, T. Meunier, L. P. Kouwenhoven, and L. M. K. Vandersypen, Nature **442**, 766 (2006).
168. H. J. Möller, *Semiconductors for Solar Cells* (Artech House, Boston, London, 1993).
169. C. Boehme, *Dynamics of spin-dependent charge carrier recombination* (Cuvillier Verlag, Göttingen, 2003).
170. B. C. Cavenett, Advance in Physics **30**, 475 (1981).
171. M. Stutzmann, M. S. Brandt, and M.W. Bayerl, J. Non–Cryst. Solids **266-269**, 1 (2000).
172. M. Xia, I. Martin, E. Yablonovitch, and H. W. Jiang, Nature (London) **430**, 435 (2004).
173. F. Jelezko, T. Gaebel, I. Popa, A. Gruber, and J. Wrachtrup, Phys. Rev. Lett. **92**, 076401 (2004).
174. D. J. Lepine, Phys. Rev. B **6**, 436 (1972).
175. F. C. Rong, W. R. Buchwald, E. H. Poindexter, W. L. Warren, and D. J. Keeble, Solid–State Electron. **34**, 835 (1991).
176. C. Boehme and K. Lips, Phys. Stat. Sol. C **1**, 1255 (2004).

177. F. Friedrich, C. Boehme, and K. Lips, J. Appl. Phys. **97**, 056101 (2005).
178. T. Eickelkamp, S. Roth, and M. Mehring, Mol. Phys. **95**, 967 (1998).
179. K. Lips and W. Fuhs, J. Appl. Phys. **74**, 3993 (1993).
180. C. Boehme and K. Lips, Phys. Rev. B **68**, 245105 (2003).
181. C. Boehme and K. Lips, in *Charge Transport in Disordered Solids with Applications in Electronics*, edited by S. Baranovski (John Wiley and Sons, Ltd., Chichester, England, 2006), Chap. 5, pp. 179–219.
182. A. G. Redfield, IBM J. Res. Dev. **1**, 19 (1957).
183. A. G. Redfield, Adv. Magn. Reson. **1**, (1965).
184. V. Rajevac, C. Boehme, C. Michel, A. Gliesche, K. Lips, S. D. Baranovskii and P. Thomas, Phys. Rev. B **74**, 245206 (2006).
185. W. Harneit, C. Boehme, S. Schaefer, K. Huebner, K. Fostiropoulos, and K. Lips, Phys. Rev. Lett. **98**, 216601 (2007).
186. B. Stich, S. Greulich-Weber, and J. M. Spaeth, J. Appl. Phys. **77**, 1546 (1994).
187. J.-M. Spaeth and H. Overhof, *Point Defects in Semiconductors and Insulators* (Springer, Berlin, 2002).
188. J. Klein and R. Volz, Phys. Rev. Lett. **36**, 1214 (1976).
189. V. Weis, K. Möbius, and T. Prisner, J. magn. Res.**131**, 17 (1998).
190. C. Boehme and K. Lips, J. Mater Sci: Mater Electron, (2007).
191. D. J. Gravesteijn and M. Glasbeek, Phys. Rev. B **19**, 5549 (1979).
192. J. Wrachtrup, C. von Borczyskowski, J. Bernard, M. Orrit, and R. Brown, Nature **363**, 244 (1993).
193. J. Köhler, J. A. J. M. Disselhorst, M. C. J. M. Donckers, E. J. J. Groenen, J. Schmidt, and W. E. Moerner, Nature **363**, 242 (1993).
194. K. Lips, C. Boehme, and T. Ehara, Journal of Optoelectronics and Advanced Materials **7**, 13 (2004).
195. M. Otte, *Modellierung der Transporteigenschaften von hydrogeniertem mikrokristallinem Silizium*, Dissertation, Paderborn (1997).
196. M. Schmidtke, *Modellrechnung zum elektronischen Transport in ungeordneten Halbleitern*, Diploma Thesis, Paderborn (1998).
197. H. van der Horst, SIAM J. Sci. Statist. Comput. **13**, 631 (1992).
198. E. Jäger and R. Perthel, *Magnetische Eigenschaften von Festkörpern* (Akademie Verlag, Berlin, 1996).

List of constants, variables and conventions

Constants of nature

$c = 299792458\,\mathrm{ms}^{-1}$	speed of light in vacuum
$k_\mathrm{B} = 1.380662 \times 10^{23}\,\mathrm{JK}^{-1}$	Boltzmann's constant
$\hbar = 1.054589 \times 10^{-34}\,\mathrm{Js}$	Planck's constant ($h = 2\pi\hbar$)
$m_e = 9.109534 \times 10^{-31}\,\mathrm{kg}$	electron mass
$e = 1.6021892 \times 10^{-19}\,\mathrm{As}$	electron charge
$\mu_\mathrm{B} = \frac{e\hbar}{2m_e} = 9.2741 \times 10^{-24}\,\mathrm{JT}^{-1}$	Bohr's magneton
$\mu_0 = 4\pi \times 10^{-7}\,\frac{\mathrm{Vs}}{\mathrm{Am}}$	permeability of vacuum (defined)

Variables used in part I

ρ	resistivity
ν	conductivity
q	charge of the carrier
n	carrier density
μ	mobility
τ	average time between two scattering events
$m^\star$	effective mass
E_V	valence-band edge

List of constants

$N(E)$	density of states of the unperturbed valence band
$F^h(E)$	Fermi distribution of holes
F^{e}	Fermi distribution of electrons
$\tilde{\rho}$	pre-exponential factor in the Arrhenius equation
Δ	activation energy
$E_V(\mathrm{r})$	local valence-band edge
$\bar{E_V}(r)$	averaged local valence-band edge
E_m	mobility edge
$\Delta\bar{E}(r)$	energy spacing between $\bar{E_V}(r)$ and E_A
MR	magnetoresistance
T	temperature
ρ_m	resistivity in presence of an external magnetic field
ρ_0	resistivity in absence of an external magnetic field
T_{C}	Curie temperature
Θ	Curie-Weiss parameter
$\mathbf{H}$	external magnetic field
H	magnetic-field intensity
$\mathcal{H}_{\mathrm{m}}$	magnetic part of the single-particle Hamilton-operator
$\mathcal{H}$	single-particle Hamilton-operator
$\mathcal{H}_{\mathrm{ex}}$	part of $\mathcal{H}_{\mathrm{m}}$ describing the exchange interaction between localized magnetic ion and carrier
$\mathbf{s}$	spin operator of a free carrier
$\mathcal{S}_i$	spin operator for magnetic ion on lattice site i
$\mathcal{H}_{\mathrm{L}}$	part of the Hamilton operator describing the diamagnetic Landau quantization
g	Landé factor of the electron
μ_{B}	Bohr's magneton
μ_0	permeability of the vacuum
$J'_{i,j}$	Heisenberg notation of the coupling constant describing the interaction between magnetic ions on lattice site i and j
J_i	Heisenberg notation of the coupling constant describing the interaction between carrier and magnetic ion on lattice site i
$< S_z >$	thermal average of the Mn ion spin
B_f	the Brillouin function
ζ'	argument of the Brillouin function
$E_V^{(m)}(j_z, T, H)$	valence-band shift of subband with pseudospin j_z for field H and temperature T (of cell with index m)
S	spin of the magnetic ion
$N_0\beta$	value of the p-d exchange integral
a	parameter representing the antiferromagnetic coupling between Mn ions

x	average Mn concentration
j_z	carrier spin
DOS	density of states
m_l	effective mass of the light hole
m_h	effective mass of the heavy hole
μ_h	mobility of the heavy hole
μ_l	mobility of the light hole
l_c	lattice constant
$N_V^{j_z}$	density of states of the valence-band subband with pseudospin j_z
$V(j_z)$	valence-band subband with pseudospin j_z
E_G	gap energy
$n_C^{(m)}$	density of electrons in the conduction band (in cell m)
$n_A^{(m)}$	density of negatively charged acceptor states (in cell m)
E_F	Fermi energy
V	an unspecified volume
x_{loc}	local concentration of Mn ions
l	edge length of a model cube
l_i	the inelastic scattering length
E	energy
K	number of model cubes in x- and y-direction
ΔE_D	local valence-band shift induced by magnetic-field independent disorder
m_D	parameter describing the magnitude of magnetic-field independent disorder
$F^e(E)$	Fermi distribution of electrons
$E_C^{(m,j_z)}$	conduction-band edge (in cell m for conduction-band subband with pseudospin j_z)
$N_C^{mj_z}$	density of states of the conduction-band subband with pseudospin j_z in cell m
p_V^{m,j_z}	density of holes in the valence-band subband with pseudospin j_z in cell m
$N_V^{m,j_z}(E)$	density of states of the valence-band subband with pseudospin j_z in cell m
$\rho_{j_z}^m$	resistivity of the valence-band subband of pseudospin j_z in cell m in presence of an external magnetic field
K_m	knot of the resistor-network cell with index m
$R_{n,m}$	resistance of the conducting connection between the network knots n and m
$U_{n,m}$	fall of potential between the network knots n and m

List of constants

I_m^i	the ith in- or outgoing current for cell m
E_A	acceptor-energy level
β	exponent in the Arrhenius law, required for the description of the transport mode dominated by variable range hopping
DOI	density of impurity atoms
γ	exponent used for the description of the temperature dependent mobility
$\tilde{N}(E)$	density of states modified by a low energy exponential tail
α	onset of the exponential tail of the density of states
δ	damping of the exponential decay of $\tilde{N}(E)$
$N(E)^{-1}$	inverse function of the ideal DOS
N_A	density of acceptor states
σ	width of the Gaussian shaped energy distribution of acceptor states
ζ	normalization constant to assure that the sum over all cell probabilities to gain an Mn ion stays one
$max_{K^2}(E_\mathrm{V})$	maximum of all K^2 local valence-band subband edges
$\check{N}(E)$	normalized sum over all valence-band subbands density of states of all cells
M	magnetisation
M_0	saturation magnetisation
W	molecular-field constant
T_A	annealing temperature
α	proportionality between Mn concentration and Curie temperature
N_Mn	number of Mn ions of a (network) cell
χ	number of atoms per cubic unit cell
$T_{\mathrm{C}^{loc}}$	local Curie temperature
δT_C	deviation of the local Curie temperature from its mean value
x_{loc}^f	filtered value of the local concentration of Mn ions
$x_{i,j}^f$	filtered local Mn concentration of cell with coordinates (i,j)
o	parameter defining the filter size
l_C	cube-edge length of the network defining the local Curie temperature
n_Mn	total number of Mn ions in the modelled sample
l_U	lattice constant of the cubic unit cell of the zinc-blende lattice
ρ_Mn^0	probability of a cell to gain a Mn ion in absence of correlations
n_{Mn}^*	number of Mn ion in a specific cell at the time of the distribution run
n_1	factor describing Mn attraction of the cell itself
n_1	attraction factor describing the influence of

	the nearest neighbor cells
$\hat{A}$	the conductivity matrix
A_{ij}	entries of the conductivity matrix
ρ_{MiC}	resistivity of the minority band of the cluster
ρ_{MaC}	resistivity of the majority band of the cluster
E_{AC}	activation energy of carriers in the cluster minority-band
ρ_C^0	pre-exponential factor in the Arrhenius equation for the transport in the cluster minority-band
H_{ex}	field intensity of the external magnetic field
ρ_{sc}	resistivity with perfect spin conservation
ρ_p	resistivity in absence of spin conservation
E_{sa}	activation energy from the majority valence-band subband into the energetically closest minority valence-band subband
η	probability of loss of spin conservation
x_C	concentration of clusters in the sample
$\rho_{\uparrow(\downarrow)}$	resistivity of the system given by the parallel connection of the two subband resistor-networks for spin up (down)
$\Delta_C(m)$	distance of a semiconducting cell with index m from the nearest cluster cell in units of l
E_{S}	depth of the Schottky barrier
$\check{E}_V^m(j_z, T, H)$	valence-band shift of subband of pseudospin j_z in presence of an external field H in a matrix cell of a hybrid structure
H_C	field intensity of the magnetic field of the cluster
ΔE_M	activation energy of the majority band of the matrix
R_i	resistor representing a cube with index i
$\phi_{(i)}$	potential of a cell (with index i)
$G_{(ij)}$	reciprocal resistance of the path between the knots i and j
E_0	valence-band edge corresponding with the average Mn concentration for an arbitrary but fixed j_z
$\bar{\delta x}$	standard deviation of the local Mn distribution
Γ	derivative of E_V after x
$\delta E_V(m)$	deviation of the local valence-band edge (for a fixed but arbitrary j_z) from the average value E_0
$\delta \bar{E}_V$	averaged deviation of the local valence-band edge from the average value E_0 (for a fixed but arbitrary j_z)
Z	partition function of a canonical ensemble
H_i	field strength of the (inner) molecular field
M_0	saturation value of the magnetisation

Variables used in part II

$\mathcal{P}$	the polarization operator
$\hat{\rho}$	the density matrix
γ	the gyromagnetic ratio
$\mathbf{B}_0$	constant external magnetic field
B_0	strength of the constant external magnetic field
$\mathbf{B}_1$	external magnetic field induced by microwave radiation
B_1	strength of the external microwave radiation
$\Delta\omega$	the pair partners Larmor-frequency difference
$\mathcal{J}$	the angular momentum operator
S	spin quantum number
r_T	recombination rate coefficient of a triplet state
r_S	recombination rate coefficient of a singlet state
g	Landé factor in general
$g_{a(b)}$	the Landé factors of the pair partners with index $a(b)$
d	dissociation-rate coefficient of a pair state
$\omega_{a(b)}$	Larmor frequency of the pair partner with index $a(b)$
G	approximation of the pair-state generation-rate in first order
$G(t)$	time dependent generation rate of a pair state
G^s	steady-state generation rate of a pair state
G^*	(first order approximation of the) generation rate of electron-hole pairs due to the continuous wave light-field source
σ	the photoconductivity
$\Delta\sigma$	the change of the photoconductivity
$\mu_{e(h)}$	the mobility of electrons and holes respectively
e	electron charge
$n_{e(h)}$	density of electrons and holes respectively
$n^s_{e(h)}$	steady-state density of electrons and holes respectively
$\rho^s_{i,j}$	steady-state density-matrix elements
$\rho_{i,j}$	density-matrix elements
τ_l	averaged carrier lifetime
$\mathcal{H}$	Hamilton operator of a single pair
$\mathcal{H}_0$	Hamilton operator of a single spin-pair in absence of time dependent electromagnetic fields
$\mathcal{H}_1$	Hamilton operator of a single spin-pair exposed to a time dependent electromagnetic field
$\mathcal{S}$	stochastic operator
$\mathcal{R}$	Redfield operator

D^d	spin-dipolar coupling constant (in high field approximation)
$\tilde{D^d}$	normalized spin-dipolar coupling constant ($\tilde{D^d} = \frac{D^d}{\hbar^2}$)
J	spin-exchange interaction constant
$\tilde{J}$	normalized spin-exchange interaction constant ($\tilde{J} = \frac{J}{\hbar^2}$))
$\hat{H}_I(t)$	matrix representation of $\mathcal{H}_1$
$\hat{U}$	transformation matrix from product basis into basis of eigenstates
$\hat{H}_{dia}$	matrix representation of $\mathcal{H}_0$ in the basis of eigenstates
A, B, C, D	abbreviation of matrix elements of $\hat{U}$
V, W	abbreviation of matrix elements of $\hat{H}_{dia}$
$\mathcal{S}_a n$	annihilation part of $\mathcal{S}$ accounting for recombination and dissociation of pairs
$\mathcal{S}_c r$	creation part of $\mathcal{S}$ accounting for generation of pairs
$\Delta(\tau)$	relative change of density-matrix elements
ν	microwave frequency given in cycles per second
S_1	spin-1 resonance
$S_{\frac{1}{2}}$	spin-$\frac{1}{2}$ resonance
δ	standard deviation of the g-factor distribution
$\delta_{a(b)}$	standard deviation of the distribution of $g_{a(b)}$
$g^i_{a(b)}$	$g_{a(b)}$ of a pair with index i
$\bar{g}_{a(b)}$	average value of $g_{a(b)}$
Δg	difference of the average g-factors
ω^i	Larmor frequency of pair with index i
$\Delta\omega^i$	Larmor-frequency difference of pair partners with index i
ω^i_0	Larmor-frequency sum of the pair partners with index i
L_B	characteristic length-scale of the inner magnetic field
L	upper boundary of the localization length of an IP
L_i	an arbitrary length-scale
M	number of intermediate pairs in the total system
ω'	average of both pair partner's Larmor frequency
E^i_k	energy level k of the IP with index i

General symbol conventions

$\mathbf{B}$	boldface letters indicate vectors
$\mathcal{H}$	mathcal style indicates operator functionals
$\hat{\rho}$	hats indicate matrix representations of operators
$\|\uparrow\rangle$	bra–ket notation of Hilbert space elements
δ_{ij}	Kronecker's delta

List of publications

C. Michel, M. T. Elm, S. D. Baranovskii, P. Thomas, W. Heimbrodt, B. Goldlücke, P. J. Klar,
Influence of non-random incorporation of Mn ions on the magnetotransport properties of $Ga_{1-x}Mn_xAs$ alloys
Phys. Stat. Sol., in print (2007).

C. Michel, S. D. Baranovskii, P. Thomas, W. Heimbrodt, M. T. Elm, P. J. Klar B. Goldlücke, U. Wurstbauer, M. Reinwald, W. Wegscheider
Quantitative modelling of the annealing-induced changes of the magneto-transport in $Ga_{1-x}Mn_xAs$
J. Appl. Phys. **102**, 073712 (2007).

V. Rajevac, C. Boehme, C. Michel, A. Gliesche, K. Lips, S. D. Baranovskii, P. Thomas,
Transport and recombination through weakly coupled localized spin pairs in semiconductors during coherent spin excitation
Phys. Rev. B **74**, 245206 (2006).

C. Michel, S. D. Baranovskii, P. J. Klar, P. Thomas, B. Goldlücke,
Strong non-Arrhenius temperature dependence of the resistivity in the regime of traditional band transport
Appl. Phys. Lett. **89**, 112116 (2006).

C. Michel, C. H. Thien, S. Ye, P. J. Klar, W. Heimbrodt, S. D. Baranovskii, P. Thomas, M. Lampalzer, K. Volz, W. Stolz, B. Goldlücke,
Spin-dependent localization effects in GaAs:Mn/MnAs granular paramagnetic-ferromagnetic hybrids at low temperatures
Superlatt. & Microstruct. **37**, 321 (2005).

W. Heimbrodt, P. J. Klar, S. Ye, M. Lampalzer, C. Michel, S. D. Baranovskii, P. Thomas, W. Stolz,
Magnetic interactions in granular paramagnetic-ferromagnetic GaAs:Mn/MnAs hybrids
J. Supercond. **18**, 315 (2005).

C. Michel, P. J. Klar, S. D. Baranovskii, P. Thomas,
Influence of magnetic-field induced tuning of disorder and band structure on the magnetoresistance of paramagnetic dilute magnetic semiconductors
Phys. Rev. B **69**, 165211 (2004).

Acknowledgements

At this point I would like to sincerely thank all those, who have contributed over the years, to making my working environment a quite positive one. In particular I thank:

My advisor Prof. Dr. Peter Thomas who provided me with not only the opportunity to do my diploma but also this PhD thesis in his group. He gave me plenty of opportunity for independent work and always supported my decisions.

Prof. Dr. Peter J. Klar for his enthusiasm and for sharing his amazing knowledge of material-science issues. From the beginning of my diploma thesis on he spent lots of time, even at weekends, for discussions and answering my questions. Without Peter's help most of our publications would never have been released.

Prof. Dr. Sergei D. Baranovskii who is the third advisor of my research studies. I thank him for many discussions about transport in disordered systems. Not least, I am grateful to him for introducing me to Christoph Boehme and Klaus Lips.

Prof. Dr. Wolfram Heimbrodt for his permanent support and many stimulating hints. His, often rather exotic, remarks have helped to eliminate low points in my work. Due to his unpretentious way he always made it easy for me to ask him for advice.

Prof. Dr. Christoph Böhme for his invitation to Salt Lake City and his hospitality while introducing us to a new subject. I want to thank him as well for spending his time when answering my numerous questions to improve this thesis.

Prof. Dr. Gerhard Weiser for his help, in particular, the illuminating discussions about ESR and EDMR spectroscopy.

Dr. Bastian Goldlücke, who has been a friend since my years of study began, also played an essential role in the success of this work. His outstanding abilities in programming and numeric skills made him the best support one could have. Bastian visited me on many of his few free weekends in Marburg and joined the research in which, for him, is a foreign field. For this unselfishness and his real friendship I am deeply grateful to him.

My friend Dr. Aric Gliesche whom I know since our years of study as well. Without Arics participation in the work on spin-dependent recombination the second part of this thesis was hardly possible. In particular I want to thank him for his spontaneous acceptance of our invitation to Utah and the excellent teamwork.

Dr. Klaus Lips for many illuminating discussions and his straightforwardness as well as for his hospitality on our visit to the Hahn-Meitner Institute in Berlin.

Dr. Klaus Maschke for the supplied hospitality in his group in Lausanne. Despite the fact that the work of Aric and myself was far from his own research interests he was always sympathetic to our project.

My colleges in the physics departments in Marburg and Gießen for the good atmosphere. In particular Martin Güngerich for his helpfulness as well as my office mates Martin Schäfer and Marco Werchner I thank for their tolerance of my frequent guests and phone calls as well as their help to fix computational problems. Matthias Elm and Jörg Teubert I thank for providing their experimental results and for the numerous discussions as well as for their willingness to share their great overview about the studied material system with me. I have learned a lot from both of them. Dr. Shuangli Ye I also want to thank since I got lots of experimental data from her as well.

My friend Dr. Brian O'Sullivan who was also an office mate of mine in Marburg and who helped me a lot to reduce the amount of language errors in this thesis down to a passable dose.

Beruflicher Werdegang des Autors

Schulausbildung

1986 – 1995	Besuch des Gymnasiums Edertalschule in Frankenberg/Hessen
1995	Abitur

Wehrdienst

1995 – 1996	Wehrdienst im FmRgmt 320, Einheit für elektronische Kampfführung

Studium und wissenschaftliche Arbeit

1996 – 2002	Studium der Physik an der Philipps-Universität Marburg Nebenfächer: Chemie, Kernchemie
2000 – 2001	Arbeit als studentische Hilfskraft im Fachbereich Mathematik
1999 – 2002	Arbeit als studentische Hilfskraft im Fachbereich Physik
2003	Diplom an der Philipps-Universität Marburg; Titel der Diplomarbeit: *Zur Theorie des Magnetotransports in verdünnten magnetischen Halbleitern*
2003 – 2007	Kollegiat/Stipendiat des Europäischen Graduiertenkollegs *Electron-Electron Interactions in Solids*
11.2005	Gastaufenthalt an der École Polytechnique Fédérale de Lausanne in der Gruppe von Dr. Klaus Maschke in Lausanne, Schweiz
05./06.2006	Gastaufenthalt an der University of Utah in der Gruppe von Prof. Dr. Christoph Böhme in Salt Lake City, USA
2003 – 2007	Doktorand an der Philipps-Universität Marburg, Anfertigung der Dissertation als wiss. Mitarbeiter der Gruppe für theoretische Halbleiterphysik unter Betreuung von Prof. Dr. Peter Thomas, Prof. Dr. Peter J. Klar und Prof. Dr. Sergei D. Baranovski